City Research Online

City, University of London Institutional Repository

Citation: Gendy, S. S. F. M. (2018). Explicit second-order mixed formulation of reinforced concrete structures under impact loading. (Unpublished Doctoral thesis, City, University of London)

This is the accepted version of the paper.

This version of the publication may differ from the final published version.

Permanent repository link: http://openaccess.city.ac.uk/19116/

Link to published version:

Copyright and reuse: City Research Online aims to make research outputs of City, University of London available to a wider audience. Copyright and Moral Rights remain with the author(s) and/or copyright holders. URLs from City Research Online may be freely distributed and linked to.

City Research Online: http://openaccess.city.ac.uk/ publications@city.ac.uk

Explicit Second-order Mixed Formulation of Reinforced Concrete Structures under Impact Loading

Samer Sabry Fahmy Mehanny Gendy

A thesis submitted in fulfilment of the requirements for the degree of

Doctor of Philosophy

at

City, University of London
School of Mathematics, Computer Science & Engineering

January 2018

TABLE OF CONTENTS

LIST OF FIGURES

LIST OF TABLES

ACKNOWLEDGEMENTS

I would like to express my deepest appreciation to my first supervisor Prof. Ashraf Ayoub for his valuable support and guidance during my doctoral program. Without his supervision and constant help, this dissertation would not have been possible. I also wish to thank my second supervisor Dr. Feng Fu for accepting my PhD research proposal and participating in my MPhil to PhD transfer exam.

I would like to thank my dissertation committee members, Prof. Andreas Kappos, Prof. Theodore Karavasilis and Dr. Tatyana Micic who provided constructive comments and valuable insight on the content of this dissertation.

I would like to express my gratitude to my mother for her love, support and prayers. I would like also to thank my wife, Mona, who encouraged and emotionally supported me during the period of my study. I also dedicate my PhD work to my lovely child Robert who fills my heart with love and joy. I would like to extend my deepest thanks to my brother, Saher, and my cousin, Sameh, for their continuous support and love.

In addition, I wish to thank my friend in the United Kingdom Rebin Mohammed and his family for the kindnesses and support they have shown to me during the period of my stay.

Finally, I would like to thank City university of London for providing me with a full doctoral studentship to fund my PhD research.

DECLARATION

I grant powers of discretion to the University Librarian to allow this thesis to be copied in whole or in part without further reference to me. This permission covers only single copies make for study purposes, subject to normal conditions of acknowledgement.

ABSTRACT

Most available research on analysis of reinforced concrete structures under impact loads focuses on using continuum models such as membrane and solid elements, which renders the problem expensive in terms of computational effort. Therefore, a gap exists in the available literature, as no simple finite element has sufficient capabilities to deal with impact and shock problems while considering detailed local parameters.

Meanwhile, the objective of this research is to develop several non-linear planar finite element models capable of accurately predicting the response of reinforced concrete structures subjected to impact dynamic loading. A mixed and displacement-based element that use an explicit time integration method and consider large deformations are being developed together with a third force-based first-order element that employs the explicit time integration method. A new algorithm that eliminates the need for iterations at the element level is proposed. The strain rate effect is accounted for in the material constitutive models.

The developed explicit fibre beam models, particularly the force-based and mixed elements, represent a simple yet powerful tool for simulating the nonlinear complex effect of impact loads on structures accurately while using very few finite elements. The elements can particularly model fibrous slender reinforced concrete structures and steel concrete panels under impact loading. A simplified procedure is also developed to employ the planar elements in solving three-dimensional problems where the load is applied in the out-of-plane direction. The proposed elements are validated using benchmark experiments available from the literature.

The results of the numerical studies proved the newly developed elements are capable of providing accurate and computationally efficient estimates of structural demands under severe impact loading conditions.

CHAPTER 1

INTRODUCTION

1.1 Overview

The finite element method is widely used for the analysis of structures under different loading conditions. The creation of the finite element dates back to 1956 when **Turner et al., (1956)** introduced the method for the analysis of structures in a project funded by the Boeing summer faculty program **(Clough, 1990)**. The method has already proven its feasibility and computational efficiency in many aspects of engineering problems through accurate simulation of complex structures and its ease of use. Yet, the development of more adequate and advanced finite element techniques is still ongoing in many branches of engineering.

In the same way, the nonlinear analysis of reinforced concrete (RC) structures is deemed interesting to many researchers and developers over the last few decades. Although many commercial software packages have already explored this area and have presented several numerical elements and algorithms for the modelling of numerous structures, still many advanced algorithms and simulation techniques are being developed in several universities and research centres around the word. These new algorithms attempt to deal with complex geometry, comprise different material properties and simulate global and local effects with higher accuracy. The resulting elements are employed in the solution of complex problems that cannot be solved using modest straightforward analytical methods or other rudimentary finite element models.

1.2 Problem statement

The main purpose of this PhD research is to develop a new finite element model able to accurately simulate complex reinforced concrete structures such as composite steel concrete (SC) beams and panels under the effect of impact dynamic loading. Currently there is a clear gap in the available literature, as no simple beam element has sufficient capabilities to deal with impact and shock problems while considering specific analysis details. The reason of this gap can be attributed to the fact that most available research focuses on using continuum models such as membrane and solid elements, which renders the problem expensive in terms of computational effort.

Subsequently there is an urge to close the gap that presently exists in the literature. For this reason, this PhD research offers to the engineering community adequate, accurate and simple finite element models that focus on impact and shock problems for RC structures. These models can contribute to increasing the life safety of reinforced concrete structures. They can also be used to suggest suitable design methods to help prevent possible collapse and failure due to impact loading.

Therefore, the presented models will use a fibre-based element formulation to simulate the nonlinear behaviour of both steel and concrete components of several reinforced concrete structures and particularly steel concrete beams and panels. In addition to this, advanced material models will be employed to capture the accurate nonlinear behaviour of the systems.

The proposed elements will also use an explicit dynamic analysis technique known for its superiority in short term dynamic problems to avoid ordinary convergence problems associated with the traditional implicit technique. Additionally, in order to include large displacement and rotations deformations,

second order effects, that probably accompany impact problems, will be accounted for using the geometric stiffness matrix technique.

The developed elements will also model different types of fibres that can be used in the concrete mix such as steel fibres and Nano fibres allowing for a higher level of accurate simulation of the pre and post cracking behaviour of fibre-reinforced concrete members under impact loading. As a result of this consideration, the elements will be able to cope with the recent advancements in concrete manufacturing technology.

Moreover, since impact problems are always accompanied by a change in the mechanical properties of the resisting materials, the strain rate effect in steel and concrete materials will be studied using available tests from the literature. Different dynamic amplification factors (DIF) will be investigated and implemented in the elements' material models for accurate prediction of the modified stress strain curves.

The present research will particularly focus on the analysis of composite steel concrete panels recently adopted in nuclear containment structures, allowing for a safer design for nuclear buildings under expected severe loads. The validation of the new elements will be accomplished by comparing their results with a considerable number of experiments available from the literature to guarantee the reliability of the developed elements.

In summary, the present work offers to the engineering community a strong and accurate tool to express the behaviour of such important structures under impact and dynamic loading. Figure (1.1) shows the four new elements presented in this research. The developed elements are all plane flexural beam-column elements that

consider an explicit time integration scheme, which accounts for the strain rate effect and can consider large displacement and rotations. The four elements will be developed, discussed and validated in detail in the next parts of this report. Several impact and shock problems from the literature will be simulated using the new fibre beam elements to demonstrate the capabilities of the improved element and their abilities to model the nonlinear behaviour of normal concrete, and concrete engineered with nanoparticles under impact loads.

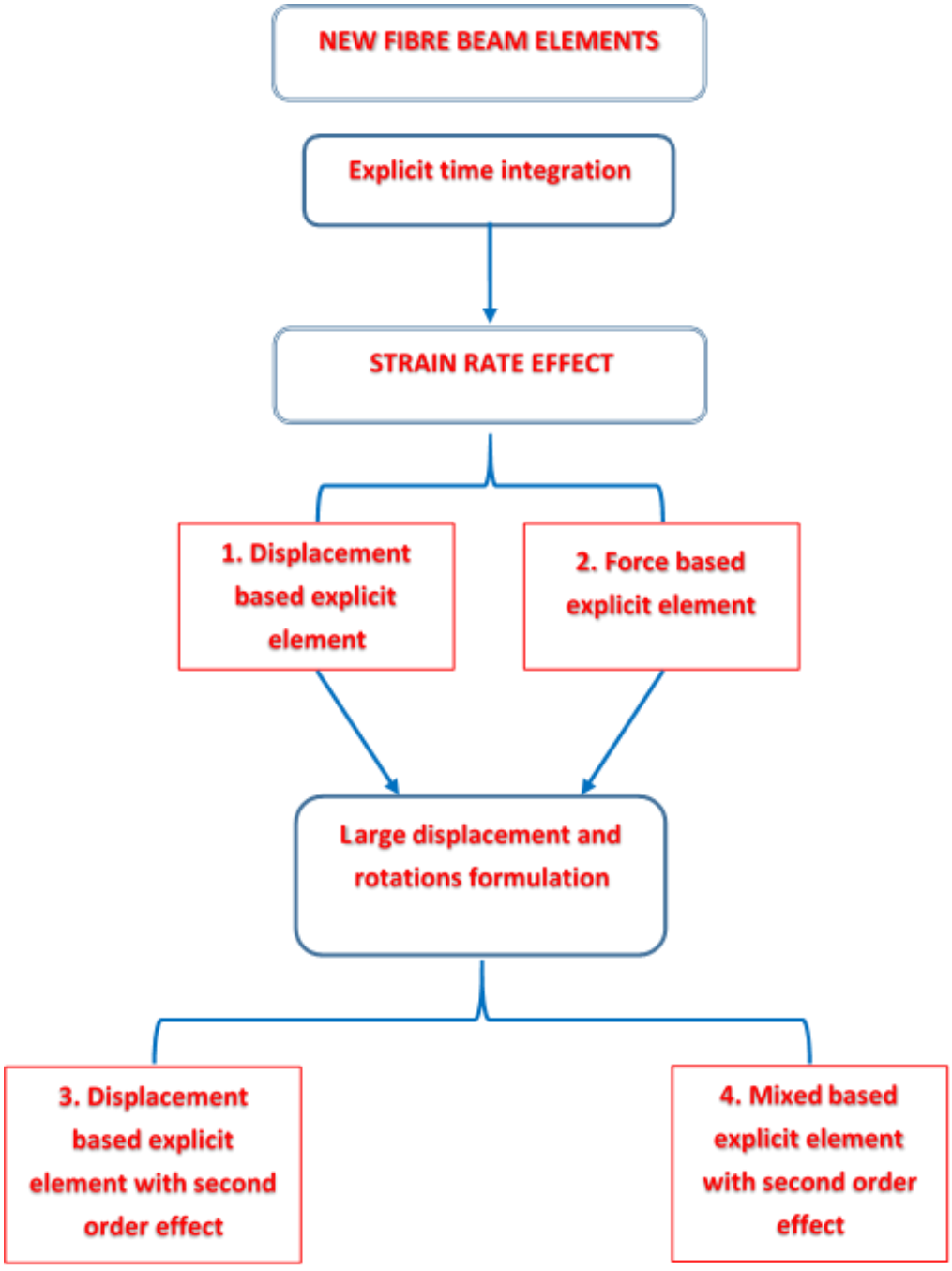

Figure 1.1: Flowchart diagram of the four proposed fibre beam elements.

1.3 Objective and scope

The main aim of this research is to develop several non-linear finite element models capable of accurately predicting the response of reinforced concrete structures subjected to impact dynamic loading. The available literature lacks a simple beam element that has sufficient capabilities to deal with impact and shock problems while accounting for specific analytical details. In particular, existing elements are based on implicit algorithms, which are not computationally robust, and the development of explicit methods was not tailored for fibre beam elements. In addition, the effect of large deformation requires the use of fine meshes, which renders the problem computationally demanding. Further, current models do not make use of advanced material models, particularly fibre-reinforced concrete, in the case of high strain rate loadings. The proposed elements will seek to resolve these shortcomings, which will significantly contribute to enhancing the capabilities of fibre beam-column elements and extend their use in modelling impact and dynamic problems.

The different tasks of this study needed to accomplish the given aims are:

- To develop a force-based element that employs an explicit time integration method.

- To develop a displacement-based element that considers large deformations and uses an explicit time integration method.

- To develop a mixed element that considers large deformations and uses an explicit time integration method.

- To consider the strain rate effects in the material constitutive models of the developed elements.

- To analyse fibrous concrete members subjected to impact loading.

- To establish an efficient and simple solution strategy for utilizing the fibre beam elements in grillage analysis of three-dimensional structures under different loading.

- To simulate the behaviour of steel concrete panels under impact loading using fibre beam elements.

- To investigate the most effective method of increasing the safety of SC panels to resist impact loading.

All the established elements in this research will be validated using benchmark experimental results available from the literature.

1.4 Structure of the thesis

The present study is organization as follows:

Chapter 1 presents the introduction, the problem statement, the objective and scope of the work and the structure of the thesis.

Chapter 2 presents a thorough literature review of previous research studies and the contribution of this PhD in closing the knowledge gap.

Chapter 3 describes the formulations of large deformations and the method of implementing them in the displacement-based and mixed-based fibre beam elements. The material models used within the elements are also presented and the effect of tension softening stiffness on the second order analysis is emphasised. Many experiments of slender structures are then used to calibrate the elements.

Chapter 4 deals with the explicit approach employed for short-time duration problems and compares it with the classical implicit analysis technique. The chapter also introduces the consideration of the strain rate effect in the material models. The developed explicit elements are validated against different impact experiments.

Chapter 5 displays the use of the fibre beam elements in the grillage analysis of different structures under cyclic and dynamic loading. A simplified and innovative technique will be used to solve three-dimensional (3D) problems using the developed planar elements. A numerical study is also presented to determine the most effective parameter in increasing the resistance of steel concrete panels under impact and shock loading.

Finally, chapter 6 presents the summary and conclusion of the current research along with possible future research work.

CHAPTER 2

LITERATURE REVIEW

2.1 Introduction

A systematic literature review is presented herein that includes numerous contributions of other researchers in the last few years. Since the present research covers several areas, the literature review will be divided into several sections where each section will focus on a specific branch of the research. All units are connected to each other through the global objective of the work, which is the development of a fibre beam element able to perform dynamic impact analysis using explicit time integration technique while considering strain rate and second order effects.

The literature review aims to discuss recent developments in the nuclear infrastructure field, particularly steel-concrete construction, and their accurate modelling techniques. For this task, fibre beam elements proved to be more numerically efficient than continuum elements, especially when considering natural hazards such as earthquake, or impact and blast loads. Accordingly, three main areas from the literature will be presented in this chapter as follows:

- Nuclear structures
- Fibre models for beams
- Material constitutive models

2.2 Nuclear structures

The importance of nuclear infrastructure is increasing as many countries are investing large amount of money to build new nuclear power plants. Many countries are planning to make huge investments in this field in order to produce vast amount of electricity **(World-nuclear.org, 2017)**. Worldwide, as of January 18, 2013, in 31 countries there exist 437 nuclear power plant units with an installed electric net capacity of about 372 GW that are in operation and 68 plants with an installed capacity of 65 GW that are in 15 countries under construction **(Marion Bruenglinghaus, 2015)**. The UK has recently committed to a long-term nuclear programme and has recently signed a contract worth £14 Billion with a French company to construct two new reactors **(Mzconsultinginc.com, 2013)**.

2.2.1 Safety of nuclear structures

As the safety of nuclear structures is vital, more research linked to this field is required as nuclear power plants can be subjected to severe dynamic loads such as aircraft impact, blast load due to possible terrorist attacks or explosions due to internal problems in the reactor.

Well-known nuclear structures were subjected to hazard risks many times before, which led to terrible disasters and strong damage to the surrounding environment and people's lives. Some of the widely known disasters are:

- The blast at Marcoule nuclear power plant in France (2011) **(IAEA-Topic: Banning atomic energy, 2016)**

- The earthquake and tsunami that destroyed the active reactor plant in Fukushima, Japan (2011) **(Lipscy et al., 2013)**

- The Chernobyl nuclear power plant explosion in Ukraine (1986) **(Chernobyl: Assessment of radiological and health impacts, 2002)**

Improving the safety of these types of structures can be achieved by adopting safer and more resistant structural systems such as steel concrete panels. The new systems will still need to be tested and modelled with advanced computer software to ensure its reliability and capability to resist impact loads.

The present PhD focuses on developing new elements able to model steel concrete beams and panels under the effect of impact loading, as discussed next. The beam elements can be used to create a full grillage to model the whole structure and can be used in modelling a particular area of the building by studying a particular strip under a specific load.

2.2.2 Steel concrete beams and panels

Composite steel-concrete beams and panels were recently adopted in nuclear containment structures. The systems consist of a thick concrete core, sandwiched between two steel plates. The steel plates are regularly connected by shear connectors (anchors) spaced in both directions as shown in Figure (2.1). The system usually does not contain any horizontal, vertical reinforcement or any stirrups.

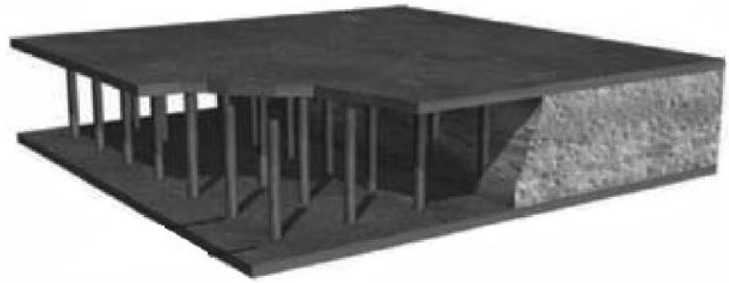

Figure 2.1: Steel concrete steel panel, Figure from **Liew and Wang (2011)**.

These panels are casted in precast yards and only welded on site. One big advantage of this system is the use of the steel plates as formwork during the construction, which accelerates the building process. There is also no need to use a steel liner as the steel plates replace them, which is an economical benefit of adopting the SC system.

One of the leading manufacturer of steel concrete panels in the UK are TATA steel **(Tatasteelconstruction.com, 2017)**. They produce the so-called Bi-Steel (steel/concrete composite panels). Bi-steel was used in several projects in the UK including the eight-storey office building in St Paul's Square in Liverpool and the 18-storey tower of the Birmingham-1 student halls of residence in south-west Birmingham.

The steel concrete beams and panels are known to be an excellent protective structure in resisting blast and impact loads. SC beams are commonly used in residential, industrial and commercial buildings. The SC panels are also widely used especially in offshore structures, liquid containments, blast walls in factories and basements, caissons, tunnels and in shear walls and cores of multi-storey buildings. The SC panel system was lately used in nuclear structures for the construction of the new generation of nuclear containment infrastructures namely the AP1000

Pressurized Water Reactor designed and sold by Westinghouse Electric Company. The SC panel system was adopted in the Shield Building Cylindrical Wall. Its design was the first Generation III+ reactor to receive final design approval from the NRC **(Westinghousenuclear.com, 2017)**.

Several researchers have tested SC beams and panels experimentally. **Liew and Wang (2011)** tested six steel-concrete-steel sandwich composite plates under field blast Load. Each specimen has a length of 1200 mm and width of 495 mm. The concrete core thickness was 70 mm and the thickness of the faceplates varied between 3 and 4 mm. An interesting finding was concluded that the steel faceplate thickness is more essential in increasing the resistance of SC panels under blast loads.

Sohel et al. (2011) discussed the importance of J-hook connectors in improving the punching and impact resistance, by avoiding local buckling, of the steel plates of SC panels. They found that the J-hook connectors are effective in resisting the transverse and vertical shear for SC panels subjected to blast loads. Later, **Sohel and Liew (2014)** used an instrumented drop-weight impact test machine to test eight SC sandwich slabs measuring 1200 × 1200 mm^2. The concrete core varied between 80 and 100 mm while the steel plate thickness varied between 4, 6 and 8 mm. J-hook shear connectors, spaced 100mm in both directions, were used to connect the two steel plates for all specimens. The authors found that J-hook connectors are one of the major controlling parameters that affect the punching resistance of the SC panels when subjected to impact load. They concluded that the use of J-hook shear connectors increases the shear resistance of the SC panels and offers an additional resistance to prevent tensile failure of the faceplates.

Similarly, **Hashimoto et al. (2005)** carried out an experimental programme on the behaviour of concrete panels with steel plate subjected to projectile impact. 40 specimens of 750mm square were tested. The experiment concluded that the steel plate is less effective at impact resistance when used on the front face of concrete panel, as opposed to the rear face.

Although experimental research is important to determine the accurate behaviour of the system and to form a deep knowledge about its variables, it is still expensive and takes a considerable amount of time to perform a comprehensive research. On the other hand, numerical simulation and analysis helps in investigating the effect of each variable on the system and in studying an unlimited number of cases while saving time and money. Therefore, accurate modelling of the system increases the confidence in adopting it and consequently helps its development and the spread of its use. Besides, the continuous improvement of these panels is necessary in order to comply with further demand on safety and reliability related to nuclear structures. That's why, in this dissertation, the steel concrete panel behaviour will be examined under the effect of impact loading using the newly developed finite element models which are based on a fibre beam element formulation.

Furthermore, the behaviour of steel-concrete panels and beams can be enhanced with the use of different types of fibres, such as carbon Nano fibres. The presence of these fibres in the concrete core of the steel concrete panels will be included in the models and investigated.

Previous efforts were made to analyse the steel-concrete panel systems under impact and dynamic loading. **Anandavalli et al. (2011)** analysed steel-concrete composite panels under blast loading using ANSYS software. Two models were

created. In the first one, solid elements were used to model the concrete core, the steel plates and the shear connectors. In the second model, shell elements were used to model the steel plates, while solid elements were employed for the modelling of the concrete core and finally shear connectors were introduced using link elements. **Kong et al. (2012)** performed a numerical simulation for SC panels under impact loading using LS-DYNA software. A 10 mm mesh was used to model the concrete core and the steel faceplates. The concrete was simulated using constant stress solid elements while the faceplates were modelled using Belytschko-Tsay shell elements. The reinforcing steel was presented using the Hughes-Liu beam element. Similarly, **Anandavalli et al. (2012)** numerically simulated SC panels subjected to blast loading. In order to reduce the number of degrees of freedom, concrete core, steel plates; and shear connectors were modelled using solid, plate and link elements, respectively. Using this simplified modelling approach, the authors found that the diameter of the shear connector has insignificant effect on the peak response of the SC panels.

Whereas, **Zhu et al. (2013)** used ANSYS/ LS-DYNA programmes to analyse SC panels under scaled-aircraft Impact. The concrete was modelled using constant stress solid element with large deformation, the reinforcement was modelled using beam elements. The damage identified at the back surface of the SC panel was greater than the one at the front surface, which concludes that the rear face steel plate is more effective in stopping the perforation and the scattering of fragments under impact force.

Later, **Sadiq et al. (2014)** analysed the impact of an aircraft on SC panels using the finite element programmes ANSYS and LS-DYNA. Three-dimensional finite element models of the SC panels, with different core thicknesses, were created. The

concrete was modelled using an 8-nodes solid element. The steel plates were introduced using a 4-node Belytschko-Tsay shell element. The shear studs were modelled using a 3-node beam element following the formulation of Hughes-Liu. The aeroplane was also simulated using solid and shell elements. The study found that the performance of LS-DYNA Winfrith concrete model in simulating the nonlinear response of concrete in case of large deformations and high strain rates is better when compared with LS-DYNA concrete constitutive model (CSCM).

On the other hand, for the steel-concrete beams, **Sohel et al. (2015)** modelled numerically lightweight steel-concrete-steel sandwich composite beams under impact loading using LS-DYNA software. The projectile, shear connectors and concrete core were meshed with 8-nodes solid elements. The steel plates were presented in the model using 8-nodes thick-shell elements. Automatic surface-to-surface contact option was used to model the contact interfaces between the steel plates and the concrete, the projectile and the steel plate, the steel plate and the support, and finally the studs and the concrete core. A beam element was used to model the interconnection of the J-hooks connectors. The pair of J-hook connectors were modelled using a bar spring model. The beam was supported on two rigid steel bars modelled using shell elements. The strain-rate effect was considered in the material models using a dynamic increase factor to enhance the material strength. The numerical three-dimensional model showed good agreement with the corresponding test results in terms of deflections, forces and failure modes. In the following sections, the fibre beam models types and formulations will be presented and discussed.

2.3 Fibre models for beams

The fibre beam model is a simplified form of the finite element method and a more advanced numerical procedure than the plastic hinge models. For lumped models, the nonlinearity of the member is concentrated at the ends of the beam elements and the body is modelled with elastic properties. Consequently, in the case of the spread of plasticity, errors are expected; while in distributed nonlinearity models, the element behaviour is calculated from the integration of the response of the sections and the material nonlinearity can occurs at any section along the element length. Therefore, numerical models based on the distributed nonlinearity assumptions are the most accurate approaches that express the nonlinear behaviour of reinforced concrete structures **(Rahai and Nafari, 2013)**.

The fibre beam method is known to be an advanced computational technique with reduced computational cost and results in a convenient execution time. The method requires less storage capacity and gives correct results. The fibre beam element has been widely used in the last decade to model static and dynamic loads for nonlinear problems. In fact, fibre beam models use detailed geometry and material models to obtain accurate representation of nonlinear behaviour along the length of the member **(Mullapudi, 2010)**. The fibre beam elements are mainly created by dividing each element into several sections. Those sections are divided into fibres that represent steel and concrete (Figure 2.2). The strain at each fibre is calculated using the section strain and the curvature with the use of the assumption that plane sections remain plane.

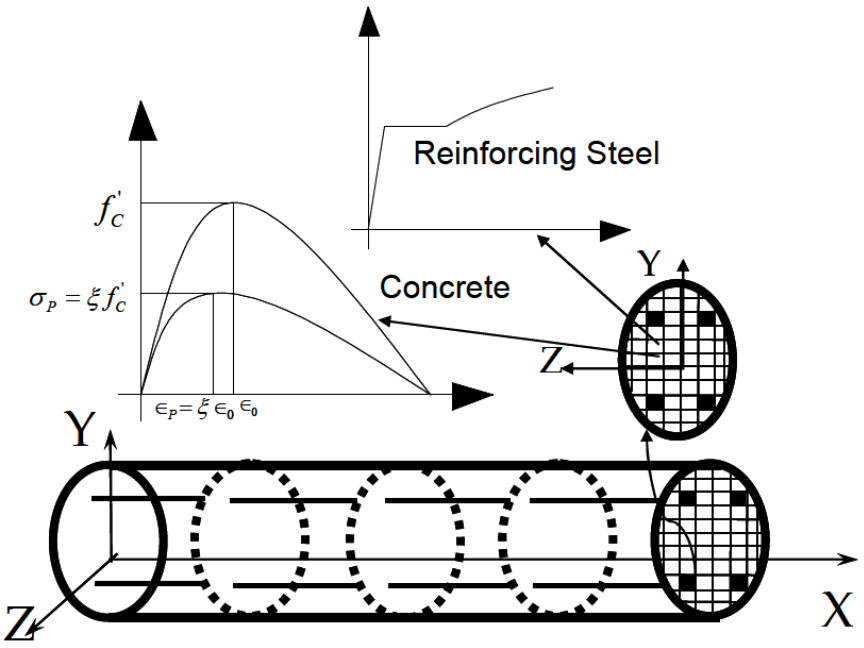

Figure 2.2: Fibre model discretization.

In this research, the finite element method will be employed to study the performance of SC beams and panels under dynamic impact loading and the effect of different factors on the resistance of SC systems against impact loading will be determined. In order to accomplish this task, new elements will be formulated that will use an explicit time integration method and will account for large displacements and rotations (the second order effect). The explicit time integration technique will improve the capability of the elements in running short-term dynamic problems without the need for internal element or external global iterations and thus will avoid convergence complications. Moreover, the second order effect will allows the elements to model slender structures, axially restraint structures and in general structures subjected to large deformations.

2.3.1 Types of fibre beam elements

Currently, there are three different types of formulations for distributed plasticity fibre beam elements available in the literature:

1- The displacement-based formulation **(Kang 1977)**.
2- The force-based formulation **(Spacone and Filippou 1992; Neuenhofer and Filippou 1997)**.
3- The mixed-based formulation **(Ayoub and Filippou 2000; Alemdar and White 2005)**.

The displacement-based element, which is the classic beam element formulation, usually faces numerical difficulties around the point of maximum resistance in the section or the element level **(Kang and Scordelis, 1977)**. Besides this, the approximation of the curvature into a linear curvature distribution is enforced along the element, which requires the adoption of a fine mesh.

In the displacement-based method, the equilibrium is satisfied in a weighted integral sense. While in the force-based method, the equilibrium is satisfied by a more strict method, on a section-by-section basis, therefore the equilibrium between the element and the section forces is exact. The mixed formulation can be considered as an update to the force method and is a hybrid formulation that uses both the element displacements and the generalized internal stress resultants to allow, in the present case, the incorporation of the geometric nonlinearity terms into the element formulation.

Until present, the available fibre beam elements developed by **Ayoub and Filippou (2000)** use only the classic implicit time integration method and do not

consider the second order effect, which limits their use in many applications (including dynamic analysis and when large displacements are expected).

In previous studies, **Otani (1974)** promoted an inelastic dynamic model that accounts for the distribution of inelastic deformation. **Soleimani et al. (1979)** presented an analytical model for nonlinear reinforced concrete beams with inelastic zone for fixed-end rotations and flexural deformations. **Meyer et al. (1983)** accounted for the finite size of the plastic regions instead of assuming a plastic hinges of zero dimensions to simulate the response of reinforced concrete frames under strong cyclic loads.

Takayanagi and Schnobrich (1979) modelled the nonlinear response of a coupled wall system under static and dynamic loading. The connecting beams were modelled as separate flexural beams with uniform elastic rigidity and connected to the wall by a rotational spring and rigid link. The wall itself was modelled as a beam with a linear variation of strain over the cross section.

Kang (1977) adopted a displacement-based formulation to analyse planar reinforced concrete frames with time dependent effects. **Mari (1984)** established three-dimensional nonlinear time dependent models to study the response of concrete frames. **Kaba and Mahin (1984)** created the first flexibility based multi-slice fibre element to model beams and columns. Later, **Zeris and Mahin (1988)** presented a more stable finite element model for nonlinear cyclic flexural analysis of reinforced concrete beams specially under softening response.

Ciampi and Carlesimo (1986) proposed a consistent implementation of the force-based element. The approach was then promoted and extended by **Taucer et al. (1991)** and **Spacone and Filippou (1992).** Later, **Nukala (1997)** addressed the

finite element modelling of three-dimensional second-order inelastic beam members for steel frames using displacement and mixed approaches. **Ayoub and Filippou (2000)** presented an inelastic beam element for the simulation of partial composite steel concrete girders subjected to monotonic and cyclic loading. Recently, **Mullapudi and Ayoub (2010)** formulated an inelastic nonlinear beam element with axial, bending and shear force interaction where the concrete material model accounts for the shear effects using the softened membrane model.

However, the fibre beam element formulation contains some limitations. According to **Kappos et al. (2012)**, fibre beam elements are considered relatively complex models, they require several iterations in order to achieve appropriate results and in general face many convergence problems. Moreover, distributed fibre beam models do not tend to capture plastic hinge rotations, but instead calculate the strains in the concrete and steel cross section fibres. The strain calculated using fibre beam models could be very sensitive to the element length, integration technique, moment gradient and strain hardening parameters **(Deierlein et al., 2010)**.

In this study, the developed elements will be used to analyse RC members under different loading types such as monotonic and cyclic loading mainly under dynamic effects, taking into account the geometric nonlinearity and benefiting from sophisticated material models that can accurately capture the nonlinear behaviour of concrete and steel materials.

The established elements are implemented in the research-oriented finite element analysis program FEAP developed by **Taylor (2014)**.

2.3.2 Initial selection of fibre beam elements mesh size

It is established in the finite element analysis method that the size of the mesh significantly affects the accuracy of the results. In general, displacement-based elements necessitate the adopting of a fine mesh because of the approximation in the calculation of the curvature in plastic zone regions.

A mesh convergence study is essential in order to determine the number of elements required to ensure that the output values are not affected by changing the mesh size. The solution is considered converging when the obtained stresses and deflections are constant regardless of the mesh size. Meaning that after convergence is achieved additional mesh refinement will not affect the results.

According to **Kotsovos (2015)**, mesh configuration and finite element size are important factors in the accuracy of linear and non-linear analysis. Mesh refinement is needed in zones of localised effects such as load concentrations and sudden changes in geometry. **Kotsovos (2015)** found using numerical experiments, that RC beams dominated by shear failure were sensitive to the adopted iterative techniques and recommended the adoption of a coarse mesh and a constant size load step throughout the entire loading history. He recommended a loading increment size between 2% and 10% of the estimated ultimate load.

For fibre beam elements, five sections are typically adopted in the model since this discretization accurately represents the plastic hinge zone in concrete structures **(Spacone et al., 1996)**. Other different studies on section discretization approaches, including recommendations for arrangement and the number of fibres, were performed by **Campbell (1994)** for steel sections and by **Berry (2006)** for circular RC columns.

Tao and Nie (2014) studied the section discretization and element mesh effect on displacement-based fibre beam elements for the nonlinear response of composite structural members. The research was performed on composite beams and concrete filled steel tubular columns. The authors found that the element mesh size has to be chosen as about half of the mid-span equivalent plastic hinge length for simply supported member. The recommendation can be used to capture the sharp jump of the curvature value at the plastic hinge region, and to control the numerical problems of pathological mesh-sensitivity arising from the strain softening behaviour.

A more general recommendation can be withdraw from **Ayoub and Filippou (2000), Alemdar and White (2005) and De Souza (2000)** work that primarily for force-based models an initial mesh size of one element can be used and at least two to four elements are needed for displacement-based elements. A convergence study has to be performed to insure the mesh independency of the solution especially for displacement-based elements.

2.3.3 Modelling of fibre reinforced concrete

The use of fibre in the concrete mix improves the properties of the concrete by increasing the compressive and tensile strength, the impact resistance, the ductility and also improves Young's modulus **[(Mullapudi et al., 2013)** and **(Sbia et al., 2014)]** which in turn improves the overall structural performance.

Different types of fibres exist such as (steel fibres, carbon Nano fibres and glass fibre). **Sanchez and Sobolev (2010)** emphasized that carbon Nano fibres are the most promising nanomaterials for enhancing the mechanical properties of cement-based materials. According to **Scrivener and Kirkpatrick (2008),** the importance

of the addition of carbon fibres to concrete is due to their high stiffness and strength, plus the very low friction of their surfaces, which make them very difficult to bind together.

Furthermore, Nanomaterials deal with the cracks presented in the concrete with a very small dimensions less than 100 nm (where 1 nm = 10^{-9} m). This allows the control of the material behaviour at the nanoscale level and thus presents fresh properties to the mix such as higher ductility and better control of the cracks **(Sanchez and Sobolev, 2010).** The new concrete mix is believed to be able to provide new functions and is considered a smart material because of its innovative performance, and its different properties including its self-sensing capabilities and its improved deterioration process **(Sanchez and Sobolev, 2010)**.

The cracking process can be explained according to **Mo and Roberts (2013)** as follows: concrete is a brittle material, when loaded, the tensile stress increases and the cracking process within the concrete starts with the formation of Nano cracks. These Nano cracks grow together to form localized micro cracks, which in turn expand to construct macro cracks. These macro cracks increase and widen to form cracks visible with the naked eye. Therefore, fibres play an important role to arrest these cracks by forming bridges across them. This is called bridging which produces a crack-free concrete that is the main reason of the improvement in the properties of the concrete mix. **Banthia et al. (1989)** used a drop weight impact machine to test plain concrete and steel-fibre-reinforced concrete under impact loading and found them to be more impact resistant. **Nataraja et al. (1999)** quantified the effect of steel fibre on compressive strength, strain at peak stress and the toughness of concrete and observed that the increase in toughness and the compressive strength is directly proportional to a reinforcing index function of the weight fraction of the fibres, the

diameter and the length of the fibres. **Lok et al. (2003)** used a 75 mm diameter split Hopkinson pressure bar (SHPB) to examine the dynamic behaviour of steel fibre reinforced concrete (SFRC). They found that different types of fibre reinforcement have the same response on the strength of concrete. **Lan et al. (2005)** tested steel fibre reinforced concrete slabs under explosive loading and recommended that 1.0% fibre concentration should be used to increase damage resistance. **Tyson et al. (2011)** utilized a three-point flexural test to investigate the addition of carbone Nano fibres to the cement matrix with 0.1 and 0.2% by weight of cement. They found that samples with carbone Nano fibres have an increase in the peak displacement up to 150% higher than plain cement samples. **Elavenil and Knight (2012)** examined different percentages of steel fibre in the concrete core of concrete plates tested under drop weight impact loading. They found that an increase in steel fibre content decrease the crack width. **Sohel and Liew (2014)** found that the addition of 1% steel fibres in the concrete core of SC panels reduced the cracks and spalling of concrete core, which in turn decreased the deflection of the panel under impact loading. **Hrynyk and Vecchio (2014)** tested steel fibre reinforced concrete slabs with fibre content between zero and 1.50% under impact loading. Their findings were that the fibres effectively increased the slab stiffness, capacity and impact resistances.

Consequently, the proper behaviour of the implementation of fibres in the reinforced concrete mix should be taken into account in the numerical models. In the present research, the concrete constitutive model will reflect the change in the concrete properties due to the presence of fibres in both the ascending and descending branches of the stress strain curve of concrete in both tension and compression zones.

In previous studies, **Sluys and de Borst (1992)** investigated the impact modelling of steel fibre reinforced concrete beams. The fibres were modelled using a macroscopic method where the addition of the fibres is taken as an increase in the ductility of the cracked material (by increasing the value of the ultimate crack strain). The authors found that the difference between a rate dependant and a rate independent formulation is very limited when considering the global response of the beams. **Campione and Letizia Mangiavillano (2008)** modelled the flexural behaviour of fibrous reinforced concrete beams with the nonlinear finite element program (DRAIN-2DX) under monotonic and cyclic loading. The model was able to simulate the load-deflection response of the simply supported beams.

On the other hand, **Abbas et al. (2010)** used ABAQUS software to compare the output of three different material models with experimental results in order to numerically model fibre reinforced concrete under static loading and found reasonable agreement between the results. **Pros et al. (2011)** proposed a numerical strategy to consider the influence of fibres in the numerical simulation of steel fibre reinforced concrete. In their approach, concrete and fibre meshes are independent, although they interact together, and the actual geometry of all fibres is defined inside the concrete mesh. To couple the two models, displacement compatibilities are imposed. Constitutive equations that depend on the angle between the fibres and the direction of the failure pattern are then used to describe the deboning between the fibres and the concrete at the mesoscale level.

Likewise, **Xu et al. (2012)** numerically simulated a number of dynamic impact tests on steel fibre reinforced concrete specimens on the Mesoscale level. They used LS-DYNA commercial software to simulate the impact test. The model was able to accurately capture the presence of the fibres in the specimens and indicated that the

crack-bridging effect of the fibres is more significant at higher strain rate. **Karadelis and Zhang (2015)** simulated numerically the tensile behaviour of steel fibre reinforced concrete using ABAQUS. The model was able to express the macro (Mesoscale) behaviour of SFRC without considering the bridging effect.

In this research, the addition of fibres to the concrete mix regarding different type of structures (beams, columns and panels) will be accounted for. The fibres effect will be comprised in the material models of the concrete through several concrete parameters including the concrete compressive and tensile strength, the concrete strain and the tension softening stiffness. The successful inclusion of the fibre effect in the numerical concrete material model requires adequate data generated from the stress-strain curve of the experimentally tested sample.

2.3.4 Enhancement of state of the art in RC Frame finite element modelling

The developed models, presented in this report, will use a fibre-based element formulation to solve short-term dynamic problems. In order to solve impact problems accurately, the enhanced elements will use an explicit dynamic analysis technique and will consider large deformations.

2.3.4.1 Impact dynamic analysis

In general, the dynamic analysis of structures has been widely performed using different numerical computational methods such as the finite element method and the boundary element method. It is well established that several commercial and research oriented software packages can simulate the behaviour of structures under dynamic impact loading. However, most available explicit-based finite elements

were developed for continuum models such as membrane and solid elements, which create computationally expensive models that require considerable execution time, large storage memory and lead to significantly slow post-processing.

In the past, researchers have addressed the numerical analysis of impact problems using the finite element method. For instance, **Saatci and Vecchio (2009.a)** modelled reinforced concrete beams under impact load, dominated by shear behaviour, using the VecTor2 finite element software developed at the University of Toronto. A smeared rotating crack approach was utilized to capture the gradual change in the direction of the cracks that takes place during loading and through the structure's response. Shell element meshes were used to model the tested beams. The supports were modelled with compression-only truss bars. The drop-weight itself was modelled with rectangular reinforced concrete elements with high rigidity and connected to the beams with rigid compression-only truss bars to eliminate the drop weight effect when it rebounds back after the collision. **Jiang et al. (2012)** used LS-DYNA software to numerically simulate impact tests on RC beams. A three-dimensional finite element mesh model was created for the RC beam and the drop weight. A surface-to-surface constraint algorithm with friction was employed in order to model the contact between the drop weight and the RC beam. Due to the short duration of the impact response, dampers were not inserted in the finite element model.

Later, **Lee and Kim (2015)** modelled SC panels under aircraft impact loading. A constant stress solid element was used to model the concrete core. The Belytschko-Tsay shell element was employed to model the steel plates and Hughes-Liu beam element was selected to model the studs. In order to avoid the penetration between the concrete and the steel plates, an automatic contact option available in

the software was applied to manage disjointed meshes and prevent nonphysical contact behaviour. However, for the concrete material model in compression, the strain softening behaviour was not accounted for. To generate the impact force of a large commercial aircraft, they used the Riera equation **(Riera, 1968)** that calculates the total force at the interface between the collapsing aircraft and the structure.

Recently, **Chen et al. (2016)** simulated the effect of a large-size truck hitting a reinforced concrete column using LS-DYNA. Shell and solid elements were utilized to model the hitting truck. While solid elements were assigned for the circular concrete column, beam elements were used for the reinforcement bars and were considered as fully bonded with the concrete. The model results indicated that the reactions and mid span deflections matched well with the test results.

Moreover, other researchers have adapted simpler analytical techniques to solve impact problems. **Fujikake et al. (2009)** presented an analytical model to estimate the maximum mid span deflection for reinforced concrete beams subjected to impact loading. The analytical model consisted of a two-degree-of-freedom mass-spring-damper system to simulate the RC beams analytically. The system entailed one degree of freedom to express the local impact response between the drop weight and the beam and another one to express the overall response of the beam. The analysis technique involved the determination of the moment-curvature relationship of the beam using section-by-section analysis procedure, whereas the strain rate effects were considered. Then the calculation of the load vs. mid-span deflection relationship using the moment-curvature relationship was performed. **Zhan et al. (2015)** proposed two empirical equations to predict the maximum and residual deflection of reinforced concrete beams under high impact loading. The equations were based on the static flexural and the input impact energy. The method was found

to slightly overestimate or underestimate the deflection when compared with experimental results.

It can be concluded that the numerical computing technique overcomes the weaknesses associated with the analytical methods. The numerical approach, in general, is time-consuming, allows for a considerable number of trials to be performed, is easier to use and produce accurate results with appropriate approximations. Next, the implication of the geometric nonlinearity will be discussed.

2.3.4.2 Large displacement and rotation

Linear elastic analysis is not able to accurately simulate the structure response when the displacements are sufficiently large to change the stiffness of the structure significantly. The change in the geometry as the structure deforms is a major issue that has to be considered. Therefore, the interaction between the axial load and the lateral deformation has to be taken into account leading to a second order analysis. The second order effects will increase the moments, forces and the deflections and will affect the stiffness matrix of the structure. Figure (2.3), illustrates four different load displacement responses for the same structure, produced from various analysis methods (first and second order analysis) plus (elastic and inelastic analysis).

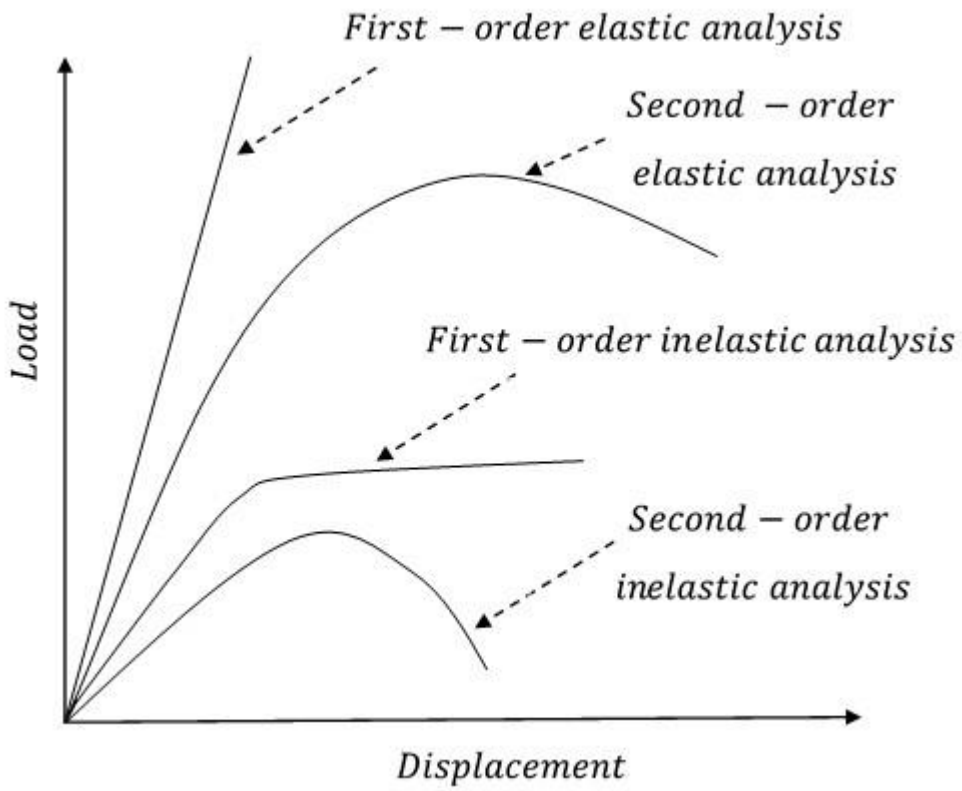

Figure 2.3: Load displacement graphs for different analysis methods.

The calculation of second order forces in numerical algorithms can be carried out using matrix analysis where the geometric stiffness is directly derived from the governing differential equation that considers the second-order effect of the axial force on the flexure. This offers a simple and accurate method for the consideration of the second order effect for beam-column elements. This method is also called the second-order computer program method due to the ease of its implementation in computer routines compared to other conventional methods. The geometric stiffness effect usually varies between 10 to 25% of the forces and displacements of the member depending on the ratio between the lateral and the axial load **(Wilson, 1998)**.

Two types of deformations are associated with the second order analysis. First, the P-δ, (called the small P-delta), where δ is related to the local deformation with respect to the chord of the element end nodes and can be considered by subdividing the element into smaller segments. Second, the P-Δ, (called the big P-delta), where Δ is related to member ends displacements. The big P-delta should be considered in the numerical formulation to accurately model the second order structural response.

In previous studies, **Kuo Mo Hsiao et al. (1988)** formulated a displacement-based beam element for large deformations of plastic plane frames. The effect of axial force was included in small deflection theory and the element was formulated in a body-attached coordinate to separate between rigid body and deformational rotations. Whereas **Crisfield (1991)** adopted a strain smoothing technique to use the average strain instead of the membrane strain, to remove shear locking in bending, encountered in displacement-based formulations.

Nukala (1997) presented two-dimensional displacement-based and generalized mixed variation finite elements that can be used to model arbitrarily large displacements and rotations with small strains. De Souza and Filippou **(De Souza, 2000)** developed a three-dimensional force-based fibre beam element that considers inelastic large displacement analysis and accounts for linear geometry and nonlinear material. However, the element was only employed to investigate the performance of steel structures.

Alemdar and White (2005) presented several beam column finite element formulations for full nonlinear distributed plasticity analysis of two-dimensional steel frame structures. For the displacement-based and the mixed elements, the second order effect was included in the corotational formulation. **Scott and Hamutçuoğlu (2008)** developed a numerically consistent regularization technique

for force-based frame elements to model reinforced concrete members, which is applicable for large displacement analysis based on **(De Souza, 2000)** formulation. **Heidarpour and Bradford (2011)** promoted a numerical model for non-linear dynamic analysis of steel beam-column elements. The formulation included large displacements. The method was utilized to investigate the behaviour of beam-column steel elements subjected to blast loading. The steel member was restrained at its ends by rotational and translational springs producing second order effect. **Denavit and Hajjar (2012)** developed a 3D distributed plasticity beam element using mixed-based formulation for composite circular concrete-filled steel tubes. The beam element was utilized for modelling nonlinear static and dynamic seismic force resisting structures. The formulation considered large displacements and rotations using corotational frame transformation.

Recently, **Nguyen and Tran (2016)** used large displacement corotational formulation to analyse planar functionally graded sandwich beams. The beams were composed of a metallic steel core and two top and bottom ceramic faces. The study highlighted the importance of considering the effect of plastic deformation in large displacement analysis.

In the subsequent section, the explicit time integration approach will be presented.

2.3.4.3 Explicit time integration

The solution of impact problems necessitates advanced computational procedures to handle the difficulties related to large short-duration loads. In this case, the explicit time integration method is typically used, instead of the traditional

implicit approach, since it offers a stable solution for problems such as the analysis of structures subjected to shock and impact loads. Moreover, the existing fibre beam elements use an implicit time integration method that requires a large number of iterations per time step to reach convergence, where in several dynamic analyses, particularly for impact and blast problems, the solution cannot be achieved due to severe numerical difficulties **[(Bathe and Cimento 1980) and (Yang et al. 1995)]**.

Gu and Wu (2013) assured that the explicit method provides a useful alternative technique to avoid difficulties of nonlinear programming associated with the implicit method. In the explicit approach, the accelerations of the nodes are calculated directly without the need to invert the stiffness matrix but only the mass matrix is inverted. No iterations are required and no convergence checks are needed, therefore a large number of inexpensive time steps is desired.

A number of researchers employed the explicit time integration technique to solve different linear and non-linear structural problems under dynamic loading. **Kujawski (1988)** presented an iterative semi-explicit algorithm for stiff non-linear transient dynamic problems using iteratively only forward substitution that allows the utilization of both consistent and lumped mass matrix. **Miranda et al. (1989)** derived an explicit predictor-corrector algorithm from the implicit alpha-method that is second-order accurate. It was found that the explicit algorithm has a better stability, higher accuracy and permits the assignment of a larger stable critical time step when compared with a Newmark-based algorithm. The algorithm is utilized for the solution of linear and non-linear structural dynamics problems such as wave propagation and single-degree-of-freedom oscillations.

Likewise, **Pezeshk and Camp (1995)** developed an explicit time integration technique for dynamic analyses of linear undamped single and multi-degree of freedom systems. The technique was based on a modified trapezoidal rule to approximate the governing ordinary differential equation. The developed explicit approach requires that the time step size be inversely proportional with the period of the structure. It was established that the new explicit procedure is more accurate in determining the transient response with the same amount of computational cost when compared with the modified Euler method procedure.

Furthermore, **Sun et al. (2000)** compared the performance of an implicit and explicit finite element methods for two linear dynamic problems (an elastic bar and a cylindrical disk on a rigid wall) using the ABAQUS finite element software. For the fast linear contact problems, it was established that the advantages of the explicit method are significant within an acceptable tolerance, regarding the computational cost. However, the authors reported that the explicit procedure requires very long time for slow linear contact problems when compared with the implicit procedure.

Chang (2009) presented a new explicit approach with unconditional stability for general instantaneous stiffness hardening systems in addition to linear elastic and instantaneous stiffness softening systems, where the instantaneous stiffness is a parameter used by the author to describe the variation of stiffness for a non-linear system. The unconditional stability was achieved by presenting the Newmark parameters β and γ in terms of an equation function of the damping ratio, the natural frequency and the size of integration time step, instead of any combinations of real numbers. It was observed that the new method is efficient for the solution of general structural dynamic problems where the response is dominated by low-frequency

modes and when high frequency responses are of no interest. The method was also found to be second-order accurate.

Likewise, **Curiel Sosa and Gil (2009)** improved an explicit continuum-based beam element involving large deformation. An adaptive time stepping was used, in order to avoid the stability limitations of the traditional fixed time stepping. **Fulei and Yungui (2011)** presented an explicit element that considers large displacements and large rotations to solve geometrical nonlinear dynamic problems. The authors formulated their element in a corotational system and used the finite rotation theory to determine the node direction vectors and the **Yoshida method (Yoshida et al. 1980)** to find the element direction vectors in order to construct the coordinate transformation matrix of the nonlinear beam element. The authors compared their results with the ANSYS explicit commercial software.

Recently, **Tenek (2015)** presented a three-dimensional explicit beam finite element with the derivation of an initial load due to temperature. The element was employed to analyse beams, arches, and frame structures.

During the preparation of this report, **Kolay and Ricles (2017)** presented a force-based frame element implementation for real-time hybrid simulation using explicit direct integration algorithms. The authors developed a procedure based on a fixed (small) number of iterations and an unconditionally stable explicit model-based integration algorithm. They presented a numerical investigation using a two-story RC frame building subjected to a maximum considered earthquake level ground motion.

In general, most of the previously published work uses continuum type elements, while the majority of them concentrated on employing simple material

models. However, the accurate prediction of the complex structural response requires more rigorous material models able to depict the performance of the structure under severe loading conditions. In this study, the presented elements use advanced nonlinear material models for both concrete and steel members for the accurate representation of nonlinear behaviour along the element length.

Moreover, other scholars presented different unconditionally stable explicit algorithms for structural dynamics. For instance, **Trujillo (1977)** presented an unconditionally stable explicit algorithm for the direct integration of the structural dynamic equations of motion. A diagonal mass matrix was adopted along with a positive definite symmetric stiffness and damping matrices. The conditional stability was established for the undamped case. **Chang and Liao (2005)** proposed an explicit integration method with unconditional stability. The method required no limitation on the time step to satisfy the stability limit. The technique was recommended for nonlinear systems where the implementation was more computationally efficient than for the constant average acceleration method. **Yina (2011)** developed an unconditionally stable explicit time-integration approach that presented a derivation of the increment of mechanical energy of undamped systems. Later, **Kolay and Ricles (2014)** established a number of unconditionally stable explicit direct integration algorithms with controllable numerical energy dissipation for linear and nonlinear structural dynamic problems.

In the present study, the developed explicit fibre beam elements use a conditionally stable explicit algorithm and a minimum stable time increment has to be respected. Next, the material constitutive models used with the fibre beam elements will be described.

2.4 Material constitutive models

Material models are a set of equations associated with the numerical elements in order to present the materials constitutive behaviour mathematically. A material model is typically created from idealized experimental results. The main role of the material model is to generate the stress-strain curve of the modelled material for use during the numerical solution. In the present case, the material models predict the concrete and steel response for different load histories. These material models are coded with subroutines that are linked to the main algorithm through common programming language commands.

In the literature, a large material library already exists, which can represent the wide range of material behaviours. The selection of the material model will significantly influence the analytical results of the proposed elements; as a result, trustful and appropriate material models are assigned to the developed elements. Therefore, the model originated by **Kent and Park (1971)** as modified by **Scott et al. (1982)** will be used for the concrete material of the developed elements. On the other hand, the **Menegotto and Pinto (1973)** stress-strain curve of mild steel bar as modified by **Filippou et al. (1983)** will be employed for the steel material of the developed elements.

When accounting for the strain rate effect during impact analysis, the models generated by **Fujikake et al. (2009)**, **Ross et al. (1989)**, and **Lok and Zhao (2004)** for concrete; and **Malvar (1998)** for steel will be used to evaluate the dynamic increase factor, which will be used to modify the former concrete and steel material models. All these fibre beam material models connected with the developed elements will be discussed more in detail in chapter (3) and (4).

2.4.1 Material strain rate effect

Concrete and steel structures subjected to impact and other dynamic loading constantly demonstrate an increase in their dynamic mechanical properties. This increase in the material resistance is linked to the loading rate effects, where the loading rate can be expressed in terms of the strain rate.

The strain rate can be defined as the rate of change in the strain of a material with respect to time. It is also defined as the speed at which deformation occurs. The strain rate has units of (s^{-1}). It was found that the strength and the fracture energy of the material generally increase with the increase of strain rate. The ranges of the strain rates for different loading conditions are shown in Figure (2.4). Quasi-static strain rates range between 10^{-6}-10^{-4} s^{-1}. For the earthquake loading, the strain rate varies between 10^{-4}-10^{-2} s^{-1}. The impact loads yield a strain rate in the range between 10^{0} to 10^{2} s^{-1}, while blast loads produce excitations related to a higher strain rate in the range of 10^{2} to 10^{4} s^{-1}.

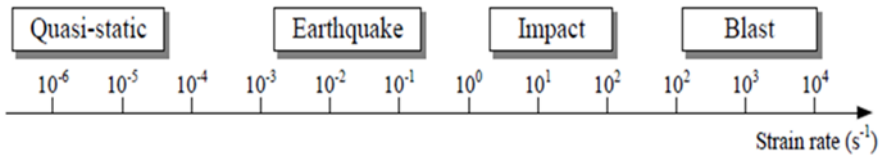

Figure 2.4: Strain rates ranges for different types of loading, Figure from **Ngo et al. (2007)**.

The strain rate can be expressed as:

$$\dot{\varepsilon} = \Delta\varepsilon/\Delta t \quad (2.1)$$

$$\varepsilon(t) = (L(t) - L_0(t))/L_0(t) \quad (2.2)$$

Where:

$\dot{\varepsilon}$: The strain rate and has the unit of s^{-1}.

Δt: The time interval.

$\varepsilon(t)$: The instantaneous Strain.

$L(t)$: The length of the object after deformation at time t.

$L_0(t)$: The original length of the object.

Usually a split Hopkinson pressure bar, invented by Bertram Hopkinson **(Hopkinson, 1914)** and modified by **Kolsky (1949)**, or an instrumented drop weight impact test are utilized to apply the impact high strain load. In the Split Hopkinson bar test, Figure (2.5), a striker bar is utilized to impose a dynamic load on a small specimen. The stress-strain responses in compression and tension at high strain rates are determined using strain gauges installed on the incident and transition bars. The split Hopkinson bar can be used to perform compression, tension and torsion testing. In the compression test setup, the specimen is installed between the transmitter and the incident bar. The striker bar is fired causing a compression stress in the specimen. Several techniques are used to investigate the effect of strain rate on tensile properties using the split Hopkinson bar. In 2013, **Dunand et al. (2013)** used a load inversion device to transform the compressive loads applied at the boundaries by the input bar to produce a tensile load into the specimen. The input bar was attached to the right specimen shoulder and the output bar was attached to the left specimen shoulder. Consequently, the pressure pulse in the incident bar generated a tensile pressure in the specimen and a compressive pressure in the transmitter bar. For the torsion testing, several techniques are also used. For instance, **Gilat and Pao (1988)** used a modified SHPB in which the input bar consisted of two sections with

different cross-sectional areas. A loading wheel and clamp were used in the setup of the apparatus. A torque is then produced between the clamp and the loading wheel by clamping the clamp and rotating the wheel. After releasing the clamp, a torsional wave is directly transmitted to the specimen.

Material models, available from the literature, created from experiments performed with SHPB devices will be used to update the constitutive models of the elements presented in this study.

In the instrumented drop weight test, Figure (2.6), an instrumented projectile is utilized to vertically hit a relatively large specimen. Guiding rails are used to guide the projectile during the free fall. A data acquisition system is used to measure the displacements and strains over a short period. The major advantage of this test is that it actually measures the behaviour of the structure as a whole and not solely the material behaviour as the Split Hopkinson bar does. However, the test is criticized for the possibility of inaccuracy that may lead to unreliable results. Yet it remains one of the important test methods of impact especially with the use of computer modelling for simulation and validation of experimental works.

Results from experiments, available from the literature, performed using several instrumented drop weight tests will be used to validate the developed elements presented in this study.

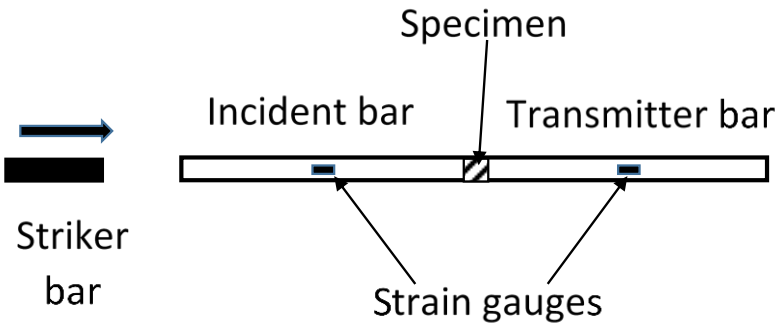

Figure 2.5: Schematic of the split Hopkinson pressure bar device.

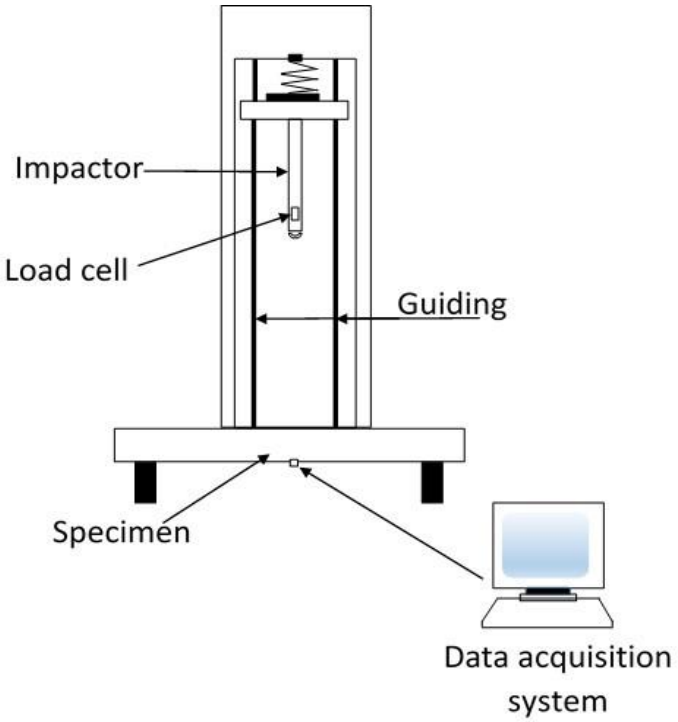

Figure 2.6: Schematic of the drop-weight impact test machine.

Furthermore, several researchers have investigated the sensitivity of concrete, fibre reinforced concrete and steel reinforcement to strain rates. **Körmeling and Reinhardt (1987)** studied the influence of strain rate on the mechanical properties of steel fibre reinforced concrete under uniaxial tension. A displacement controlled servo-hydraulic testing device was used for static and intermediate strain rates while

a split Hopkinson bar was employed for the high strain rate. Results showed an increase in the tensile strength of plain and steel fibre concrete due to high strain rates. **Lok et al. (2003)** experimentally tested steel fibre reinforced concrete using SHPB and found that the dynamic tensile strength is more influenced by the strain rate effect than the dynamic compressive strength. **Yousuf et al. (2011)** also used the SHPB to determine the dynamic strength of concrete under strain rate that ranges between (14 and 55 s^{-1}). The results stated that the concrete dynamic compressive strength is 2.5 times more than the static compressive strength.

Later, **Zhang et al. (2013)** studied the dynamic properties of polypropylene fibre concrete (PFRC) when subjected to different high-strain rates using an improved 74mm diameter SHPB. They proved that PFRC has damage softening performance under high strain rate and used Weibull damage model to describe the non-linear and fracture process of concrete and PFRC and implemented it into a dynamic constitutive model of concrete which was modified from Zhu-Wang-Tang constitutive model. They also compared the experimental work with the constitutive model and found that the calculated stress-strain curves of PFRC with different polypropylene fibre contents under different strain rates fitted well with the experimental stress strain curve.

Pająk (2011) collected numerous data on the strain rate effect from a wide range of experiments and compared them. Figure (2.7) shows the effect of strain rate on the compressive strength of concrete while Figure (2.8) displays the effect of strain rate on the tensile strength of concrete. A clear increase in the concrete compressive and tensile strengths is spotted in the two Figures. However, the results were divided in two parts where a limited increase is seen in the first phase but in the second phase, the strain rate exceeds 10^1 s^{-1}, therefore a much higher dynamic

increase factor was observed. For compression strength, the dynamic increase factor reached 3.5 while for tension strength, the DIF jumped up to 13, where the dynamic increase factor, also called the dynamic amplification factor, is a non-dimensional ratio used to present the difference between the properties of the materials under static and dynamic loading. This load factor can be applied to forces and stresses. Therefore, the load factor can be employed in order to implement the strain rate effect inside the concrete and steel constitutive material models.

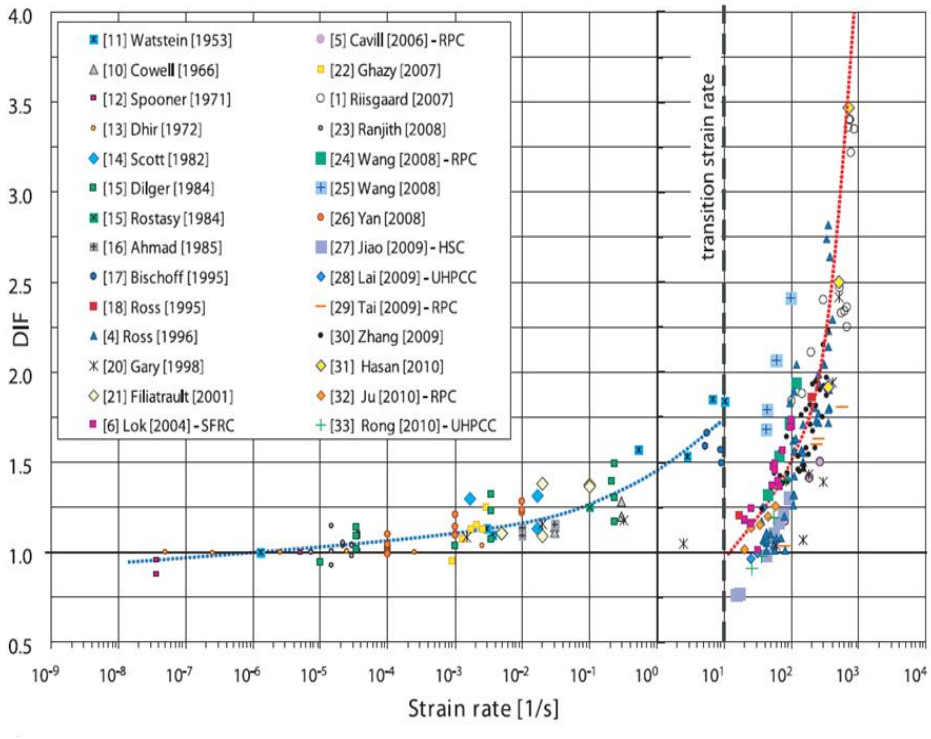

Figure 2.7: Effect of strain rate on concrete compressive strength, Figure from **Pająk (2011)**.

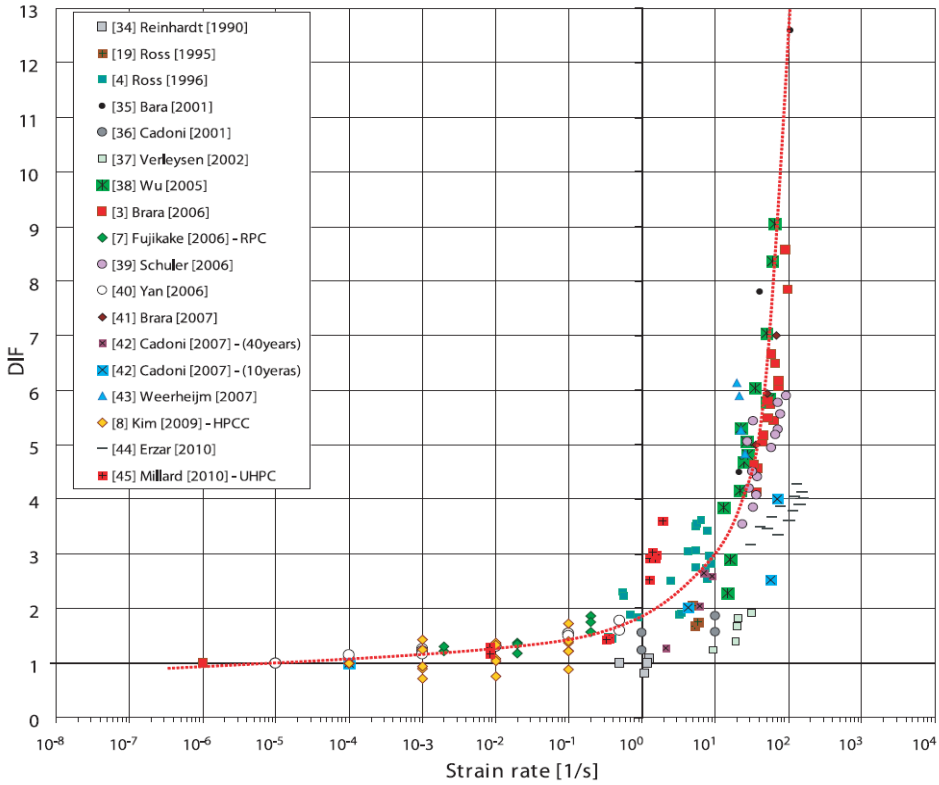

Figure 2.8: Effect of Strain rate on concrete tensile strength, Figure from **Pająk (2011)**.

Different formulas and equations, from the literature, can be used to describe the change in the material properties of concrete, fibre reinforced concrete and steel in which the DIF is presented as function of the static and dynamic strain. For instance, the comprehensive design code for concrete **(Fib Model Code for Concrete Structures 2010, 2013)** stated that the DIF for concrete under high strain rates could be determined by the following equations:

$$DIF_{compression} = \left(\frac{\dot{\varepsilon}}{\dot{\varepsilon}_{c0}}\right)^{0.014} \quad for\ \dot{\varepsilon} \leq 30s^{-1} \tag{2.3}$$

$$DIF_{compression} = 0.012\left(\frac{\dot{\varepsilon}}{\dot{\varepsilon}_{c0}}\right)^{1/3} \quad for\ \dot{\varepsilon} > 30s^{-1} \tag{2.4}$$

$$DIF_{tension} = \left(\frac{\dot{\varepsilon}}{\dot{\varepsilon}_{cto}}\right)^{0.018} \qquad for\ \dot{\varepsilon} \leq 10^{-4}s^{-1} \tag{2.5}$$

$$DIF_{tension} = 0.0062\left(\frac{\dot{\varepsilon}}{\dot{\varepsilon}_{cto}}\right)^{1/3} \qquad for\ \dot{\varepsilon} > 10s^{-1} \tag{2.6}$$

Where:

$\dot{\varepsilon}$: Is the dynamic strain rate in s^{-1}.

$\dot{\varepsilon}_{c0}$: $30x10^{-6}$ s^{-1}.

$\dot{\varepsilon}_{ct0}$: $1x10^{-6}$ s^{-1}.

Malvar (1998) studied the strength enhancement of steel reinforcing bars under the effect of high strain rates from the available literature and proposed a formula for the DIF function of the strain rate and yield stress. The equations were derived and are valid for a yield stress that ranges between 290 and 710 MPa and are as follows:

$$DIF = \left(\frac{\dot{\varepsilon}}{10^{-4}}\right)^{\alpha} \tag{2.7}$$

For yield stress calculation: $\alpha = \alpha_{fy}$; $\quad \alpha_{fy} = 0.074 - 0.04\left(f_y/414\right)$ (2.8)

For ultimate stress calculation: $\alpha = \alpha_{fu}$; $\quad \alpha_{fu} = 0.019 - 0.009\left(f_y/414\right)$ (2.9)

Where:

$\dot{\varepsilon}$: Is the strain rate is in s^{-1}.

f_y : The bar yield strength in MPa.

Furthermore, the DIF for steel plates and connectors were presented by the Cowper-Symonds equation **(Cowper and Symonds, 1957)**:

$$DIF_{steel} = 1 + \left(\frac{\dot{\varepsilon}}{D}\right)^{\frac{1}{q}} \tag{2.10}$$

Where:

$\dot{\varepsilon}$: Is the strain rate is in s^{-1}.

D = 40.4 S^{-1} and q = 5.

Zhou and Hao (2008) also investigated the inertia force effect on DIF and found that inertial confinement effect on the compressive strength is negligible when strain rate is less than 200 s^{-1} and that the contribution becomes more significant when the strain rate is higher than 1000 s^{-1}.

They proposed a tensile dynamic increase factor (TDIF) and compressive dynamic increase factor (CDIF) empirical equations for concrete-like materials as follows:

$$TDIF = 0.0225 \log \dot{\varepsilon} + 1.12 \quad for \quad (\dot{\varepsilon} \leq 0.1\, S^{-1}) \tag{2.11}$$

$$TDIF = 0.7325(\log \dot{\varepsilon})^2 + 1.235(\log \dot{\varepsilon}) + 1.6 \; for \; (0.1\, S^{-1} \leq \dot{\varepsilon} \leq 50\, S^{-1}) \tag{2.12}$$

$$CDIF = 0.0225 \log \dot{\varepsilon} + 1.12 \quad for \; (\dot{\varepsilon} \leq 10\, S^{-1}) \tag{2.13}$$

$$CDIF =$$

$$0.2713(\log \dot{\varepsilon})^2 - 0.3563(\log \dot{\varepsilon}) + 1.2275 \; for \; (10\, S^{-1} \leq \dot{\varepsilon} \leq 2000\, S^{-1}) \tag{2.14}$$

Similarly other researhers have presented different DIF equations including **Ross et al. (1989), Lok and Zhao (2004) and Fujikake et al. (2009)**. These equations will be presented and discussed in chapter (4) in detail.

2.5 Closing the Knowledge Gap

From the available literature review, it can be demonstrated that there is a clear knowledge gap in the existing literature, as no simple beam element has enough features to simulate impact problems while considering important analysis details. Therefore, the main contribution of this PhD study is to offer four new fibre beam elements that can be used in modelling reinforced concrete and composite structures under impact loading. The proposed elements will use an explicit dynamic analysis

technique, will consider large displacement and rotations, will account for the strain rate effect in the material constitutive models, will model different types of fibres and will focus on the analysis of composite steel concrete panels under impact loading. The research, in general, enhances the capabilities of fibre beam elements in order to employ them in the analysis of impact and dynamic problems.

The implementation of the mentioned futures in a single element is presented for the first time to the engineering community especially the explicit second-order mixed fibre beam element. The newly developed elements will help avoid the complications associate with computational complexity and high numerical cost of continuum models.

In the next chapter, the consideration of the second order effect in the formulation of the displacement-based and mixed beam-column elements will be presented in detail.

Chapter 3

LARGE DISPLACEMENTS AND ROTATIONS FIBRE BEAM ELEMENTS

3.1 Introduction

In this chapter, the formulation of two proposed elements will be presented. Both finite elements are based on a distributed plasticity fibre beam element formulation. The two elements can consider second order effects by taking into account the geometric stiffness matrix in the element formulation.

When an axial compressive force accompanies another bending force, additional bending moment in the member is created and should be considered in the element formulation as the element load vector and the element stiffness matrix are modified by the presence of this axial load. Thus the Second-order analysis will increase the forces, moments and deflections values.

The presented elements are used to predict the response of axially restrained reinforced concrete structures and slender reinforced concrete members using the geometric nonlinearity (the actual structure deformation) and the material nonlinearity (the nonlinear concrete and steel constitutive material models).

The proposed elements are based on the work by **Ayoub and Filippou (2000)** and **Alemdar and White (2005)**; to incorporate second order effects into displacement and mixed-based elements. Unlike the element of **Alemdar and White (2005)**, which was used to analyse simple steel members under static monotonic loads only, the proposed elements developed herein are able to model normal and high-

performance reinforced concrete as well as steel members under monotonic, cyclic, and severe dynamic loads. They can also monitor the behaviour of the structures at the element, section and fibre level.

3.2 Transformation between the corotational and global systems

The two elements formulated in this chapter follow Navier's three principles of mechanics: The stress equilibrium, the strain compatibility and the constitutive relationships of the steel and concrete. First the two elements are formulated in a corotational system where rigid body modes (R.B.M.) are removed and small strains are assumed.

According to **Crisfield (1990)**, co-rotational elements are introduced to overcome the problems that non-linear beam elements face under rotations including a significant rigid-body component, producing over-stiff solutions due to self-straining. Moreover, the corotational formulation is needed for a force-based model since the model aims to find the element flexibility first then invert it. For a system with R.B.M., this flexibility does not exist since the stiffness is singular.

For two-dimensional planar elements, the number of degrees of freedom (DOF) in the corotational system are three. An axial elongation q_1 and two rotations q_2 & q_3 relative to the element chord. The conjugate forces are the axial force Q_1 and the moments Q_2 & Q_3 at both ends (Figure 3.1.a). On the other hand, the global system consists of 6 DOF including 4 translations ($\bar{q}_1, \bar{q}_2, \bar{q}_4$ &$\bar{q}_5$) and 2 rotations ($\bar{q}_3$ &$\bar{q}_6$) (Figure 3.1.b) and β is the final angle of inclination of the beam element with respect to the global frame.

For the present formulation, the axial force is constant and does not change along the element, while distributed loads are not considered in the current fibre beam element formulation. Only internal loads on the members are lumped at nodal points along the members, and are transformed to end loaded members.

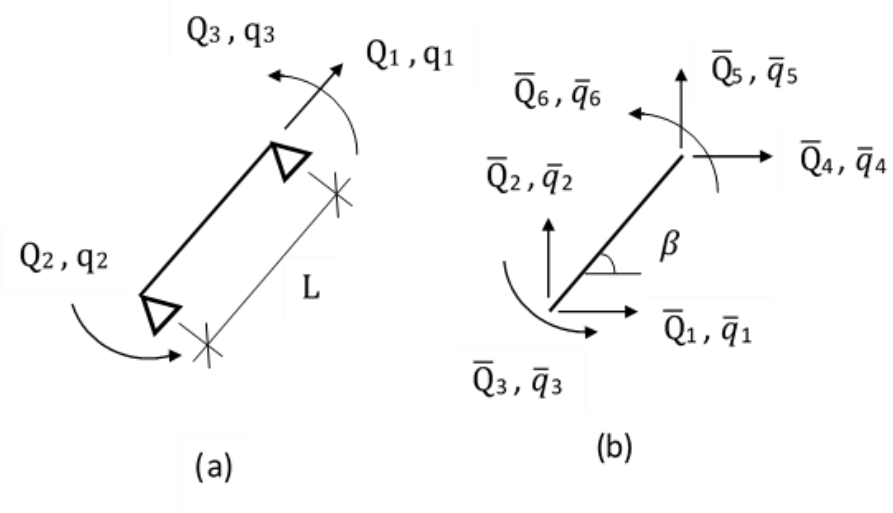

Figure 3.1: Element forces and displacement degrees of freedom in: (a) corotational and (b) global system.

The element internal forces in the corotational system, shown in Figure 3.2, from the equilibrium can be calculated as:

$$V_1 = \frac{Q_2+Q_3}{L} \tag{3.1}$$

$$V_2 = -\frac{Q_2+Q_3}{L} \tag{3.2}$$

$$H_1 = -Q_1 \tag{3.3}$$

$$H_2 = +Q_1 \tag{3.4}$$

Where V and H are the internal vertical and axial forces in the corotational system and are displayed in Figure (3.2). The element nodal forces in the global system are connected to the element internal forces by:

$$\begin{Bmatrix} \bar{Q}_1 \\ \bar{Q}_2 \\ \bar{Q}_3 \end{Bmatrix} = \begin{bmatrix} \cos\beta & -\sin\beta & 0 \\ \sin\beta & \cos\beta & 0 \\ 0 & 0 & 1 \end{bmatrix} \begin{Bmatrix} H_1 \\ V_1 \\ M_1 \end{Bmatrix} \tag{3.5}$$

$$\begin{Bmatrix} \bar{Q}_4 \\ \bar{Q}_5 \\ \bar{Q}_6 \end{Bmatrix} = \begin{bmatrix} \cos\beta & -\sin\beta & 0 \\ \sin\beta & \cos\beta & 0 \\ 0 & 0 & 1 \end{bmatrix} \begin{Bmatrix} H_2 \\ V_2 \\ M_2 \end{Bmatrix} \tag{3.6}$$

When combining the two sets of equations and rearranging we can obtain the transpose of the tranformation matrix T_r.

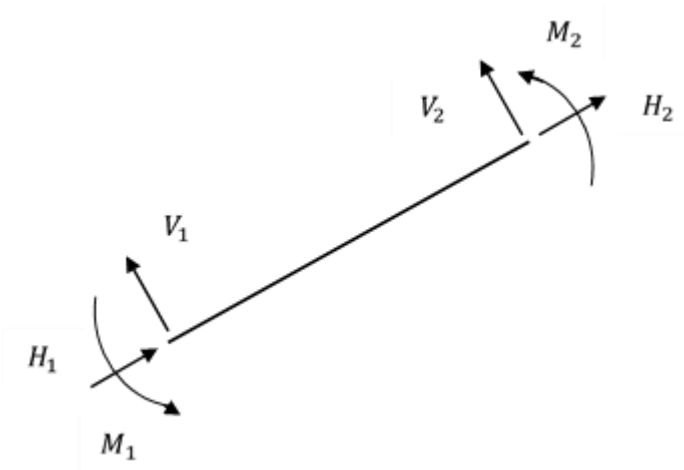

Figure 3.2: Internal element loading with respect to corotational system.

$$\begin{Bmatrix} \bar{Q}_1 \\ \bar{Q}_2 \\ \bar{Q}_3 \\ \bar{Q}_4 \\ \bar{Q}_5 \\ \bar{Q}_6 \end{Bmatrix} = \begin{bmatrix} -\cos\beta & -\frac{\sin\beta}{L} & -\frac{\sin\beta}{L} \\ -\sin\beta & \frac{\cos\beta}{L} & \frac{\cos\beta}{L} \\ 0 & 1 & 0 \\ \cos\beta & \frac{\sin\beta}{L} & \frac{\sin\beta}{L} \\ \sin\beta & -\frac{\cos\beta}{L} & -\frac{\cos\beta}{L} \\ 0 & 0 & 1 \end{bmatrix} \begin{Bmatrix} Q_1 \\ Q_2 \\ Q_3 \end{Bmatrix} \tag{3.7}$$

The matrix T_r links the element nodal forces in the global system with the element internal forces in the corotational system.

$$\bar{Q} = {T_r}^T Q \tag{3.8}$$

In addition, the transformation matrix is used for the transformation of the displacements between the corotational and global system.

$$\delta\bar{q} = {T_r}^T \delta q \tag{3.9}$$

Where $q = \begin{Bmatrix} q_1 \\ q_2 \\ q_3 \end{Bmatrix}$ such that q_1 is the axial deformation of the element and q_2 & q_3 are the chord rotations (Figure 3.1.a).

Similarly, the stiffness matrix will be transformed between the two systems using the same mapping matrix. However, an additional term K_G that includes the effects of element internal forces on the element stiffness must be included.

$$k_{elem(global)} = {T_r}^T K_{elem}\, T_r + K_G \tag{3.10}$$

Where K_G is called the external geometric stiffness matrix and is presented in Appendix 1.

While the transformation matrix T_r is in fact the multiplication of the matrix that removes the R.B.M. and the matrix that accounts for the member inclination.

$$T_r = \begin{bmatrix} -1 & 0 & 0 & 1 & 0 & 0 \\ 0 & \frac{1}{L} & 1 & 0 & -\frac{1}{L} & 0 \\ 0 & \frac{1}{L} & 0 & 0 & -\frac{1}{L} & 1 \end{bmatrix} \times \begin{bmatrix} cos\,\beta & sin\,\beta & 0 & 0 & 0 & 0 \\ -sin\,\beta & cos\,\beta & 0 & 0 & 0 & 0 \\ 0 & 0 & 1 & 0 & 0 & 0 \\ 0 & 0 & 0 & cos\,\beta & sin\,\beta & 0 \\ 0 & 0 & 0 & -sin\,\beta & cos\,\beta & 0 \\ 0 & 0 & 0 & 0 & 0 & 1 \end{bmatrix} \tag{3.11}$$

$$T_r = \begin{bmatrix} -\cos\beta & -\sin\beta & 0 & \cos\beta & \sin\beta & 0 \\ -\frac{\sin\beta}{L} & \frac{\cos\beta}{L} & 1 & \frac{\sin\beta}{L} & -\frac{\cos\beta}{L} & 0 \\ -\frac{\sin\beta}{L} & \frac{\cos\beta}{L} & 0 & \frac{\sin\beta}{L} & -\frac{\cos\beta}{L} & 1 \end{bmatrix} \quad (3.12)$$

The $(\cos\beta)$ and $(\sin\beta)$ can be determined from the current position of the element nodal coordinates. The element nodal coordinates are displayed in Figure (3.3). In the initial state, the two-dimensional coordinates system are (x_1, y_1) for node 1 and (x_2, y_2) for node 2. After deformation of the element and at its final state the coordinates becomes $(x_1 + u_1, y_1 + v_1)$ for node 1 and $(x_2 + u_2, y_2 + v_2)$ for node 2. Where u is the end displacement in the X direction and v is the end displacement in the Y direction. Then using trigonometric rules $(\cos\beta)$ and $(\sin\beta)$ can be calculated as follows:

$$\cos\beta = \frac{x_2+u_2-x_1-u_1}{L} \quad (3.13)$$

$$\sin\beta = \frac{y_2+v_2-y_1-v_1}{L} \quad (3.14)$$

The original length of the element between the nodes is:

$$L_0 = \sqrt{(x_2 - x_1)^2 + (y_2 - y_1)^2} \quad (3.15)$$

While the current length of the element, after deformations, can be calculated using:

$$L = \sqrt{(x_2 + u_2 - x_1 - u_1)^2 + (y_2 + v_2 - y_1 - v_1)^2} \quad (3.16)$$

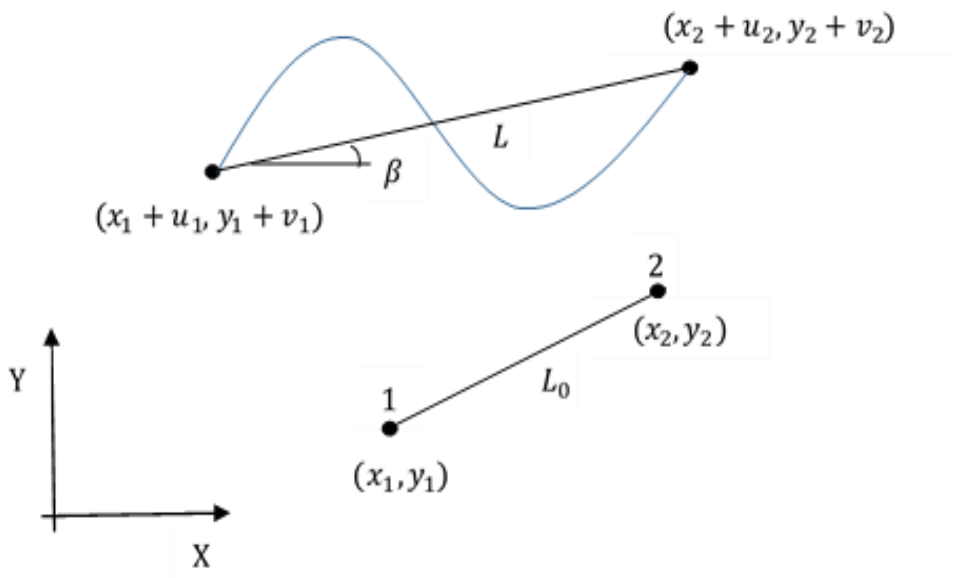

Figure 3.3: Initial state and final element configuration.

The angle β can correspondingly be calculated using the following equation:

$$\beta = \arctan\left(\frac{(y_2+v_2)-(y_1+v_1)}{(x_2+u_2)-(x_1+u_1)}\right) \tag{3.17}$$

Consequently large rigid body rotations are well considered during the transformation from the corotational to the global system, while in the original corotational formulations only small rotations and deformations are expected.

However, equation (3.17) is valid only for $|\beta| < \pi/2$ and if β exceed this limit an arctangent function (ARCTAN2) has to be used to calculate the value of the β angle **(Yaw, 2009)**.

After the elements are formulated in the corotational system, which will be presented next, they are transformed back to the global system with the help of the same transformation matrix.

3.3 Displacement-based element with second order effect formulation

First, the displacement-based element is presented. The element is easier to implement than more complex force-based elements, but nevertheless gives accurate results although a large number of members division is required to accurately simulate the response of the structure, mainly in plastic zones regions, because the calculation of the curvature is performed using a linear equation that is derived from a cubic shape function. If a small number of element division is adopted, the inelastic curvature will not be properly presented and the efficacy of the element will become questionable.

In the displacement-based method, the equilibrium is achieved only in a weighted integral sense. The displacements serve as primary variables and are interpolated from the DOF of the element and the principle of virtual displacements is implemented to obtain the solution.

The proposed element is formulated in the corotational system using the weak form of the equilibrium equations. Then the element stiffness matrix is calculated by the linearization of the weak form of the equilibrium equations where the linearization is the linear approximation of the nonlinear system by consistent linearization of the principle of virtual displacements **(Nukala, 1997)**, and this approximation is only valid in a small region.

A linear shape function is selected for the axial displacement of the beam:

$$u = \begin{bmatrix} \frac{x}{L} & 0 & 0 \end{bmatrix} q \tag{3.18}$$

Letting:

$$N_u^T = \begin{bmatrix} \frac{x}{L} & 0 & 0 \end{bmatrix} \tag{3.19}$$

The axial strain is calculated as the first derivative of the axial displacement $\frac{du}{dx}$.

A cubic displacement shape function is designated for the transverse displacement of the beam:

$$v = \begin{bmatrix} 0 & x - \frac{2x^2}{L} + \frac{x^3}{L^2} & -\frac{x^2}{L} + \frac{x^3}{L^2} \end{bmatrix} q \tag{3.20}$$

Letting:

$$N_v^T = \begin{bmatrix} 0 & x - \frac{2x^2}{L} + \frac{x^3}{L^2} & -\frac{x^2}{L} + \frac{x^3}{L^2} \end{bmatrix} \tag{3.21}$$

The curvature is calculated as the second derivative of the transverse displacement $\left(\frac{d^2v}{dx^2}\right)$.

Then the equilibrium is satisfied in a weighted integral sense by multiplying the equilibrium equation by a weighting function and integrating along the element length. This is known as the weak form of equilibrium. Therefore, the variations and the weighting functions are:

$$\delta u = N_u^T \delta q \tag{3.22}$$

$$\delta v = N_v^T \delta q \tag{3.23}$$

The Green-Lagrange strain-displacement relation is used to evaluate the strain. The relation leads to the classical strain calculation method used in solid mechanics:

$$\hat{\varepsilon} = \frac{du}{dx} + \frac{1}{2}\left(\frac{dv}{dx}\right)^2 + \frac{1}{2}\left(\frac{du}{dx}\right)^2 \tag{3.24}$$

The third term in the previous equation is neglected since the axial deformation of the element chord within the corotational system is relatively small.

Therefore, the variation of the Green-Lagrange strain is:

$$\hat{\varepsilon} = \delta u' + \delta v' v' \tag{3.25}$$

And,

$$\delta u' = \left(\frac{1}{L}\right) \delta q_1 \tag{3.26}$$

$$v' = \left[1 - \frac{4x}{L} + \frac{3x^2}{L^2} \quad -\frac{2x}{L} + \frac{3x^2}{L^2}\right] \begin{Bmatrix} q_2 \\ q_3 \end{Bmatrix} \tag{3.27}$$

$$\delta v' = \left[1 - \frac{4x}{L} + \frac{3x^2}{L^2} \quad -\frac{2x}{L} + \frac{3x^2}{L^2}\right] \begin{Bmatrix} \delta q_2 \\ \delta q_3 \end{Bmatrix} \tag{3.28}$$

After substitution equations (3.22) and (3.23) into (3.24) and neglecting $\frac{1}{2}\left(\frac{du}{dx}\right)^2$, the variation becomes:

$$\hat{\varepsilon} = \left(N_u'^T + q^T N_v' N_v'^T\right) \delta q \tag{3.29}$$

Similarly for the curvature:

$$\delta \widehat{K} = \left(N_v''^T\right) \delta q \tag{3.30}$$

So the variation in the generalized strains can be stated as:

$$\delta \hat{d} = \begin{Bmatrix} \delta \hat{\varepsilon} \\ \delta \widehat{K} \end{Bmatrix} = N_\delta \, \delta q \tag{3.31}$$

Where $N_\delta = \begin{Bmatrix} \left(N_u' + q\, N_v'^T N_v'\right) \\ N_v'' \end{Bmatrix}$ (3.32)

After substitution with the displacement shape function and their derivatives we obtain:

$N_\delta =$

$$\begin{bmatrix} \frac{1}{L} & \left(1-\frac{4x}{L}+\frac{3x^2}{L^2}\right)^2 q_2 + & \left(1-\frac{4x}{L}+\frac{3x^2}{L^2}\right)\left(-\frac{2x}{L}+\frac{3x^2}{L^2}\right) q_2 \\ & \left(1-\frac{4x}{L}+\frac{3x^2}{L^2}\right)\left(-\frac{2x}{L}+\frac{3x^2}{L^2}\right) q_3 & +\left(\frac{2x}{L}+\frac{3x^2}{L^2}\right)^2 q_3 \\ 0 & -\frac{4}{L}+\frac{6x}{L^2} & -\frac{2}{L}+\frac{6x}{L^2} \end{bmatrix} \quad (3.33)$$

Consequently, the generalized strains is:

$$\hat{d} = \begin{Bmatrix} \hat{\varepsilon} \\ \hat{K} \end{Bmatrix} = \begin{Bmatrix} N_u'^T \\ N_v''^T \end{Bmatrix} q + \frac{1}{2}\begin{Bmatrix} 0 \\ 1 \end{Bmatrix} q^T N_v' \, N_v'^T q \quad (3.34)$$

In addition, the increment in the generalized strains is specified as:

$$\Delta\hat{d} = N_1 \Delta q + \begin{Bmatrix} 0 \\ 1 \end{Bmatrix} \Delta q^T N_2 q^t + \frac{1}{2}\begin{Bmatrix} 0 \\ 1 \end{Bmatrix} \Delta q^T N_2 \Delta q \quad (3.35)$$

Where:

$$N_1 = \begin{Bmatrix} N_u'^T \\ N_v''^T \end{Bmatrix} = \begin{bmatrix} \frac{1}{L} & 0 & 0 \\ 0 & \frac{-4}{L}+\frac{6x}{L^2} & \frac{-2}{L}+\frac{6x}{L^2} \end{bmatrix} \quad (3.36)$$

$N_2 = N_v' \, N_v'^T =$

$$\begin{bmatrix} 0 & 0 & 0 \\ 0 & \left(1-\frac{4x}{L}+\frac{3x^2}{L^2}\right)^2 & \left(1-\frac{4x}{L}+\frac{3x^2}{L^2}\right)\left(\frac{-2x}{L}+\frac{3x^2}{L^2}\right) \\ 0 & \left(1-\frac{4x}{L}+\frac{3x^2}{L^2}\right)\left(\frac{-2x}{L}+\frac{3x^2}{L^2}\right) & \left(-\frac{2x}{L}+\frac{3x^2}{L^2}\right)^2 \end{bmatrix} \quad (3.37)$$

Where N_1 and N_2 are the final shape functions containing the higher order terms.

Where Δq is the element end displacements increment and is taken as the difference between the current step and the step just before; while q^t is the total value of the displacement at the current step.

After satisfying the equilibrium, a linearization of the equilibrium equations is performed in order to obtain the element stiffness matrix K_{elem}.

$$K_{elem}\Delta q = F_{ext} - F_{elem} \quad (3.38)$$

$$K_{elem} = \int_0^{L_0} (\Lambda + {N_\delta}^T \, k_{sec} \, N_\delta) dx \tag{3.39}$$

and the first term of the right-hand-side of the equation is later defined in equation (3.41).

F_{ext} is the applied external nodal load vector and F_{elem} is the internal resisting load vector and equal:

$$F_{elem} = \int_0^{L_0} {N_\delta}^T \, F_{sec} \, dx \tag{3.40}$$

Where F_{sec} is the section resisting forces and is shown in vector form as $\begin{Bmatrix} P \\ M \end{Bmatrix}$.

While P is the section axial force and M is the section bending moment.

$$\text{And } \Lambda = Q_1 \begin{bmatrix} 0 & 0 & 0 \\ 0 & (1 - \frac{4x}{L} + \frac{3x^2}{L^2})^2 & (1 - \frac{4x}{L} + \frac{3x^2}{L^2})(-\frac{2x}{L} + \frac{3x^2}{L^2}) \\ 0 & (1 - \frac{4x}{L} + \frac{3x^2}{L^2})(-\frac{2x}{L} + \frac{3x^2}{L^2}) & (-\frac{2x}{L} + \frac{3x^2}{L^2})^2 \end{bmatrix} \tag{3.41}$$

And can be further simplified by solving the integral to:

$$K_g = \int_0^{L_0} \Lambda \, dx = Q_1 \begin{bmatrix} 0 & 0 & 0 \\ 0 & \frac{2L}{15} & \frac{-L}{30} \\ 0 & \frac{-L}{30} & \frac{2L}{15} \end{bmatrix} \tag{3.42}$$

Where K_g is termed the internal geometric stiffness matrix.

3.4 Displacement-based element state determination

The state determination of the displacement-based element starts by calculating the generalized section deformation increment. Averaging the second and third terms of the generalized strain equations along the element length is useful for obtaining

appropriate results and avoiding the membrane locking effect **(Crisfield, 1991)**. Therefore, equation (3.35) becomes:

$$\Delta\hat{d} = N_1\Delta q + \begin{Bmatrix}0\\1\end{Bmatrix}\frac{1}{L}\int_0^{L_0}\Delta q^T N_2 q^t + \frac{1}{2}\begin{Bmatrix}0\\1\end{Bmatrix}\frac{1}{L}\int_0^{L_0}\Delta q^T N_2 \Delta q \tag{3.43}$$

And then updating the generalized section deformations

$$\hat{d}^{i+1} = \hat{d}^i + \Delta\hat{d} \tag{3.44}$$

Where the 'i' index denotes the previous step of the Newton-Raphson iteration at the global level and 'i+1' symbolises the current step.

Using the section state determination, the section flexibility and the section resisting forces are calculated from the fibre discretization (the integration of the response of the fibres) using the section deformation increment and following the assumption that plane sections remain plane.

The section flexibility is then inverted into a section stiffness.

The element stiffness matrix and the element internal resisting load vector are then calculated by the integration of the section stiffness matrix and the section resisting force respectively along the element length:

$$K_{elem} = \left(K_g + \int_0^{L_0} N_\delta^T\, k_{sec}^{i+1}\, N_\delta dx\right) \tag{3.45}$$

$$F_{elem} = \int_0^{L_0} {N_\delta}^T\, F_{sec}^{i+1}\, dx \tag{3.46}$$

3.5 Mixed-based element with second order effect formulation

The mixed (hybrid) beam element is formulated to overcome the weakness of the displacement-based element. The mixed element overcomes the complexity of

accounting for the second order effect in a force-based formulation **(De Souza, 2000)**, where the mixed formulation effectively represents the curvature and the strain in the localized plastic zones with a small number of element divisions. Even under cyclic loading and degrading strength, appropriate results can be achieved with a very small number of elements. The resulting element merges the robustness of the flexibility method with the ease of implementing the second order effect. However, the creation of the mixed element is computationally more complicated and involving than the displacement-based element.

In the two-field mixed technique, displacement variables and stress resultant forces are casted individually. Both the displacements and the internal forces are interpolated along the length of the element. The equilibrium equations and compatibility equations are satisfied in a weighted integral sense and the stress resultant forces respect the equilibrium equations at any section along the element length.

The mixed element is also formulated in the corotational system. All definitions and numerical expression previously identified in the displacement-based formulation are also valid for this formulation. Weighting functions are multiplied by the equilibrium equations and then integrated along the element length. Cubic and linear interpolation shape functions are chosen for the transverse (v) and axial (u) displacements:

$$\begin{Bmatrix} v \\ u \end{Bmatrix} = \begin{bmatrix} 0 & x - \frac{2x^2}{L} + \frac{x^3}{L^2} & \frac{-x^2}{L} + \frac{x^3}{L^2} \\ \frac{x}{L} & 0 & 0 \end{bmatrix} \begin{Bmatrix} q_1 \\ q_2 \\ q_3 \end{Bmatrix} \tag{3.47}$$

Taking N_u and N_v the same as in the displacement-based formulation.

The force shape function is formed from a constant axial force field and a linear moment field:

$$\begin{Bmatrix} P \\ M \end{Bmatrix} = \begin{bmatrix} 1 & 0 & 0 \\ 0 & \frac{x}{L} - 1 & \frac{x}{L} \end{bmatrix} \begin{Bmatrix} Q_1 \\ Q_2 \\ Q_3 \end{Bmatrix} \tag{3.48}$$

Considering:

$$N_D = \begin{bmatrix} 1 & 0 & 0 \\ 0 & \frac{x}{L} - 1 & \frac{x}{L} \end{bmatrix} \tag{3.49}$$

Where N_D is the force shape function.

The variations and the weighting functions are:

$$\delta v = N_v^T \delta q \tag{3.50}$$

$$\delta u = N_u^T \delta q \tag{3.51}$$

The Green-Lagrange strain-displacement relation is:

$$\hat{\varepsilon} = \frac{du}{dx} + \frac{1}{2}\left(\frac{dv}{dx}\right)^2 + \frac{1}{2}\left(\frac{du}{dx}\right)^2 \tag{3.52}$$

After ignoring the third term, the variation of the strain will be:

$$\hat{\varepsilon} = \delta u' + \delta v' v' \tag{3.53}$$

Then:

$$\hat{\varepsilon} = \left(N_u'^T + q^T N_v' N_v'^T\right) \delta q \tag{3.54}$$

Therefore the variation in the generalized strains is:

$$\delta \hat{d} = \begin{Bmatrix} \delta \hat{\varepsilon} \\ \delta \hat{K} \end{Bmatrix} = N_\delta \, \delta q \tag{3.55}$$

Where:

$$N_\delta = \begin{Bmatrix} \left(N_u' + q\, {N_v'}^T N_v'\right) \\ N_v'' \end{Bmatrix} \tag{3.56}$$

After substitution with the displacement shape function and their derivatives we obtain that:

$N_\delta =$

$$\begin{bmatrix} \frac{1}{L} & \left(1 - \frac{4x}{L} + \frac{3x^2}{L^2}\right)^2 q_2 + & \left(1 - \frac{4x}{L} + \frac{3x^2}{L^2}\right)\left(-\frac{2x}{L} + \frac{3x^2}{L^2}\right) q_2 \\ & \left(1 - \frac{4x}{L} + \frac{3x^2}{L^2}\right)\left(-\frac{2x}{L} + \frac{3x^2}{L^2}\right) q_3 & + \left(\frac{2x}{L} + \frac{3x^2}{L^2}\right)^2 q_3 \\ 0 & -\frac{4}{L} + \frac{6x}{L^2} & -\frac{2}{L} + \frac{6x}{L^2} \end{bmatrix} \tag{3.57}$$

The generalized strains are:

$$\hat{d} = \begin{Bmatrix} \hat{\varepsilon} \\ \hat{K} \end{Bmatrix} = \begin{Bmatrix} {N_u'}^T \\ {N_v''}^T \end{Bmatrix} q + \frac{1}{2}\begin{Bmatrix} 0 \\ 1 \end{Bmatrix} q^T N_v'\, {N_v'}^T q \tag{3.58}$$

In addition, the increment in the generalized strains is specified by:

$$\Delta\hat{d} = N_1 \Delta q + \begin{Bmatrix} 0 \\ 1 \end{Bmatrix} \Delta q^T N_2 q^t + \frac{1}{2}\begin{Bmatrix} 0 \\ 1 \end{Bmatrix} \Delta q^T N_2 \Delta q \tag{3.59}$$

Where:

$$N_1 = \begin{Bmatrix} {N_u'}^T \\ {N_v''}^T \end{Bmatrix} = \begin{bmatrix} \frac{1}{L} & 0 & 0 \\ 0 & \frac{-4}{L} + \frac{6x}{L^2} & \frac{-2}{L} + \frac{6x}{L^2} \end{bmatrix} \tag{3.60}$$

$N_2 = N_v'\, {N_v'}^T =$

$$\begin{bmatrix} 0 & 0 & 0 \\ 0 & \left(1 - \frac{4x}{L} + \frac{3x^2}{L^2}\right)^2 & \left(1 - \frac{4x}{L} + \frac{3x^2}{L^2}\right)\left(\frac{-2x}{L} + \frac{3x^2}{L^2}\right) \\ 0 & \left(1 - \frac{4x}{L} + \frac{3x^2}{L^2}\right)\left(\frac{-2x}{L} + \frac{3x^2}{L^2}\right) & \left(-\frac{2x}{L} + \frac{3x^2}{L^2}\right)^2 \end{bmatrix} \tag{3.61}$$

At that point, the compatibility is imposed using the weak form by multiplying the weighting function with the difference of the strains calculated from the

displacement shape function $\hat{d}$, and the strains calculated from the force shape function d, then integrating along the element length.

$$\int_0^{L_0} \delta {F_{sec}}^T \left(\hat{d} - d\right) dx = 0 \tag{3.62}$$

Next, the weak form of equilibrium equations is combined with the weak form of the compatibility equations resulting in two equations:

Firstly, the element equilibrium equation:

$$g = \int_0^{L_0} N_\delta^T F_{sec} dx - F_{ext} \ = 0 \tag{3.63}$$

Secondly, the element strain displacement compatibility equation:

$$V = \int_0^{L_0} N_D^T \left(\hat{d} - d\right) dx = 0 \tag{3.64}$$

Together with the incremental cross section constitutive equation:

$$\Delta F_{sec} = K_{sec}\, \Delta d \tag{3.65}$$

Then the section constitutive equations, the element compatibility equations and the equilibrium equations are linearized.

From the linearization of the section constitutive equations we get:

$$\Delta d = f_{sec}(F_{sec} - \ F_R) \tag{3.66}$$

Where:

F_R: The section resisting forces.

f_{sec}: The section flexibility.

And from the linearization of the element compatibility equations we get:

$$\Delta F_{elem} = {f_{elem}}^{-1}(\mathrm{V} + G\ \Delta q) \tag{3.67}$$

Where:

$$f_{elem} = \int_0^{L_0} N_D^T \, f_{sec} \, N_D dx \tag{3.68}$$

$$G = \int_0^{L_0} N_D^T \;\; N_\delta dx \tag{3.69}$$

And G is the integration of the product of the displacement and force shape functions along the element length. It contains higher order terms to include the second order effect.

$$G = \begin{bmatrix} 1 & \frac{2Lq_2}{15} - \frac{Lq_3}{30} & -\frac{Lq_2}{30} + \frac{2Lq_3}{15} \\ 0 & 1 & 0 \\ 0 & 0 & 1 \end{bmatrix} \tag{3.70}$$

Lastly, the element stiffness is determined from the linearization of the equilibrium equations:

$$K_{elem} \, \Delta q = F_{ext} - F_{elem} \tag{3.71}$$

Where:

$$K_{elem} = \left(K_g + \int_0^{L0} G^T \, f_{elem}^{-1} \, G \, dx \right) \tag{3.72}$$

$$F_{elem} = G^T F_{elem} + G^T \, f_{elem}^{-1} \, V \tag{3.73}$$

3.6 Mixed-based element state determination

In the following state determination, residuals at the section and element stages are eliminated using the internal element iteration and the Newton-Raphson global iteration respectively. Hence “i” index represents the Newton-Raphson iteration at the global level and “j” index symbolises the internal iteration at the element level.

First, we start by calculating the element end force increments ΔF_{elem}

$$\Delta F_{elem}^{j} = \mathcal{K}_{elem}^{j-1}\,\Delta \mathrm{q} \tag{3.74}$$

Where $\mathcal{K}_{elem}^{j-1}$ is the element stiffness calculated from the previous step and the deformation increment Δq:

$$\Delta \mathrm{q} = G\,\Delta\bar{q} \tag{3.75}$$

Where $\bar{q}$ was previously defined in Figure (3.1) and equation (3.9).

Then element end forces are updated using the previous converged step:

$$F_{elem}^{j} = F_{elem}^{j-1} + \Delta F_{elem}^{j} \tag{3.76}$$

Then the section force increments ΔF_{sec} is primarily evaluated from the force shape function:

$$\Delta F_{sec}^{j} = N_D(x).\,\Delta F_{elem}^{j} \tag{3.77}$$

And the section forces are updated using the previous converged value:

$$F_{sec}^{j} = F_{sec}^{j-1} + \Delta F_{sec}^{j} \tag{3.78}$$

The section deformation increments derived from the interpolated stress-resultant can now be calculated:

$$\Delta d^{j} = f_{sec}^{j-1}\,\Delta F_{sec}^{j} \tag{3.79}$$

And the section deformations are at that point updated using the previous converged value:

$$d^{j} = d^{j-1} + \Delta d^{j} \tag{3.80}$$

The Green-Lagrange equation is used to calculate the increment in the generalized strains:

$$\Delta\hat{d}^{i} = N_1\Delta q + \begin{Bmatrix}0\\1\end{Bmatrix}\Delta q^{T} N_2 q^{t} + \frac{1}{2}\begin{Bmatrix}0\\1\end{Bmatrix}\Delta q^{T} N_2 \Delta q \tag{3.81}$$

And then the total generalized strains are obtained using the values at the previous converged step:

$$\hat{d}^i = \hat{d}^{i-1} + \Delta\hat{d}^i \tag{3.82}$$

The first residual is then evaluated:

$$V^j = \int_0^L N_D^T(x)(\hat{d}^i - d^j) \tag{3.83}$$

And the element flexibility matrix f_{elem} is calculated

$$f_{elem}^j = \int_0^{L_0} N_D^T(x).\, f_{sec}^j(x).\, N_D(x).\, dx \tag{3.84}$$

Further, the section stiffness and force vector are determined from the fibre discretization using the section deformation increment and the assumption of plane sections remaining planes. The section residual deformations Δd^j are determined by multiplying the section flexibility f_{sec}^j and the section unbalanced forces, where, the unbalanced forces are the difference between the applied section forces F_{sec}^j and the section resisting forces F_{R}^j.

$$\Delta d^{j+1} = f_{sec}^j(F_{sec}^j - F_{\mathrm{R}}^j) \tag{3.85}$$

The section residual deformations are then used to update the section deformations:

$$d^{j+1} = d^j + \Delta d^{j+1} \tag{3.86}$$

The section residuals deformations are integrated along the element to calculate the element residual deformations:

$$R^j = \int_0^L N_D^T(x).\, \Delta d^{j+1}.\, dx \tag{3.87}$$

Then by inverting the element flexibility f_{elem}, the element stiffness matrix $\mathcal{K}_{elem}$ is obtained.

And the internal geometric stiffness matrix K_g is added to the element stiffness.

$$K_{elem}^j = \left({K_g}^j + \mathcal{K}_{elem}^j\right) \tag{3.88}$$

Where:

$$K_g = Q_1 \begin{bmatrix} 0 & 0 & 0 \\ 0 & \frac{2L}{15} & \frac{-L}{30} \\ 0 & \frac{-L}{30} & \frac{2L}{15} \end{bmatrix} \tag{3.89}$$

When updating the element end resisting forces both the element residuals and compatibility equation have to be considered.

$$\Delta F_{elem}^{j+1} = K_{elem}^{j} \, (V^j - R^j) \tag{3.90}$$

Then the element end resisting forces are updated this time from the previous step.

$$F_{elem}^{j+1} = F_{elem}^{j} + \Delta F_{elem}^{j+1} \tag{3.91}$$

Later an update to the forces and deformations of all sections has to be performed using the updated element end resisting forces.

Iterations have to be performed until the residuals diminish and the subsequent criteria is met:

$$\Sigma \left| V^j \right| \leq tolerance \tag{3.92}$$

For the mixed element only, it will be required upon convergence that the element force vector F_{elem} and element stiffness matrix K_{elem} be multiplied by the G matrix, previously defined in (3.70), before being transformed to the global system by the transformation matrix T_r as shown below:

For the element forces:

$$F_{elem_{(G)}} = G^T \, F_{elem} \tag{3.93}$$

And for the element stiffness matrix:

$$K_{elem_{(G)}} = \; G^T \, K_{elem} \, G \tag{3.94}$$

3.7 The fibre beam element material model

Advanced material models were assigned to the displacement and the mixed fibre beam elements that consider the second order effect, to allow the proper simulation and the prediction of the response of reinforced concrete members under different monotonic and cyclic loading. However, the effect of the bond slip is neglected in this study. For the concrete material model in compression, the model of **Kent and Park (1971)** as modified by **Scott et al. (1982)** is employed.

The model simulates the nonlinear behaviour of concrete and the expected strain softening behaviour that occurs with the reduction of the stresses after its peak value that is accompanied by an upsurge in the deformation. The model also acknowledges the ductility of concrete that helps in achieving considerable amount of deformations before failure occurs. Meaning that the adopted concrete material model respects the pre-peak and post-peak behaviour of concrete, also the effect of concrete confinement in compression and the softening that occurs to the concrete in compression due to the propagation of cracks. Furthermore, the model reflects the ability of concrete to carry tension.

For the tensile behaviour in the concrete material model, the model accounts for the effect of the tension stiffening and the degradation of the unloading and reloading stiffness for increased peak tensile strains after early cracking, where the tension stiffening is the capability of the cracked concrete to carry tensile stresses and to participate in the stiffness of the member. As the cracks increase, this participation diminishes and the tension stiffening decreases progressively. So the concrete stress-strain relation simulates this behaviour by reducing the tensile stress, after reaching the tensile strength, until it reaches a zero value. The reduction of the tensile

strength can follow a linear, multilinear or exponential path. In the present material model, the linear path is the only possible choice. Meanwhile, if the tension stiffening is ignored, the calculated deflection of the members will be significantly overestimated.

The concrete material model with tensile strength and linear tension softening requires the input of a number of parameters in order to create the full stress strain curve. These parameters are shown in Figure (3.4) and defined below. The hysteretic concrete stress-strain curve is also shown in Figure (3.5). The model contains the unloading, reloading and transition between tension and compression curves for the concrete while the cyclic behaviour is modelled by a number of straight lines.

INPUT PARAMETERS FOR THE CONCRETE MATERIAL MODEL:

$f_c', \varepsilon_0, \varepsilon_{cu}, \lambda, f_t, E_{ts}$

Where:

f_c' : Concrete compressive strength at 28 days (negative for compression)

ε_0 : Concrete strain at maximum strength

ε_{cu} : Concrete strain at crushing strength

λ : $\frac{E_U}{E_C}$ (For cyclic loading only)

f_t: Tensile strength (positive for tension)

E_{ts} : Tension softening stiffness (absolute value)

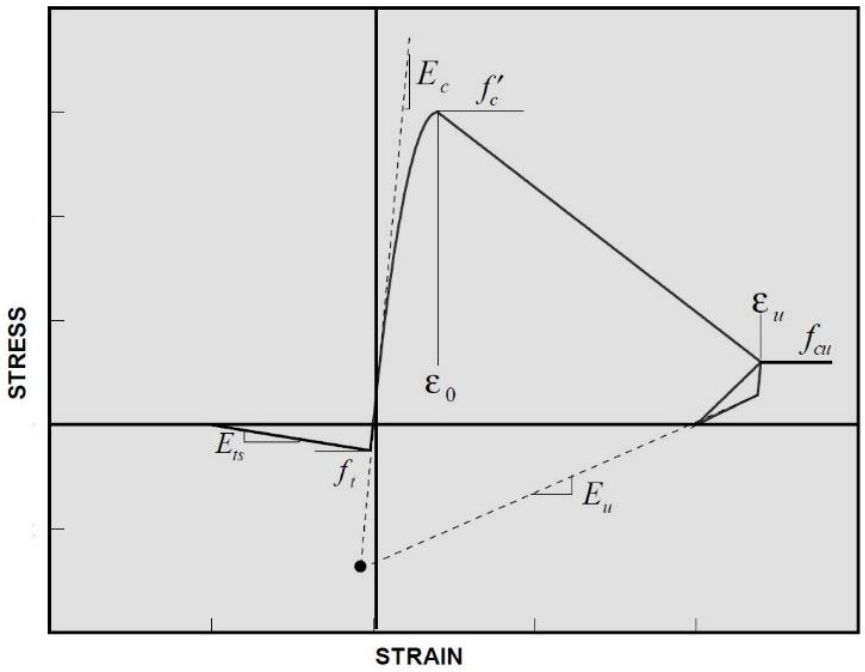

Figure 3.4: Material Parameters for concrete model.

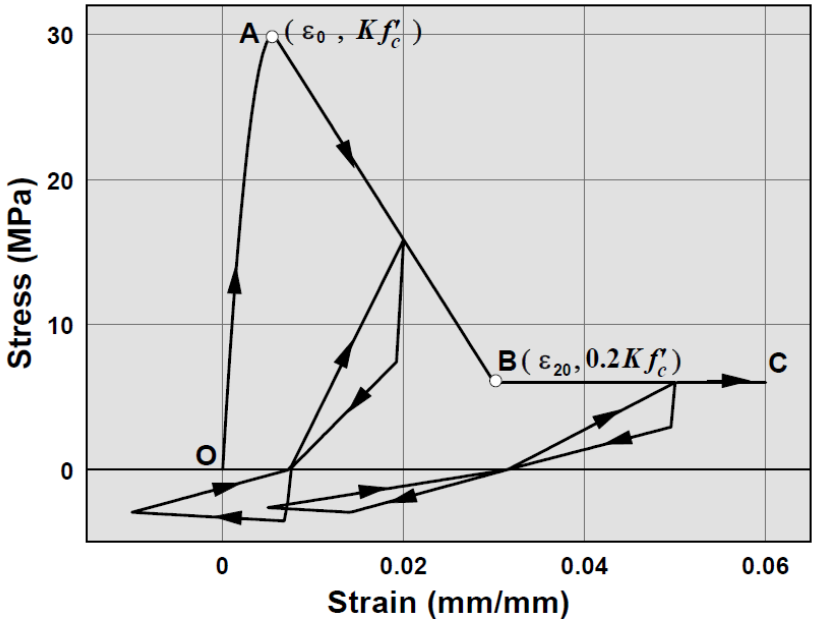

Figure 3.5: Concrete cyclic material model.

For the steel material model, the modified Menegotto-Pinto cyclic stress-strain curve of mild steel bar is employed. **Filippou et al. (1983)** improved the **Menegotto and Pinto (1973)** model by including the isotropic strain hardening effect. The

model contains the monotonic envelope, the ascending and the descending branches. However, the yield plateau and the nonlinear work hardening are approximated through curved transitions with a straight-line asymptote with slope E to another straight-line asymptote with slope E_p and controlled by a strain hardening ratio b.

The steel material model with isotropic strain hardening requires the input of a number of parameters in order to create the full stress-strain curve. These parameters are shown in Figure (3.6) and defined below. The hysteresis steel stress- strain curve is also shown in Figure (3.7).

INPUT PARAMETERS FOR THE STEEL MATERIAL MODEL:

f_y, E, b, R_0, C_1, C_2

a_1, a_2, a_3, a_4

Where:

f_y : yield strength.

E : Young's modulus.

b : $\frac{E_p}{E}$ Strain hardening ratio

R_0 : Exponent number for the control of the transition between elastic and hardening zones.

C_1& C_2 : Parameters for the change of R_0 with cyclic loading.

a_1, a_2, a_3& a_4: Isotropic hardening parameters.

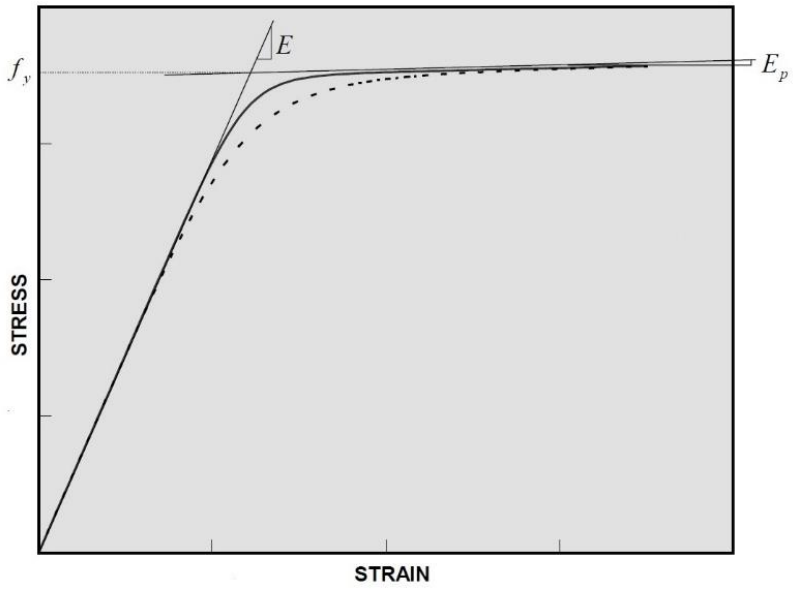

Figure 3.6: Material Parameters for Steel model.

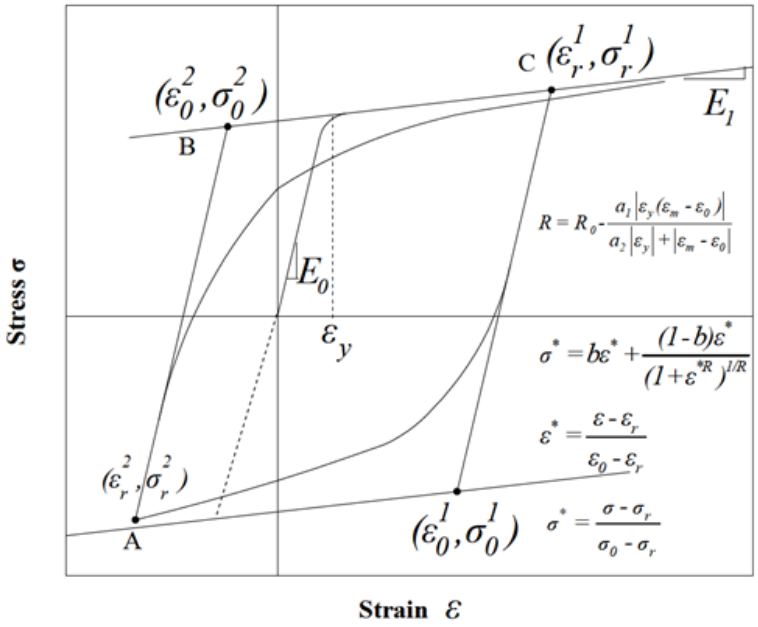

Figure 3.7: Menegotto-Pinto Cyclic stress-strain curve of steel.

3.8 Validation of the finite element models

The newly developed models are verified by comparing their results with a number of experiments available from the literature. All the chosen experiments are

subjected to large deformations because of the slenderness of the adopted sections and the dimensions of the members. Fibrous materials were utilized in some specimens and were accounted for in the models. Their effect is displayed and discussed in the next sections. After the calibration of the numerical models, the elements can be extensively used to simulate the response of different reinforced concrete structures subjected to large displacements and rotations.

3.8.1 William's toggle frame

First, the two elements will be validated against the well-known experiment of **Williams (1964)** that has been studied previously by many researchers to validate their models. The frame is shown in Figure (3.8) with its circular cross section. The importance of this exercise is that the beam undergoes considerable large deformations. It is considered a good tool to examine the formulation of geometrically nonlinear elements due to its highly nonlinear response. The experiment was first devised by **Williams (1964)** and later analysed by many researchers including **Chan (1988)** who used an elastic perfectly plastic material and two different values of yield stress in the analysis. Similarly, **De Souza (2000)** used a force-based element to model the cantilever.

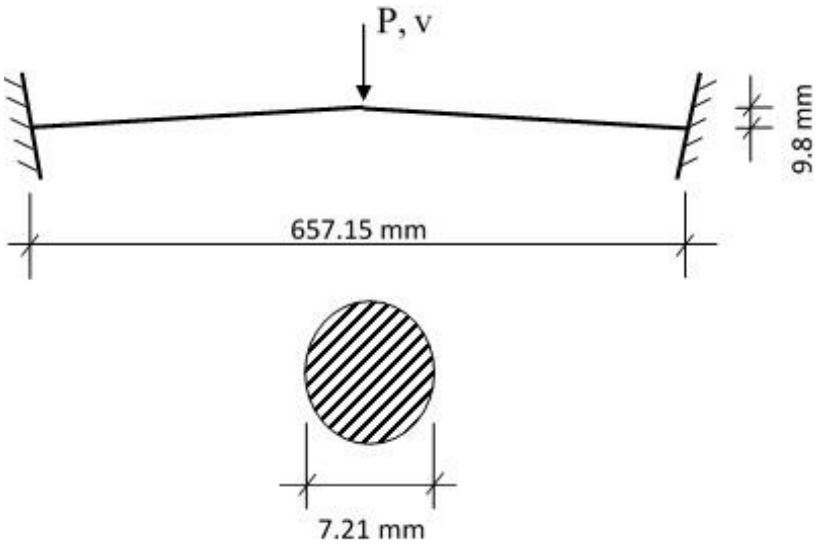

Figure 3.8: Williams toggle frame.

The developed fibre beam elements were used to model the William toggle frame with three different yield stress values. Young's modulus was taken as 199,714 MPa and the circular cross section was divided into 10 fibres. The displacement-based model was divided into 8 elements, while the mixed-based model was divided into 4 elements only. The boundaries were fixed and the load was applied at the centre using a displacement control procedure.

The load-deformation plot shown in Figure (3.9) confirms that the two fibre beam elements were both able to follow the equilibrium path of the William toggle frame for the three yield stress values accurately. Both the elastic and inelastic regions were modelled accurately although only in the elastic region the equilibrium path was identical.

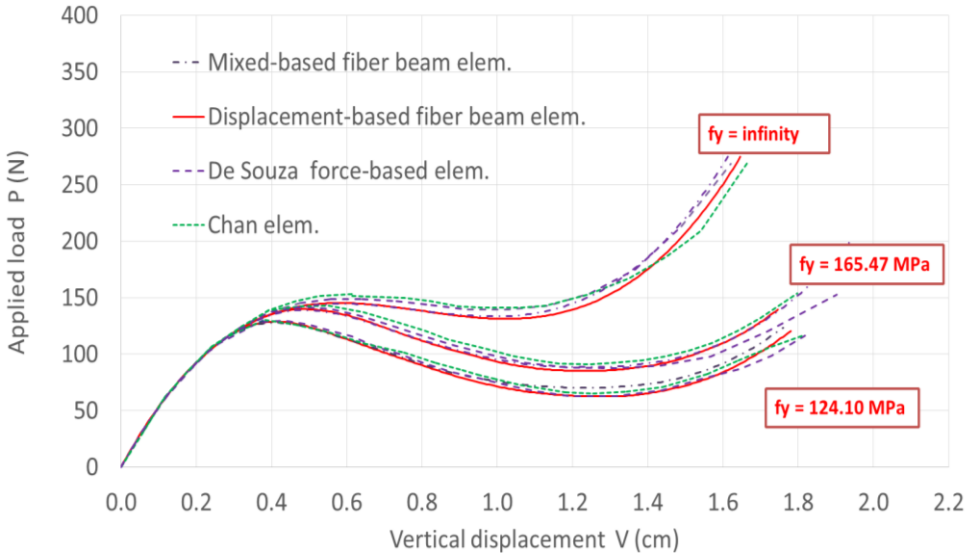

Figure 3.9: Equilibrium paths for the toggle frame.

Although many scholars modelled the previous William toggle frame, none of them went further and showed the distribution of straining actions along the length of the frame. The distribution of curvatures, moments and axial forces can be used for the design of structures. It can form a better understanding of the behaviour of the structural elements. Therefore, the displacement-based element was nominated to produce the distribution for the case of infinite yield strength. Figure (3.10) shows the curvature distribution along the toggle frame length at displacement values of 0.5, 1.0 and 1.5 cm, while Figure (3.11) shows the moment distribution along the toggle frame length at displacement values of 0.5, 1.0 and 1.5 cm. Finally, Figure (3.12) shows the axial distribution along the toggle frame length at the same displacements. Only the calculation of the axial force faced some slight numerical deviations for the displacement value of 1.5 mm because of the high displacements exerted on the frame. However, the elements were able to run stably in all cases.

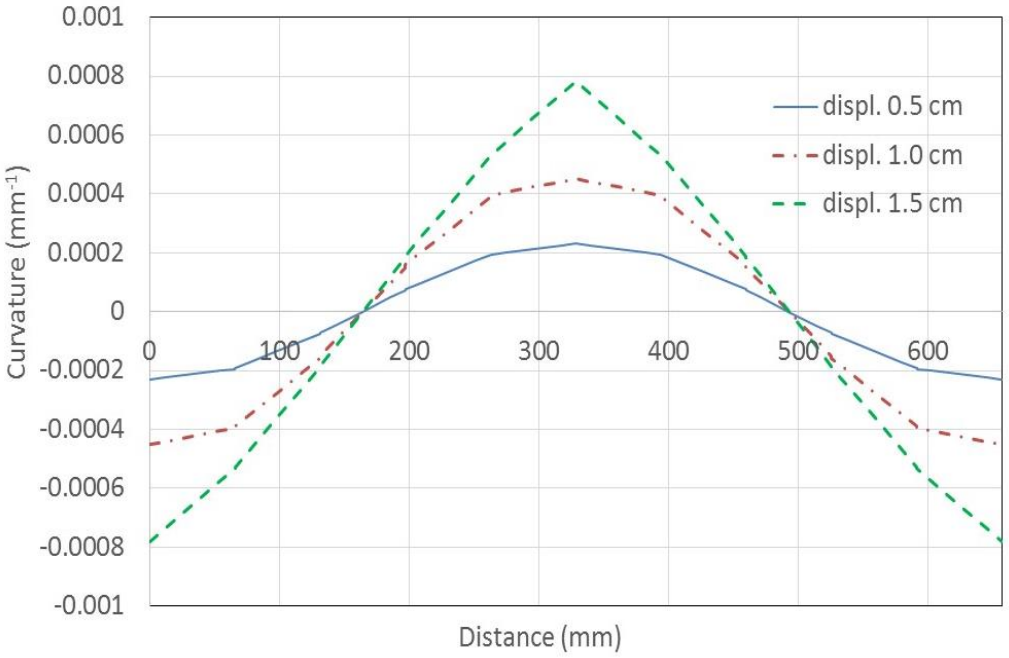

Figure 3.10: Curvature distribution for the toggle frame under 3 different displacement values.

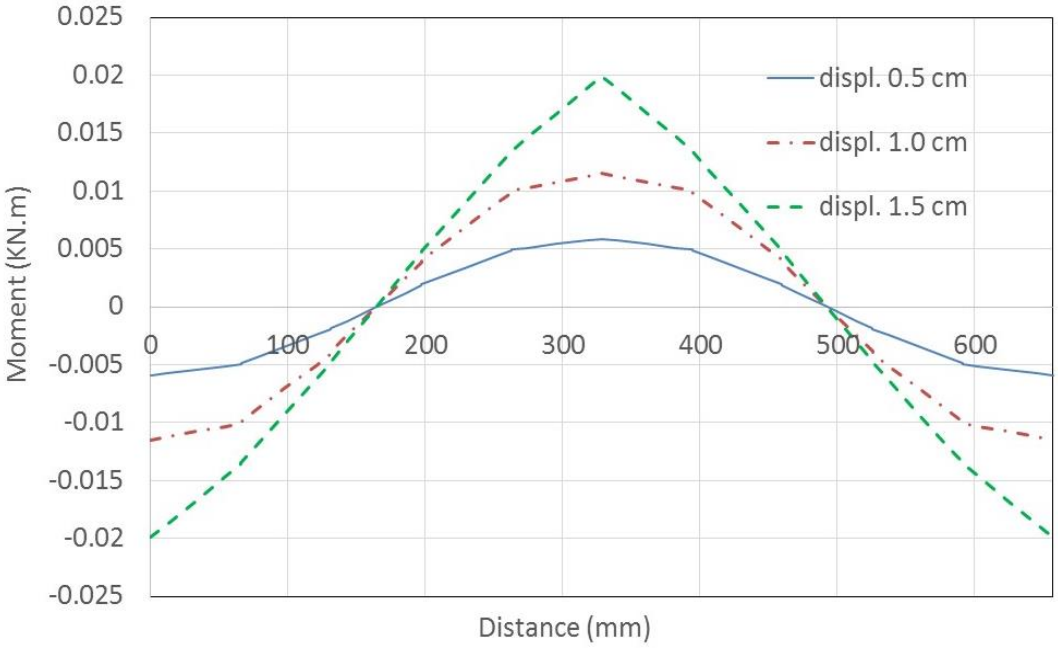

Figure 3.11: Moment distribution for the toggle frame under 3 different displacement values.

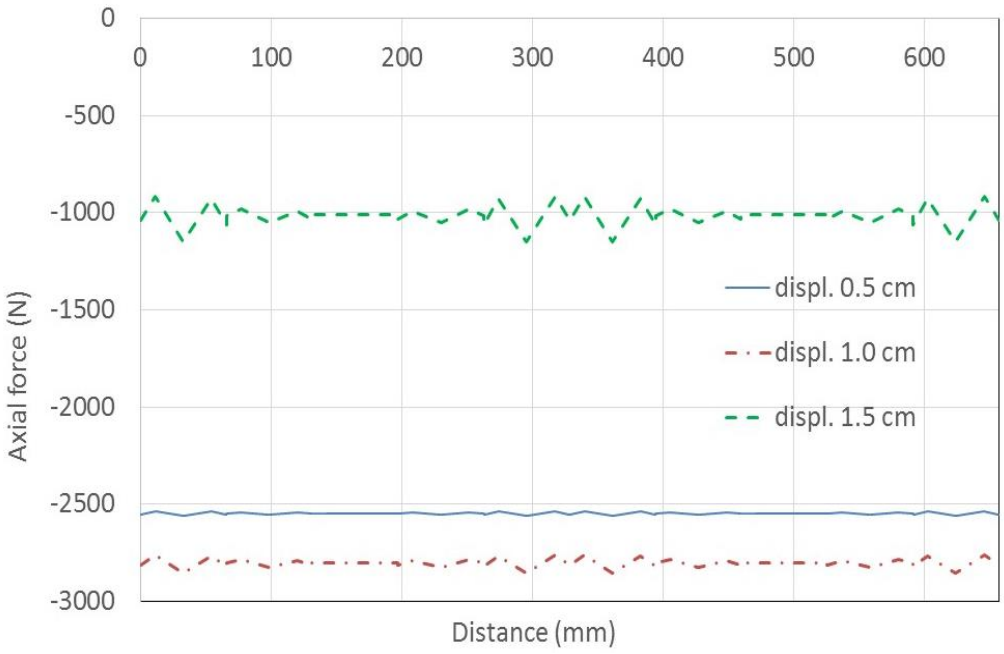

Figure 3.12: Axial distribution for the toggle frame under three different displacement values.

3.8.2 Cantilever beam with a vertical load at the tip

In the second example, a cantilever beam of hollow circular cross section with external diameter of 355.46 mm and a thickness of 3.8 mm was loaded from its tip by a vertical load (Figure 3.13). The beam had a length of 4000 mm and a Young's modulus of 20 GPa. The significance of this beam is that it considers large displacements compared to its cantilever length. **Chan (1988)** analysed this problem using an elastic perfectly plastic material and used two different values of yield stress. In addition, **De Souza (2000)** used a force-based element to model the cantilever.

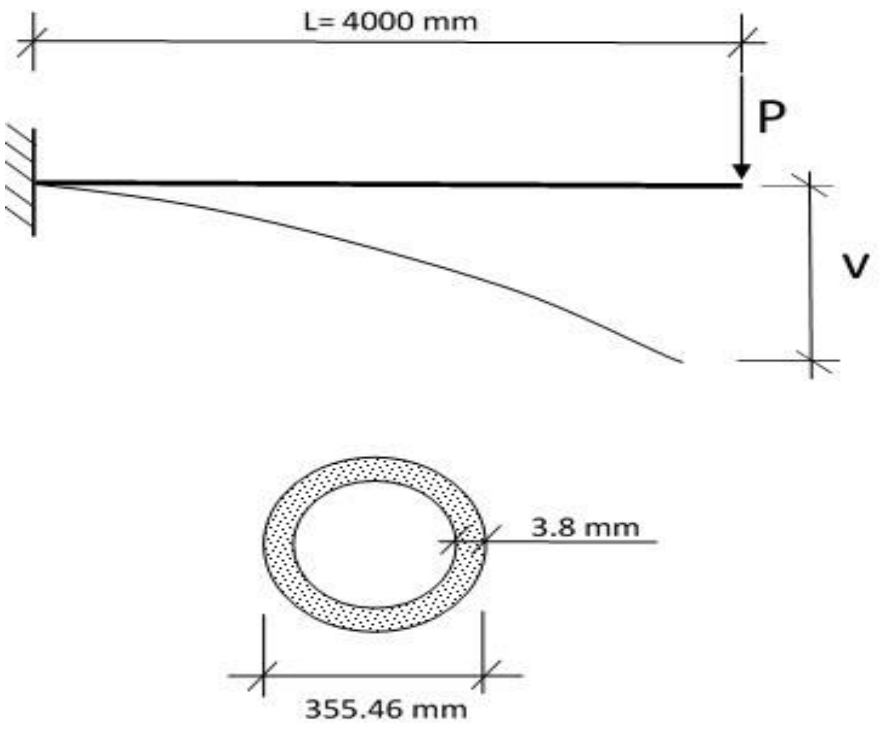

Figure 3.13: Cantilever beam with a vertical load at the tip.

In order to analyse the cantilever beam, the displacement-based model was divided into 8 elements, while the mixed-based model was divided into 4 elements only. Figure (3.14) shows the equilibrium path of the cantilever beam for three yield stress values. The displacement and mixed fibre beam elements, as shown from the equilibrium path, were able to accurately simulate the behaviour of the member for the three different values of yield stress.

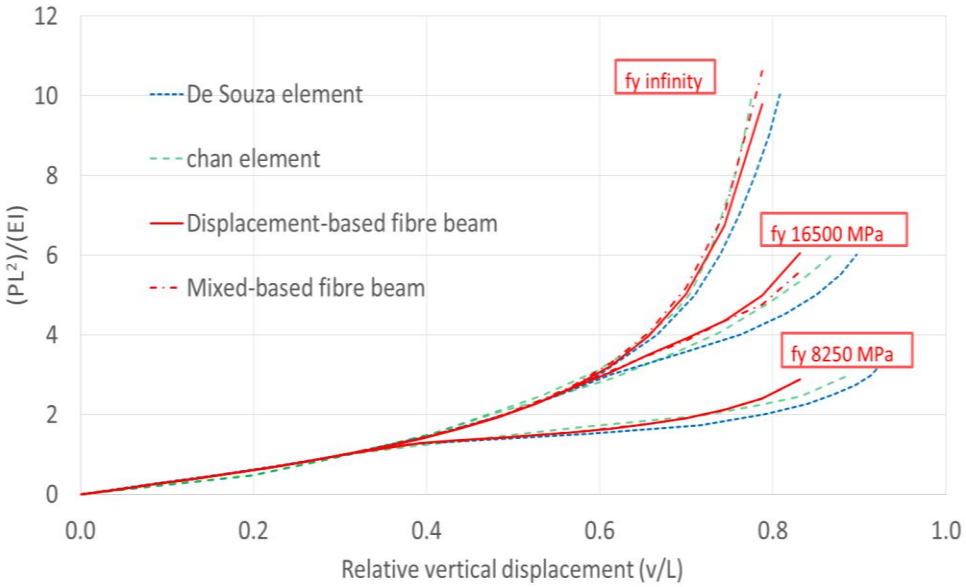

Figure 3.14: Equilibrium paths for the cantilever beam.

Additionally, the mixed element is nominated to draw the bending moment distribution along the length of the beam for four relative displacement values with the yield value of 16500 MPa (Figure 3.15). Results show consistency and confirm the stability of the numerical solution along the cantilever beam length.

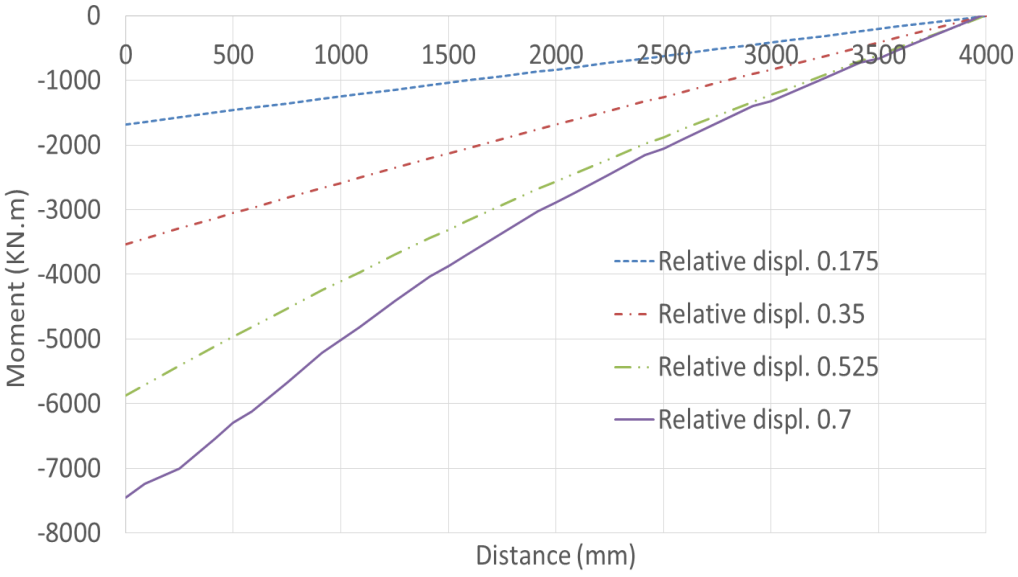

Figure 3.15: Moment distribution along the cantilever beam for four different relative displacement values.

3.8.3 Barrera experiment

The first experiment that will be used for the calibration of the new elements for reinforced concrete structures is a test performed by **Barrera et al. (2011)** to examine forty-four rectangular slender reinforced concrete columns, with different sections, under combined axial load and lateral force. The use of high strength concrete (HSC) in the column produced smaller cross sections which increased its slenderness and produces a major second order effect. A constant axial load and a monotonic lateral force were applied up to failure of the columns. The test outlines and settings are displayed in Figure (3.16). After the testing, two simplified methods from Eurocode 2 and ACI-318 were used by the authors for comparison with the experiments and were both found very conservative.

The tested specimens simulate two semi-columns of two consecutive levels linked together by a central element, which acts as a stiffener to represent an intermediate floor or the connection between a column and the foundation represented by a stub element. Each semi-column has a total length of 1.5 m, such that 1.32 m is the reinforced concrete member and the remaining 0.18 m represents the hinge support of the sample. The steel hinges enable the free rotation of the specimen. They are maintained by a steel plate with installed rollers to permit horizontal movements. The complete geometry and dimensions of the specimens are given in Figure (3.17).

The developed elements are then used to compare the results of specimen (H60-10.5-C0-2-30). This sample has a cross section of 200x150 mm and a nominal concrete strength of 60.5 MPa, steel young's modulus of 200 GPa, longitudinal steel

yielding stress of 537 MPa and longitudinal reinforcement of 6Ø10 bars. The sample was subjected to an axial load equal 432 kN.

On the other hand, the fibre beam model was constructed using only 4 elements. This was enough to reach convergence for both the displacement and the mixed elements. Further, every element was divided internally into 5 sections and the sections were divided into 10 concrete fibres and 6 steel fibres that represent the column reinforcement (Figure 3.18).

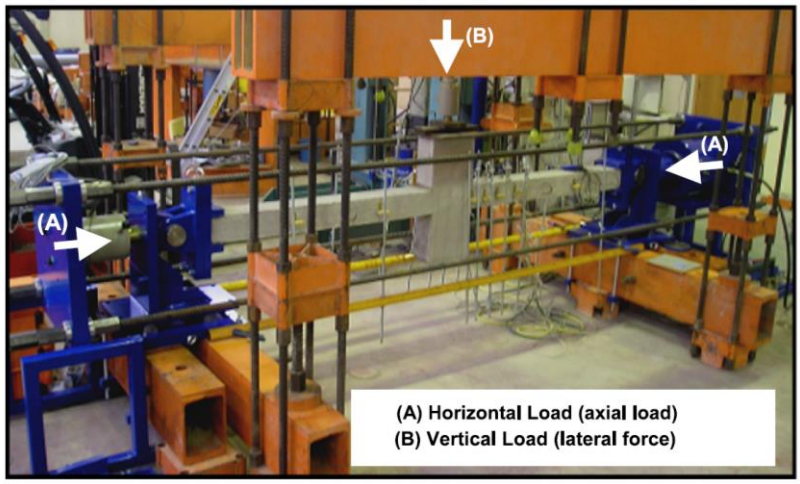

Figure 3.16: Test framework, Figure from **Barrera et al. (2011)**.

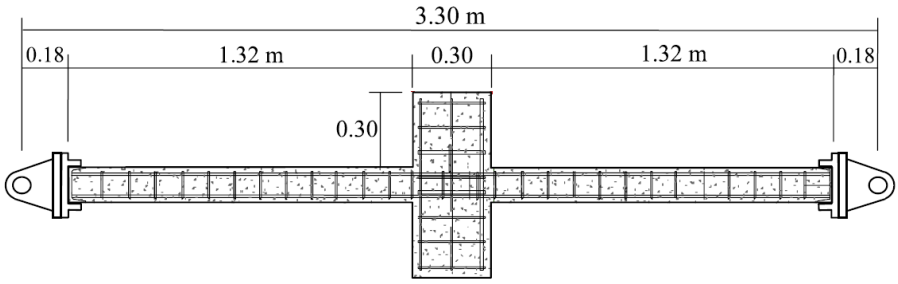

Figure 3.17: Geometry and dimensions of the specimen, Figure from **Barrera et al. (2011)**.

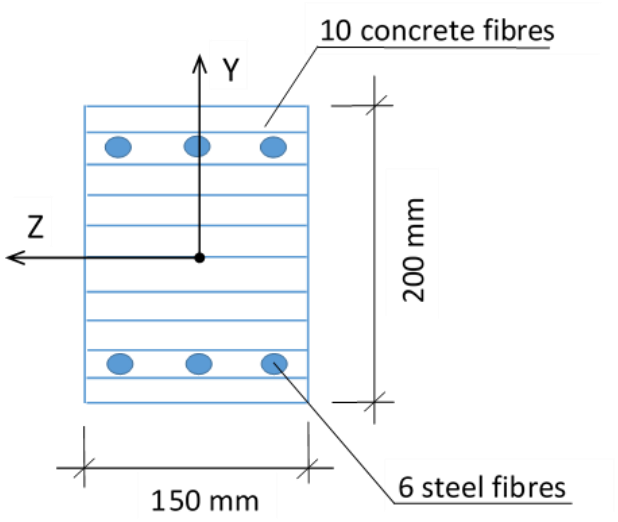

Figure 3.18: Fibre beam element cross section mesh for specimen H60-10.5-C0-2-30.

Figure (3.19) shows the load displacement curve of the tested column. It is clear that both fibre beam elements were able to follow the output path of the experiment until failure. The previous displacement-based element that did not consider the second order analysis strongly missed the path and produced an error up to double the value near failure. It is noticeable that the more the load becomes stronger the more the second order effect increases (at a small displacement of 5 mm the second order effect was 33% and at higher displacement of 20 mm the second order effect increased to 69%).

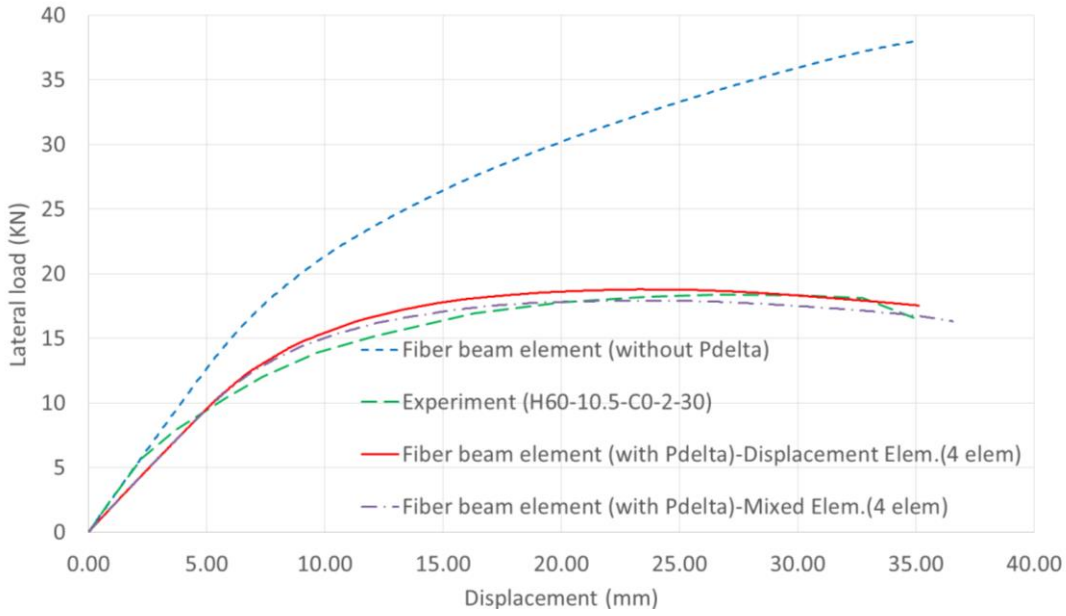

Figure 3.19: Load displacement curve for column H60-10.5-C0-2-30 tested by **Barrera et al. (2011)** and compared with the fibre beam elements.

Using the mixed element, Figure (3.20) presents the full vertical displacement under four different lateral force values along the element length. These deformed shapes are very similar to the one retrieved from the experiment. For instance, the experimental deformed shape at a lateral force of 16.56 kN is plotted in Figure (3.20) for comparison with the mixed element results. The difference between the deformed shape of experimental results and the numerical solution was about 5%. For this specimen, the maximum vertical load (Vmax) achieved during the experiment was 18.43 kN.

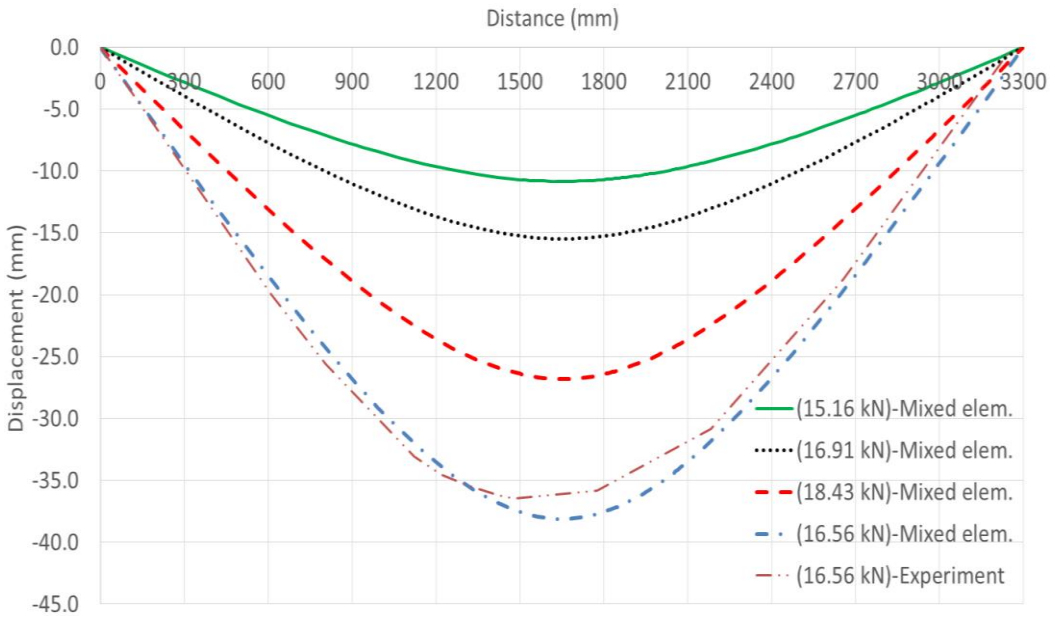

Figure 3.20: Vertical displacements along the column H60-10.5-C0-2-30 under different Lateral forces values.

In Figure (3.21), a comparison is presented between the curvatures (at lateral force 15 kN) for the displacement and mixed elements with and without the second order effect. It is clear that the P-delta effect is higher near the stub where the load is applied and the effect lessens as we move near the supports. It can also be seen that there is no considerable difference between the accuracy of the displacement and mixed elements at this stage since not much of inelastic deformation is occurring at that level and the curve is almost linear.

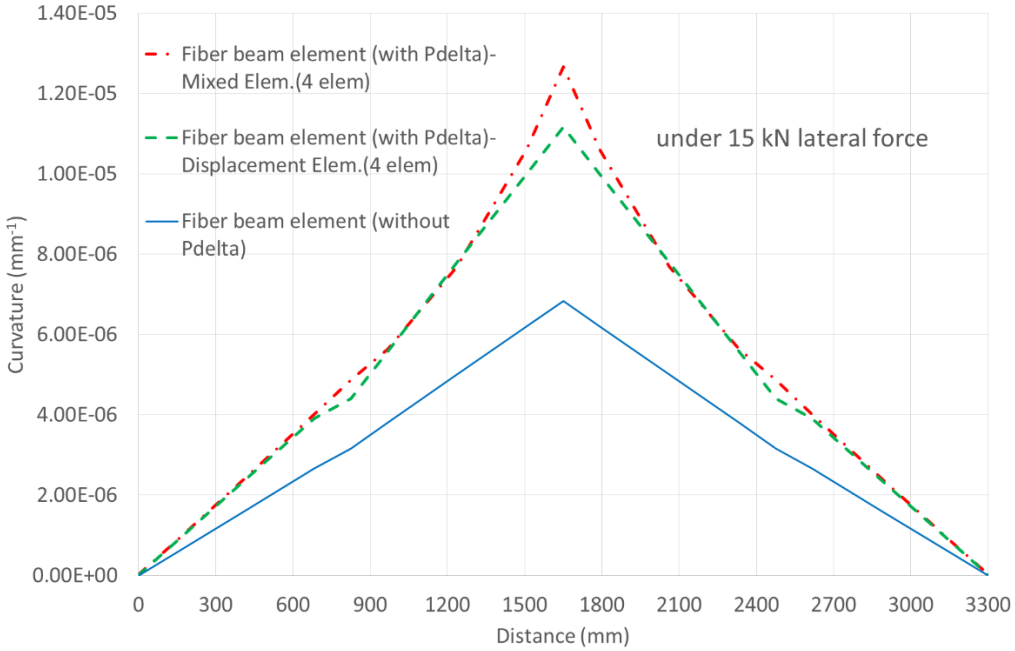

Figure 3.21: Comparison between the curvature at maximum lateral load for the fibre beam elements with and without second order effect.

However, when comparing the maximum curvature at the maximum vertical load level, Figure (3.22), it is clear that while the mixed element still produces a smooth curve, the displacement element requires more divisions to avoid kinks and match with the mixed elements results. This is linked to the occurrence of inelastic deformations at this level. The output curve of the displacement-based element with higher element divisions (12 elements) approaches the one of the mixed element (4 divisions); however, the produced curve was still not sufficiently smooth. Consequently, the higher accuracy of the mixed element in the determination of the curvature in the case of inelastic deformations is apparent.

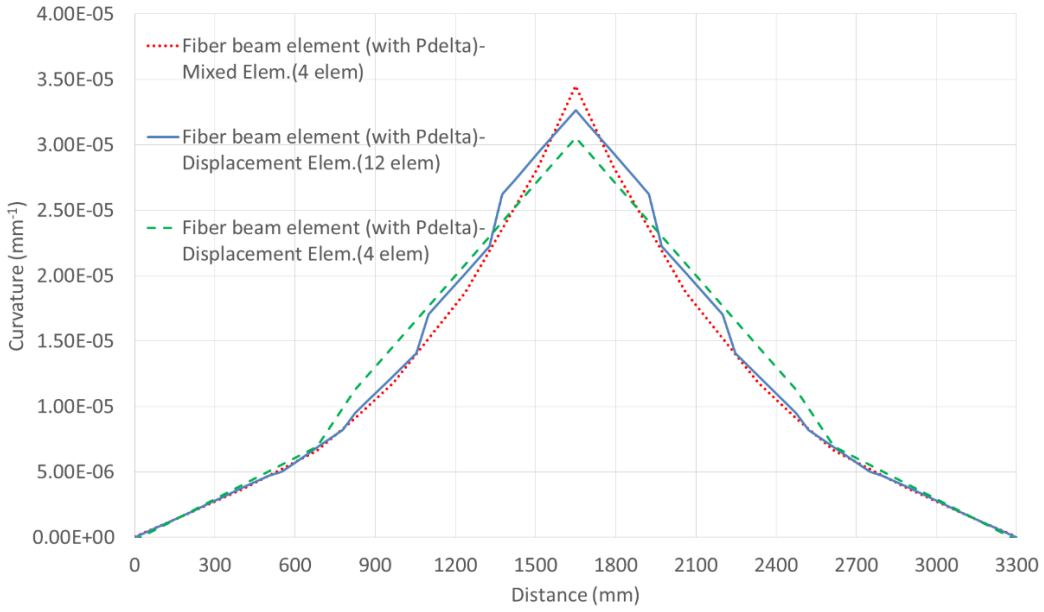

Figure 3.22: Comparison between the displacements based elements (4 and 12 divisions) vs the mixed element (4 divisions) for curvature at maximum lateral load.

Moreover, the developed fibre beam elements are an advanced tool to study in detail the global and local behaviour of reinforced concrete structures. First, the structural behaviour was studied by the load displacement curves (Figure 3.19). Second, the section behaviour will be investigated using moment curvature curves of the five sections of elements 2 (Figures 3.23 to 3.27). Finally, the fibre behaviour will be studied and monitored for some particular fibres. This capability is only possible in advanced fibre based elements.

The mixed element with four elements is employed for this exercise. The moment curvature curves for all sections of element 2 are shown in Figures (3.23) to (3.27). It is clear that the second order analysis, at the section level, produced moments modified up to 9% than the moments produced without second order analysis.

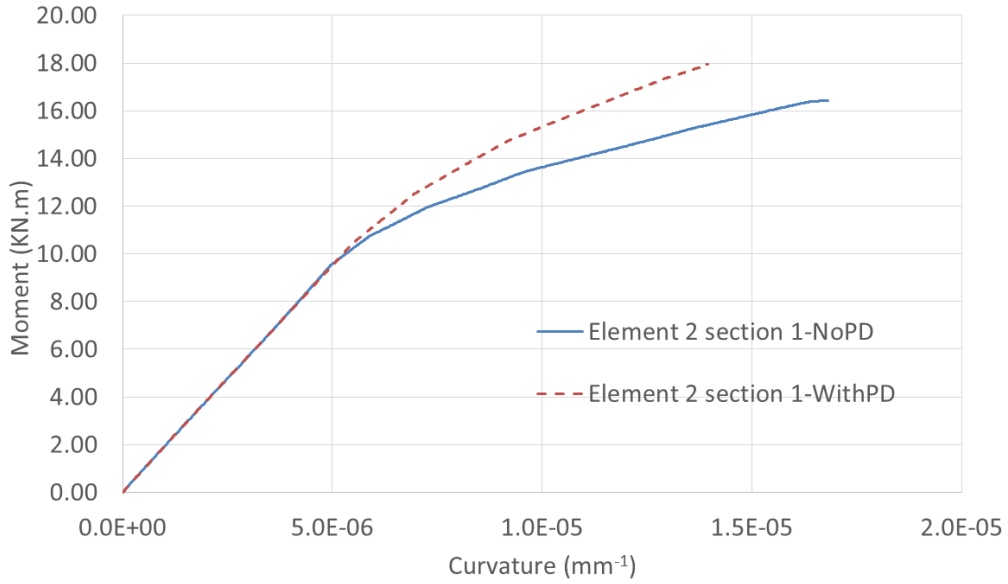

Figure 3.23: Comparison between the moment curvature relationship for (element 2-section 1) using the mixed element for cases with and without second order analysis.

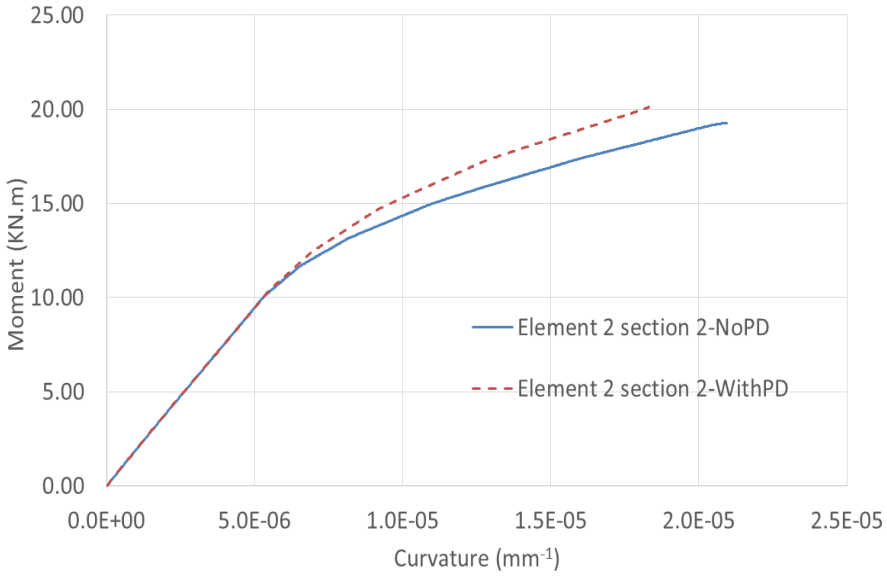

Figure 3.24: Comparison between the moment curvature relationship for (element 2-section 2) using the mixed element for cases with and without second order analysis.

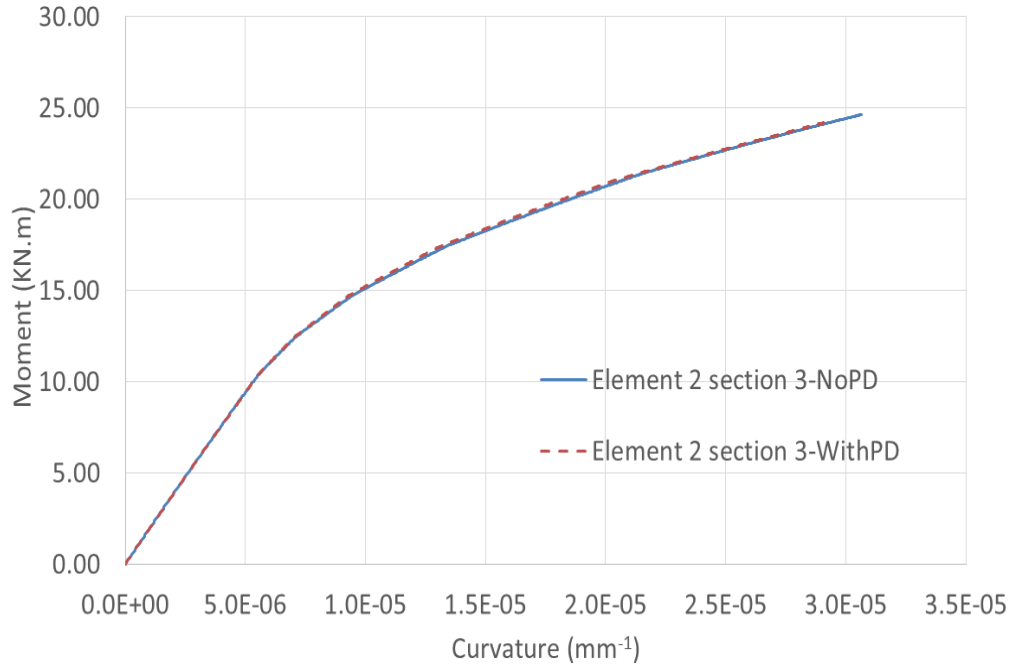

Figure 3.25: Comparison between the moment curvature relationship for (element 2-section 3) using the mixed element for cases with and without second order analysis.

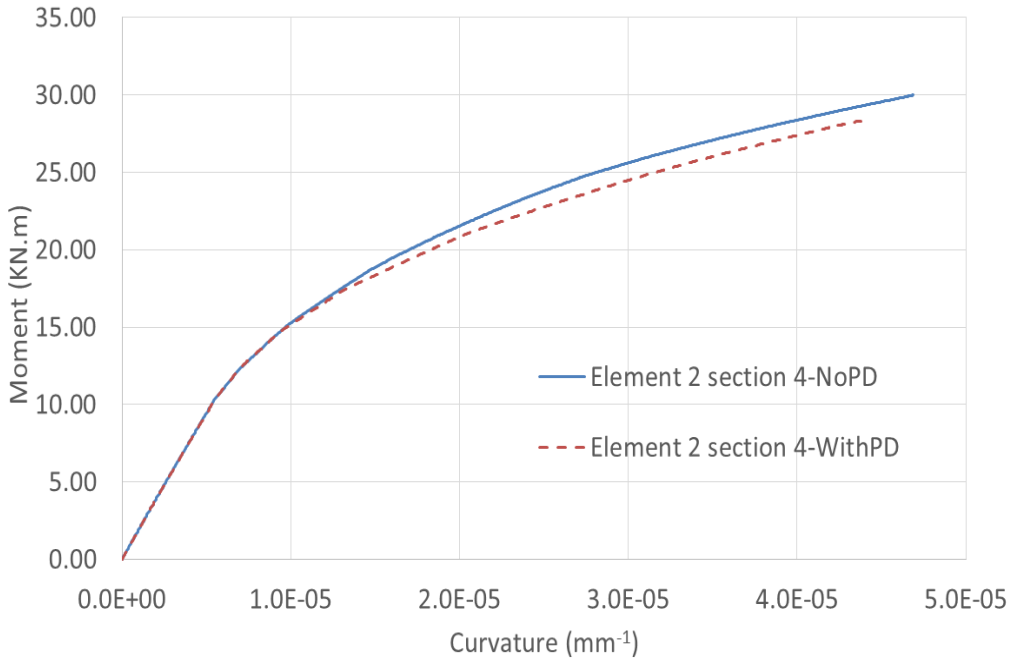

Figure 3.26: Comparison between the moment curvature relationship for (element 2-section 4) using the mixed element for cases with and without second order analysis.

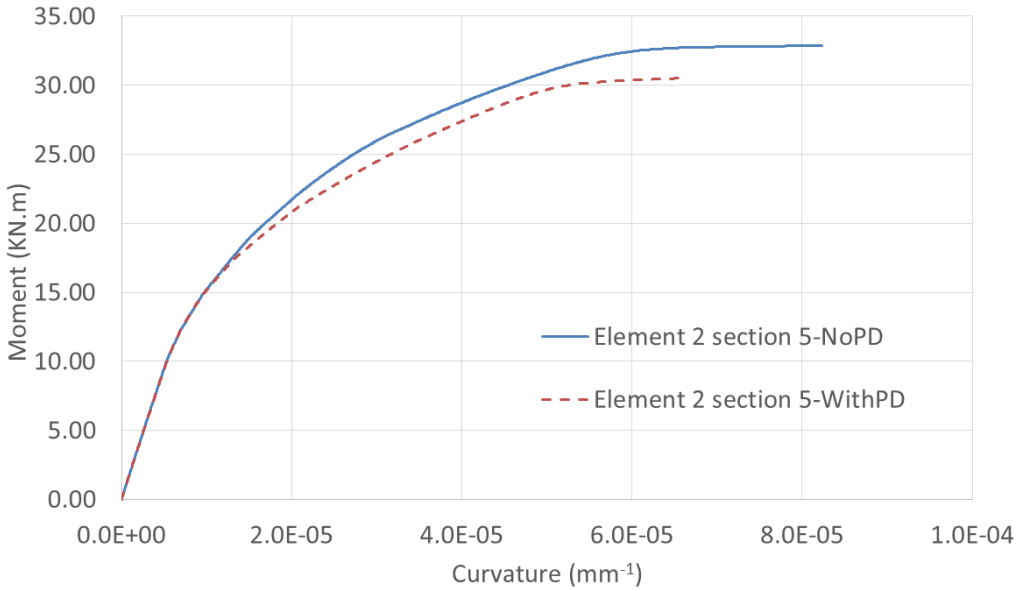

Figure 3.27: Comparison between the moment curvature relationship for (element 2-section 5) using the mixed element for cases with and without second order analysis.

Further, the stress-strain curves of particular fibres (either concrete or steel) are monitored and displayed. Such capabilities can be adequately used by the designer to take economical decisions regarding the design of different reinforced concrete elements. The monitored fibres are labelled and shown in Figure (3.28). Where fibre 1 is the top concrete fibre, fibre 2 is the bottom concrete fibre and fibre 3 is a bottom steel bar fibre.

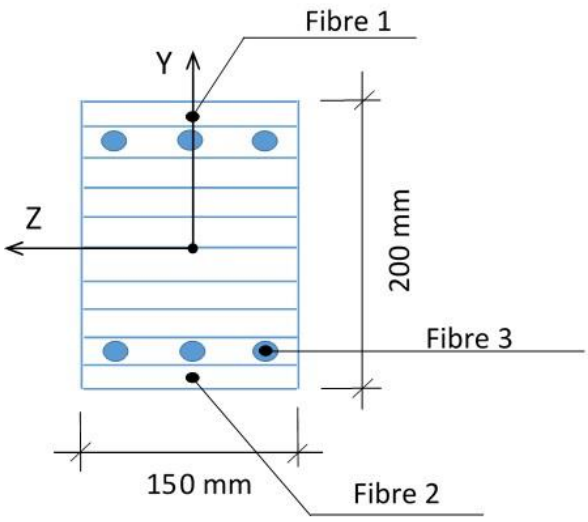

Figure 3.28: labelling of monitored fibres for Barrera experiment.

Figures (3.29) and (3.30) display the stress strain behaviour of concrete fibre 1. For (fibre 1 - sec 1 at element 2) the concrete fibre is at the end of the elastic range, for the case where the analysis was performed with the second order effect, the fibre is stressed with a final stress of 49.77 MPa at a strain of 0.0012 while when no second order effect is performed the fibre reached a stress of only 46.4 MPa with a lower strain of 0.00108. While for (fibre 1 – sec 4 at element 2) the concrete fibre was clearly in the ductile nonlinear zone. The second order effect in this region produced a final stress of 62.27 MPa at a strain value of 0.00261 compared to a final lower stress of 62.05 MPa at a higher strain value of 0.00299. It is clear that both curves produced the same stress strain path but with different final stress values under different strains.

For the concrete (fibre 2 - element 3 at sec 2), the second order effect did not produce much difference for the loading and unloading behaviour (Figure 3.31).

For the steel (fibre 3 – sec 2 at element 2), shown in Figure (3.32), the fibre is in the linear zone and the second order effect is strongly spotted in this fibre behaviour at this particular section. The second order analysis stressed the fibre under much less stress of 119 MPa with a small strain of 0.00048 compared to a higher stress value of 205.8 MPa with a higher strain of 0.0008 when no second order analysis is performed. Finally for the steel (fibre 3 – sec 5 at element 2), Figure (3.33), the fibre behaved elastically until a nonlinear effect was observed and the curves entered the partial plasticity zone and the second order effect produced a small change in the final stress strain values of the fibre. The initial negative part of the stress-strain curves shown in Figures (3.32) and (3.33) can be attributed to the effect of the axial force on the fibre behaviour.

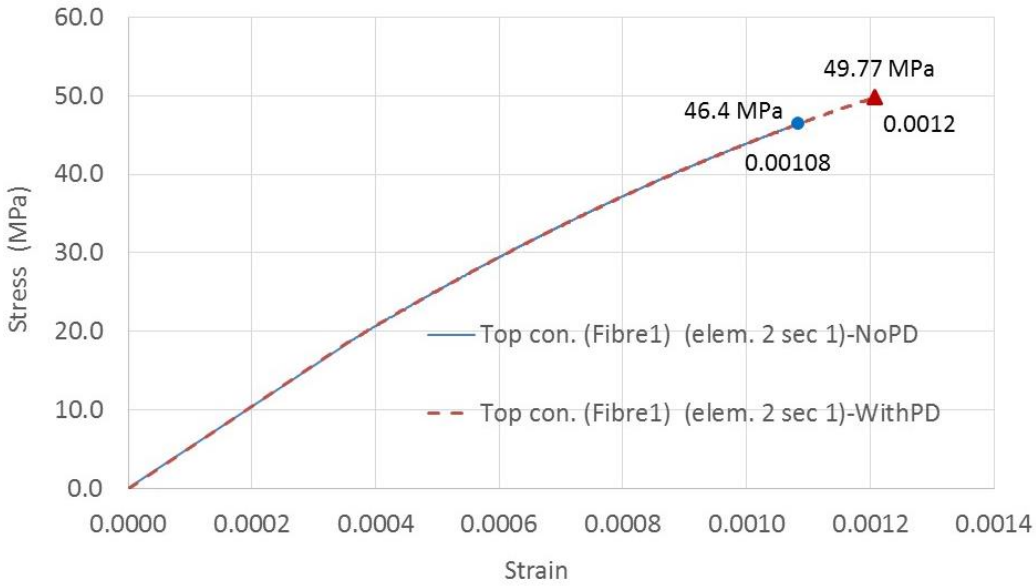

Figure 3.29: Comparison between the stress strain curves for fibre 1 for element 2 at sec 1 using the mixed element with and without second order effect.

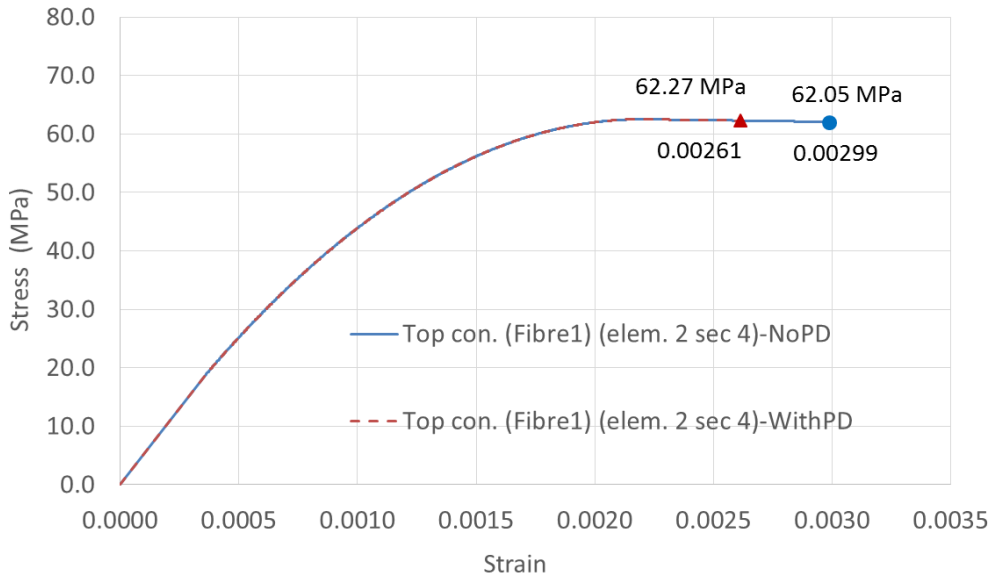

Figure 3.30: Comparison between the stress strain curves for fibre 1 for element 2 at sec 4 using the mixed element with and without the second order effect.

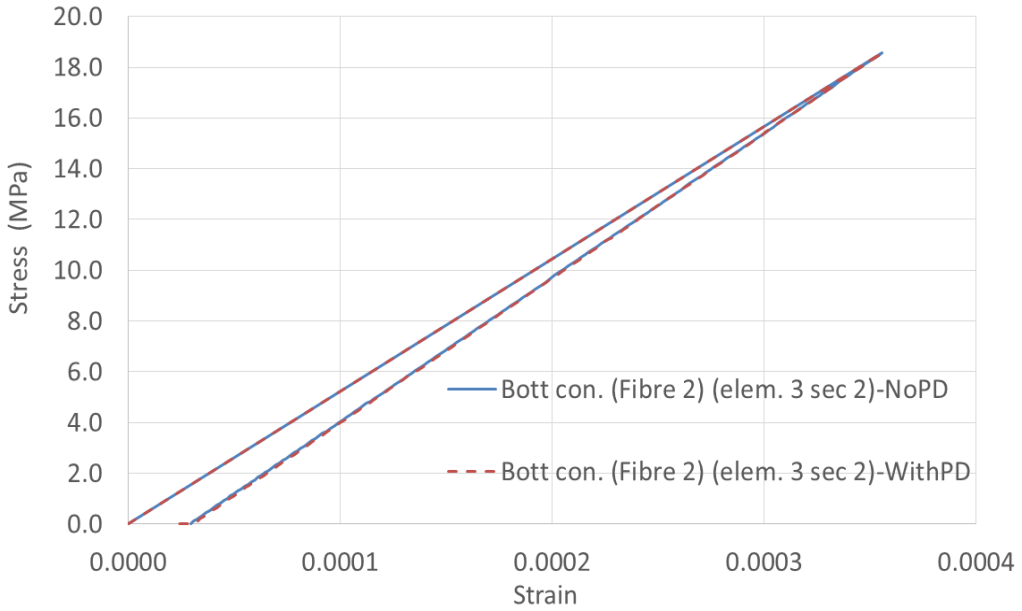

Figure 3.31: Comparison between the stress strain curves for fibre 2 for element 3 at sec 2 using the mixed element with and without the second order effect.

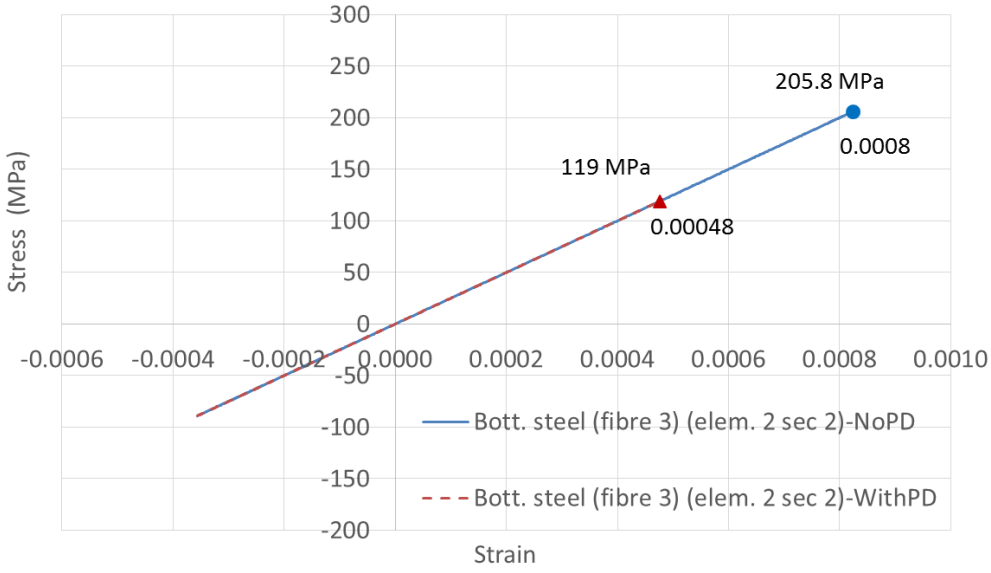

Figure 3.32: Comparison between the stress strain curves for fibre 3 for element 2 at sec 2 using the mixed element with and without the second order effect.

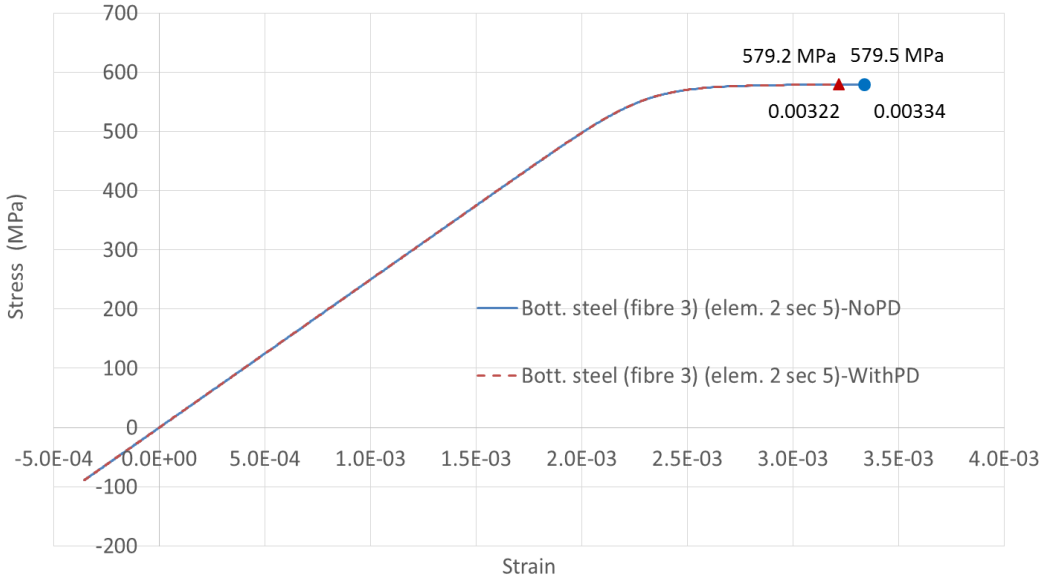

Figure 3.33: Comparison between the stress strain curves for fibre 3 for element 2 at sec 5 using the mixed element with and without the second order effect.

It can then be concluded that the new proposed elements are able to accurately model high strength reinforced concrete slender columns with high accuracy under monotonic loading. From the distribution of the curvature and moment along the element length, it can be established that the second order effect is much higher near the applied load and diminish near the supports. The mixed element requires less number of divisions to efficiently predict the curvature and produces smoother output curves when compared with the displacement-based element.

In general, the second order effect tends to decrease the final stress and strain forces of most fibres. However, different behaviours can be spotted in each individual fibre.

3.8.4 Morrison SFRC experiment

Later, **Caballero-Morrison et al. (2013)** used the same previous type of specimen, that represent two columns of two connected floors joined by a stub, to test steel fibre-reinforced high strength concrete (SFRC) slender columns, but this time under cyclic loading. HSC was used for the slender columns to increase its deformation capacity in order to overcome the expected increase of the second-order effect, while the presence of the steel fibres will result in a considerable increase in toughness and in the strain at peak stress together with a slight increase in the peak stress itself. This can reduce the deformation of the concrete under cyclic loading and delays the spalling of concrete. The test procedure consisted of first applying a constant compression horizontal load corresponding to a relative normal force, and then a cyclic lateral load is applied.

Two samples were selected to be modelled using the fibre beam elements. The detailed geometries of the specimens are the same as the ones used in the previous experiment in this chapter and are displayed in Figure (3.17). The first sample (NF00L05V2S100) is a normal strength concrete, with fc= 33.57 MPa, a cross section of 260x150 mm and longitudinal reinforcement of 6Ø12. No steel fibres were added to this sample. The second specimen (HF60L05V1S50) is a HSC, with fc= 81.10 MPa, a cross section of 260x150 mm, with longitudinal reinforcement of 6Ø12 and with steel fibre content of 60 kg/m^3 (equivalent to a volumetric ratio of 0.76%). The fibre content was modelled by increasing the element tensile strength by 1%.

The first sample was subjected to an axial force equal 491.7 kN while the second sample was subjected to an axial force equal 333.9 kN. Figure (3.34) shows the fibre beam element cross section mesh used for the two specimens. The same finite element model described in the previous experiment in this chapter was used. The cyclic load was implemented using a displacement control method with the same loading history used in the experiment, which is shown in Figure (3.35).

A sensitivity study was performed for the two models and it was found that the displacement-based model requires to be constructed with 14 elements division to reach convergence and to capture the external retraction hysteric path. Whereas, the mixed-based model required only 4 elements to match with the output of the experiment and to achieve full convergence.

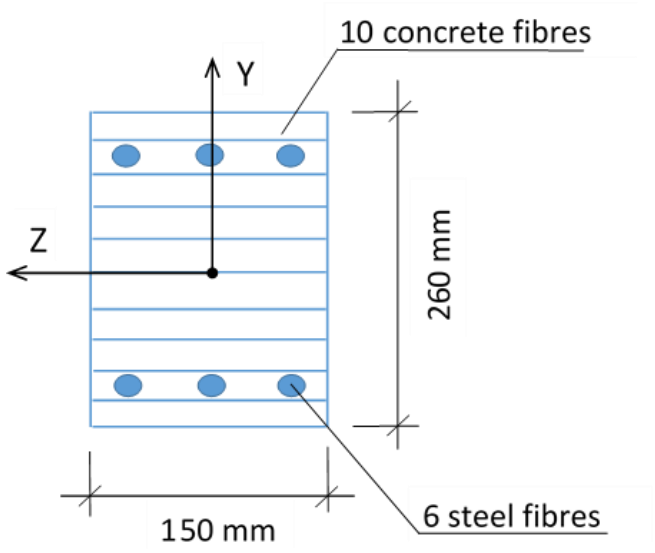

Figure 3.34: Fibre beam element cross section mesh for specimens NF00L05V2S100 and HF60L05V1S50.

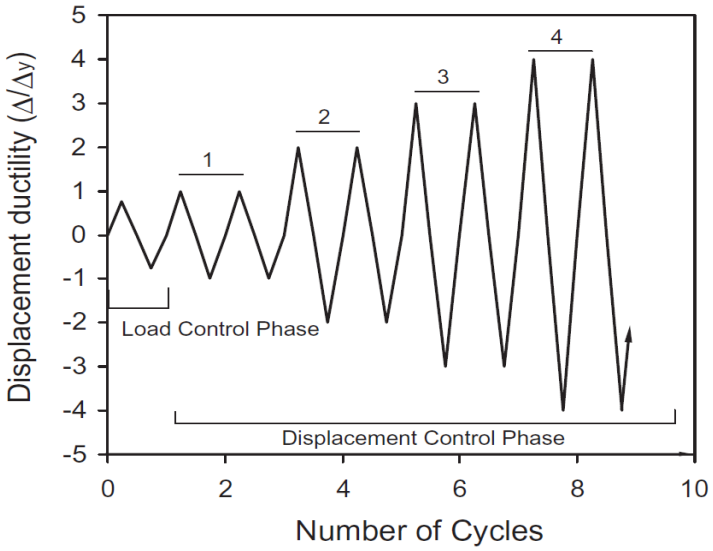

Figure 3.35: loading history, Figure from **Caballero-Morrison et al. (2013)**.

Subsequently, in Figure (3.36), the two fibre beam elements are compared with the experiment results. It is clear that they were both able to model the specimen (NF00L05V2S100) and to agree with the test results. If the second order effect was not considered a higher load-displacement path could be expected and is not shown

herein only for clarity. The maximum difference in the displacement values, between considering and not considering the second order effect, was about 10-15% in the first three cycles and then jumped to about 30% in the later cycles. For this sample, the maximum bending moment at critical section (70 mm from the column-stub) calculated from the experiment was 71.68 kN.m and from the mixed fibre beam element with second order analysis was 71.28 kN.m with an error less than 0.1%.

In Figure (3.37), the elements were compared with the experimental results of sample (HF60L05V1S50); also, the numerical solution matched with the experimental results. For this sample, the maximum bending moment at critical section (70 mm from the column-stub) calculated from the experiment was 78.37 kN.m and from the mixed fibre beam element with second order analysis was 85.92 kN.m with an error up to 9.6%.

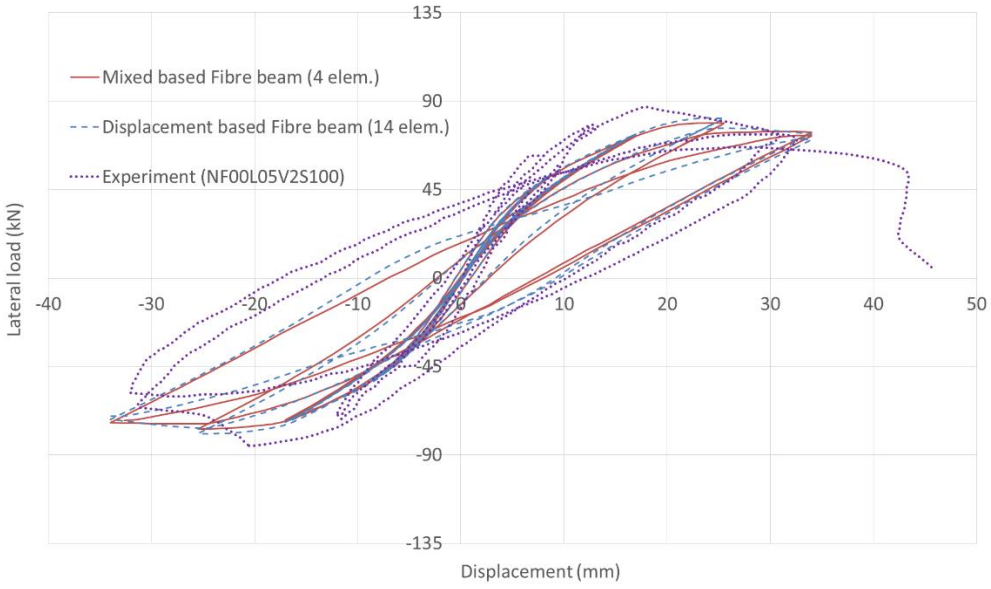

Figure 3.36: Load displacement curve for the experimental results of column NF00L05V2S100 Vs the mixed and displacement-based elements.

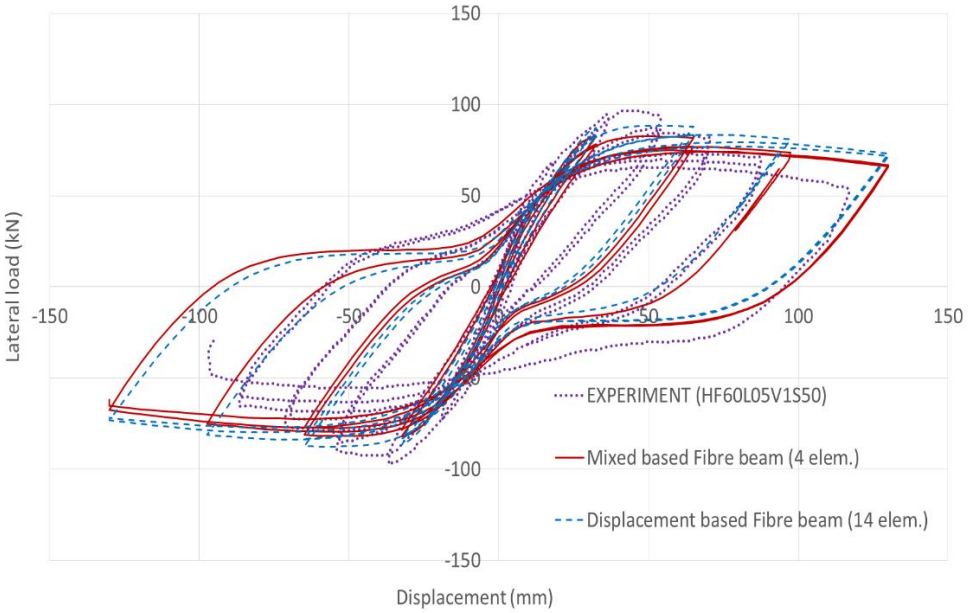

Figure 3.37: Load displacement curve for the experimental results of column HF60L05V1S50 Vs the mixed and displacement-based elements.

From the plots, it can be noticed the influence of using HSC and adding fibrous materials on the second sample (HF60L05V1S50) regarding the deformation that the sample has undergone and the shape of the hysteric curves. Therefore, this example establishes the ability of the enhanced elements to model slender reinforced concrete members subjected to cyclic loading while accounting for the presence of steel fibres in the concrete mix.

Later, the elements capabilities are employed to draw the moment distribution along the length of the two columns. The mixed element was used for this task with the 4 element division model. From Figures (3.38 & 3.39) accurate and consistent distributions can be spotted.

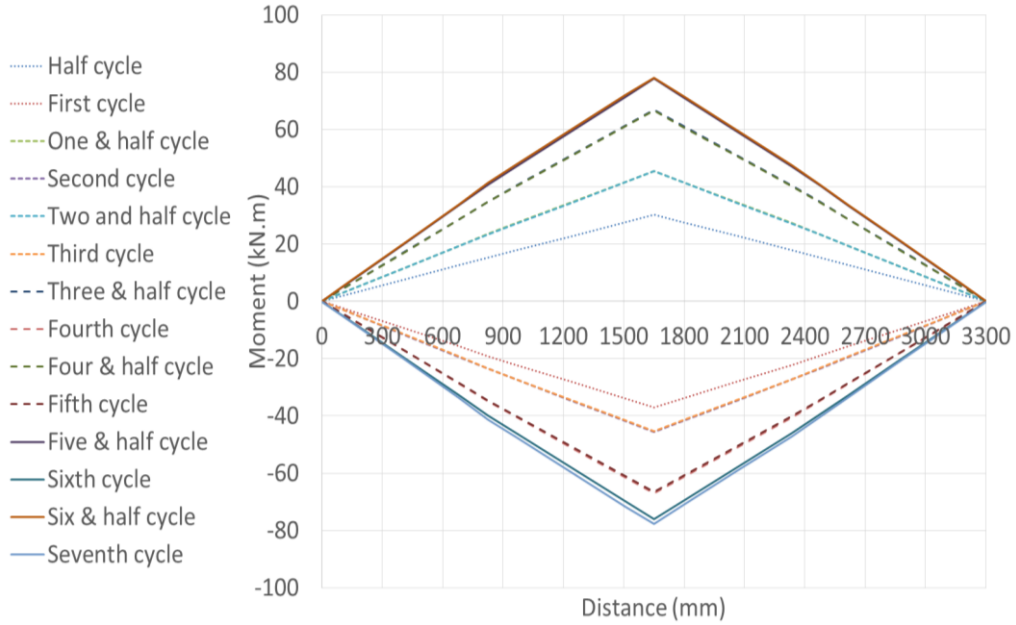

Figure 3.38: Moment distribution along column NF00L05V2S100 at the middle and the end of each load cycle.

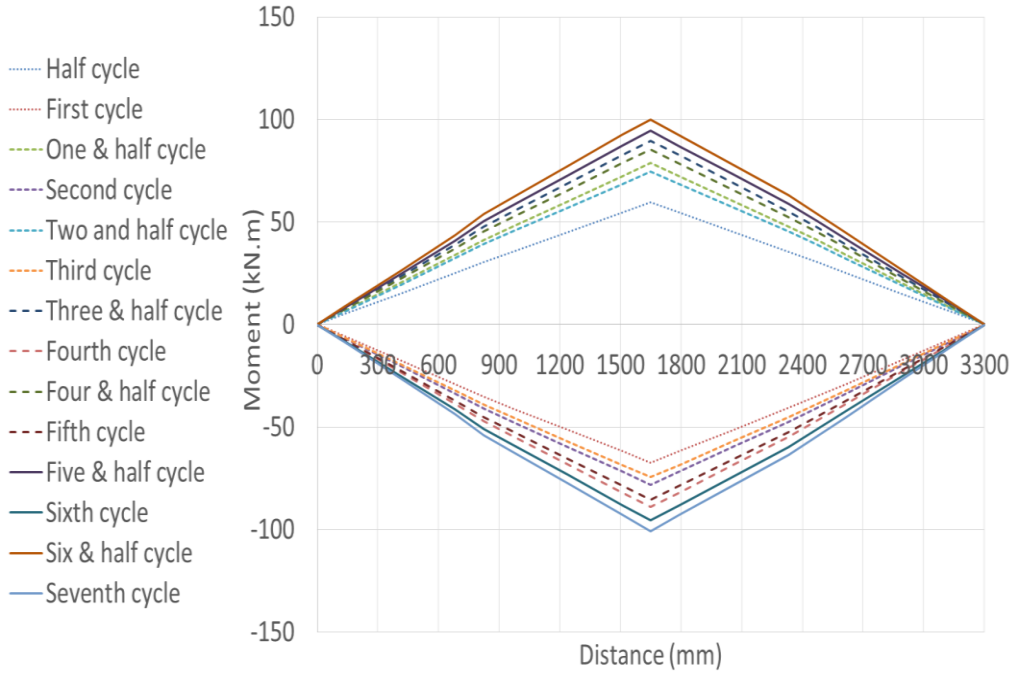

Figure 3.39: Moment distribution along column HF60L05V1S50 at the middle and the end of each load cycle.

When comparing between the two graphs in Figures (3.38 & 3.39) that were created using the mixed element, it can be observed that the distribution of the moments is clustered together in the case of the HSC column that contain the steel fibre content for all the cycles. Meaning that the presence of the HSC and fibres did not allows jumps in the values of the bending moment from a cycle to another (Figure 3.39). While in Figure (3.38), jumps in the values of moment can be clearly seen. A conclusion can be drawn from this observation that HSC and fibres help to improve the ductility of reinforced concrete members subjected to cyclic and second order effect.

Next, the fibre beam element is used to monitor the behaviour of particular fibres. Figure (3.40) shows the labelling of the monitored fibres for sample NF00L05V2S100 and for sample HF60L05V1S50. The stress strain behaviour of each fibre is created by the programme and the second order effect is investigated at the fibre level using the mixed element with four members.

Figures (3.41, 3.42 and 3.43) show the stress strain curves for the normal concrete sample NF00L05V2S100 with no steel fibres. When the second order effect is omitted, higher strain values were produced. Figures (3.44, 3.45 and 3.46) shows the stress strain curves for the HSC concrete sample HF60L05V1S50 with steel fibres. In this case, neglecting the second order effect produces lower strain values.

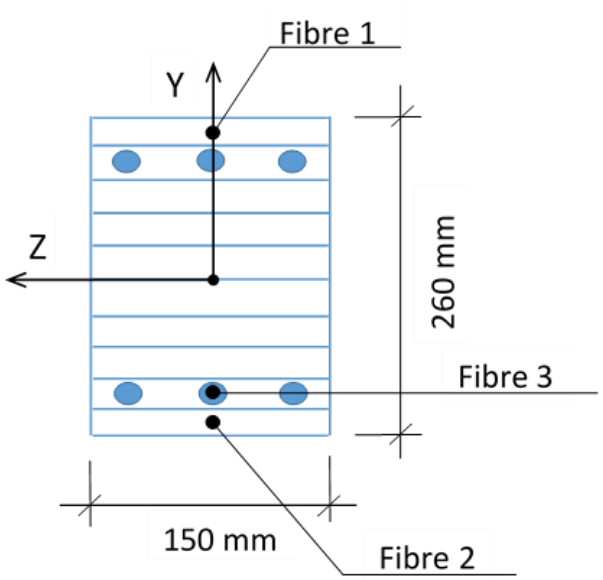

Figure 3.40: labelling of monitored fibres for Morrison experiment.

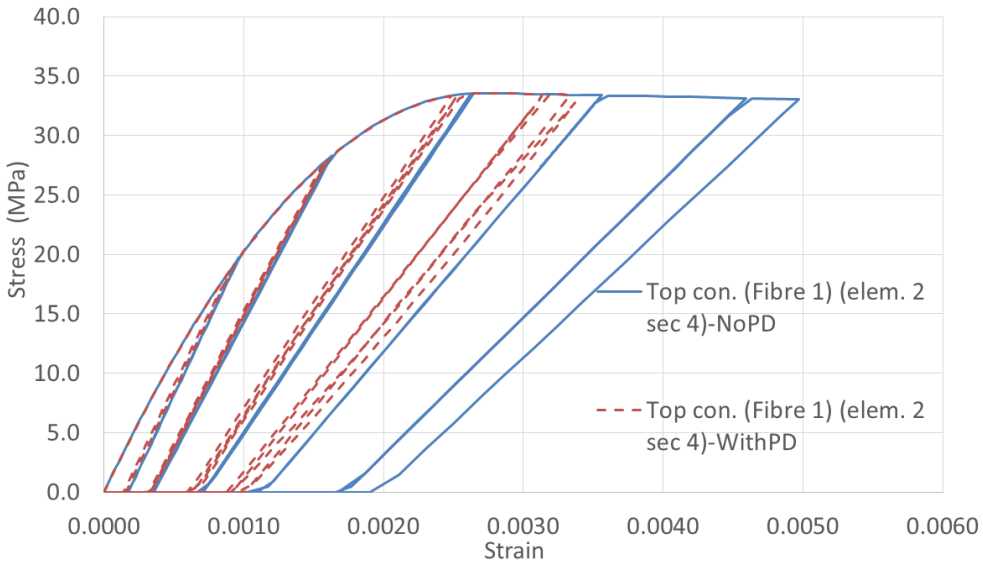

Figure 3.41: Comparison between the stress strain curves of top concrete fibre 1 for element 2 at sec 4 using the mixed element with and without the second order effect (sample NF00L05V2S100).

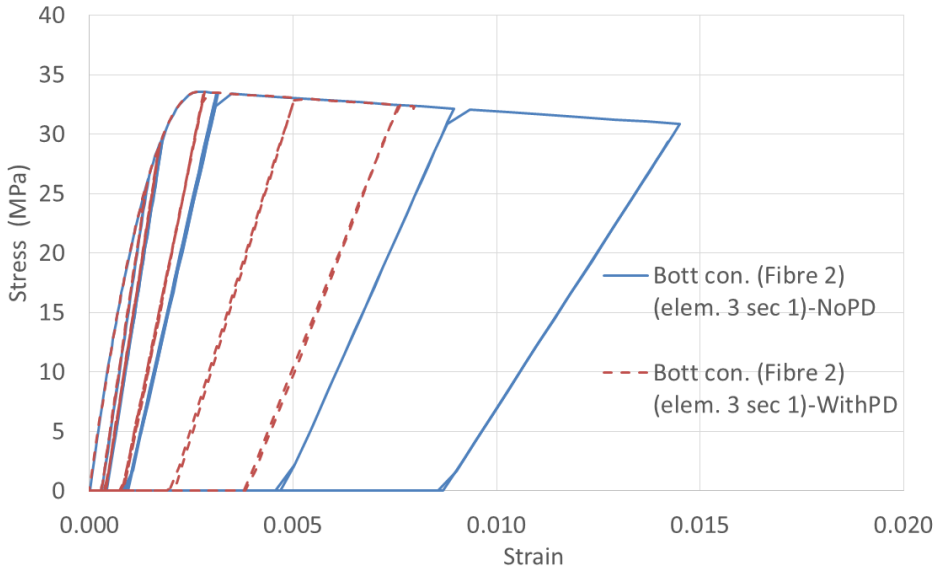

Figure 3.42: Comparison between the stress strain curves of bottom concrete fibre 2 for element 3 at sec 1 using the mixed element with and without the second order effect (sample NF00L05V2S100).

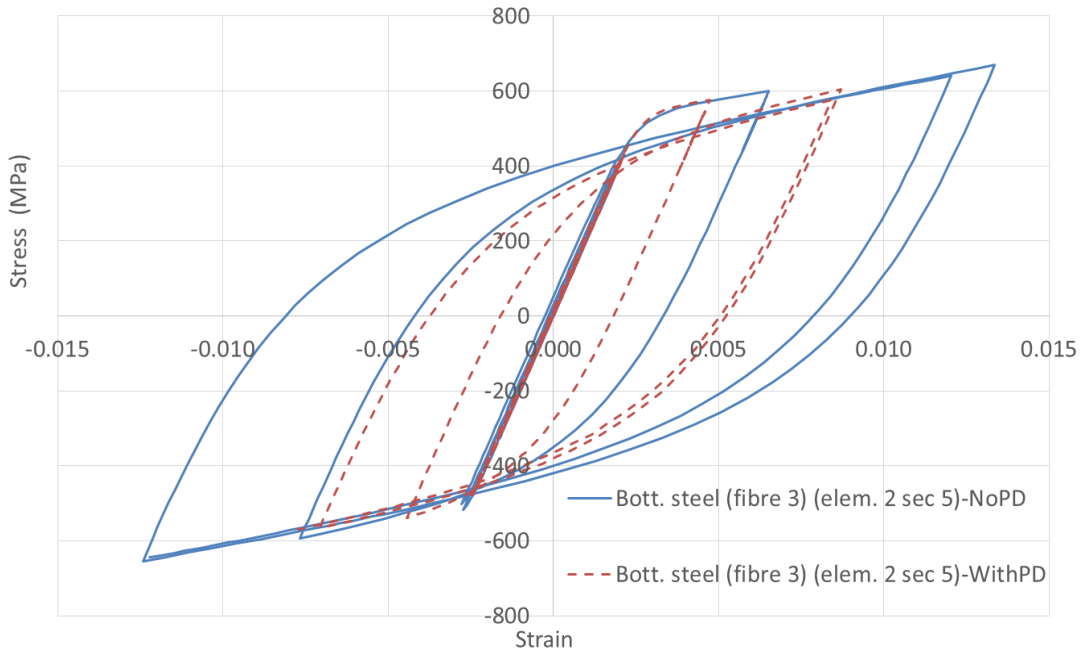

Figure 3.43: Comparison between the stress strain curves of bottom steel fibre 3 for element 2 at sec 5 using the mixed element with and without the second order effect (sample NF00L05V2S100).

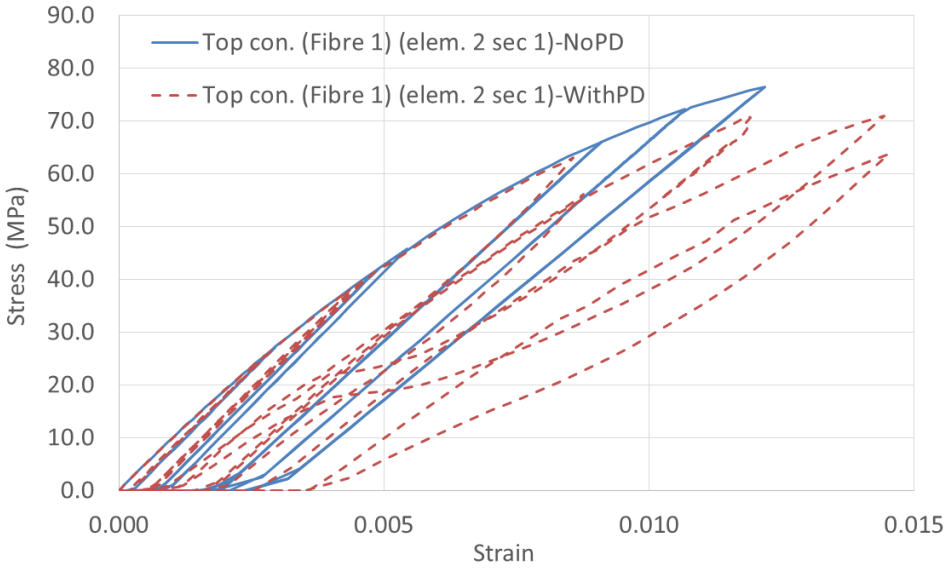

Figure 3.44: Comparison between the stress strain curves of bottom concrete fibre 1 for element 2 at sec 1 using the mixed element with and without the second order effect (sample HF60L05V1S50).

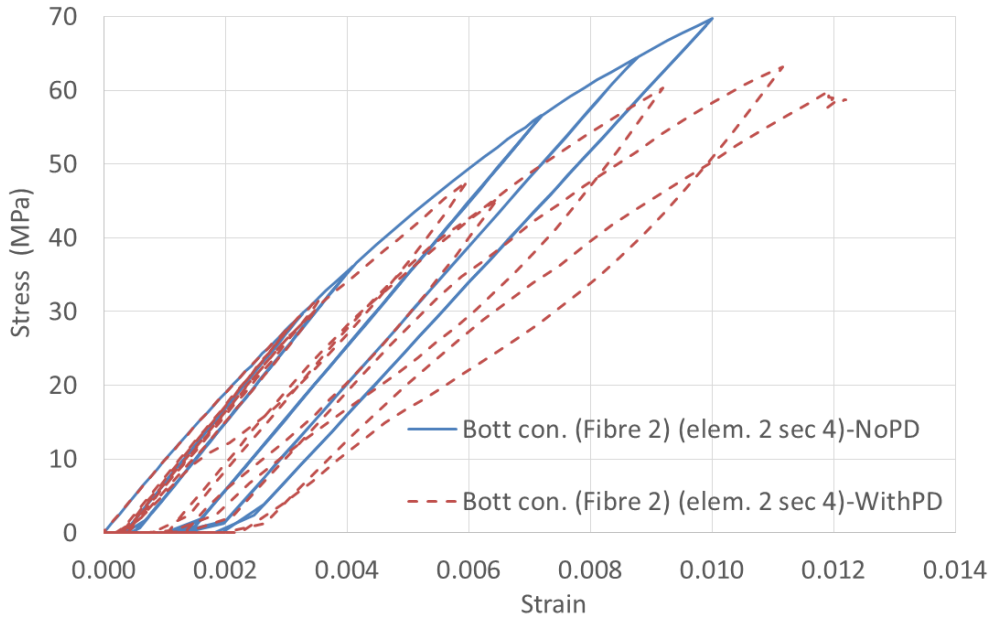

Figure 3.45: Comparison between the stress strain curves of bottom concrete fibre 2 for element 2 at sec 4 using the mixed element with and without the second order effect (sample HF60L05V1S50).

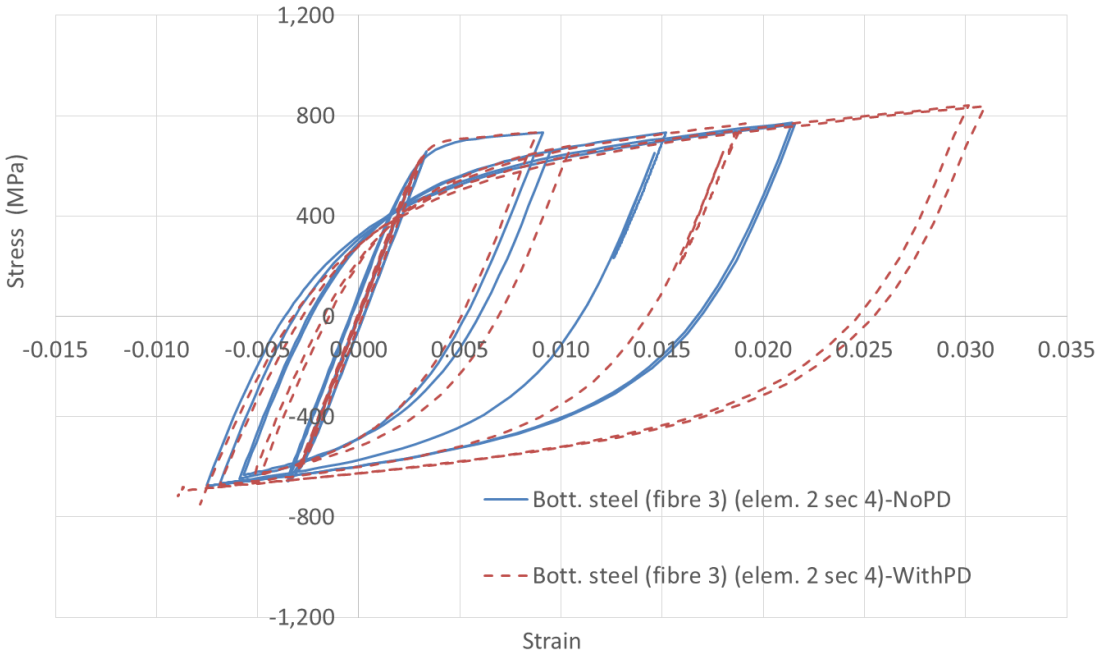

Figure 3.46: Comparison between the stress strain curves of bottom steel fibre 3 for element 2 at sec 4 using the mixed element with and without the second order effect (sample HF60L05V1S50).

The experiment confirms the ability of the proposed fibre beam elements in modelling reinforced concrete slender structures subjected to second order forces under cyclic loading.

3.8.5 Dundar experiment

The fibre beam elements are used to model the experimental work of **Dundar et al. (2015),** where slender reinforced concrete columns strengthened with steel fibres and carbon fibre polymer sheets were tested under combined axial load and biaxial bending in order to determine their behaviour.

The tested columns had a length of 1300 mm, a cross section of 125x125 mm along with two heavily reinforced concrete brackets with dimensions of 200x200x200 mm, that were installed at the columns ends to allow for the application of biaxial loads. The columns had a slenderness ratio of 34.67. Figure (3.47) shows the experiment setup.

For all tested columns, the longitudinal reinforcement was Ø8 at each corner of the section and the lateral reinforcement was Ø6 with spacing 100 mm. The yield strength of the longitudinal reinforcement was 550 MPa. The columns were loaded with pinned end conditions and lateral deformations of the specimens were recorded at column mid height.

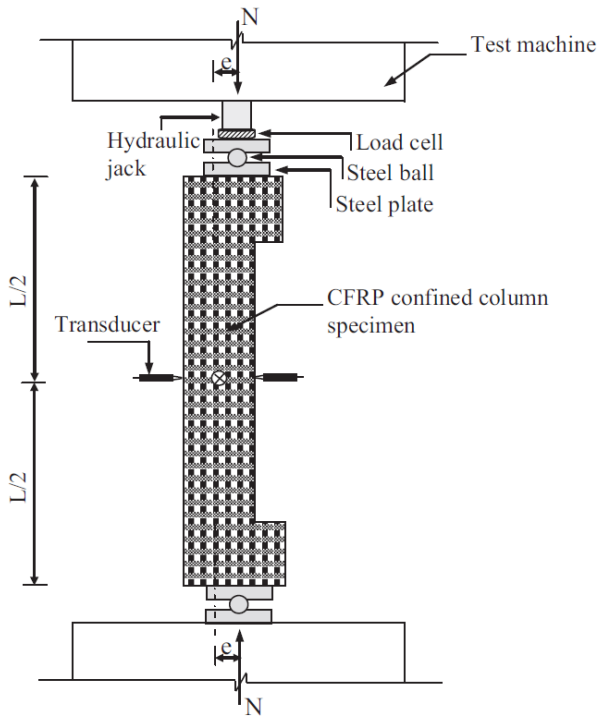

Figure 3.47 Experiment setup, Figure from **Dundar et al. (2015)**.

Two specimens were chosen to be modelled with the fibre beam elements. Specimen (C2-II) with a concrete strength of 61.91 MPa and specimen (C2-II-SF)

with a concrete strength of 53.13 MPa and contains 60 kg/m^3 steel fibre in the concrete mix. Both specimens had two layers of carbon fibre reinforced polymer (CFRP). The two samples were subjected to an eccentricity of 50 mm around the two horizontal axis. For specimen (C2-II), the applied axial load was 267 kN, while for specimen (C2-II-SF) was 283 kN. Every column was divided into a number of elements and each element was divided internally into 5 sections. Two different types of cross sections were defined in the finite element models. The first one (125x125 mm), for the intermediate cross sections, and was divided into 10 concrete fibres and 4 steel fibres and the second one (200x200 mm), was assigned to the column ends, and was divided into 10 concrete fibres and 9 steel fibres as shown in Figures (3.48 & 3.49).

The presence of the CFRP sheets and the steel fibres material affect the strength, ductility and confinement of the columns and has to be taken into account in the finite element model by assigning higher compression post-peak stiffness values for the concrete material model ($\varepsilon_{cu} = 0.04$). Further, the addition of steel fibres was accounted for by increasing the concrete tensile strength f_t to $6.0\ MPa$ and taking the tension softening (E_{ts})values 0.001.

The column was divided into only 4 members for the mixed element (the minimum possible number of division as the full model is considered and two different sections are assigned) and 12 members for the displacement-based element. The two fibre beam elements with the second order analysis, were able to model the two slender columns accurately and to follow the load displacement path for both (C2-II) & (C2-II-SF). It can be seen that disregarding the second order effect gives exaggerated path for the load displacement curves, as seen in Figures (3.50 & 3.51).

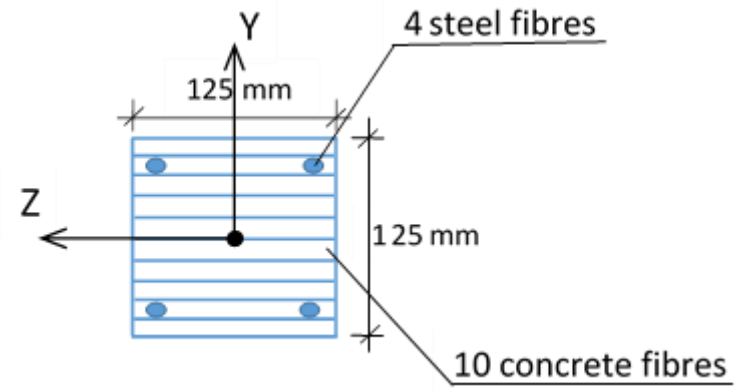

Figure 3.48: Fibre beam element cross section mesh for intermediate section.

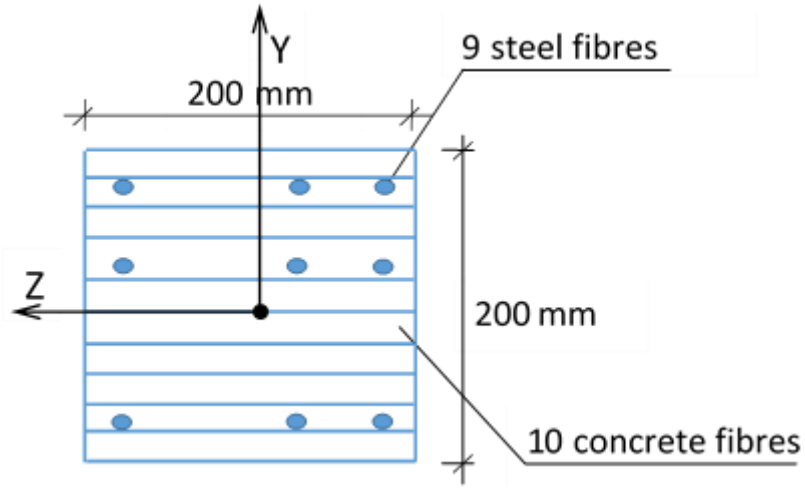

Figure 3.49: Fibre beam element cross section mesh for end sections.

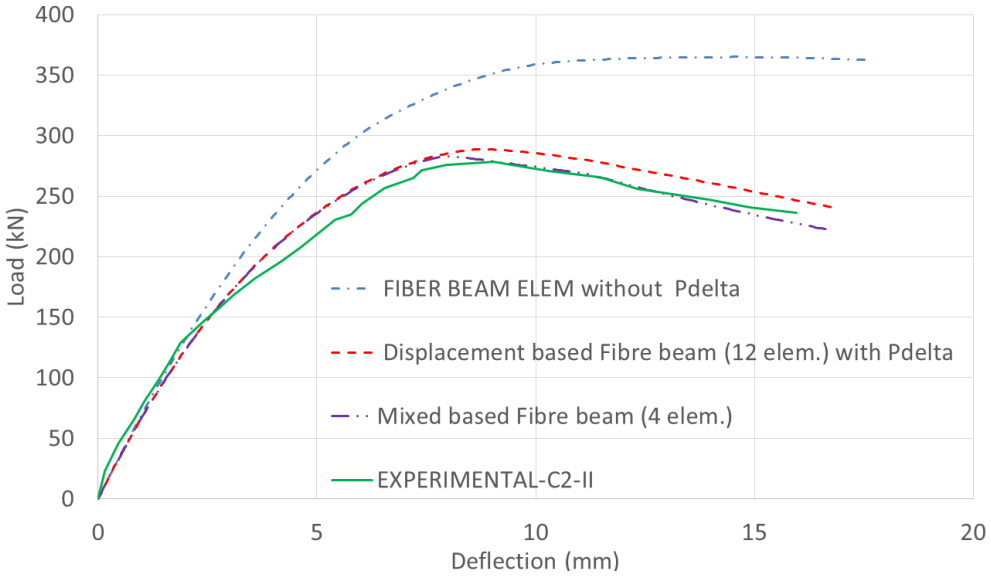

Figure 3.50: Load-deflection curve for column C2-II tested by **Dundar et al. (2015)** and compared with the fibre beam elements.

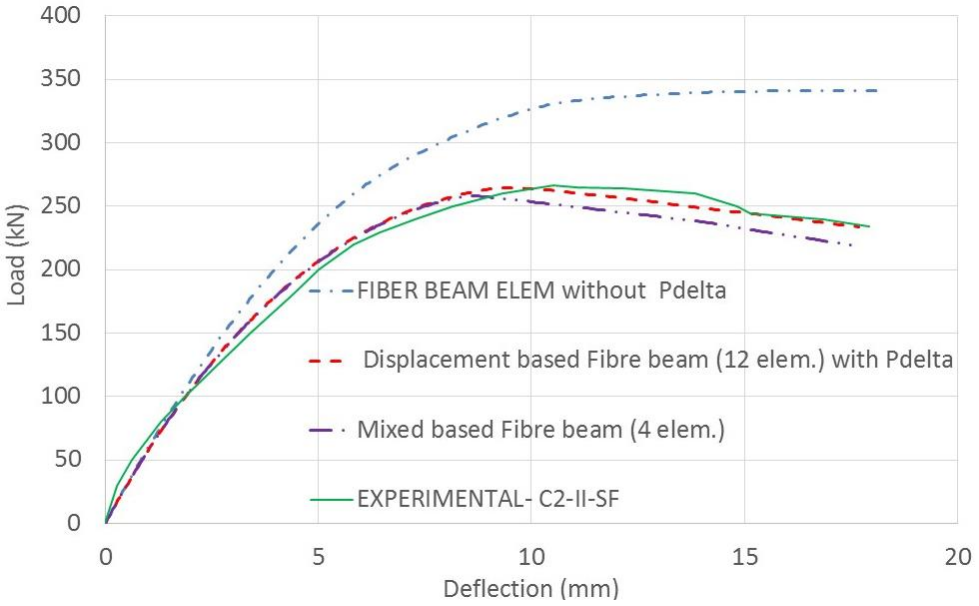

Figure 3.51: Load-deflection curve for column C2-II-SF tested by **Dundar et al. (2015)** and compared with the fibre beam elements.

By comparing the two specimens' output curves using the displacement-based element, Figure (3.52), and the mixed element, Figure (3.53), the effect of the presence of the steel fibre in sample C2-II-SF can be easily noticed. This accomplishes that both elements can recognise and simulate the presence of the fibrous material while taking into account the second order effect.

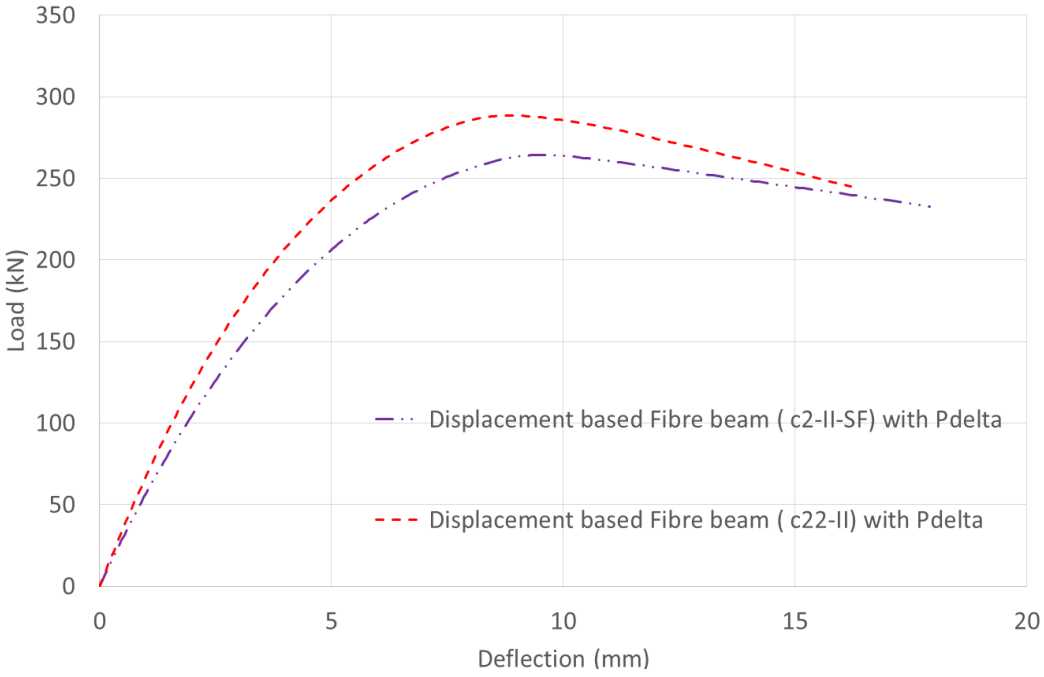

Figure 3.52: Load-deflection curve for columns C2-II & C2-II-SF using the displacement fibre beam element.

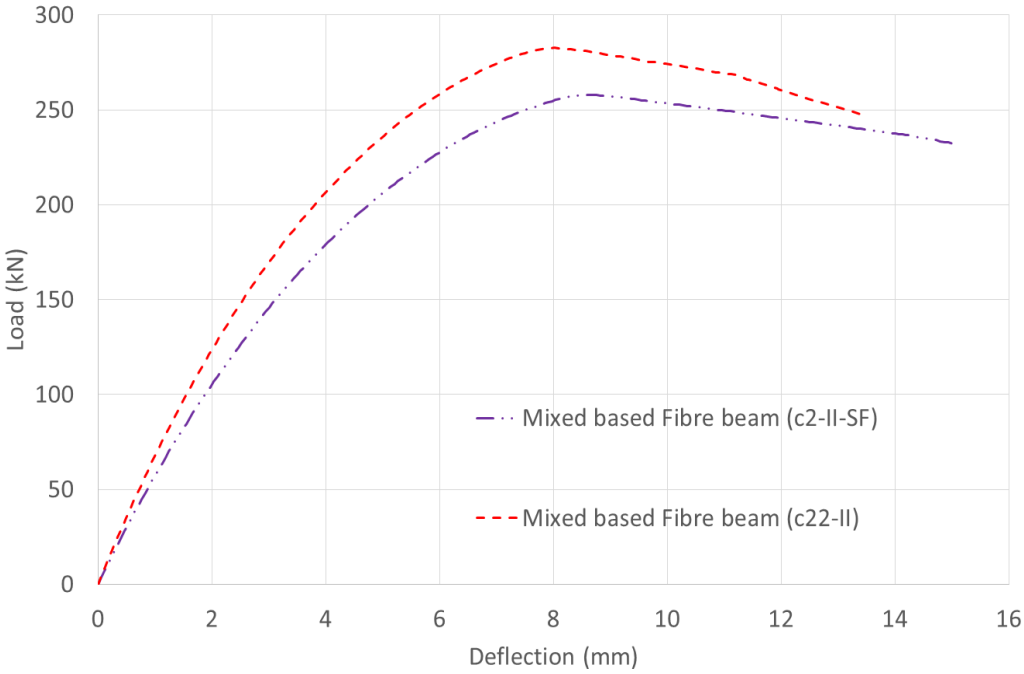

Figure 3.53: Load-deflection curve for columns C2-II & C2-II-SF using the mixed fibre beam element.

Further, the mixed element with four divisions is then used to generate the vertical displacement (Figure 3.54) and moment distributions, at load axis, along the length of the column (Figure 3.55). The results were selected at the case of maximum load (257.94 kN), where the middle of the column was subjected to the highest displacement of about 8.5 mm and a bending moment of 2.4 kN.m.

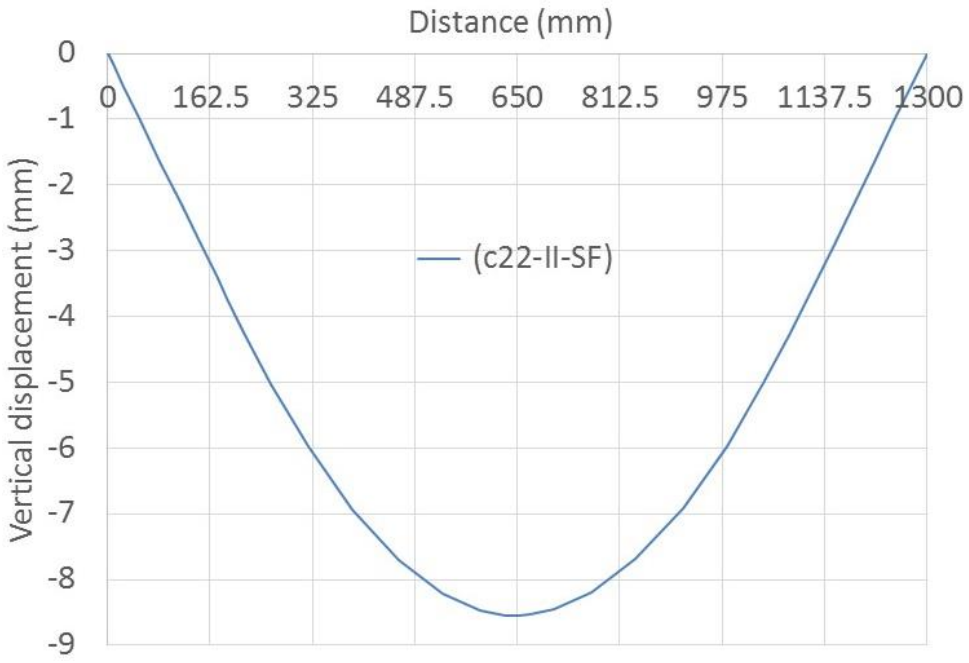

Figure 3.54: Vertical displacement along the column length at maximum load for column C2-II-SF using the mixed fibre beam element.

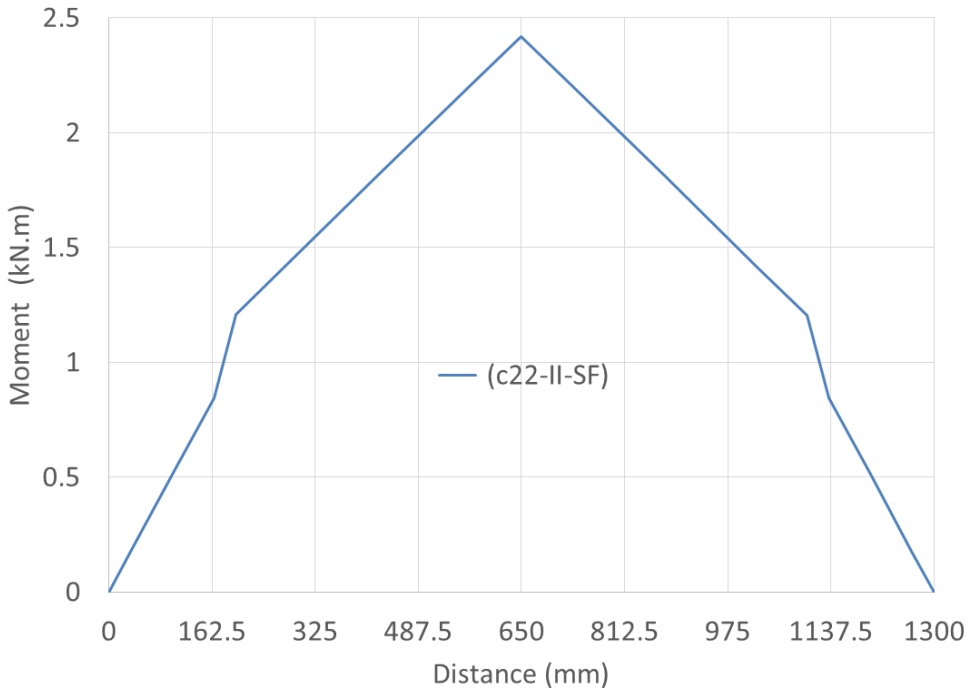

Figure 3.55: Moment at load axis along the column length at maximum load for column C2-II-SF using the mixed fibre beam element.

3.9 Column with horizontal displacement at the tip

The simulation of fibrous material is accomplished by controlling the values of the concrete tensile strength and tension softening stiffness. It is established, from recent researches, that the addition of steel and Nano fibres increases these two parameters **(Faghih et al., 2016)**.

In order to study the tension softening effect on the second order analysis, another case will be investigated. In this application, the sampling will be more sensitive to Nano parameters (the tensile strength and the tension softening stiffness). This will be achieved by modelling a sample with no or smaller longitudinal reinforcement ratio to allow the concrete tensile strength to have more significance on the response of the structure. By this way, the developed elements can investigate the outcome of the concrete tensile strength and the tension softening stiffness on the second order effect clearly.

In the investigated problem, an unreinforced concrete column is subjected to an axial load of 4000 N and a lateral displacement up to 167 mm. Due to the lack of available experimental tests in this field, the column dimensions and loading were chosen from the verification example of the commercial programme SAP2000 **(Wiki.csiamerica.com, 2017)**. However, the concrete linear stress strain behaviour used in the verification example was replaced by a full nonlinear stress strain response.

The cantilever column was fixed from the bottom and free from the top end and had a total length of 10000 mm with a cross section of 100x100 mm. The concrete was assigned an f_c of 30 MPa.

When adding carbon fibre or steel fibre to the concrete mix, according to **Faghih et al. (2016)**, it is expected that the tensile strength increases and tension softening stiffness changes.

For this study, three cases were chosen to be examined as follows:

Case 1: simulates the presence of a high percentage of fibres, so that the tensile strength f_t was chosen more than 10% of the compression strength and the tension softening stiffness slope was chosen zero to model the shape of the ideal constant line state ($E_{ts} = 0.001$) (Figure 3.56.a).

Case 2: simulates the presence of a small percentage of fibres, so that the tensile strength was chosen as 1% of the compression strength and the tension softening stiffness value was chosen as a linear moderate decreasing line ($E_{ts} = 1000$) (Figure 3.56.b).

Case 3: simulates the absence of fibres leading to negligible tensile strength and an infinity slope to simulate a brittle tension failure ($E_{ts} = 10^6$) (Figure 3.56.c).

All other parameter were retained the same for the three investigated cases.

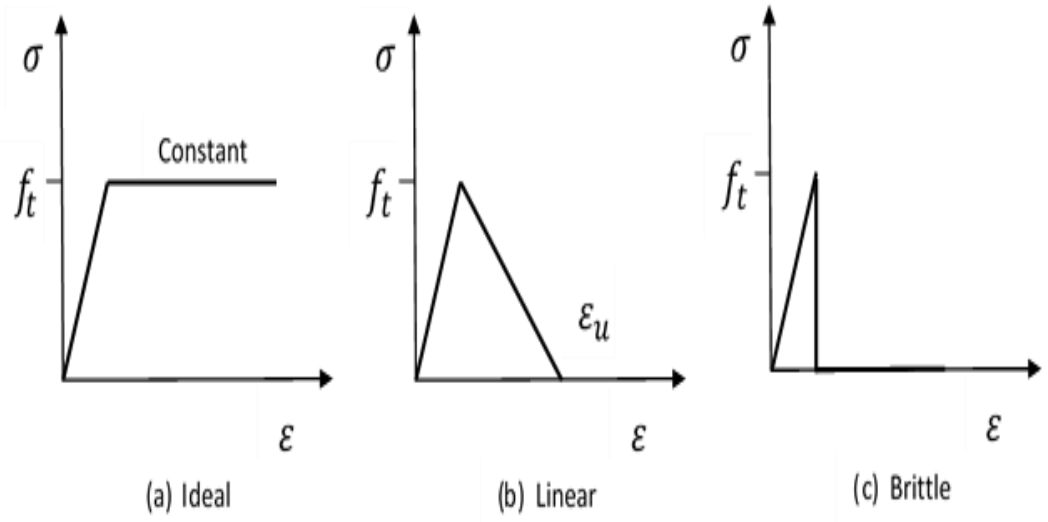

Figure 3.56: Different tension softening stiffness.

From the output of the moment vs the lateral displacement plot shown in Figure (3.57), it is noticeable that for the three cases, the consideration of the P-delta produced a lower moment – displacement curve. Therefore, the new elements can differentiate between the different values of tensile strength and different behaviours of the tension softening stiffness while considering the second order effect. This means that the programme simulates the effect of the addition of fibres and Nano fibres to the concrete elements with different percentages whereas the second order analysis is accounted for.

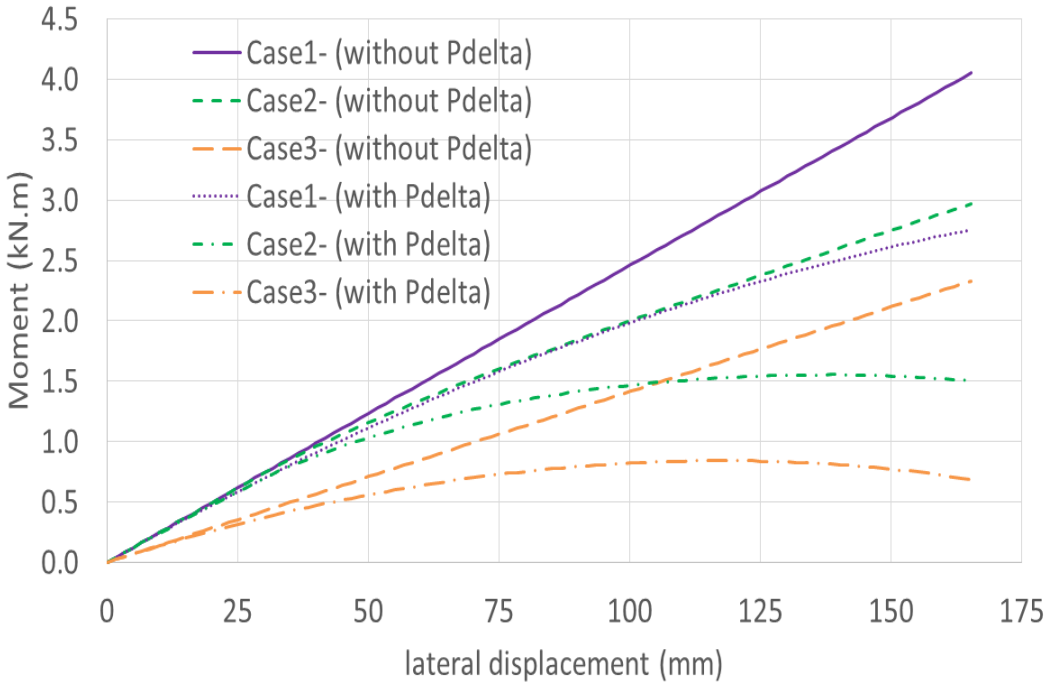

Figure 3.57: Load-displacement curves for the three different cases with and without the P-Delta effect.

3.10 Conclusion

In this chapter, two elements, one displacement-based and one mixed were developed that can consider the second order effect and can be used to model reinforced concrete structures. The two elements consider large displacements and rotations but small strains. The stiffness matrix was modified by the internal and external geometric stiffness matrix. The load vector was also modified by higher terms contained within the shape function. An advanced transformation matrix that accounts for the removal of R.B.M. and the member inclination was used to transform between the corotational and the global system.

The two elements were validated against different reinforced concrete experiments and benchmark nonlinear problems available from the literature. The

effect of the second order analysis on the curvature, moment and internal forces was emphasised at the global, section and fibre level. The study of the tension softening stiffness effect on second order analysis was also investigated.

In the next chapter, explicit large-deformation fibre beam elements will be formulated and employed to solve impact problems.

Chapter 4

EXPLICIT DYNAMIC ANALYSIS UNDER IMPACT LOADING

4.1 Introduction

In this chapter, an advanced explicit technique is presented within the context of fibre beam element formulations for the solution of structures subjected to impact and shock loading. The new explicit fibre-based beam elements are mainly developed to overcome the difficulties associated with implicit analysis of large short-duration loads. The traditional implicit method of analysis typically fails to provide numerical stable behaviour for such short time duration problems. The adopted explicit time integration method offers a stable and numerically efficient solution for dynamic problems without the need for iterations or convergence checks.

In fact, the fibre beam element permits the simulation of the global structural behaviour with identically limited degrees of freedoms, while accounting for the detailed material nonlinearity along the element length. On the other hand, the majority of explicit finite element software packages available in the market, were developed for continuum models such as solid and membrane elements. These models render the solution computationally expensive, involve a large disk space memory, and require a long runtime analysis when compared with fibre beam elements.

In this research, two fibre beam elements are developed that consider an explicit time integration scheme for the solution of the dynamic equation of motion are

presented. The first element uses a displacement-based formulation, while the second element uses a force-based formulation. For the latter case, a new algorithm that eliminates the need for iterations at the element level is proposed. The developed elements involve the use of a lumped mass matrix and a small time-increment to ensure numerical stability.

Furthermore, the strain rate effect of the concrete and steel is carefully introduced to the material models of these elements using several equations available from the literature to accurately model the behaviour of concrete and steel under high strain rates. Besides, the explicit displacement element will take into consideration the second order effect that usually accompanies dynamic problems. On the other hand, the explicit force-based element will be upgraded to a mixed element in order to account for the second order effect. The large displacement analysis formulation was covered in detail in chapter (3) of this dissertation and will only be briefly visited in this chapter. Therefore, the developed elements tend to improve the computational efficiency of the explicit time integration schemes for impact analysis using fibre beam elements.

Finally, a number of studies will be presented in this chapter to display the efficacy of the developed explicit fibre beam elements in modelling impact dynamic problems. These examples confirm the accuracy and reliability of the recently developed elements and allow their use in simulating large and complex reinforced concrete structures. The developed explicit fibre beam models, particularly the force-based element, represents a simple yet powerful tool for simulating the nonlinear complex effect of impact loads on structures accurately while using very few finite elements.

4.2 Explicit vs implicit time integration approaches

Explicit dynamic analysis is a mathematical method for integrating the equations of motion through time. It is recommended for high-speed short duration transient loading and impact problems. Hence, it can be used in many applications such as simulating drop weight tests, shock and collision, material degradation, ballistic missiles, detonation and blast analysis. The explicit analysis approach is conditionally stable, which means that a small time-increment has to be used to ensure that the solution is stable. As a result, longer analysis runtime has to be expected in the explicit analysis. However, the explicit method does not require convergence check and uses the inversion of the mass matrix, which is a lumped (diagonal) matrix and its inversion is an easy single step process. In addition, in the explicit method, the nodal accelerations are calculated directly by multiplying the inverse of the mass matrix by the force vector. On the contrary, the implicit method is unconditionally stable and entails convergence checks at all times, requires small number of expensive time steps, and is typically suitable for static and quasi-static problems. Table (4.1) shows a detailed comparison between the explicit and implicit approaches.

Moreover, for the explicit force-based element, a new element-level convergence criterion is introduced to avoid internal element iterations. The condition is checked at each time step, and the time step is reduced accordingly if necessary.

Table 4.1 Comparison between explicit and implicit time integration methods

Explicit approach	**Implicit approach**
Suitable for short transient dynamic problems	Suitable for static and quasi static problems
Use the inversion of the mass matrix	Use the inversion of the stiffness matrix
Conditionally stable	Unconditionally stable
Convergence check is not required	Convergence check is required
Requires many relatively inexpensive time steps	Requires small number of expensive time steps

For the implicit transient solution employed in this study, the Newmark method **(Newmark, 1959)** is used for nonlinear time dependent problems using second order ordinary differential equations in which β and γ are two parameters used to control the stability and numerical dissipation.

4.3 Transient Solution

The dynamic behaviour of structures can be expressed by linear and nonlinear differential equations using numerical integration techniques, where a time integration scheme is utilized to evaluate the system of equations of a structure that depends on time. In Figure (4.1), a graph illustrates the displacement of a structure and the time taken by the structure to perform this displacement. In this graph, the distance is plotted on the vertical axis and the time is plotted on the horizontal axis, (t) is the elapsed time and (Δt) is the time increment.

For the explicit analysis, dynamic values for the next step are calculated from the state of the structure already known from the previous step by solving for time $(t + \Delta t)$ using values from the preceding time(t). However, for the implicit method, values for the next step are determined from the state of the structure from both the current step and the later one by solving for time $(t + \Delta t)$ using data from time (t) and $(t + \Delta t)$. Therefore, a Newton-Raphson iteration technique is used, in implicit analysis, to obtain the solution and to enforce the equilibrium by iterating until convergence is accomplished. In general, in dynamic analysis, the implicit method can lead to convergence difficulties, as it is more sensitive to initial conditions and nonlinear behaviour.

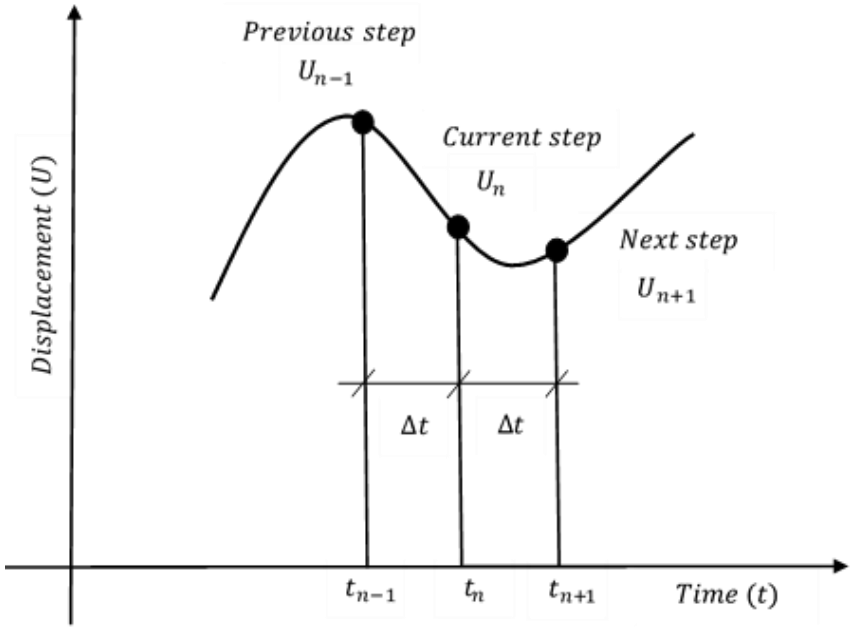

Figure 4.1: Time integration scheme.

4.4 Stability of the explicit method

Numerical stability of the explicit method must be maintained in order to yield an accurate solution. For that reason, a small time-step leading to many small time

increments is essential for the explicit analysis. A minimum stable time increment (Δt_{min}) has to be determined first and then the chosen global time increment (Δt) must be taken less than, or equal to, the minimum stable time increment. Thus, the stable time increment will be governed by the smallest element in the mesh. The choice of the time increment will have a major effect on the required runtime of the solution and the size of the output files.

For zero damping, the stable time increment is calculated by:

$$\Delta \mathrm{t}_{min} = \frac{L}{c_d} \tag{4.1}$$

Where:

L is the element length.

c_d is the dilatational wave speed.

And according to **Segel and Handelman (2007)**:

$$c_d = \sqrt{\frac{\lambda+2\mu}{\rho}} \tag{4.2}$$

The Lame's constants originated from the strain-stress relationships can be given in terms of other material properties. According to **Timoshenko and Goodier (1951)**:

$$\lambda \equiv \frac{\nu\, E}{(1+\nu)(1-2\nu)} \tag{4.3}$$

$$\mu \equiv \frac{E}{2(1+\nu)} \tag{4.4}$$

Where:

E is the material Young's modulus, ρ is the material density, ν is Poisson's ratio, λ and μ are Lame's constants.

Decreasing L or increasing c_d will reduce the stable time increment. Whereas c_d can be increased by decreasing the material density or by increasing the element stiffness.

4.5 Dynamic formulation of the explicit method

In the dynamic analysis, the input load is a function of time and according to Newton's law of motion:

$$F_t = M\ddot{U}_t \tag{4.5}$$

After D'Alembert's principle, if an external force is applied to the system in a direction opposite to the acceleration, the system will be in a dynamic equilibrium under the actual force F and the inertia force $M\ddot{U}$.

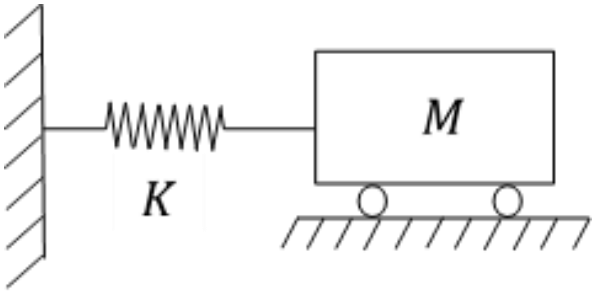

Figure 4.2: Mass on a spring system.

For the mass on a spring system shown in Figure 4.2:

$$-M\ddot{U}_t - KU_t = 0 \tag{4.6}$$

This equation of motion is for an ideal system with no damping and subjected to free vibration and means that the system is in equilibrium at each step. Consequently:

$$\ddot{U}_t + \frac{K}{M} U_t = 0 \tag{4.7}$$

And

$$\omega = \sqrt{\frac{K}{M}} \tag{4.8}$$

$$T = \frac{2\pi}{\omega} \tag{4.9}$$

Where ω is the natural circular frequency of vibration and T is the natural period of the vibration.

Consequently, the dynamic problem is transformed into a set of equations of motion that define the dynamics of the system, where the dynamic displacement and the full response of the structural system can be expressed using these equations of motion.

For the more general dynamic equilibrium equation of motion that describes the motion of the body subjected to a force, it can be stipulated in the following form:

$$M\ddot{U}_t + C\dot{U}_t + KU_t = F_t \tag{4.10}$$

Where M is the mass matrix and K is the stiffness matrix and $M\ddot{U}_t$ represents the inertia force while $C\dot{U}_t$ denotes the damping force.

The damping matrix C can be determined using the Rayleigh damping equation:

$$C = \alpha_m M + \beta_k K \tag{4.11}$$

Where α_m is the mass proportional Rayleigh damping parameter and β_k is the stiffness proportional Rayleigh damping parameter. They are calculated based on the natural frequencies of the first modes and their damping ratios. The solution of the

dynamic equation of motion for the newly developed fibre beam elements is conducted in a corotational reference system as described next.

4.6 Corotational formulation of the developed elements

The elements are formulated in a corotational system where the motion is decomposed into rigid body and local deformations then the rigid body modes are removed. Later, the dynamic effect is added in the global system. The element forces and displacement degrees of freedom in the corotational and the global system were presented and defined in detail in chapter (3) of this dissertation and are applicable herein unless noted otherwise. Concisely, for the developed elements, the corotational element has three natural degrees of freedom, an axial elongation q_1 and two rotations q_2 and q_3 at each end of the element. The axial force Q_1 and the moments Q_2 and Q_3 at both ends are the corresponding element nodal forces.

4.7 Explicit formulation of the displacement-based element

In the first explicit fibre beam element, a displacement-based formulation is used where equilibrium is satisfied in a weighted integral sense.

The internal and external forces are summed at each node point, and the nodal accelerations are computed by multiplying the forces with the inverse of the nodal mass:

$$[M]\{\ddot{U}\}_t = [F_{external}]_t - [F_{internal}]_t \quad (4.12)$$

The explicit algorithm uses the Newmark beta-gamma method with the primary variables being displacement increments to calculate the displacement, velocity and acceleration. Accordingly, the solution of equation (4.10) leads to the following:

$$U_{t+1} = U_t + \Delta t\dot{U}_t + \frac{1}{2}(1-\beta)\Delta t^2\ddot{U}_t + \frac{1}{2}\beta\Delta t^2\ddot{U}_{t+1} \quad (4.13)$$

$$\dot{U}_{t+1} = \dot{U}_t + (1-\gamma)\Delta t\ddot{U}_t + \gamma\Delta t\ddot{U}_{t+1} \quad (4.14)$$

$$M\ddot{U}_{t+1} + C\dot{U}_{t+1} + KU_{t+1} - F_{t+1} = 0 \quad (4.15)$$

For an implicit solution, $\beta = 0.25$ and $\gamma = 0.5$, while the explicit algorithm assumes $\beta = 0$ and $\gamma = 0.5$, then calculates the acceleration $\ddot{U}_t$ at time (t) by making use of the inversion of the mass matrix based on equation (4.12), followed by calculating the displacement U_{t+1} using equation (4.13). The evaluation of the mass matrix is described in detail in section 3.9. The velocity $\dot{U}_{t+1}$ and the acceleration $\ddot{U}_{t+1}$ are then calculated explicitly at time (t+1) by using the two equations (4.14) and (4.15).

The algorithm starts by assuming an Explicit Parameter to equal 1 for explicit dynamic analysis. The equivalent global dynamic stiffness $\widehat{K}_{elem(global)}$ is substituted by the lumped mass matrix:

$$\widehat{K}^{t+1}_{elem(global)} = Explicit\ Parameter\ \times\ M \quad (4.16)$$

And the global internal dynamic load $\widehat{F}_{elem(global)}$ is determined as:

$$\widehat{F}^{t+1}_{elem(global)} = F^{t+1}_{elem(global)} + M\ \ddot{U}^{t+1} + (\alpha_m M + \beta_k K)\dot{U}^{t+1} \quad (4.17)$$

Where $F_{elem(global)}$ is the static element load vector in the global system. This is calculated through integration of sections along the element length and discretization

of each section into fibres with prescribed nonlinear material behaviour. The global element force increment is:

$$\Delta\hat{F}^{t+1}_{elem(global)} = \hat{F}^{t+1}_{external} - \hat{F}^{t+1}_{elem(global)} \tag{4.18}$$

Where $\hat{F}_{external}$ is the applied external force corresponding to the load step.

Then at the global level, the finite element solution for an acceleration increment in the global system $\Delta\ddot{U}_{(global)}$ is computed by:

$$\Delta\ddot{U}^{t+1}_{(global)} = \left[\hat{k}^{t+1}_{elem(global)}\right]^{-1} \times \Delta\hat{F}^{t+1}_{elem(global)} \tag{4.19}$$

In the explicit solution, ΔU is estimated from $\Delta\ddot{U}_{(global)}$ using equations (4.13) to (4.15) as detailed before. At this point, the evaluation of the stiffness matrix K_{elem} and load vector F_{elem} is first calculated in the corotational system, and then transformed to the global system by adding the rigid body modes as follows:

$$k^{t+1}_{elem(global)} = T^T\, K^{t+1}_{elem}\, T \tag{4.20}$$

$$F^{t+1}_{elem(global)} = T^T\, F^{t+1}_{elem} \tag{4.21}$$

Where T is the transformation matrix:

$$T = \begin{bmatrix} -1 & 0 & 0 & 1 & 0 & 0 \\ 0 & \frac{1}{L} & 1 & 0 & -\frac{1}{L} & 0 \\ 0 & \frac{1}{L} & 0 & 0 & -\frac{1}{L} & 1 \end{bmatrix} \tag{4.22}$$

To determine the value of K_{elem} and F_{elem} using the displacement-based method in the corotational system, the section deformation increment of the element reference axis in the corotational system is first evaluated as:

$$d_s^{t+1} = S\,\Delta q^{t+1} \tag{4.23}$$

Where S is the displacement shape function in the explicit formulation:

$$S = \begin{bmatrix} \frac{1}{L} & 0 & 0 \\ 0 & \frac{-4}{L} + \frac{6\,x}{L^2} & \frac{-2}{L} + \frac{6\,x}{L^2} \end{bmatrix} \tag{4.24}$$

The calculation of the displacement increment Δq in the corotational system is accomplished by using the matrix T:

$$\Delta q^{t+1} = T\ \Delta U^{t+1} \tag{4.25}$$

The element stiffness can then be calculated as:

$$K_{elem}^{t+1} = \int_0^L S^T\ k_{sec}^{t+1}\ S\ dx \tag{4.26}$$

Where k_{sec} is the section stiffness.

The element internal resisting force vector is equal to:

$$F_{elem}^{t+1} = \int_0^L S^T\ F_{sec}^{t+1}\ \ dx \tag{4.27}$$

Such that F_{sec} is the section forces in the corotational system and represents the vector $\begin{Bmatrix} P \\ M \end{Bmatrix}$, where P is the section axial force and M is the section bending moment.

The section stiffness k_{sec} and force vector F_{sec} are determined from fibre discretization as noted earlier using the section deformation increment and following the assumption of plane sections remaining planes:

$$\varepsilon_1\,(x, y) = \varepsilon(x) - y\ \emptyset(x) \tag{4.28}$$

Where ε_1 is the fibre axial strain, ε is the axial strain at the beam axis, y is the distance from the neutral axis, and $\emptyset$ is the section curvature. The fibre strain is used along with the fibre nonlinear material constitutive law to determine the fibre force

and stiffness, which are integrated along the section depth to evaluate the section force and stiffness.

To consider the second order effect, as in chapter (3), the stiffness matrix must be updated by adding the internal geometric stiffness matrix term K_g:

$$K_{elem}^{t+1} = \left(K_g^{t+1} + \int_0^L N_\delta^T \, k_{sec}^{t+1} \, N_\delta dx\right) \tag{4.29}$$

$$\text{Where } K_g^{t+1} = {Q_1}^{t+1} \begin{bmatrix} 0 & 0 & 0 \\ 0 & \frac{2L}{15} & \frac{-L}{30} \\ 0 & \frac{-L}{30} & \frac{2L}{15} \end{bmatrix} \tag{4.30}$$

And Q_1 is the axial force in the corotational system.

Therefore, equation (4.26) is replaced by equation (4.29), while the resisting load vector is evaluated by:

$$F_{elem}^{t+1} = \int_0^L N_\delta^T \, F_{sec}^{t+1} \, dx \tag{4.31}$$

Where:

$$N_\delta = \begin{bmatrix} \frac{1}{L} & \left(1 - \frac{4x}{L} + \frac{3x^2}{L^2}\right)^2 q_2 + & \left(1 - \frac{4x}{L} + \frac{3x^2}{L^2}\right)\left(-\frac{2x}{L} + \frac{3x^2}{L^2}\right) q_2 \\ & \left(1 - \frac{4x}{L} + \frac{3x^2}{L^2}\right)\left(-\frac{2x}{L} + \frac{3x^2}{L^2}\right) q_3 & + \left(\frac{2x}{L} + \frac{3x^2}{L^2}\right)^2 q_3 \\ 0 & -\frac{4}{L} + \frac{6x}{L^2} & -\frac{2}{L} + \frac{6x}{L^2} \end{bmatrix} \tag{4.32}$$

Thus, equation (4.27) is replaced by equation (4.31) and the transformation matrix T in equation (4.22) will be replaced by the transformation matrix T_r that includes large rotations.

$$T_r = \begin{bmatrix} -\cos\beta & -\sin\beta & 0 & \cos\beta & \sin\beta & 0 \\ -\frac{\sin\beta}{L} & \frac{\cos\beta}{L} & 1 & \frac{\sin\beta}{L} & -\frac{\cos\beta}{L} & 0 \\ -\frac{\sin\beta}{L} & \frac{\cos\beta}{L} & 0 & \frac{\sin\beta}{L} & -\frac{\cos\beta}{L} & 1 \end{bmatrix} \tag{4.33}$$

Where the current length of the element L, $(\cos\beta)$ and $(\sin\beta)$ were all explained and defined in detail in chapter (3). Accordingly, the element global stiffness matrix can be specified as:

$$k^{t+1}{}_{elem(global)} = {T_r}^T K_{elem}^{t+1} T_r + K_G^{t+1} \tag{4.34}$$

Where K_G is the external geometric stiffness matrix and can be found in Appendix 1. And the element nodal forces in the global system can be identified as:

$$F_{elem(global)}^{t+1} = {T_r}^T F_{elem}^{t+1} \tag{4.35}$$

4.8 Explicit formulation of the force-based element

In the second explicit fibre beam element, a force-based formulation is used where the equilibrium is satisfied in a section-by-section basis along the element length. In the proposed algorithm, normal internal iterations are avoided and the solution procedure is only conducted once to calculate the element stiffness matrix and the load vector. The use of this technique is accurate as long as the time step is set to be smaller than a critical value. However, if adopting a time step larger than the critical value, performing internal iterations would be needed to minimize the internal residual error. In this case, the solution is transformed into a mixed explicit-implicit approach.

Equations (4.12 to 4.15) are used to calculate the global acceleration, velocity and displacement explicitly at time (t+1). The dynamic stiffness $\widehat{K}_{elem(global)}$ and the dynamic load $\widehat{F}_{elem(global)}$ are then evaluated using equations (4.16 & 4.17).

Here, K_{elem} and F_{elem} are determined using a force-based procedure in the corotational reference system. The same matrix T described in equation (4.22) is used to transform the system to and from the corotational system. $\Delta q^{t+1}$is again evaluated using equation (4.25).

First, the element initial end force increments are calculated with the use of the stiffness of the element at the previous step:

$$\Delta F_{elem}^{t+1} = \mathcal{K}_{elem}^{t}\, \Delta q^{t+1} \tag{4.36}$$

Then the element end forces $F_{elem}^{t+1}$are updated by ΔF_{elem}^{t+1}:

$$F_{elem}^{t+1} = F_{elem}^{t} + \Delta F_{elem}^{t+1} \tag{4.37}$$

Where $(t+1)$ denotes the new increment step and (t) denotes the previous step as the external load is imposed in an incremental sequence.

Using the force interpolation function, the section force increments ΔF_{sec} are determined by:

$$\Delta F_{sec}^{t+1} = b\, \Delta \mathrm{F}_{elem}^{t+1} \tag{4.38}$$

Where b is the force interpolation function, in the explicit formulation, and can be expressed as:

$$b = \begin{bmatrix} 1 & 0 & 0 \\ 0 & \frac{x}{L} - 1 & \frac{x}{L} \end{bmatrix} \tag{4.39}$$

The total section forces $F_{sec}(x)^{t+1}$ are calculated by adding the section force increments ΔF_{sec}^{t+1} to the previous section forces $F_{sec}^{t}(x)$:

$$F_{sec}^{t+1}(x) = F_{sec}^{t}(x) + \Delta F_{sec}^{t+1} \tag{4.40}$$

The section deformation increments are at that moment established by the linearization of the section force-deformation and then used to update the section deformation d_{sec}^{t}.

$$d_{sec}^{t+1} = d_{sec}^{t} + f_{sec}^{t+1}\, \Delta F_{sec}^{t+1} \tag{4.41}$$

Where f_{sec}^{t+1} is the section flexibility retrieved from the previous step.

To avoid violating the equilibrium, the section unbalanced forces are considered; which are the difference between the calculated total section forces and the section resisting forces. The section resisting forces are assessed from the discretization of the section into fibres using the updated section deformation d_{sec}^{t+1} and following the assumption of plane sections remaining planes. Therefore, the section unbalanced forces are:

$$F_{U}^{t+1}(x) = F_{sec}^{t+1}(x) - F_{R}^{t+1}(x) \tag{4.42}$$

Where F_U is the section unbalance force vector, and F_R is the resisting force vector. Subsequently, the unbalanced forces are converted to a residual section deformation $r(x)$ using the current section flexibility:

$$r^{t+1}(x) = f_{sec}^{t+1}\, F_{U}^{t+1}(x) \tag{4.43}$$

The residual element deformations are then calculated by integrating the residual section deformations along the element length:

$$R^{t+1} = \int_{0}^{l} b^{T}(x)\, r^{t+1}(x)\, dx \tag{4.44}$$

To ensure numerical stability of the force-based element, the residual R has to be minimized to a very small acceptable value. In the implicit force-based algorithm,

an element iteration is needed in order to eliminate the section residual deformation $r(x)$. This is performed using the following energy criteria:

$$\sum_1^3 F_{\ unbalanced} \cdot \Delta q \ \leq \ absolute\ tolerance \tag{4.45}$$

In the explicit algorithm, a similar approach could be used, which requires an element-level iteration until convergence is achieved. However, the element iteration becomes unnecessary if the analysis time step is sufficiently small to satisfy the previous energy condition.

In this case, $(\sum_1^3 F_{\ unbalanced} \cdot \Delta q)$ is compared to the '$absolute\ tolerance$' for each element; and if found smaller this means that the element converges with one iteration only. If found larger, however, the algorithm calculates a new critical time step $\Delta t_{critical}$:

$$\Delta t_{critical}^{\ \ new} = \Delta t_{critical}^{\ \ old} \times \sqrt{\frac{absolute\ tolerance}{\sum_1^3 F_{\ unbalanced} \cdot \Delta q}} \tag{4.46}$$

Where the tolerance value is typically varied between 10^{-4} to 10^{-8} N.mm depending on the problem being analysed and the accuracy desired by the user.

Finally, the chosen $\Delta t_{critical}$ is the minimum $\Delta t_{critical}$ of all elements. Hence, the time step is reduced to equal $\Delta t_{critical}$.

Therefore in addition to the condition of the stable time increment Δt_{min}, if the time step is smaller than or equal to $\Delta t_{critical}$, a single iteration is sufficient to satisfy the element-level convergence criteria described in equation (4.46), and the entire solution algorithm would not require any iterations.

Once the element residual deformations are reduced to within the specified tolerance value, the element flexibility f_{elem} is estimated by the integration of the

section flexibility f_{sec} along the element length and the element stiffness K_{elem} is computed by inverting the flexibility of the element.

$$(\mathcal{K}_{elem}^{t+1})^{-1} = f_{elem}^{t+1} = \int_0^L b^T f_{sec}^{t+1} b \, dx \tag{4.47}$$

Then the element end resisting forces are updated using a new ΔF_{elem}.

$$\Delta F_{elem}^{t+1} = -\mathcal{K}_{elem}^{t+1}(R^{t+1}) \tag{4.48}$$

$$F_{elem}^{j+1} = F_{elem}^{t+1} + \Delta F_{elem}^{t+1} \tag{4.49}$$

As a last step, the forces and deformations of all sections are updated using the new element end resisting forces. Following this, the element stiffness and the element end resisting forces are transformed to the global system.

To consider the second order effect, as in chapter (3), the force-based element has to be converted into a mixed element. This allows the use of the displacement variables to calculate the Green-Lagrange strain that includes the higher second order terms. Then the compatibility is imposed to ensure a smooth differentiable displacement field.

It can be noted that the force-based element satisfies the equilibrium on a section-by-section basis, while the mixed element satisfies the equilibrium equations and the compatibility in a weighted integral sense while the stress resultant forces respect the equilibrium equations at any section along the element length.

Accordingly, the element end resisting forces, equation (4.48), is replaced by the next formula that accounts for both the element residuals (R) and the compatibility equation (V):

$$\Delta F_{elem}^{t+1} = K_{elem}(V^{t+1} - R^{t+1}) \tag{4.50}$$

Where the element strain displacement compatibility equation is calculated as follows:

$$V^{t+1} = \int_0^L b^T \left(\hat{d}^{t+1} - d^{t+1}\right) dx = 0 \tag{4.51}$$

The Green-Lagrange strain-displacement relation is employed to calculate the generalized strains and their increments:

$$\Delta\hat{d}_{sec}^{t+1} = N_1\, \Delta q^{t+1} + \begin{Bmatrix} 0 \\ 1 \end{Bmatrix} (\Delta q^{t+1})^T N_2 q^{t+1} + \frac{1}{2}\begin{Bmatrix} 0 \\ 1 \end{Bmatrix} (\Delta q^{t+1})^T N_2 \Delta q^{t+1} \tag{4.52}$$

Where N_1 and N_2 were defined in chapter (3). Then, the internal geometric stiffness matrix K_g is added to the element stiffness previously calculated in equation (4.47) using the force interpolation function:

$$(\mathcal{K}_{elem}^{t+1})^{-1} = f_{elem}^{t+1} = \int_0^L b^T\, f_{sec}^{t+1}\, b\, dx \tag{4.53}$$

And

$$K_{elem}^{t+1} = \left({K_g}^{t+1} + \mathcal{K}_{elem}^{t+1}\right) \tag{4.54}$$

For the mixed element that includes the second order effect only, it will be required that the element force vector F_{elem} and element stiffness matrix K_{elem} be multiplied by another matrix G before being transformed by the transformation matrix T_r as shown below:

For the element forces:

$$F_{elem_{(G)}} = G^T\, F_{elem} \tag{4.55}$$

And for the element stiffness matrix:

$$K_{elem_{(G)}} = G^T\, K_{elem}\, G \tag{4.56}$$

The G matrix that includes the higher order terms was previously defined in chapter (3).

Then the transformation that contains the higher order terms is applied:

$$k_{elem(global)} = {T_r}^T K_{elem_{(G)}} T_r + K_G \tag{4.57}$$

$$F_{elem(global)} = {T_r}^T F_{elem_{(G)}} \tag{4.58}$$

In addition, the transformation matrix T_r is used to transform the displacements between the corotational and global system:

$$\delta \bar{q} = {T_r}^T \delta q \tag{4.59}$$

A detailed flowchart diagram summarizing the algorithm of the proposed explicit fibre beam elements is shown in Figure (4.3).

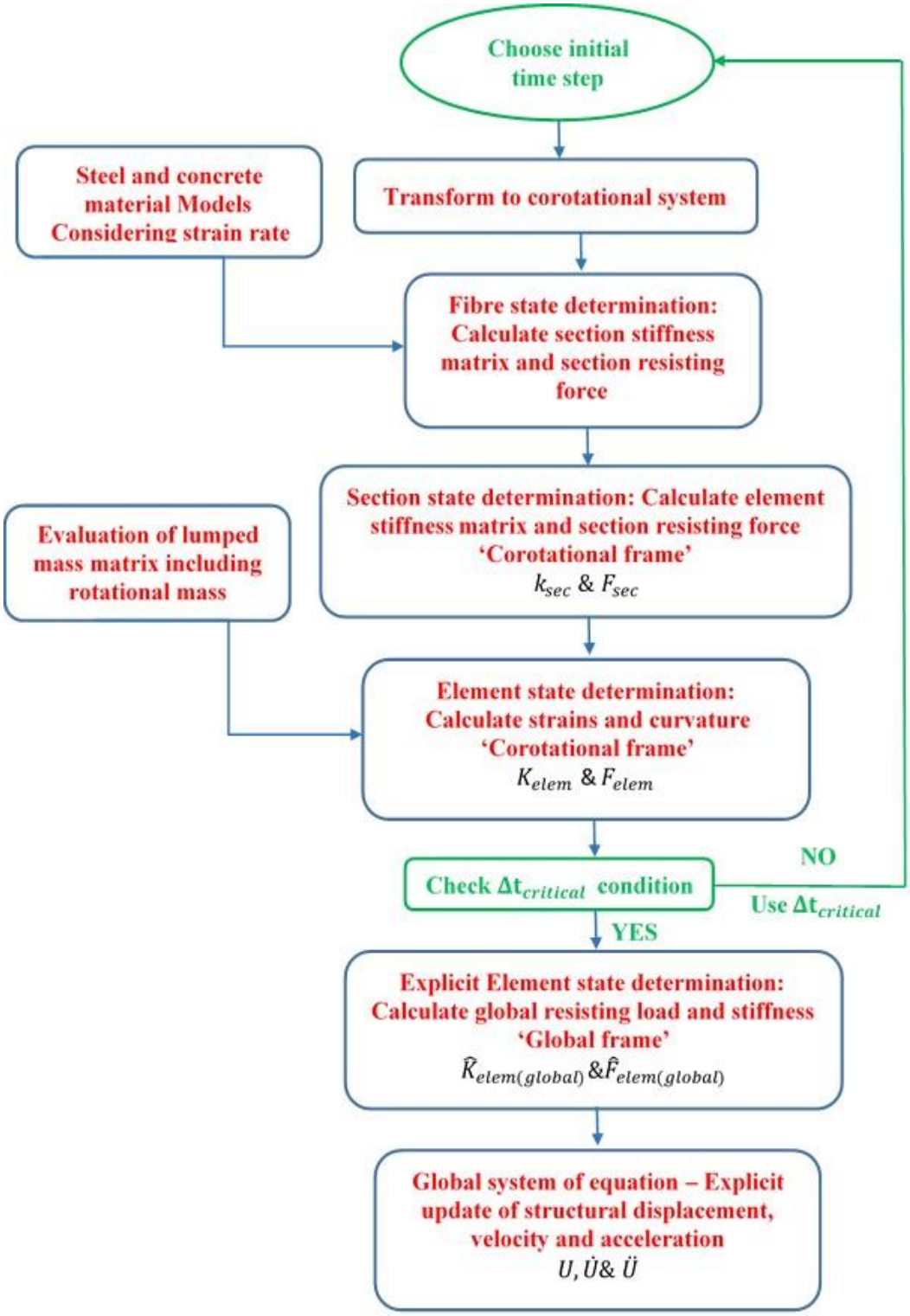

Figure 4.3: Flowchart diagram of the proposed explicit fibre beam elements.

4.9 Construction of the mass matrix for explicit elements

In the traditional implicit dynamic analysis, a consistent mass matrix can typically be constructed in local coordinates, used and transformed to the global system. However, the formulation of the explicit elements necessitates that a diagonal mass matrix be constructed instead of the consistent one to make the inversion of the mass matrix trivial.

The diagonal mass matrix is based on direct lumping and can be stored as a vector. All diagonal terms of the lumped mass matrix have to be defined, as shown in Figure (4.4), including a rotational mass. To evaluate the mass matrix due to the self-weight of a beam with element length L, cross section area A and a uniform mass density ρ:

The translational nodal masses in both horizontal and vertical directions equal:

$$\frac{1}{2}\ \rho AL \tag{4.60}$$

While the rotational mass at each node equal:

$$\alpha\rho \mathrm{A}L^3 \tag{4.61}$$

Where from **Felippa (2013)** the value of α varies between 0 and 1/100.

However, higher values of α might stabilize the system without scarifying its accuracy. If the α value is taken as zero this leads to a singular mass matrix, which cannot be used in an explicit formulation.

For the presented elements, the value of α was taken equal to $(3.5/100)$ and was found to yield stable and accurate results for the displacement and the force-based explicit elements. For the implicit analysis, the value of α can be taken equal to zero.

In addition to the self-weight mass, all the external masses supported by the element should be lumped at the element ends.

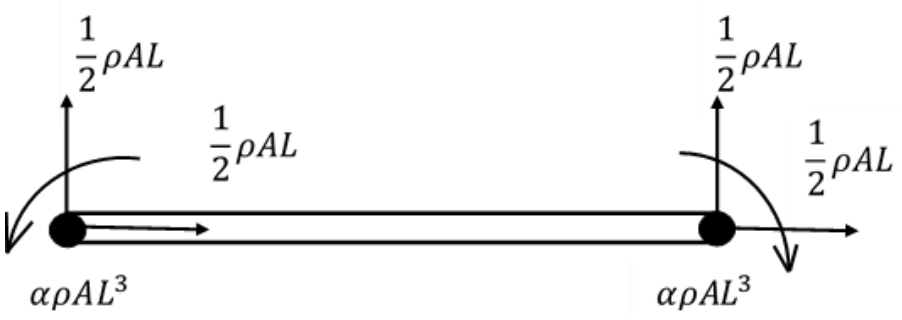

Figure 4.4: Direct mass lumping for two-node plane beam element.

4.10 Material models of the explicit elements

For the proposed explicit elements, the strain rate effects have to be accounted for in the material models. To consider the strain rate effect in the material models, the material parameters for concrete and steel were modified using the dynamic increase factor (DIF) where the DIF is a non-dimensional parameter and is used to present the difference between the properties of the materials under static and dynamic loading. The DIF can be applied to the concrete and steel material parameters to reflect the strain rate effect.

For the concrete stress strain curve (Figure 4.5), the value of the concrete compressive strength, the concrete strain at maximum strength and the concrete tensile strength are amplified, while for the steel reinforcement stress strain curve (Figure 4.6), the value of the yield strength is augmented.

Many researchers have tested several types and samples of concrete and steel materials in order to determine their DIF. Typically, the split Hopkinson pressure bar or an instrumented drop weight impact test were employed to investigate these parameters.

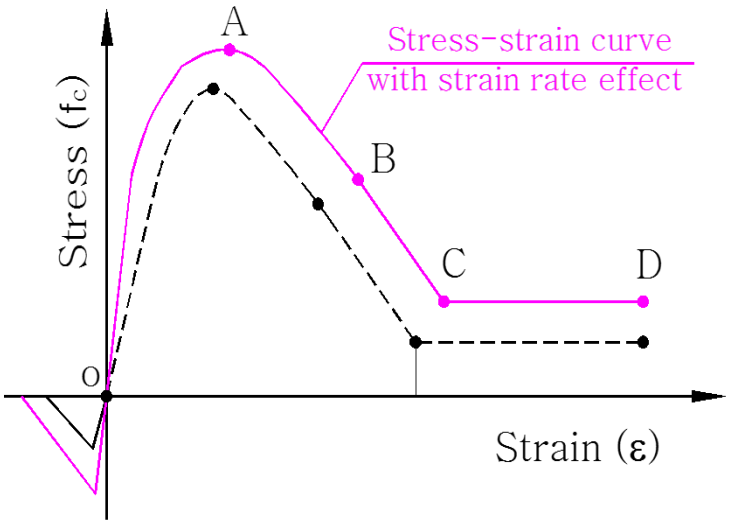

Figure 4.5: Concrete material model with and without strain rate effect.

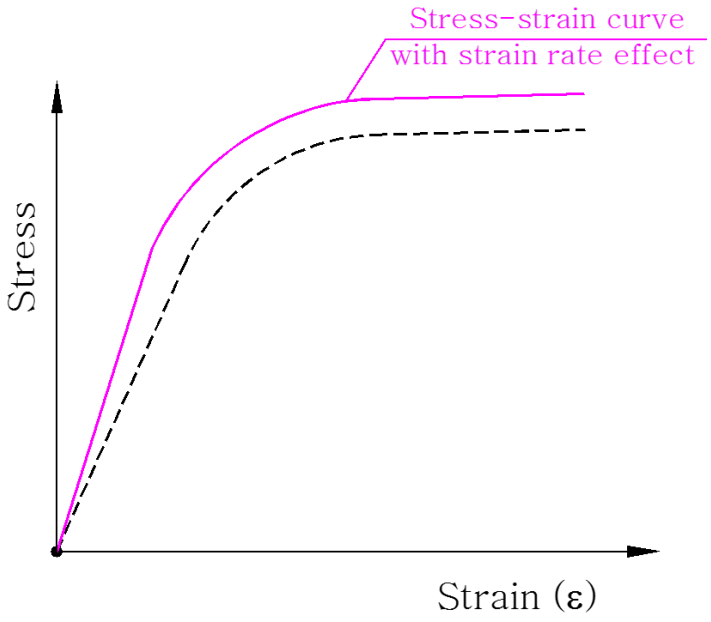

Figure 4.6: Menegotto-Pinto monotonic stress-strain curve of mild steel bar with and without strain rate effect.

The following equations retrieved from the literature were used in the explicit fibre beam element material models. For normal concrete, the dynamic compressive strength was determined by **Fujikake et al. (2009)**:

$$f'_{cd} = f'_c \left(\frac{\dot{\varepsilon}}{\dot{\varepsilon}_{sc}}\right)^{0.006[\log \dot{\varepsilon}/\dot{\varepsilon}_{sc}]^{1.05}} \quad for\ \dot{\varepsilon} \geq \dot{\varepsilon}_{sc} \tag{4.62}$$

And the strain corresponding to the dynamic compressive strength was calculated as:

$$\varepsilon'_{cd} = \varepsilon'_c \left(\frac{\dot{\varepsilon}}{\dot{\varepsilon}_{sc}}\right)^{-0.036+0.01\log(\dot{\varepsilon}/\dot{\varepsilon}_{sc})} \quad for\ \dot{\varepsilon}\ \geq \dot{\varepsilon}_{sc} \tag{4.63}$$

Where:

f'_{cd} = The dynamic concrete tensile strength at strain rate $\dot{\varepsilon}$ in MPa.

f'_c = The static compressive strength in MPa.

ε'_{cd} = The dynamic strain corresponding to f'_{cd}.

ε'_c = The static strain corresponding to f'_c.

$\dot{\varepsilon}_{sc} = 1.2 \times 10^{-5}$.

For the dynamic tensile strength of normal concrete, the **Ross et al. (1989)** equation was used:

$$f_{td} = f_t \exp\left[0.00126\left(\log_{10}\frac{\dot{\varepsilon}}{\dot{\varepsilon}_{st}}\right)^{3.373}\right] \quad for\ \dot{\varepsilon} \geq\ \dot{\varepsilon}_{st} \tag{4.64}$$

Where:

f_{td} = The dynamic concrete tensile strength at strain rate $\dot{\varepsilon}$.

$f_t =$ The static concrete tensile strength.

$\dot{\varepsilon}_{st} = 1.0 \times 10^{-7}$.

The **Lok and Zhao (2004)** equations were used to account for the effect of the presence of fibres in the concrete mix on the DIF. They used the Split Hopkinson pressure bar in the development of the strain rate tests that ranged between 20 and 100 S^{-1} and proposed two equations to express the compressive response of steel fibre-reinforced concrete subjected to different strain rates as follows:

$$DIF = 1.080 + 0.017\ \log(\dot{\varepsilon})\ \ 0 \le \dot{\varepsilon} \le 20\ S^{-1} \quad (4.65)$$

$$DIF = 0.067 + 0.796\ \log(\dot{\varepsilon})\ \ \ 20 \le \dot{\varepsilon} \le 100\ S^{-1} \quad (4.66)$$

For the reinforcing steel, and according to **Limberger et al. (1982)** and **Ammann et al. (1982)**, the steel elastic modulus E_S and the strain hardening modulus E_{SP} are not affected by the loading rates. So in the steel material model, only the effect on the yield strength is considered. The dynamic yield strength f_{syd} at strain rate $\dot{\varepsilon}$ is estimated by the **Malvar (1998)** equations. **Malvar (1998)** studied the strength enhancement of steel reinforcing bars under the effect of high strain rates and proposed a formula to approximate the straight line on the logarithmic scale of the dynamic increase factor versus the strain rate.

The equations were derived and are valid for a yield stress f_y that ranges between 290 and 710 MPa and are as follows:

$$DIF = \left(\frac{\dot{\varepsilon}}{10^{-4}}\right)^{\gamma} \quad (4.67)$$

For yield stress calculation:

$$\gamma = \alpha_{fy}; \quad \alpha_{fy} = 0.074 - 0.04\left(f_y/414\right) \quad (4.68)$$

For ultimate stress calculation:

$$\gamma = \alpha_{fu}\ ; \quad \alpha_{fu} = 0.019 - 0.009\left(f_y/414\right) \quad (4.69)$$

Where:

$\dot{\varepsilon}$: The strain rate is in S^{-1}.

f_y : The bar yield strength in MPa.

However, it is first necessary to estimate the dynamic strain rate before being able to use the previously mentioned equations. For this, **Perrone and Bhadra (1984)** studied the strain rate effect on mild steel and aluminium wires and the work

was then extended by **Jones (1990)** to calculate the mean strain rate for beams using the following simplified equation:

$$\dot{\varepsilon} = 4w_p V_0/(3\sqrt{2}L^2) \quad (4.70)$$

Where:

w_p: is the maximum permanent displacement in mm and can be calculated from **Jones (1990)**.

V_0: is the impact velocity.

L: is the length of the beam in mm.

Similarly, **Liew et al. (2009)** used the same formulation to evaluate the strain rate of sandwich structures subjected to impact force.

Theses promising models cover a wider range of cases not covered by the **Fib Model Code for Concrete Structures 2010 (2013)** equations (i.e. when fibres are introduced to the concrete mix and for steel reinforcement).

4.11 Validation of the finite element models

The developed explicit models are verified by comparing their results with three benchmark experiments available from the literature. In the selected experiments, instrumented drop weight impact tests were used to examine the dynamic behaviour of doubly reinforced concrete beams, steel fibre-reinforced concrete beams and SC panel system. After the calibration of the numerical models, the elements can be widely used to simulate the response of large structures subjected to impact while considering the effect of the presence of fibres in the concrete core.

4.11.1 Saatci and Vecchio experiment

An instrumented experimental program was carried out by **Saatci and Vecchio (2009.b)** where eight reinforced concrete beam specimens were tested under free-falling drop-weights. All the specimens had a section of 250 mm x 410 mm and a total length of 4880 mm. The beams were simply supported with a clear span of 3000 mm. All the specimens were doubly reinforced with equal top and bottom reinforcement that consists of 4 bars with diameter 29.9 mm and a yield stress of 464 MPa. Figure (4.7) illustrates the impact test setup used in the experiment.

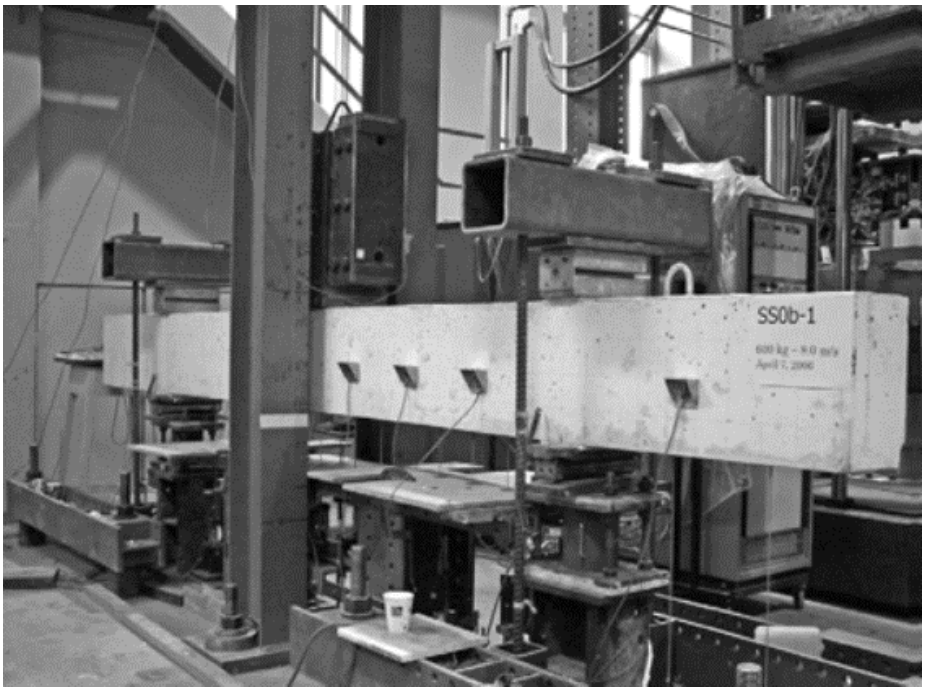

Figure 4.7: Test setup of the beams, Figure from **Saatci and Vecchio (2009.b)**.

For specimen SS3a-1, the drop-weights impacted the specimen once at the midspan, from a clear height of 3.26 m, with a small drop weight (211 kg). A bending failure mode dominated the sample under the static loading with visible

wide vertical flexural cracks at the midspan. However, shear cracks also developed under the impact test mainly after other multiple impacts.

Specimen SS3a-1 was chosen to be modelled with the fibre beam elements. The Specimen had a compressive strength of 46.7 MPa and a strain at peak compressive stress equal to 2.51×10^{-3}. The strain rate effect in this sample was small and did not change the material properties much. Figure (4.8) displays the impact force and the reaction forces obtained from the experiment.

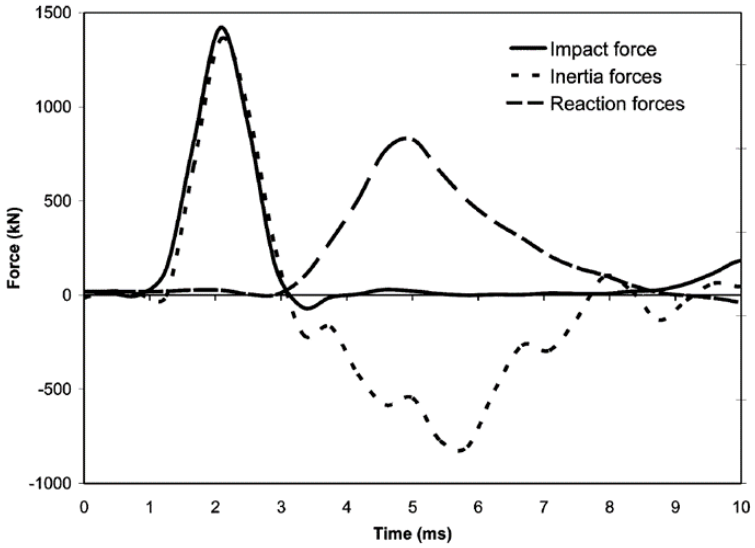

Figure 4.8: Impact and reaction forces vs time for sample SS3a-1, Figure from **Saatci and Vecchio (2009.b)**.

In the finite element models, each element was divided into 5 sections and the sections were further divided into 12 concrete fibres and 4 steel fibres (Figure 4.9).

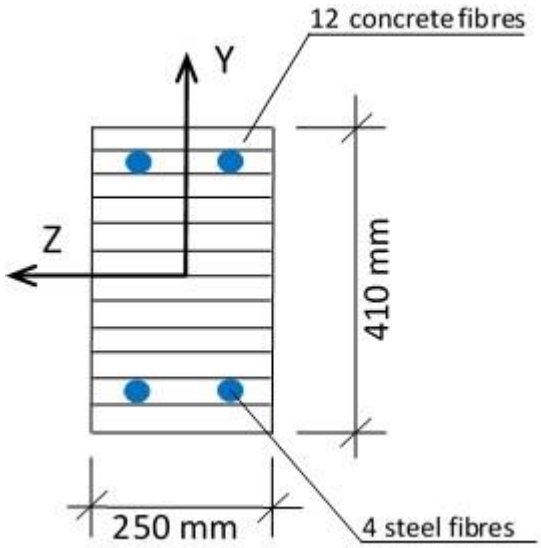

Figure 4.9: Fibre beam element cross section mesh for sample SS3a-1.

A convergence study was first performed for the explicit displacement-based element. The beam was modelled with 10, 14, 18 and 22 elements including the cantilever parts. Figure (4.10) shows that 18 explicit-based elements are sufficient to reach convergence.

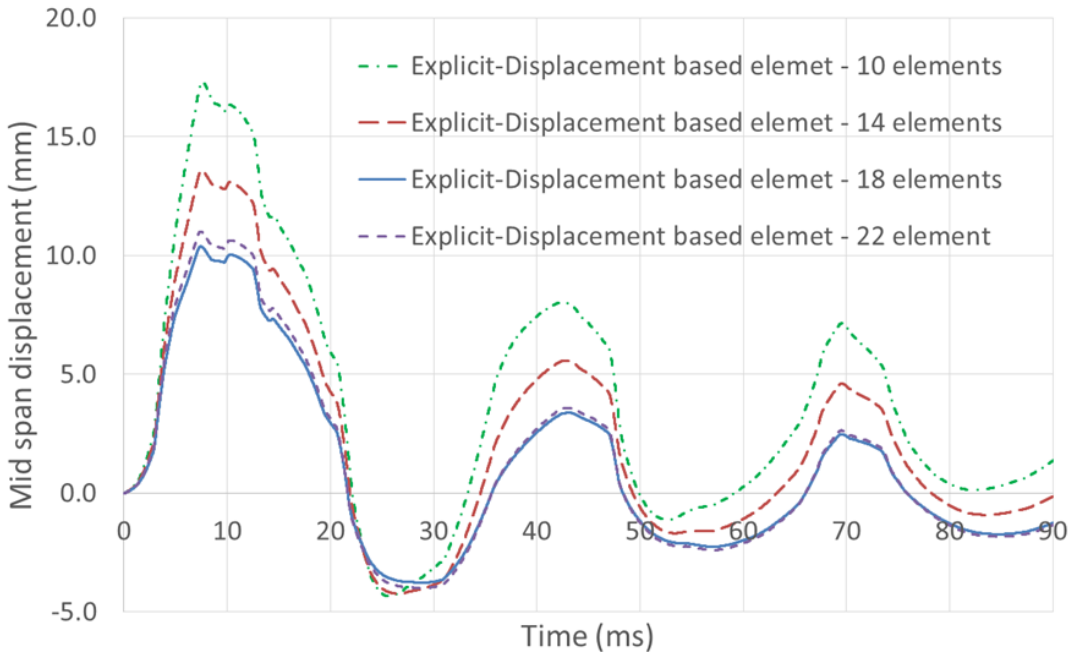

Figure 4.10: Conversion study for the explicit displacement-based element for sample SS3a-1.

Therefore, for the displacement-based elements, the beam was subdivided into 18 finite elements. Regarding the displacement-based implicit element a step of 0.01 was adopted while for the displacement-based explicit element, a step of 0.01 was found unstable and a smaller step of 0.001 was used. The impact load was applied in the middle of the beam under a force control and the displacement time history was then compared with the experimental results.

Similarly, for the force-based elements, the beam was divided into 12 elements to reach convergence. The same time step used with the displacement-based element is also implemented.

Figure (4.11) shows the midpoint displacement vs time response retrieved from the explicit and implicit displacement and force-based elements. All four elements produced similar results. Matching can be seen for both, the impact and the free vibration phases.

The displacement-based implicit element performed on average 4 global iterations in every step to reach convergence. While the force-based implicit element performed on average 2 internal iterations and 4 global iterations in every step to reach convergence.

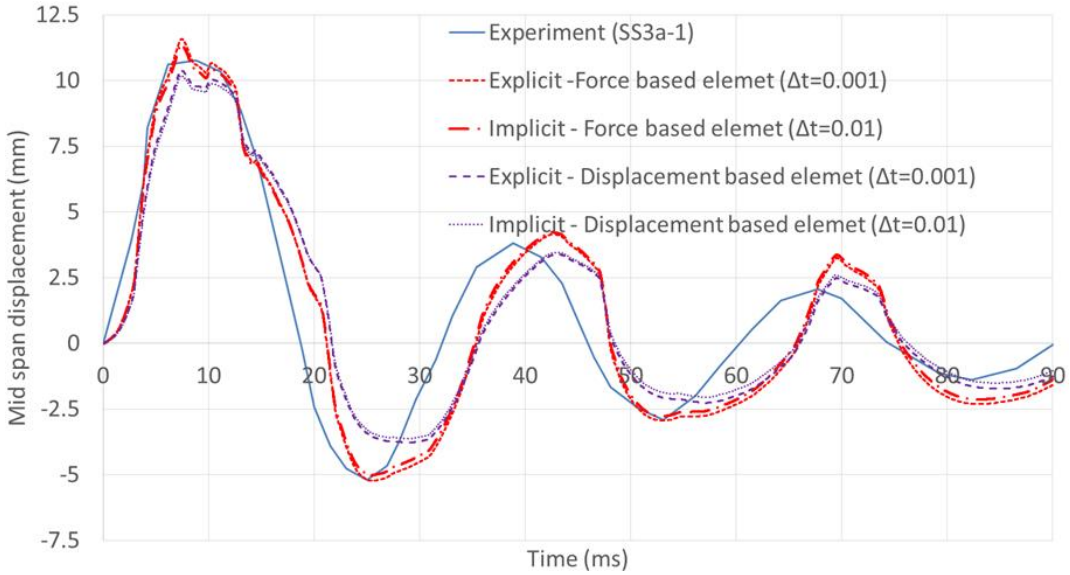

Figure 4.11: Midpoint displacement time history of sample SS3a-1.

For the fully explicit force-based element, the element was initially assigned a large time step of 0.01 and the behaviour of the element was monitored as follows: First, the element was facing stability problems from an early stage. For the solution for time steps between 0 and 0.04 sec, the largest $\sum_1^3 F_{unbalanced} \cdot \Delta q$ ranged between (1.30E-06 and 2.74E-05 N.mm) and element residual deformations R ranged between 0.3E-7 and 0.6E-5. For the largest value of $\sum_1^3 F_{unbalanced} \cdot \Delta q = 2.74E-05$, using Equation (4.46) and assuming a tolerance value of $1.00E-05$:

$\Delta t_{critical}{}^{new} = 0.01 \times \sqrt{\frac{1.00E-05}{2.74E-05}} = 0.00604\ sec$ (Which is the minimum $\Delta t_{critical}$ of the 12 elements). This new time step was used in the analysis to avoid internal element iterations.

For the rest of the time steps, $\sum_1^3 F_{unbalanced} \cdot \Delta q$ ranged between (-0.23E-05 and 0.10E-02 N.mm):

$\Delta t_{critical}{}^{new} = 0.01 \times \sqrt{\frac{1.00E-05}{0.10E-02}} = 0.001$ sec.

Using the new time step 0.001, the element did not perform any internal iterations and the element residual deformations R ranged between 0.10E-30 and 0.10E-10, satisfying convergence.

Table (4.2) shows the execution time each element used to solve the problem and the size of the main output file. From the table, it can be observed that because implicit elements use larger time step they require less execution time (about one fifth of that of explicit elements in this case), and smaller output files. However, the explicit force-based element requires a smaller execution time than the explicit displacement-based element mainly because a coarse mesh is adopted. The elimination of the iterations requires considerable longer execution time as the selected time step played the major role in determining the execution time.

Table 4.2. Comparison between execution time of the implicit and the explicit displacement and force-based elements for sample SS3a-1.

Element type	Displacement-based		Force-based	
	Implicit	Explicit	Implicit	Explicit
Time step	0.01	0.001	0.01	0.001
Elements mesh size	18	18	12	12
Execution time (mn:sec)	00:28.8	02:16.5	00:23.9	01:50.6
Main output file size (MB)	6.83	13.40	6.62	13.39

This experiment confirms the ability of the explicit elements in modelling the impact behavior of reinforced concrete beams while avoiding internal and external element iterations.

4.11.2 Fujikake et al. experiment

Fujikake et al. (2009) tested several reinforced concrete (RC) beams under impact loadings using a drop hammer impact test. Figure (4.12) shows the drop hammer impact test setup used in the experiment. The beams were designed to allow for an overall flexural failure. The authors also used an analytical model that consisted of a two-degree-of-freedom mass-spring-damper system to simulate the RC beams analytically. The system consisted of one degree of freedom to express the local impact response between the drop weight and the beam and another one to express the overall response of the beam. The analysis technique involved the determination of the moment-curvature relationship of the beam using section-by-section analysis procedure whereas the strain rate effects were considered. Then the

calculation of the load-midspan deflection relationship using the moment-curvature relationship was performed.

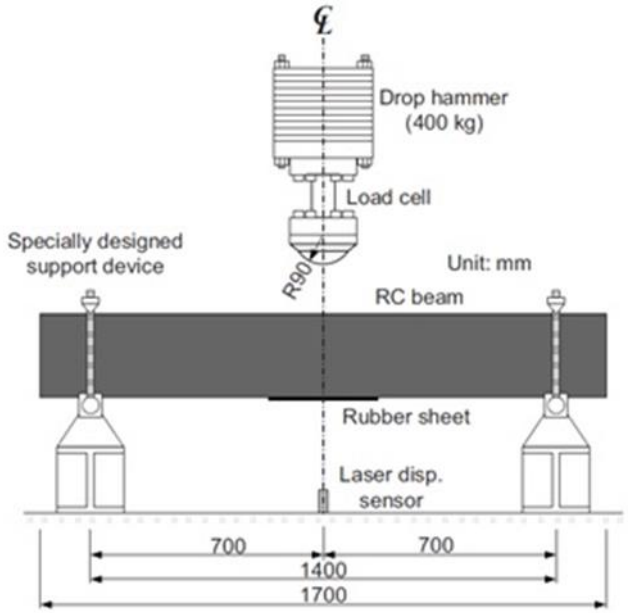

Figure 4.12: Drop hammer impact test setup, Figure from **Fujikake et al. (2009)**.

The two Specimens S1616-A and S1616-D were chosen to be modelled with the fibre beam elements. The RC beam specimens had a rectangular cross section of 250x150 mm and a total span length of 1400 mm. The beams were simply supported at their ends and were allowed to freely rotate while preventing them from moving out of plane. The beams were reinforced with 2Ø16 top and bottom bars with yield strengths of 426 MPa. The concrete compressive strength was 42 MPa.

The impact forces applied in the middle of the beams retrieved from the experiment are shown in Figure (4.13) for sample S1616-A and Figure (4.14) for sample S1616-D. Both the implicit and explicit fibre beam elements were used to simulate the behaviour of the two beams under the impact force. Due to symmetry, only half of the beams was modelled with a variable number of elements. The beam in this problem was assumed simply supported, which allowed free rotation at the

ends while preventing vertical displacements; and the symmetry in the middle was respected by allowing the vertical movement and preventing the horizontal movement and rotations. Consequently, no second order effect was expected in this case.

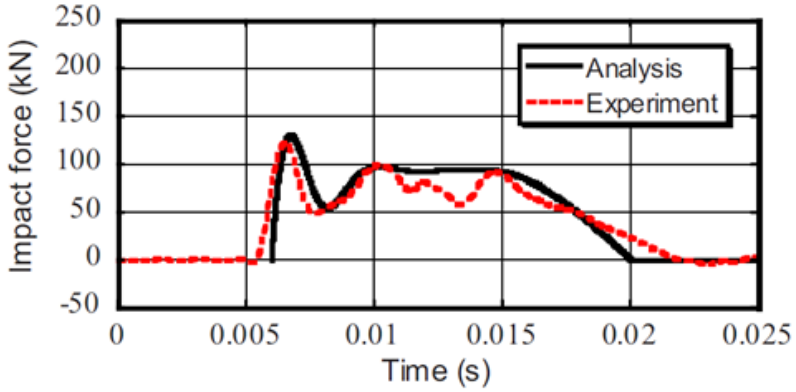

Figure 4.13: Impact load history for sample S1616-A, Figure from **Fujikake et al. (2009)**.

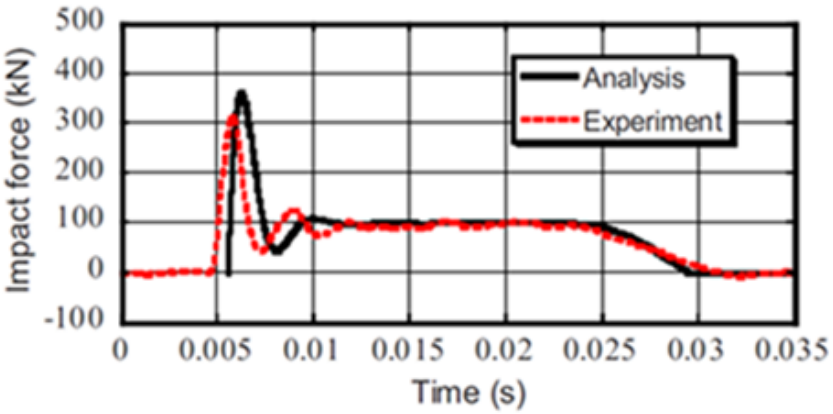

Figure 4.14: Impact load history for sample S1616-D, Figure from **Fujikake et al. (2009)**.

Each element was divided into five sections, and each section was further divided into 12 concrete fibres and 4 steel fibres that represented the top and bottom reinforcement (Figure 4.15), where five sections are typically adopted in fibre beam

models since this discretization can accurately represent the plastic hinge zone in reinforced concrete structures **(Spacone et al., 1996)**.

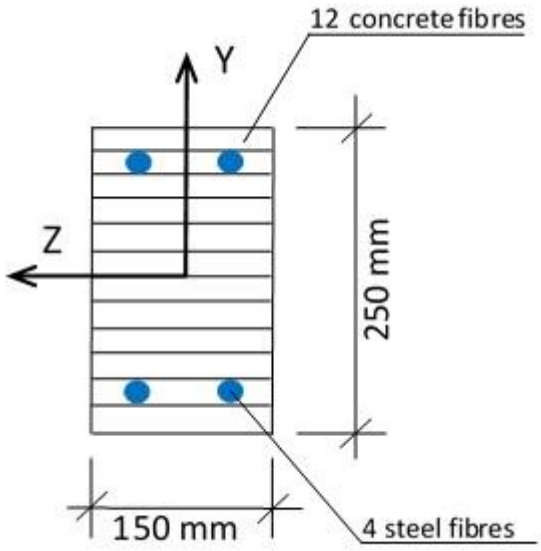

Figure 4.15: Fibre beam element cross section mesh for sample S1616-A and S1616-D.

In the experiment, the drop hammer used had a mass of 400 kg. It was dropped freely onto the top surface of the RC beam at the midspan from different heights. For specimen S1616-A, the drop height was the smallest with 0.15m, and for specimen S1616-D the drop height was the highest with 1.2m.

A laser displacement sensor was used to measure the midspan deflection of the beam and a dynamic load cell was utilized to measure the contact force between the hammer and the beam.

4.11.2.1 Specimen S1616-A

The impact force-time history was used as input for the two fibre beam elements and was retrieved from the experiment. In the implicit model, the step size was chosen as 0.001 sec and an excessive maximum of 20 iterations per step was allowed

(although usually 4 to 8 iterations are commonly sufficient). The total number of steps is 2500. In the explicit force-based model, the time step size was chosen as 0.00001 to satisfy Δt_{min} and $\Delta \mathrm{t}_{critical}$ based on a fully explicit element with no iteration and a required tolerance of 1.00E-06, thus 250000 steps was used.

For the proposed criteria of the force-based explicit model, the element was first assigned a large time step of 0.001, and the behaviour of the element was monitored below:

The element worked well at the initial stage between steps 0 and 0.544 sec, $\sum_1^3 F_{\ unbalanced} \cdot \Delta \mathrm{q}$ ranged between (0.12E-46 and 0.83E-30 N.mm) and the element residual deformations R ranged between 0.2E-14 and 0.7E-29.

Then from steps 0.544 to 1.23 sec, the largest $\sum_1^3 F_{\ unbalanced} \cdot \Delta \mathrm{q}$ ranged between (0.95E-05and 0.43E-10 N.mm) and element residual deformations R ranged between 0.29E-06 and 0.95E-11).

For the largest value of $\sum_1^3 F_{\ unbalanced} \cdot \Delta \mathrm{q} = 0.95\mathrm{E}-05$ and, using equation (4.46) with a tolerance value of 1.00E-06, $\Delta \mathrm{t}_{critical}{}^{new} = 0.001 \times \sqrt{\frac{1.00\mathrm{E}-06}{0.95\mathrm{E}-05}} = 0.00032\ sec$. This new time step ensured no element iterations were performed.

Later, between time steps 1.23 sec and the end of the analysis, $\sum_1^3 F_{\ unbalanced} \cdot \Delta \mathrm{q}$ ranged between (0.50E-02 and 0.44E-07 N.mm)

Thus $\Delta \mathrm{t}_{critical}{}^{new} = 0.001 \times \sqrt{\frac{1.00\mathrm{E}-06}{0.50\mathrm{E}-02}} = 0.000014$ sec

Using a new time step of 0.000014 sec, the element did not perform any internal iterations and R ranged between 0.10E-30 and 0.10E-16.

For the explicit displacement-based model, the time step size was chosen as 0.0001 to fulfil the Δt_{min} requirement. A diagonal lumped mass was adopted for the

explicit analysis. The material constitutive parameters used in the finite element model considering the strain rate effect were taken as follows:

$f'_{cd} = 52$ MPa, $\varepsilon'_{cd} = 0.009$, $f_{td} = 3$ MPa and $f_{syd} = 580.0$ MPa.

With only two elements, the two explicit models were able to follow the input load-time curve and to predict the displacement-time history accurately as shown in Figure (4.16). On the other hand, both implicit models, the displacement and force elements, suffered from severe convergence issues and resulted in an unstable behaviour and inaccurate displacement estimates (Figure 4.16). It is worth mentioning that both explicit elements converged with only two elements, as the impact load was small for this specimen. Figure (4.17) shows the bending moment distribution along the span of beam S1616-A at the maximum displacement using the explicit force-based element. Due to the assumption of the force-based formulation, the bending moment is linear within each element.

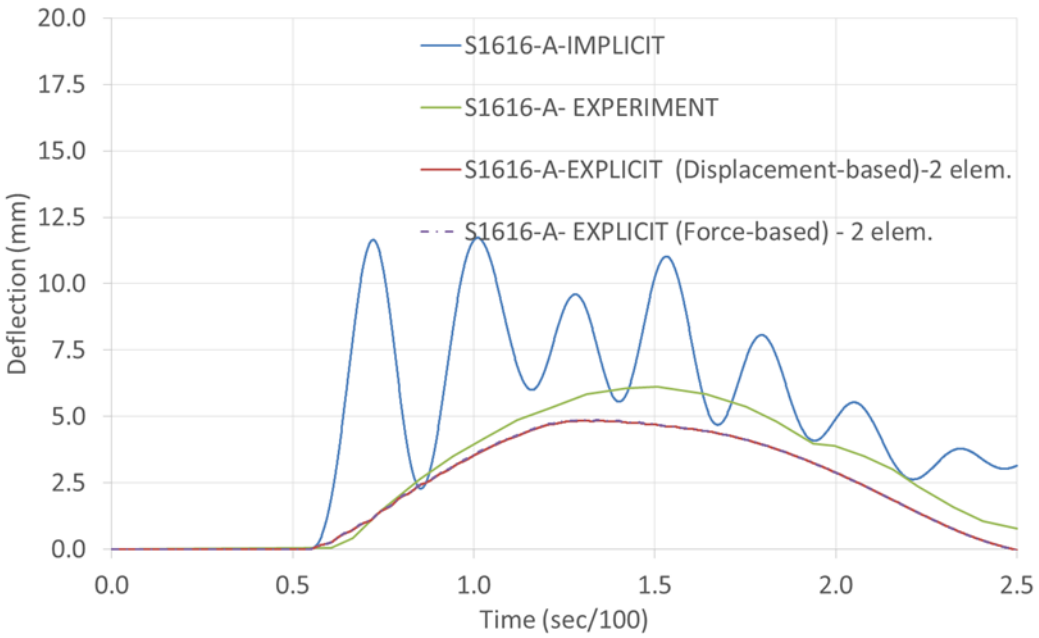

Figure 4.16: Deflection time history for specimen S1616-A.

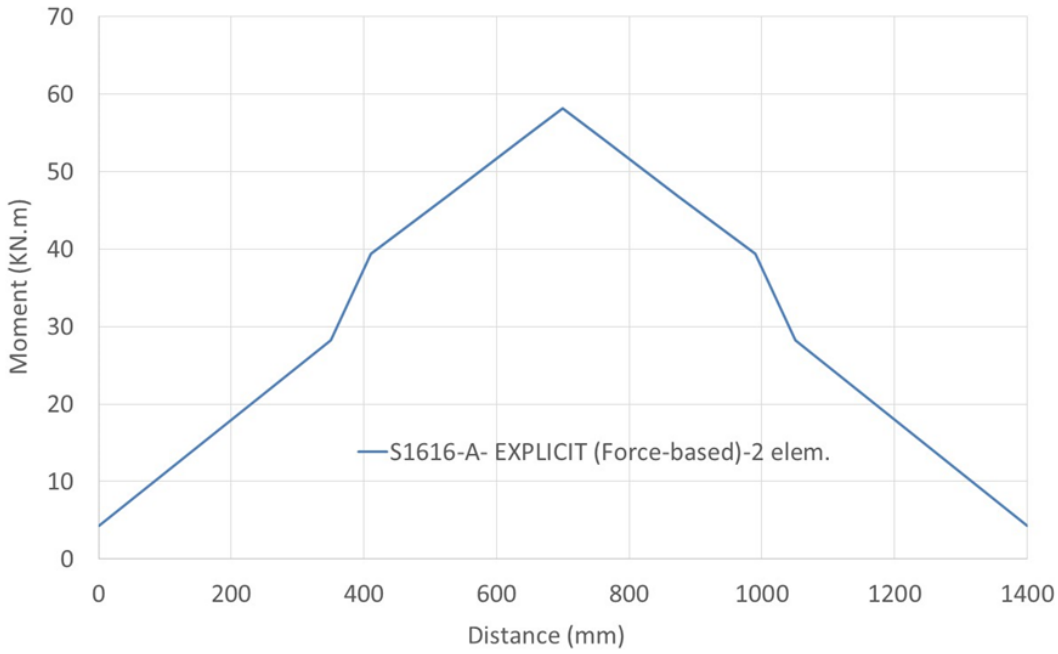

Figure 4.17: Bending moment at maximum displacement using the explicit force-based element (specimen S1616-A).

Further, the section behaviour was monitored using the moment curvature relationship for section 4 of element 2 and is displayed in Figure (4.18). The curve started by an increase in the bending moment proportional to an increase in the curvature value up to a moment of 58 kN.m then a reversed behaviour was detected and a decrease in the bending moment values escorted a decrease in the curvature. This behaviour can be explained from the deflection time history of the specimen. The first phase of the response happened due to an increase in the deflection value up to a time of 1.4 (sec/100) then the second phase occurred where the deflection value decreased until reaching zero. In addition, section 5 of element 2 behaved in the same manner as both sections are situated in the middle of the beam model.

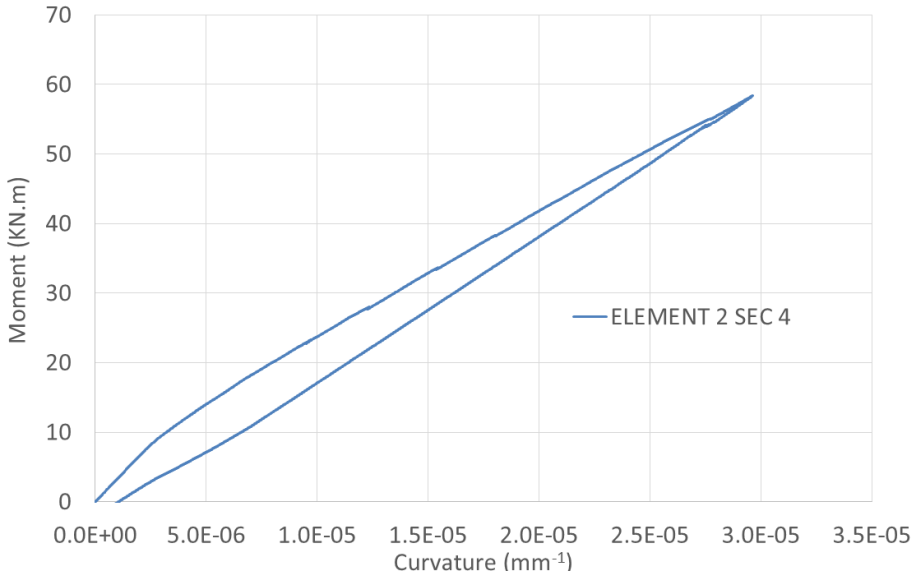

Figure 4.18: Moment curvature relationship for (element 2-section 4) using the mixed element.

Additionally, three different fibres were observed for specimen S1616-A. Figure (4.19) shows the location of the top concrete fibre (1), the bottom concrete fibre (2) and a bottom steel fibre (3). The stress strain curve of concrete fibre (1) for section 4 of element 2 is shown in Figure (4.20). The concrete fibre was under compression and behaved in an elastic manner until it reached a stress of 30 MPa at a strain of 0.0031 then the concrete loss its ductility and started an unloading failure.

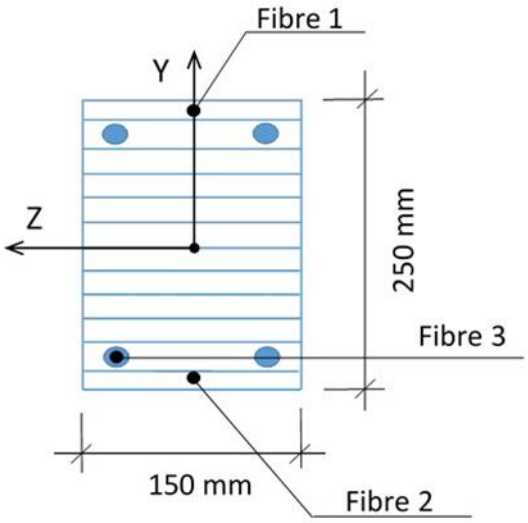

Figure 4.19: labelling of monitored fibres for Fujikake experiment.

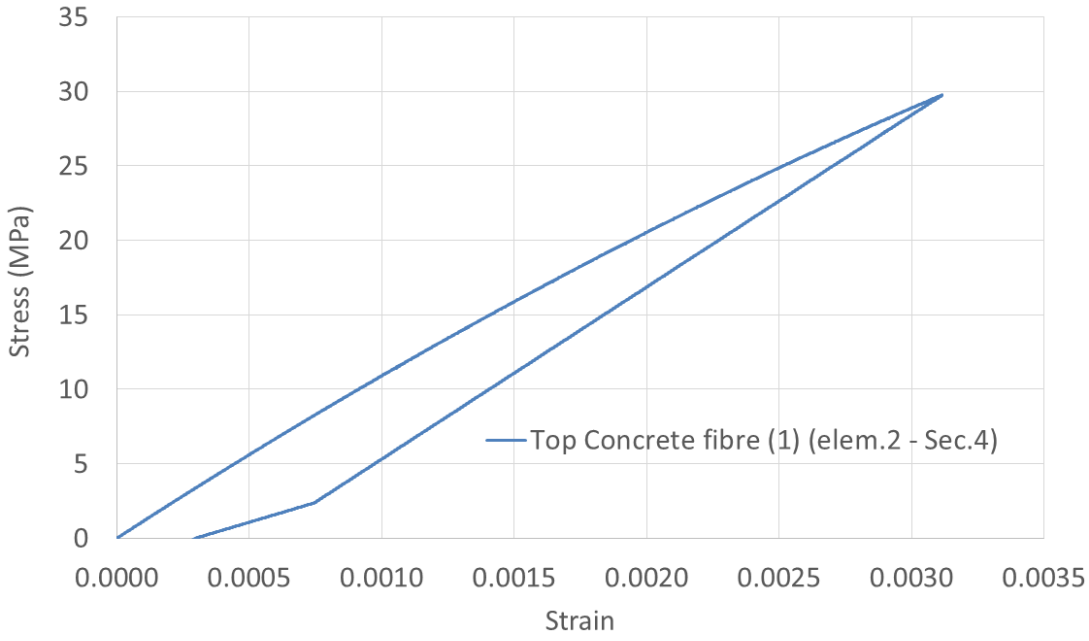

Figure 4.20: Stress strain curve for top concrete fibre (1) (element 2 at sec 4) using the mixed element.

For bottom concrete fibre (2) at section 4 of element 2, the stress strain curve is shown in Figure (4.21). The bottom concrete fibre was under pure tension and reached a stress of 3.0 MPa at a strain of 0.0025 then a clear linear ductile

performance was observed with a tension softening stiffness behaviour until a large strain value of 0.00325 was achieved.

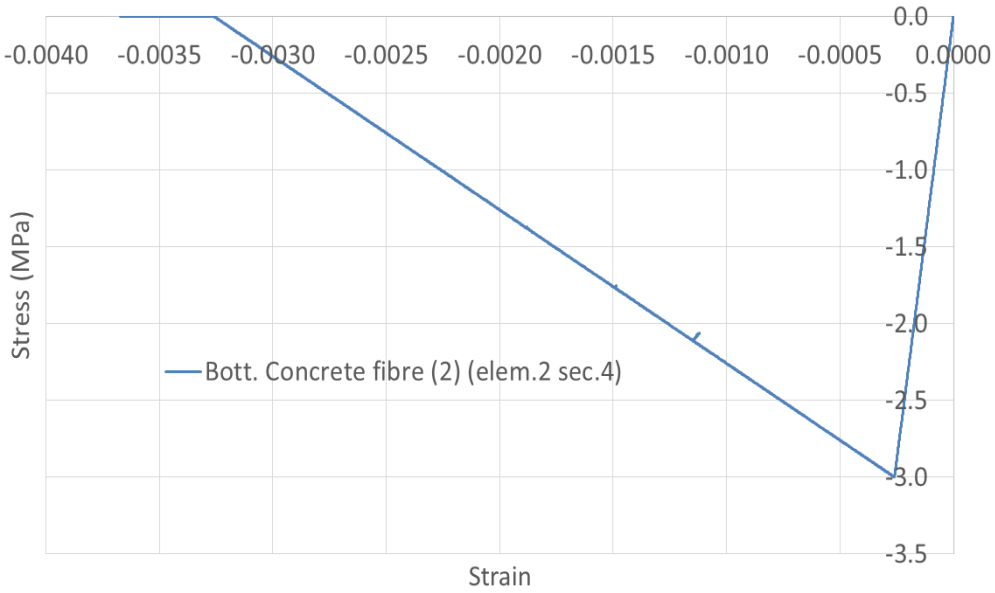

Figure 4.21: Stress strain curve for Bottom concrete fibre (2) (element 2 at sec 4) using the mixed element.

Finally, the steel fibre (3) at section 5 of element 2 is presented in Figure (4.22). A linear elastic behaviour was observed for fibre (3) and the maximum stress achieved was 580 MPa mainly due to the presence of the strain rate effect. The displayed Figures (4.20 to 4.22) allowed a detailed understanding of the fibre behaviour of each part of the modelled structure.

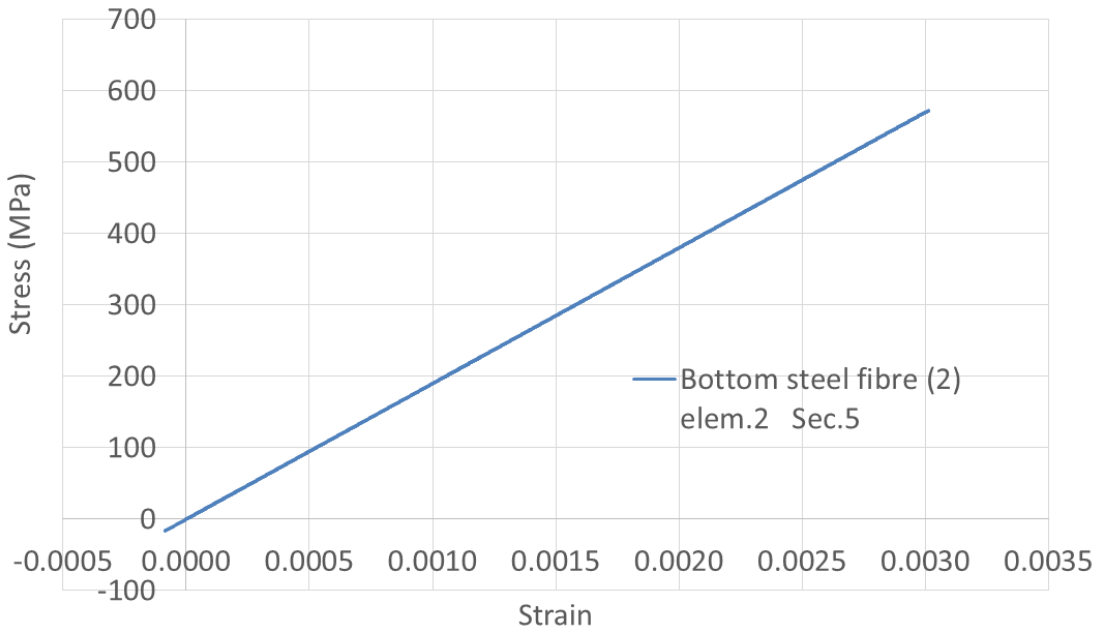

Figure 4.22: Stress strain curve for steel fibre (2) (element 2 at sec 5) using the mixed element.

The difference between the capabilities of the explicit and implicit elements is very clear in this problem. Although 10 iterations are routinely allowed, for this example, the implicit element was allowed to perform the double of the standard number of iterations. However, this did not help the element to converge. Meaning that, increasing the number of the global iterations for the implicit element will not yield better results. Consequently, this emphasises the superiority of the explicit time integration methods for short time duration impact problems.

It should be noted that the explicit force-based element requires a higher number of time steps in case no internal element iterations are allowed when compared with the mixed explicit implicit force-based element or the explicit displacement-based element.

4.11.2.2 Specimen S1616-D

For the implicit model, the step size was also chosen as 0.001 and the total number of steps was 3500. In the explicit force-based model, the time step size was initially chosen as 0.00001 based on a fully explicit element with no iteration at all and a tolerance of 1.00E-06, thus 350000 steps were used. For the explicit displacement-based model, the time step size was chosen the same as the one used to solve specimen S1616-A. A diagonal lumped mass was created for the explicit element.

For the material parameters, the values considering the strain rate effect were taken as follows:

$f'_{cd} = 44.0$ MPa, $\varepsilon'_{cd} = 0.0950$, $f_{td} = 1.0$ MPa and $f_{syd} = 430.0$ MPa.

In Figure (4.23), only the two explicit models were able to predict the behaviour of the impact problem with four elements for the force-based and eight elements for the displacement-based approach. Both of the implicit models, the displacement and force-based elements, failed to follow the input path and produced exaggerated deflection values. The two explicit fibre beam elements overcome the complexity of the analysis method used by **Fujikake et al. (2009)**. Further, the force-based explicit element produced better results than the displacement-based explicit element as it requires less number of elements to reach convergence (Figure 4.23).

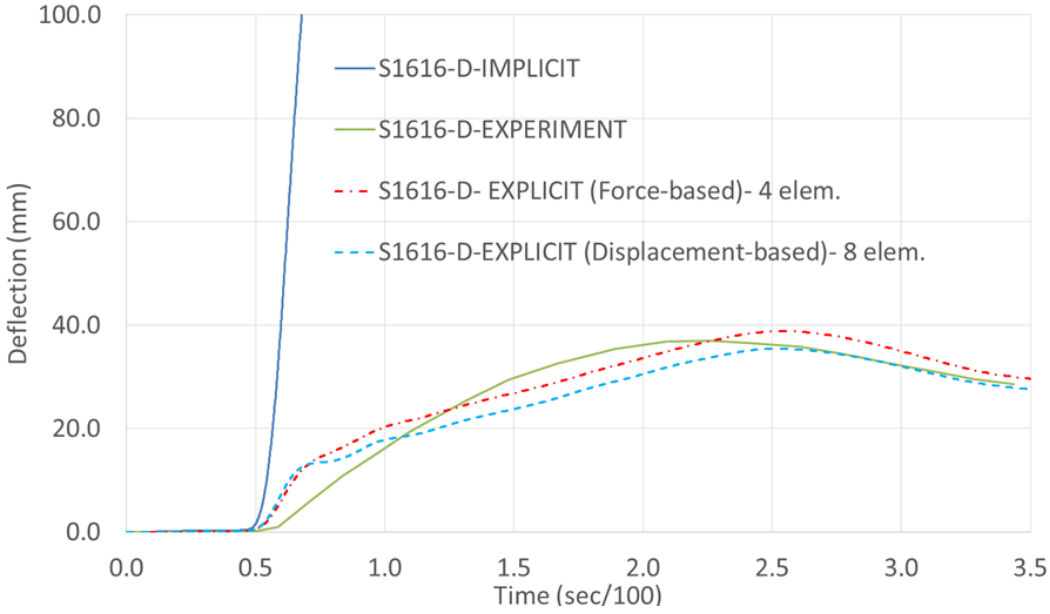

Figure 4.23: Deflection time history for specimen S1616-D.

Figure (4.24) shows the bending moment along the span of beam S1616-D at the maximum displacement using the explicit force-based element. It also confirms the linear distribution of the moment function.

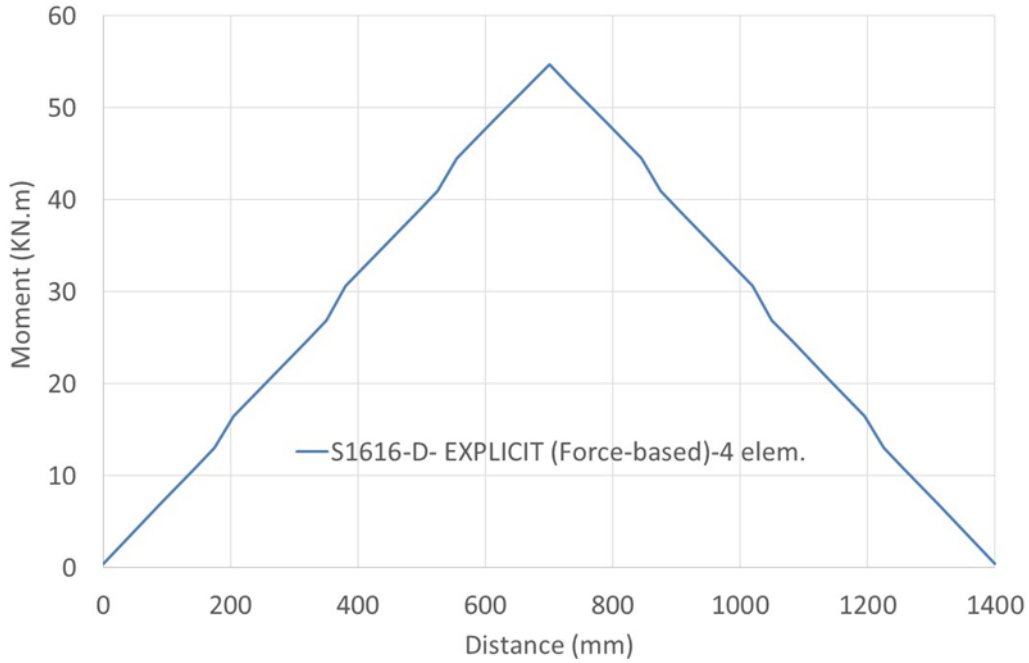

Figure 4.24: Bending moment at maximum displacement using the explicit force-based element (specimen S1616-D).

In a further attempt to study the new explicit force-based element, the bending moment output of the 1, 2 and 4 elements are compared with each other's. It is clear from Figure (4.25) that only 2 elements were sufficient to reach convergence because in the force-based formulation the relation of curvature is linear.

Whereas in Figure (4.26), a comparison between the load-displacement curves for the 1, 2, 4 and 6 elements is shown. It can be seen that the 2 elements model produced an output curve slightly away from experimental results, while when comparing the 4 and 6 elements, convergence was noticeable.

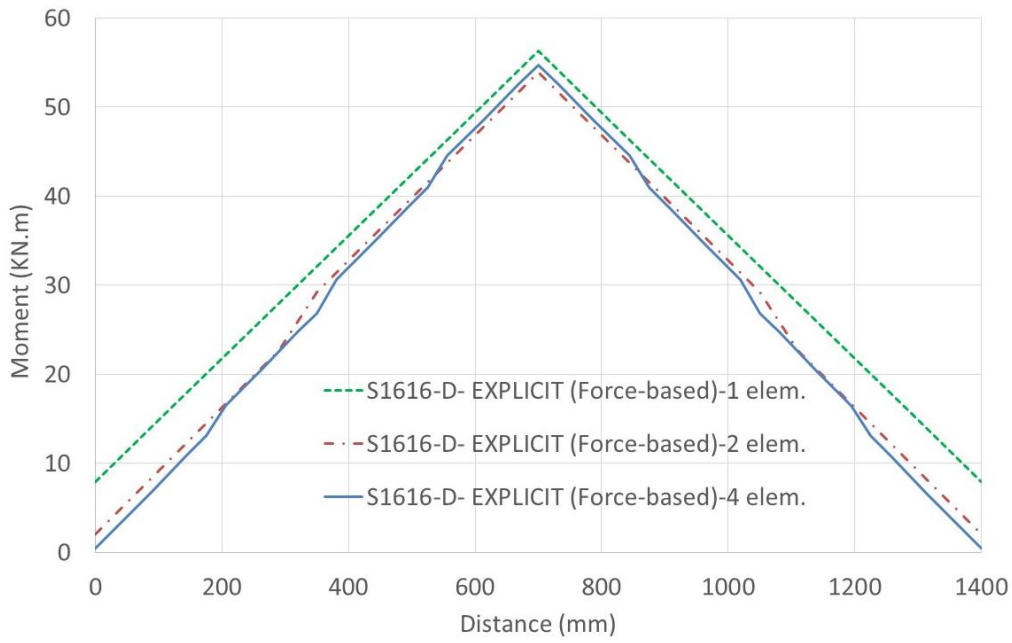

Figure 4.25: Comparison between the Bending moments at maximum displacement using the explicit force-based element (specimen S1616-D) for 1, 2 and 4 elements.

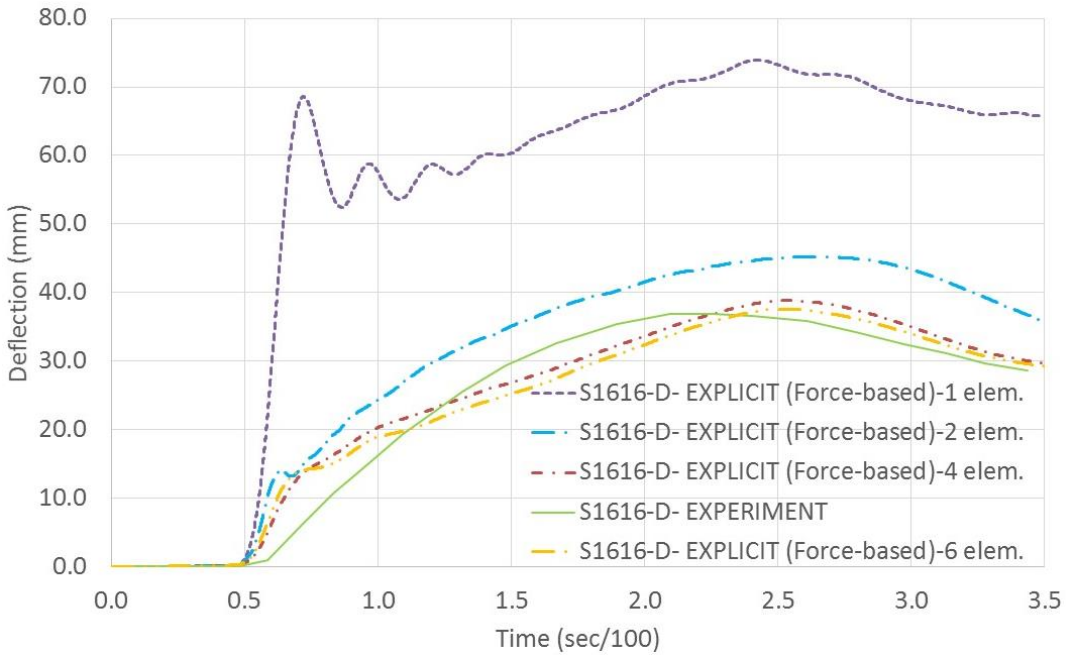

Figure 4.26: Comparison between deflection time history for specimen S1616-D using the explicit force-based element (specimen S1616-D) for 1, 2, 4 and 6 elements.

It can also be established from Figures (4.25) and (4.26) that the load displacement curves are more sensitive to element mesh division than the calculation of the bending moment.

Next, the section and fibre behaviour of specimen S1616-D is studied. In Figure (4.27), the moment curvature relationship for section 5 of element 4 is shown. The moment curvature relationship can be divided into three phases. In the first phase, the relation is linear and happens in a small strain range. The second phase is nonlinear and occurs in a large strain range; and is followed by the third and last phase were failure is happening. It can be spotted that a numerical error occurred at strain values 0.0003 with a sudden drop and rise in the value of moment. However, this numerical error did not affect the stability of the solution and the element was able to converge until the end.

The same three fibres shown previously in Figure (4.19) are monitored. Different behaviour is observed for sample S1616-D than the one retrieved from sample S1616-A. In Figure (4.28), the stress strain curve of concrete fibre (1) for section 5 of element 4 is presented. The concrete fibre is under compression and behaves in an elastic manner until it reaches a stress of 30 MPa at a strain of 0.0431 then the concrete starts an unloading path characterised by the decrease of loads and displacements until failure. The proposed element was able to capture this behaviour, which is similar to near-fault ground motions. For the bottom concrete fibre (2) of section 3 of element 4, the stress-strain curve is shown in Figure (4.29). The bottom concrete fibre is under pure tension and reaches a stress of only 1.0 MPa at a strain of 0.001 then a clear linear ductile behaviour is observed with tension softening stiffness until a large strain value of 0.0022 is achieved.

Finally, the steel fibre (3) for section 5 of element 4 is presented in Figure (4.30). A linear elastic behaviour is observed for fibre (3) and the maximum stress achieved due to the presence of strain rate effect is only 420 MPa but followed by a clear ductile behaviour with strain hardening until a stress of 510 MPa is attained at a large strain value of 0.043.

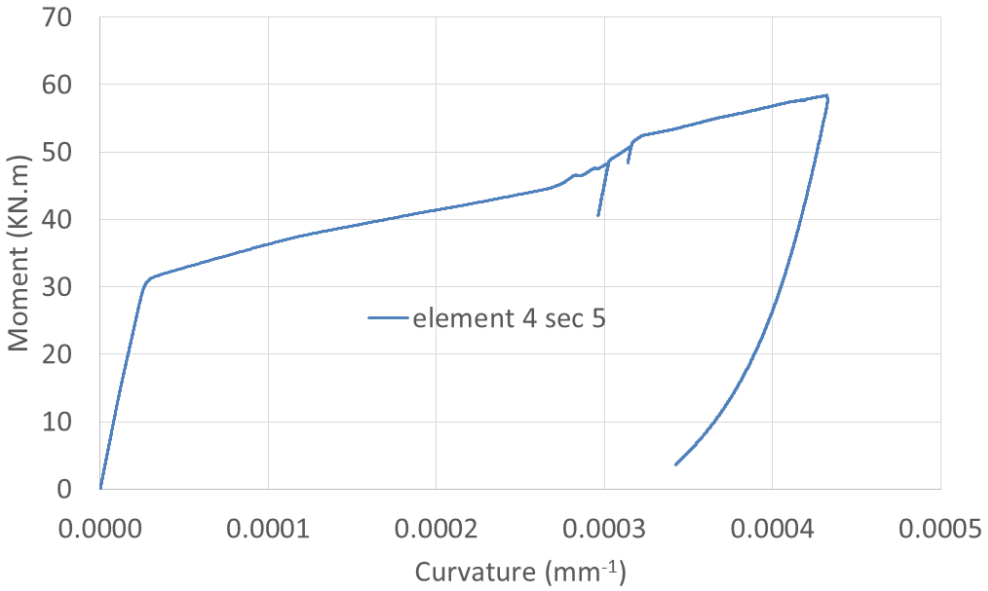

Figure 4.27: Moment curvature relationship for (element 4-section 5) using the mixed element.

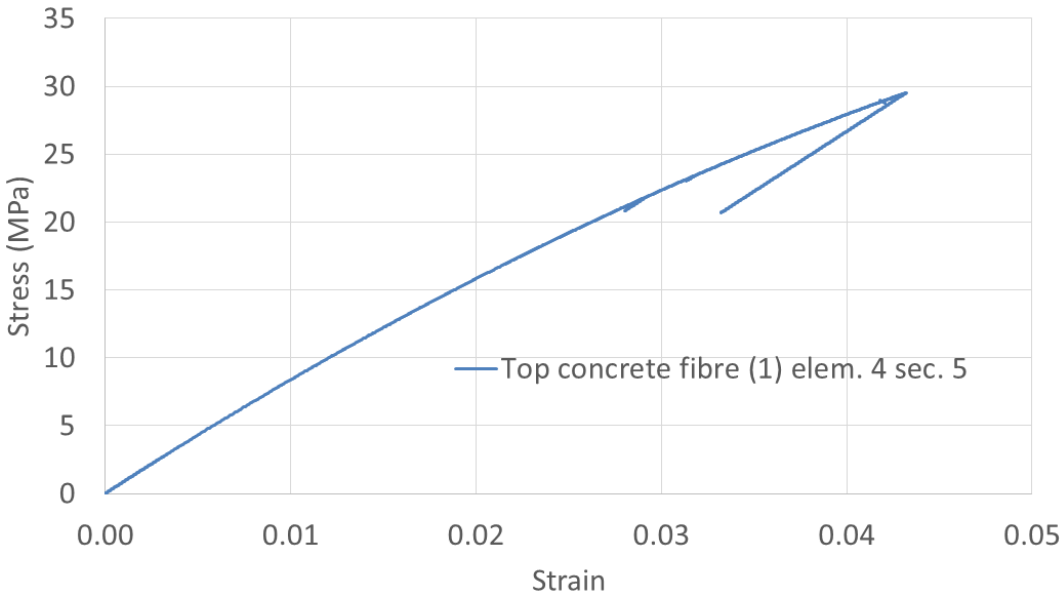

Figure 4.28: Stress strain curve for top concrete fibre (1) (element 4 at sec 5) using the mixed element.

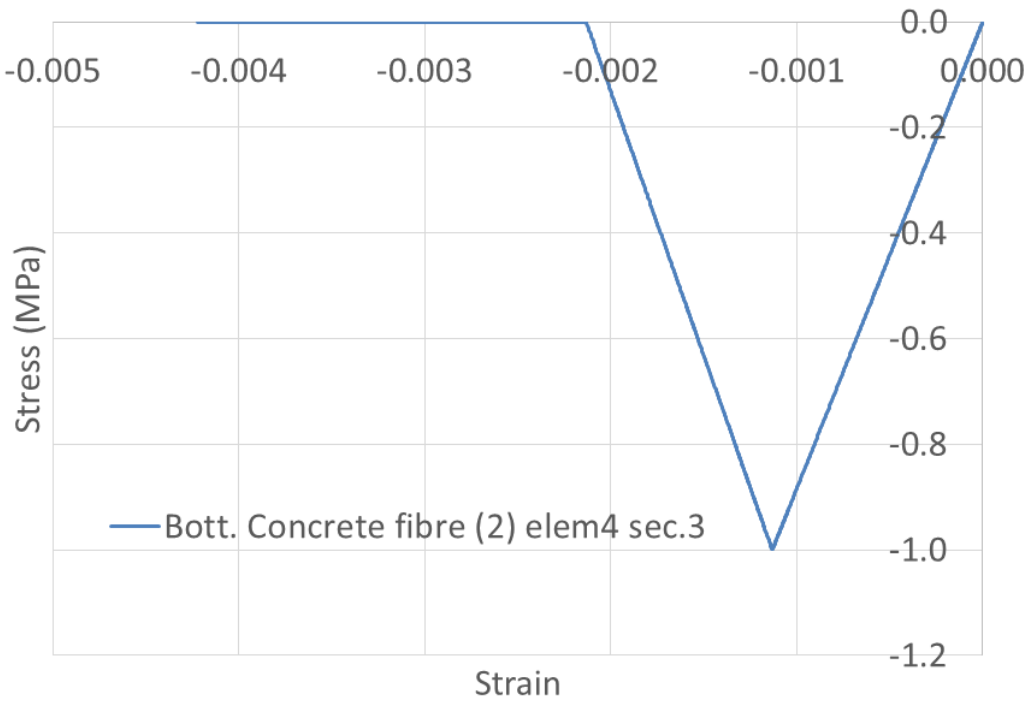

Figure 4.29: Stress strain curve for Bottom concrete fibre (2) (element 4 at sec 3) using the mixed element.

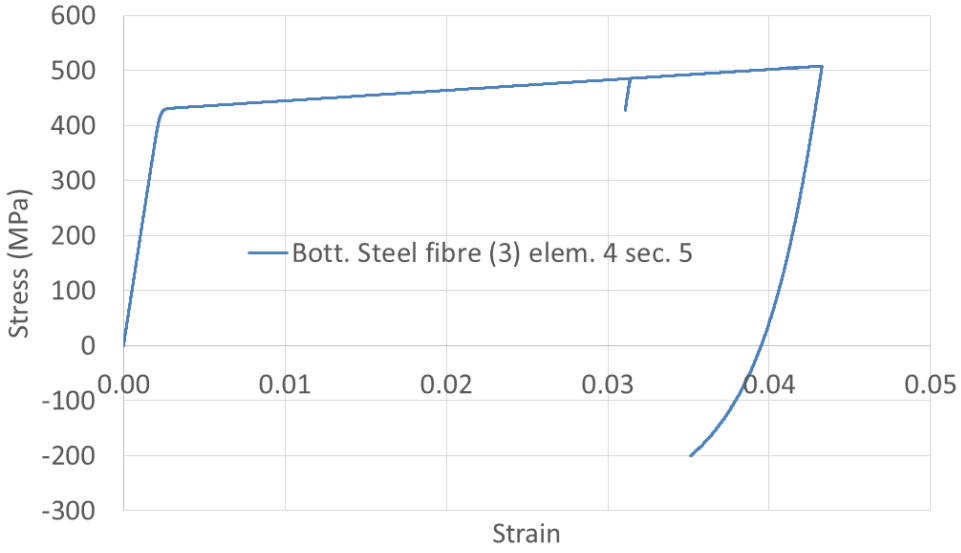

Figure 4.30: Stress strain curve for steel fibre (3) (element 4 at sec 5) using the mixed element.

The ability of the implicit element to solve short-term dynamic problems is limited and can be linked to several factors including the impact force intensity, the load input path complication, the duration of the load and the nonlinear material behaviour. On the other hand, the use of explicit techniques with the fibre beam element is an advanced method to solve highly nonlinear dynamic problems without the need for iterations and convergence complications. The elements benefit from their simplicity, which makes them competitive with complex continuum elements available in commercial finite element software.

4.11.3 Sohel and Liew experiment

The test conducted by **Sohel and Liew (2014)** is used to verify the ability of the explicit fibre beam element to model an SC panel system. In the experiment, eight SC sandwich slabs measuring 1200 × 1200 mm^2 were tested under impact loading (Figure 4.31). The SC panels were simply supported with a span of 1000mm. The drop height was chosen as 3m while the projectile mass was about 1246 kg. Panel SLFCS6-80 had a steel plate thickness of 5.96 mm, a Lightweight concrete core with 1% fibre of 80 mm thickness. The concrete density was equal to 1445 kg/m^3, the cylinder strength of the concrete was 28.5 MPa, the elastic modulus of concrete was 14.0 GPa and the yield strength of steel plate was 315.0 MPa. The low velocity impact of the large mass produced mainly local punching for the tested SC panels.

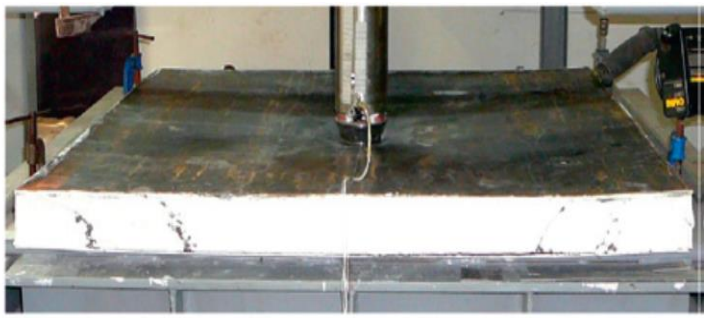

Figure 4.31: Sample SLFCS6-80 under impact loading with cracking but no spalling behaviour, Figure from **Sohel and Liew (2014)**.

Panel SLFCS6-80 was chosen to be simulated using the explicit displacement and force-based fibre beam elements. The 1% fibre in the concrete mix was considered in the model using a high tensile strength value of 9.0 MPa and a constant zero slope tension softening stiffness.

For the explicit displacement-based element, only half of the panel was modelled first using one element then using four elements. Every element was divided into five sections. Each section was further divided into 12 concrete fibres and 2 steel fibres that represent the top and bottom steel plates (Figure 4.32). The impact forces, retrieved from the experiment, are shown in Figure (4.33). The impact forces were applied in the middle of the panel using a force control method.

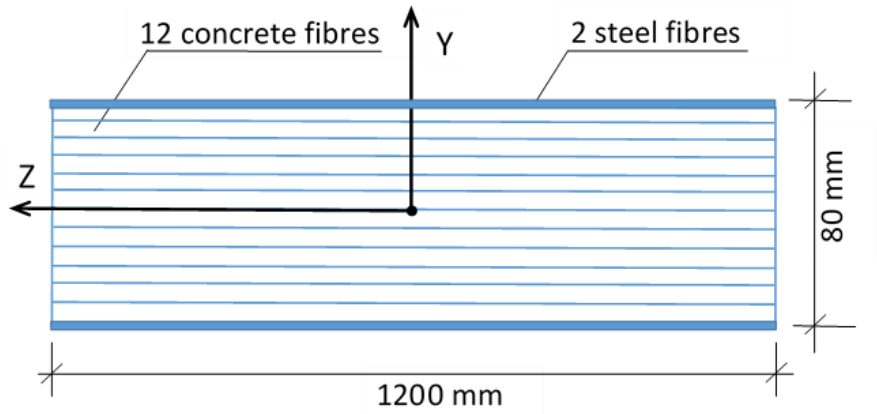

Figure 4.32: Fibre beam element cross section mesh for sample SLFCS6-80.

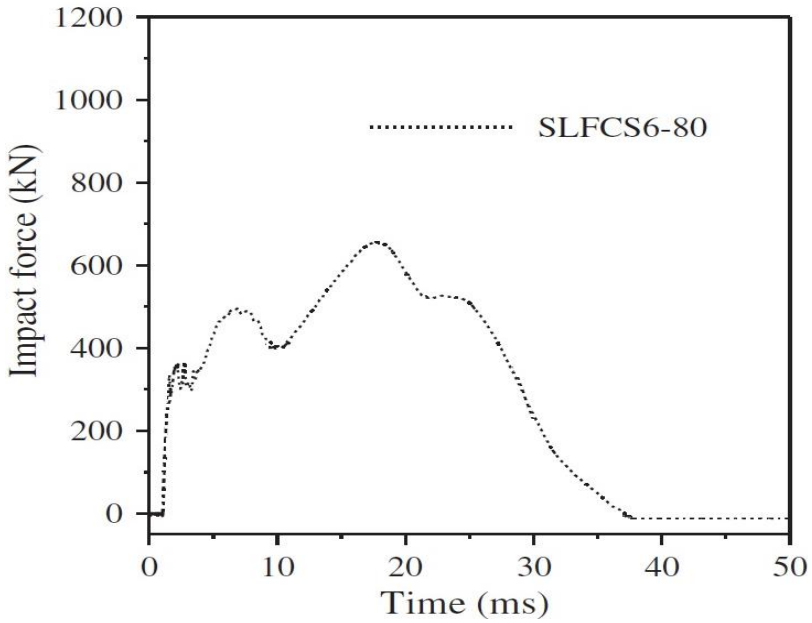

Figure 4.33: Impact load history for sample SLFCS6-80, Figure from **Sohel and Liew (2014)**.

Several time steps were studied, the largest time step was 0.01 sec and the smallest one was 0.00001 sec. From Figures (4.34 & 4.35), It was found that the solution became stable only when a small enough time increment was used. For instance, when the panel was modelled with one element division, the stable time

step was 0.0001 sec while when the panel was divided into four element divisions only a time step of 0.001 sec was sufficient to reach full convergence. For both element divisions, the time step 0.01 sec did not satisfy Δt_{min} and the output was numerically unstable. This complies with the displacement-based elements' necessity to adopt fine meshing, and confirms the effect of the length of the element on the stable time increment.

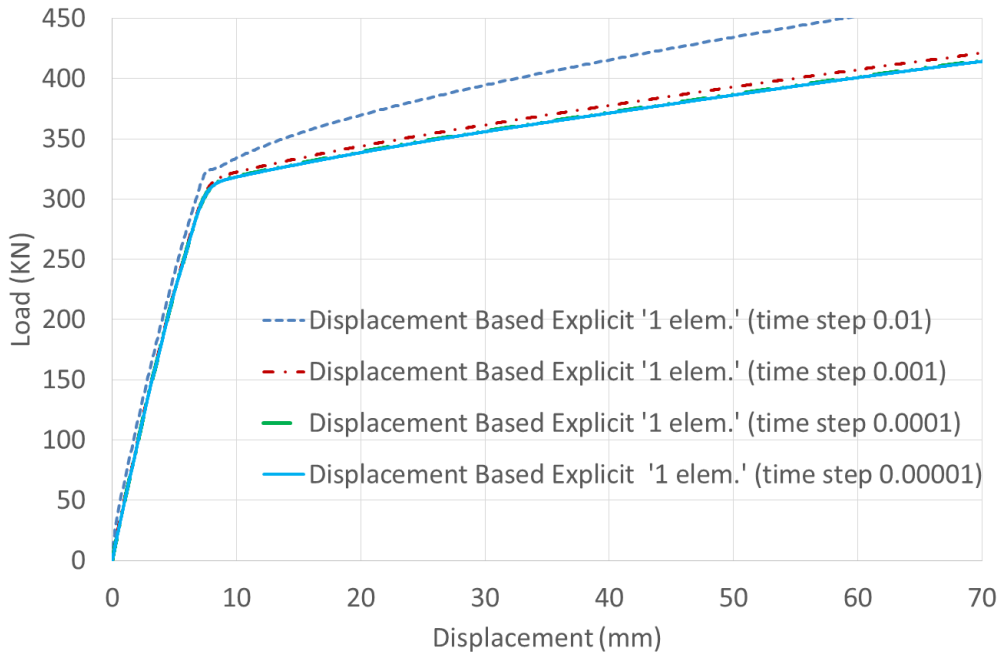

Figure 4.34: Load-Deflection Comparison of the displacement-based Explicit Fibre Beam Element for SC panel SLFCS6-80 using different time step values and one element division.

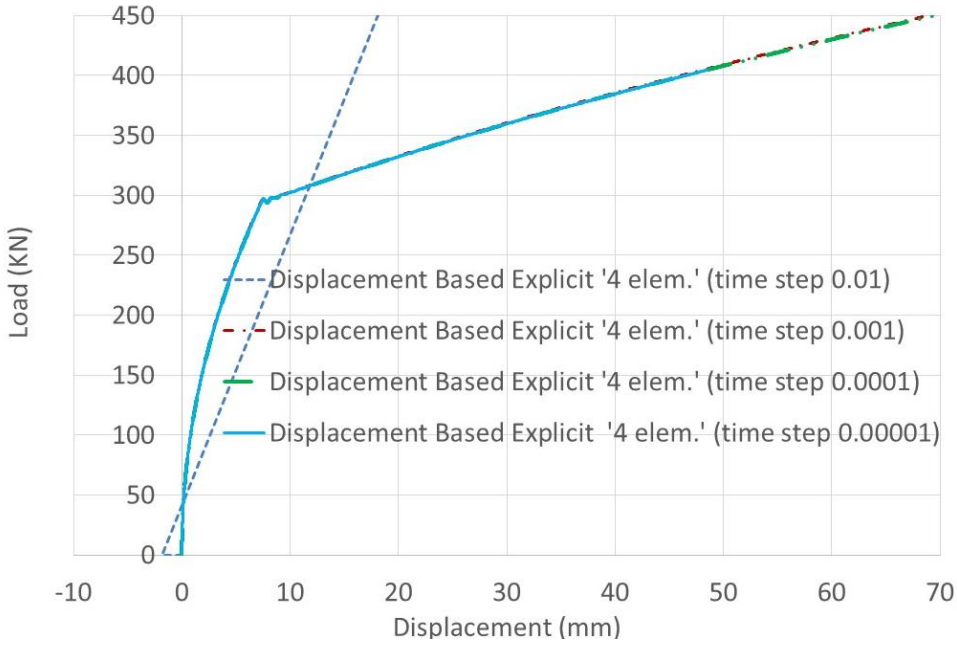

Figure 4.35: Load-Deflection Comparison of the displacement-based Explicit Fibre Beam Element for SC panel SLFCS6-80 using different time step values and four-element division.

In Figure (4.36), the two stable displacement-based solutions with one and four elements divisions are compared with the experimental results. Both solutions agreed with the experimental load displacement path except when the model failed to capture the valley in the experimental curve. This could be attributed to the strain hardening of the steel subsequent to the concrete strength degradation.

In conclusion, the more the number of element divisions increases, a larger step size can be accepted.

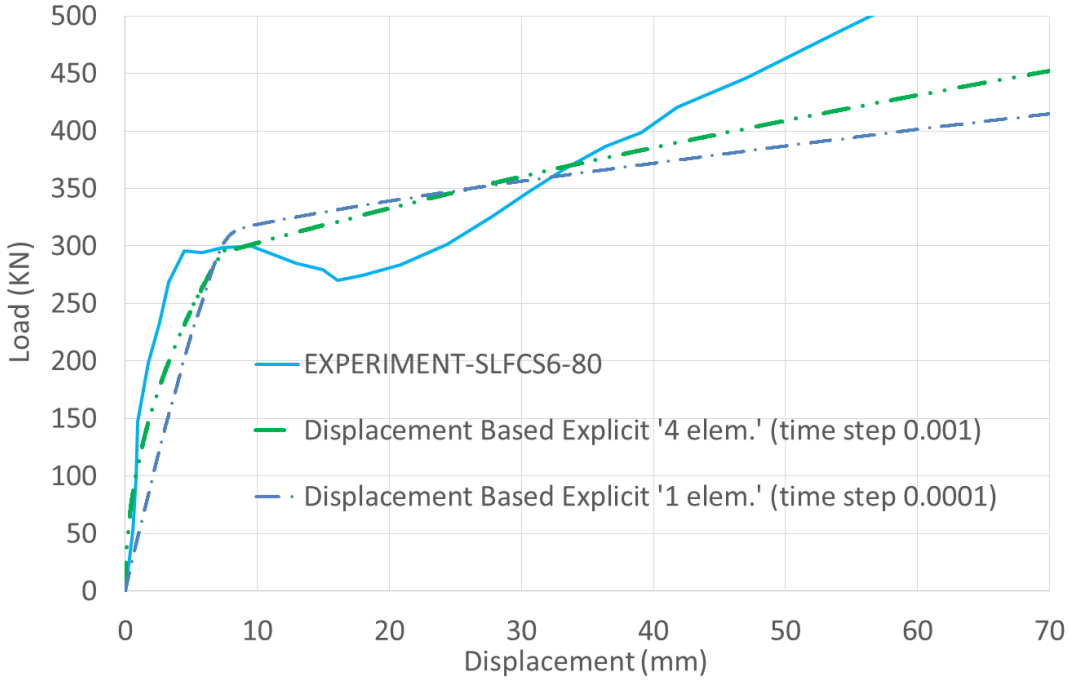

Figure 4.36: Load-Deflection Comparison of the force-based Explicit Fibre Beam Element for SC panel SLFCS6-80 using different time step values.

For the explicit force-based element, also half of the panel was modelled using one and four elements. Figure (4.37) shows a comparison between using the two different element divisions for the explicit force-based element with a time step of 0.001 sec. It is clear that both results match each other.

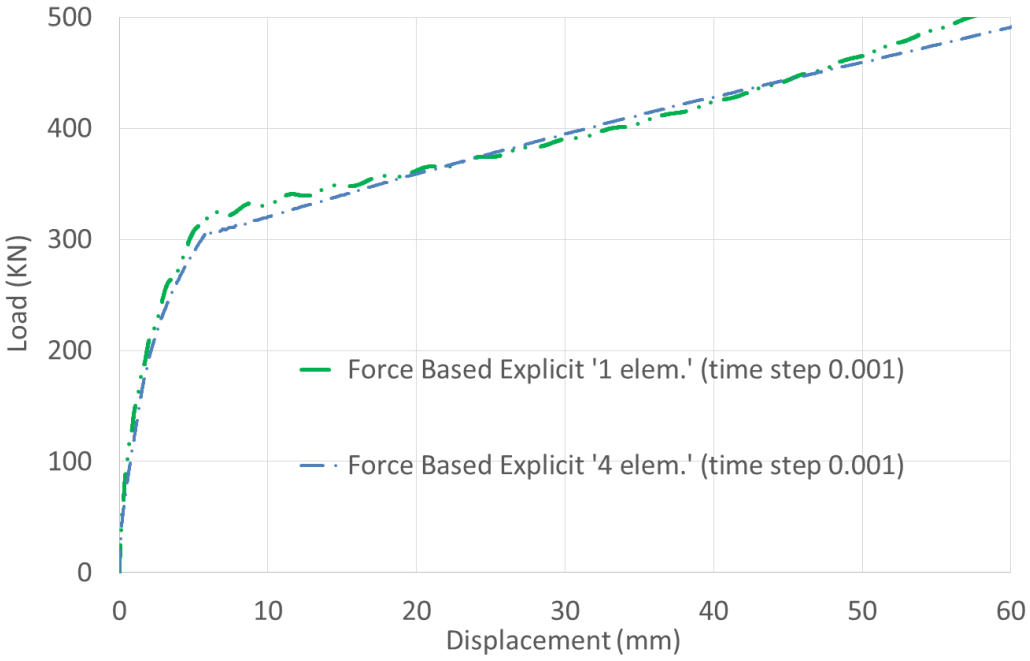

Figure 4.37: Load-Deflection Comparison between the one and four elements division of the explicit force-based elements for SC panel SLFCS6-80.

Finally, in Figure (4.38), the explicit force-based elements together with the explicit displacement-based element are compared with the experimental results. The four element divisions were used for this comparison although one element was sufficient to reach adequate results especially for the force-based elements. For the area under the load displacement curve, the difference between the experimental results and the displacement-based fibre beam model was 2%, while the difference increased for the force-based fibre beam model to 8.2%. However, it is clear that the explicit force-based element better simulated the post peak behaviour. Care should be taken when using explicit beam elements to ensure the numerical stability of the solution.

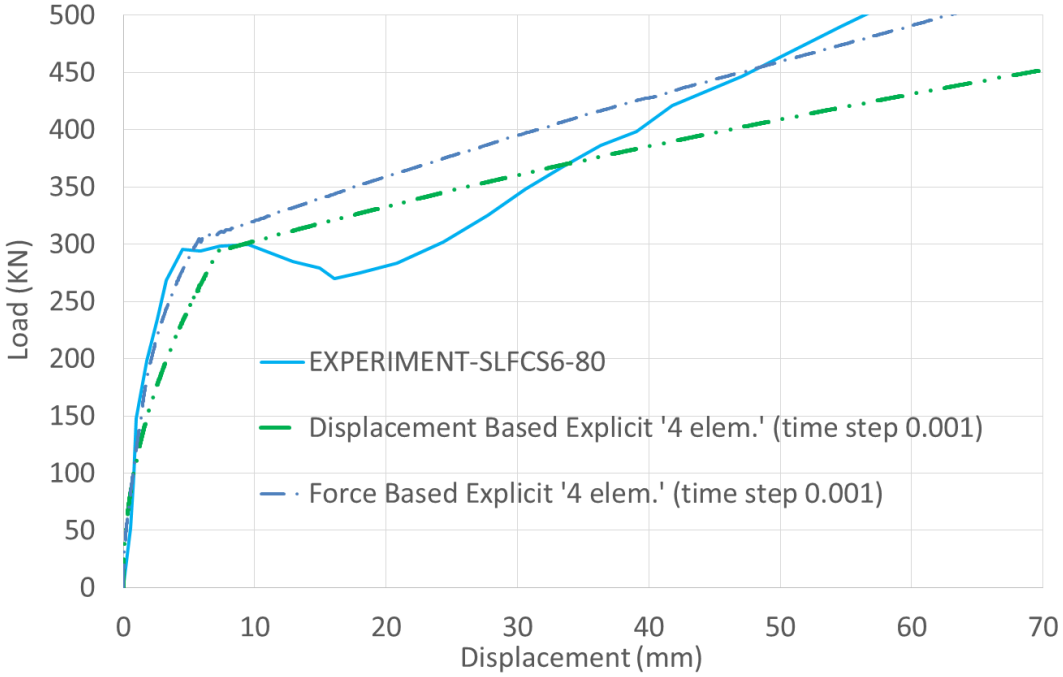

Figure 4.38: Load-Deflection Comparison between the experiment results and the displacement and force-based elements for SC panel SLFCS6-80.

This experiment confirms the ability of the explicit elements in modelling the impact behavior of steel concrete panels while avoiding internal and external element iterations. The experiment also confirms the ability of the force-based explicit element in modelling such problems with the minimum possible number of elements while preserving numerical stability and accuracy.

4.12 Conclusion

In this chapter, two-plane fibre beam elements were presented that adopt an explicit time integration scheme to solve short-term dynamic problems, particularly impact problems where a high force is applied over a very short duration of time. The elements use a displacement-based and a force-based formulation respectively, and benefit from advanced material constitutive models that can simulate the nonlinear behaviour of concrete and steel materials.

The developed elements overcome the difficulties and complications that are associated with the implicit time integration method, such as the need to iterate in every time step and the convergence requirements. Yet, the explicit element necessitates the use of a diagonal lumped mass matrix and the chosen time increment has to be smaller than the stable time increment required to maintain the stability of the numerical solution. Additionally for the fully explicit force-based element, a single iteration can be used if a critical time step is respected. The developed explicit fibre beam-column models, particularly the force-based element, represent a simple yet powerful tool for analysis of complex impact problems efficiently while using a limited number of finite elements. Both elements can be used reliably to analyse different reinforced concrete structures to ensure their safety against impact loading.

In the next chapter, different RC and SC panels will be modelled with the developed elements using different techniques including grillage modelling under static and impact loading.

Chapter 5

GRILLAGE ANALYSIS AND ELEMENTS APPLICATIONS

5.1 Introduction

Many researchers have contributed to the development of different fibre beam elements. The elements until present were effectively utilized in modelling simple structures such as columns and beams. However, the fibre beam elements can be used to model large-scale walls and slabs using grillage-modelling techniques. The approach offers a wider area of application for beam elements and reduces the cost of static and impact analysis when compared to continuum models such as membrane and solid models. With this approach, efficient statistical studies on large complex RC systems under hazard loads would be computationally possible. In this chapter, the fibre beam element will be employed to model different experiments using the grillage technique. The slabs or walls will be simulated as a series of beam elements connected and restrained at their joints.

In grillage modelling, the slab or wall is divided into a network of longitudinal and transversal grid lines in one-dimensional plane. Each grid is assigned a beam and given the properties of the part of the slab it represents. The beams are connected together at their nodes. The transversal beams are mainly used to link the longitudinal beams together and help in the accurate distribution of the load. Therefore, the longitudinal and transversal members represent the stiffness of the slab, in both directions. Extra grid lines might be required in order to improve the accuracy of the results as it is always recommended to adopt fine meshes in grillage modelling (usually a spacing ratio limit of 2:1 has to be respected). Care should be

taken not to double the own weight of the structure as it has to be assigned only in one direction.

Such modelling practice is common especially in bridge deck analysis and shear walls. According to **Booth (2008)**, the simplification of a plate structure into an equivalent beam element is generally acceptable and the approximation in the resulting midpoint displacement can be satisfactory. For instance, **Hambly and Feng (1991)** presented several techniques and recommendations for modelling bridge slab decks using beam elements. **O'Brien and Keogh (1999)** emphasized the reliability of modelling a slab by a network of beam elements stating that the method is inexpensive and easy to use. Similarly, **Kubin et al. (2008)** modelled shear walls using a grillage of beam elements. By the same technique, **Youssef et al. (2014)** used grillage analysis to calculate the nonlinear lateral behaviour of flat plate buildings. They reported that using shell elements to predict the seismic behaviour of such structure is cumbersome due to material and geometric nonlinearities. **Hajializadeh et al. (2015)** also utilized beam elements to analyse linear and nonlinear isotropic slab bridges under extreme traffic loading.

O'Brien and Keogh (1999) provided some important recommendations that can be used as a guide for grillage analysis. The recommendations included the following major points:

1- Longitudinal members should be provided along lines of strength in the slab (such as concentration of reinforcement, tendons or existing beams).
2- Nodes should coincide with the location of supports.
3- Transverse beams should have similar spacing of longitudinal beams.

Furthermore, **Kappos et al. (2012)** discussed the idealization of bridge decks using longitudinal and traversal elements. The author provided detailed guidance for the calculation of members' properties for different types of bridges including girder and slab deck sections. The provided equations were valid for the usual square configuration of grillages.

5.2 Grillage modelling using fibre beam elements

In the next sections, the fibre beam elements are used to create a network of beams (grillage) to simulate three different experiments available from the literature to establish the ability of the fibre beam element in general to implement such procedure in modelling large-scale walls and slabs. The technique is validated against experimental work to display its feasibility and practicality. Initially, two large-scale walls will be used in the validation, where in-plane loadings are applied to the tested walls. Later, the formulation of the fibre beam elements will be modified, using a simple innovative technique, in order to allow for out-of-plane loading. The emerging technique can be considered a 3D model, as two dimensions define the geometry while the load acts on the third perpendicular dimension.

5.2.1 Hube experiment

Hube et al. (2014) tested six half-scale reinforced concrete structural walls. The walls were subjected to a quasi-static cyclic lateral in-plane displacement load accompanied by a constant axial load to simulate earthquakes effect. The walls were fixed at the base and their top part was allowed to freely rotate and horizontally

move. Figure (5.1) shows the test setup of the experiment. A flexural failure mode was observed for the tested specimens due to their relatively large aspect ratio.

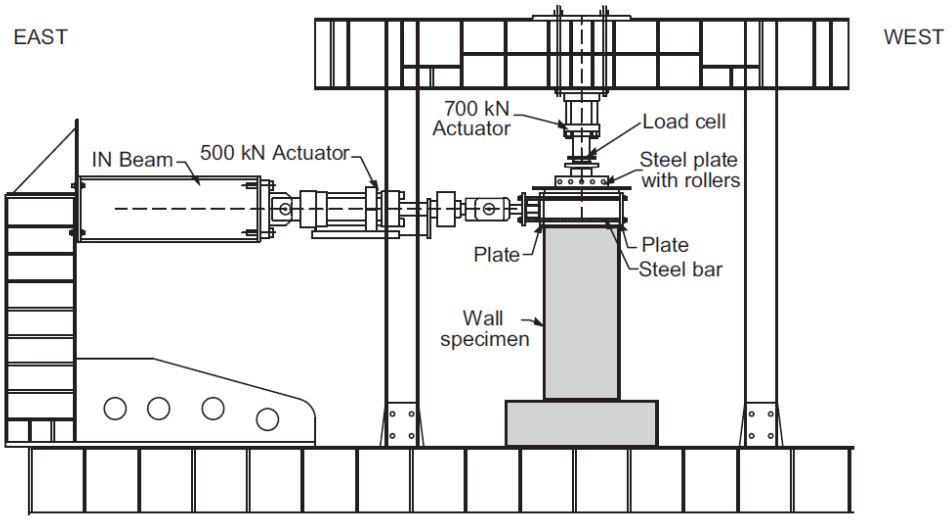

Figure 5.1: Test setup of the experiment, Figure from **Hube et al. (2014)**.

Wall W1 was selected to be modelled with a grillage of fibre beam elements. The wall had a length of 700 mm, a thickness of 100 mm and a height of 1600 mm. The wall was reinforced with 4Ø10 vertical bars at each corner plus 6Ø8 vertical bars distributed in two sides along the rest of the wall length. The concrete had a strength of 27.4 MPa; the Ø10 reinforcement had a yield strength of 469.2 MPa and a modulus of elasticity of 224.7 GPa while Ø8 reinforcement had a yield strength of 445.6 MPa and a modulus of elasticity of 225.8 GPa.

The wall was subjected to a constant axial load of 287 kN and a quasi-static cyclic horizontal displacement at a constant rate of 10 mm/min. The displacement loading protocol is shown Figure (5.2) and was retrieved from another publication of the authors **(Alarcon et al., 2014)**.

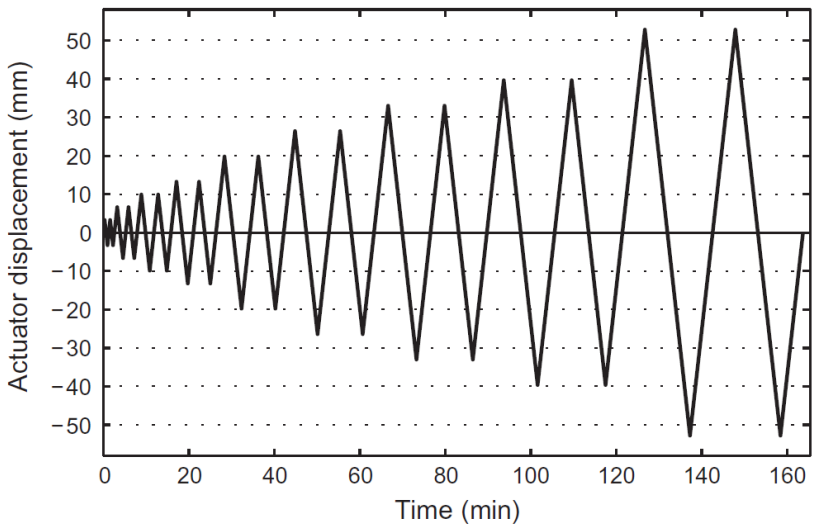

Figure 5.2: Horizontal cyclic loading protocol, Figure from **Alarcon et al. (2014)**.

The grillage model was constructed with 36 longitudinal fibre beam element and 27 transversal fibre beam element forming 40 joints. Each element was divided into 5 sections and each section was additionally divided into 10 concrete fibres and another number of steel fibres that represent the reinforcement available in each section. Figure (5.3) shows a schematic of the grillage model with joints and elements labelling. Each longitudinal member was assigned a section of 175x100 mm with its specific reinforcement depending on which part of the wall it simulates. For the transversal members a section of 200x100 mm was assigned. The beam was also modelled by planar (one directional) element and the corresponding results were compared.

In the present grillage model, the dimensions of the transversal members did not affect much the results; however, their presence is vital for the accuracy of the solution as they link the longitudinal members together. Joints 1, 2, 3 &4 were fixed and the horizontal and vertical loads were assigned to joints 37, 38, 39 &40 equally.

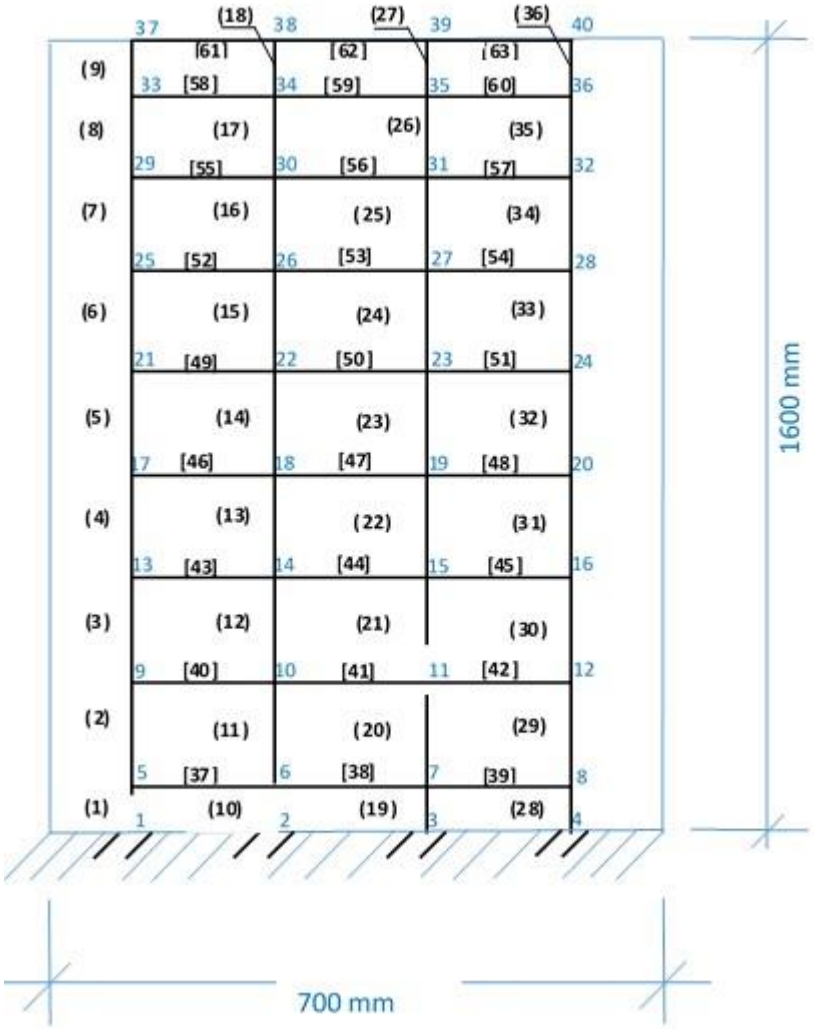

Figure 5.3: Schematic of the grillage model for wall W1 with joints and elements labelling.

The aim of this exercise is to show that the wall can be modelled as a set of grillage elements in the horizontal and transversal directions. Therefore, a static displacement-based element was selected to solve the problem since the load was imposed in a quasi-static process. However, the concept of dividing the wall into a number of horizontal and vertical members forming a grillage can be adopted similarly to any other problem with the newly developed elements previously presented in chapter (3) and (4) of this dissertation.

Figures (5.4 & 5.5) shows a comparison between the experimental results and the grillage model results. The load–displacement curves of the grillage model matched the experimental behavior and good correlation is observed. The difference in the dissipated energy between the envelope of the experimental results and the envelope of the fibre beam grillage model was 4.2%. In Figure (5.6), the grillage model output is compared with the planar model. Both models were able to analyse the problem, as an in-plane loading was applied to the wall. However, some differences can be observed in the hysteric curves.

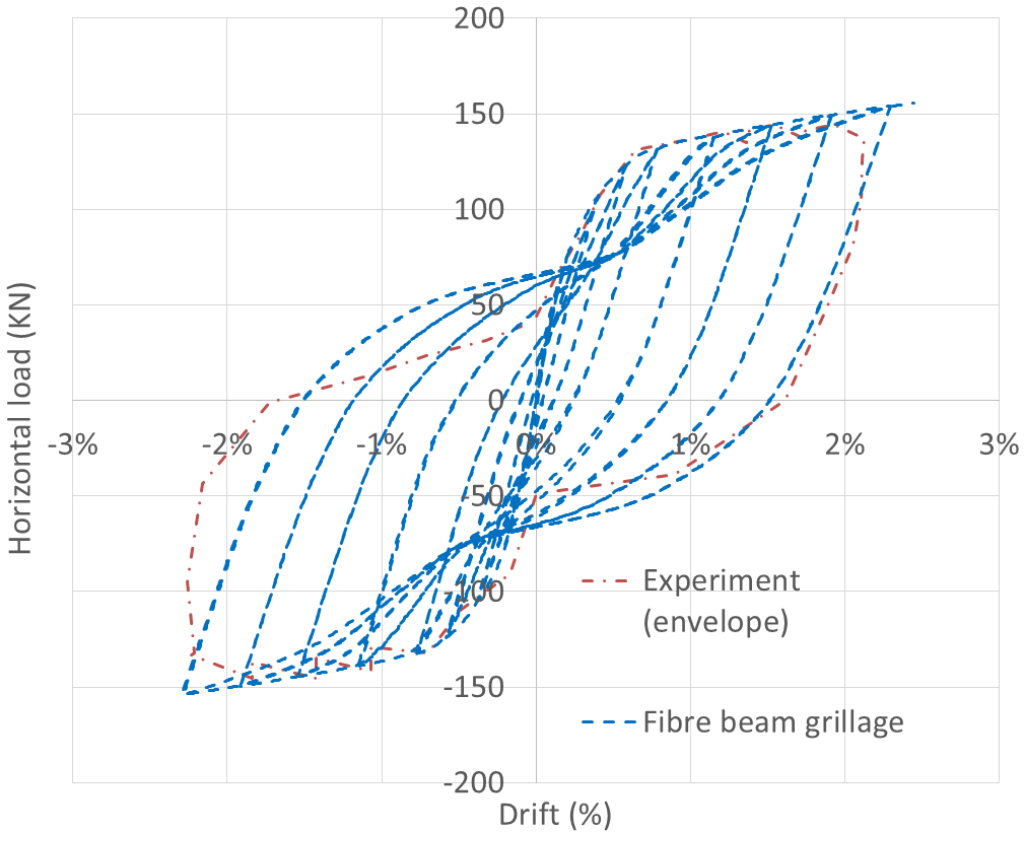

Figure 5.4: Comparison between the load displacement curves of the fibre beam grillage model and the envelope of the results retrieved from the experiment (Wall W1).

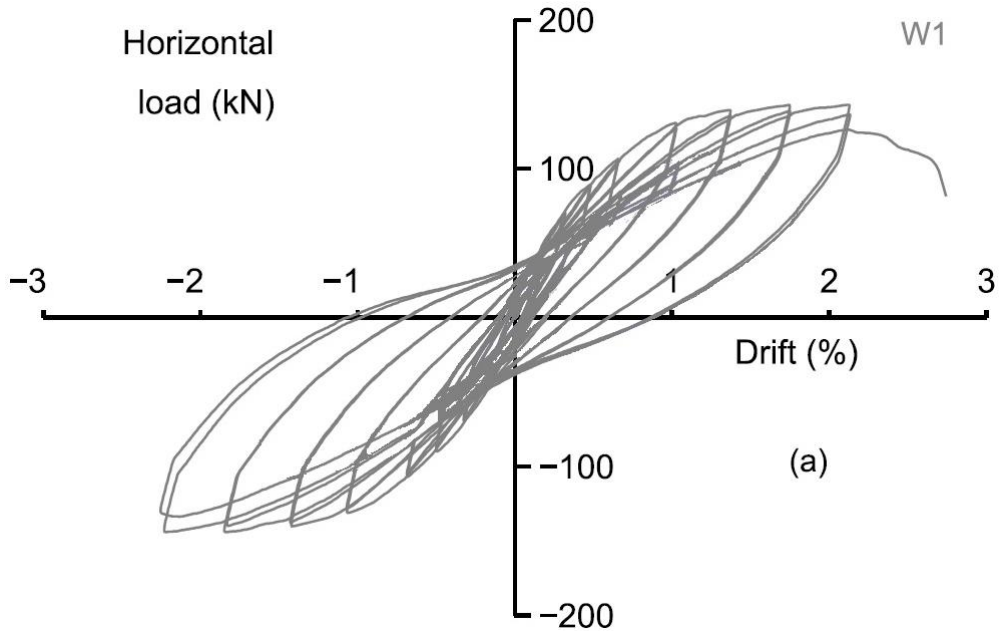

Figure 5.5: Full experimental load–displacement hysteretic relationship for wall W1, Figure from **Hube et al. (2014)**.

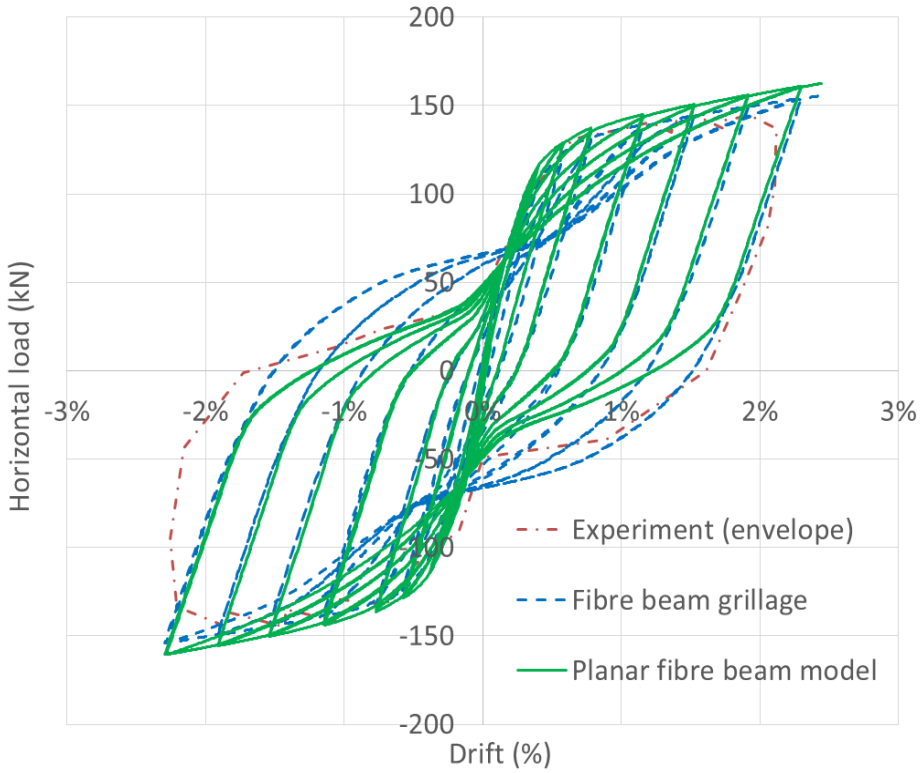

Figure 5.6: Comparison between the load displacement curves of the fibre beam grillage model and the planar fibre beam model.

5.2.2 Epackachi experiment

Epackachi et al. (2015) performed an experimental study on four rectangular large-scale steel-plated composite walls under in-plane inelastic cyclic lateral loading. The tested walls had an aspect ratio of 1.0 and failed in a flexural mode. The SC walls were fixed to a rigid foundation using posttensioned bars. Figure (5.7) shows the steel-plate composite wall test setup.

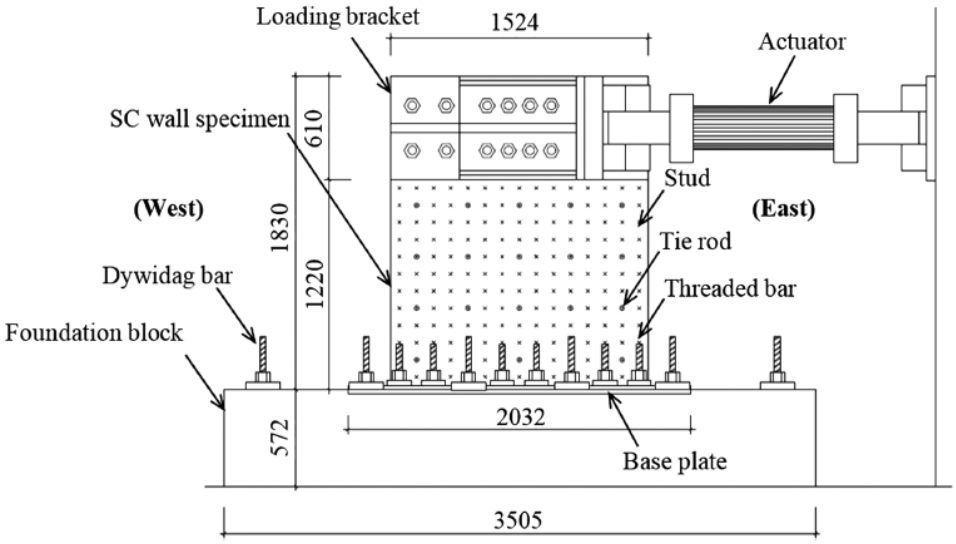

Figure 5.7: steel-plate composite wall test setup, Figure from **Epackachi et al. (2015)**.

Wall SC1 was selected to be modelled by a grillage of fibre beam elements. The wall had a dimension of 1524x1524x305 mm. The steel faceplates had a thickness of 4.8 mm and a yield strength of 262 MPa. The concrete core had a thickness of 295.4 mm and a nominal compressive strength of 27.5 MPa. Quasi-static cyclic lateral loads were applied at the top of the SC walls. The displacement-controlled reversed cyclic loading protocol is shown in Figure (5.8).

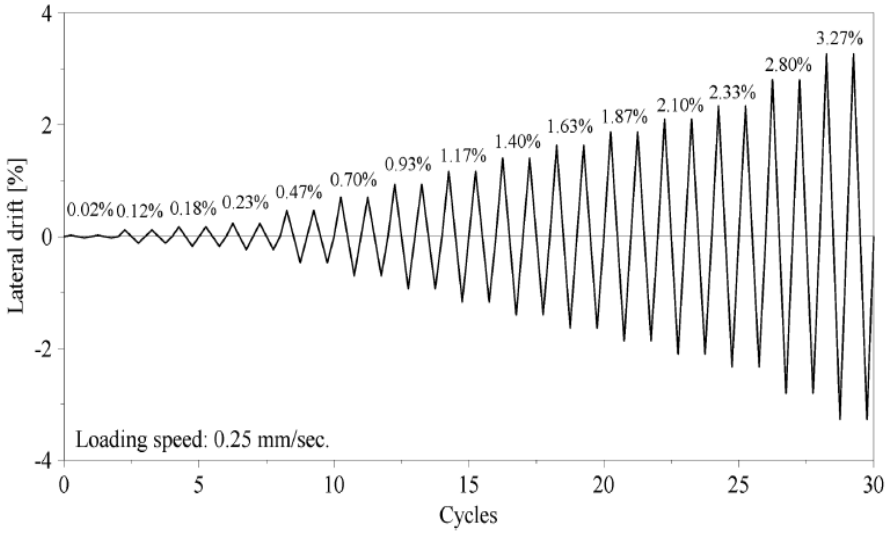

Figure 5.8: Loading protocol, Figure from **Epackachi et al. (2015)**.

The grillage model was constructed with 15 longitudinal fibre beam elements and 10 transversal fibre beam elements forming 18 joints. Each element was divided into 5 sections and each section was further divided into 10 concrete fibres and 2 steel fibres that represents the steel faceplates. Figure (5.9) shows a schematic of the grillage model with the joints and elements labelling. Each longitudinal member was assigned a section of 508x305 mm including the faceplates. The transversal members were assigned a section of 305x305 mm. Joints 1, 2& 3 were fixed and the horizontal displacement control load was assigned to joints 16, 17& 18.

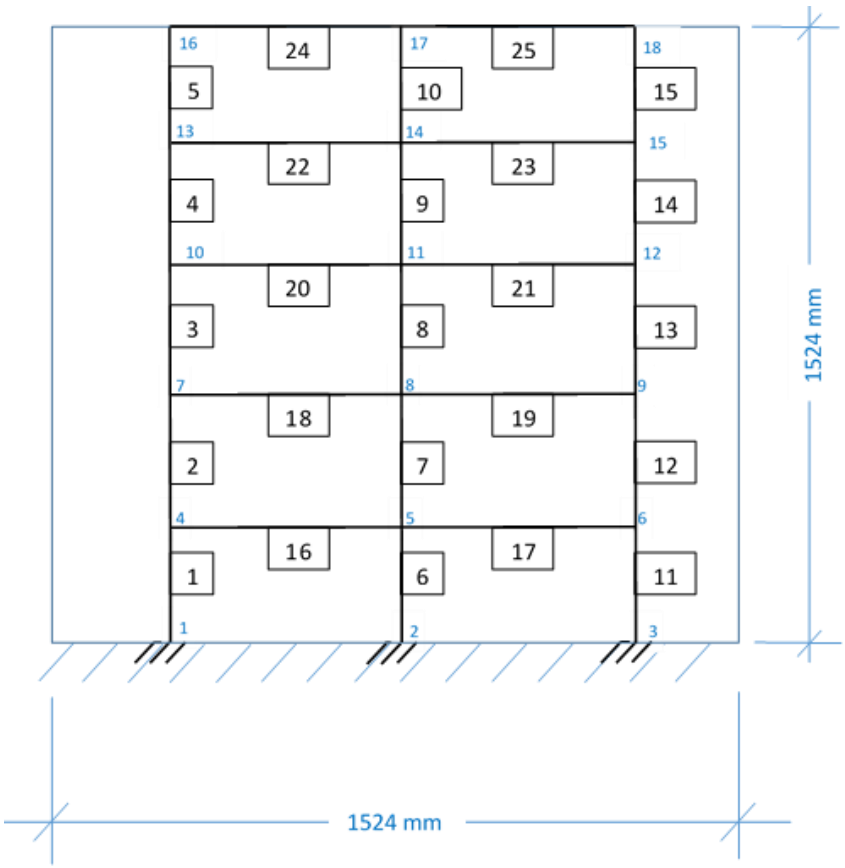

Figure 5.9: Schematic of the grillage model for wall SC1 with joints and elements labelling.

Similarly, a static force-based element was employed to simulate the experiment since the load was imposed in a quasi-static process. However, the concept of dividing the SC wall into a number of horizontal and vertical members forming a grillage can be adopted correspondingly under other types of loading. Figures (5.10 & 5.11) show a comparison between the experimental results and the grillage model results. The load-displacement curves display that the grillage model was able to simulate the experimental behavior using the force-based element. The difference in the dissipated energy between the envelope of the experimental results and the envelope of the fibre beam grillage model was 17%.

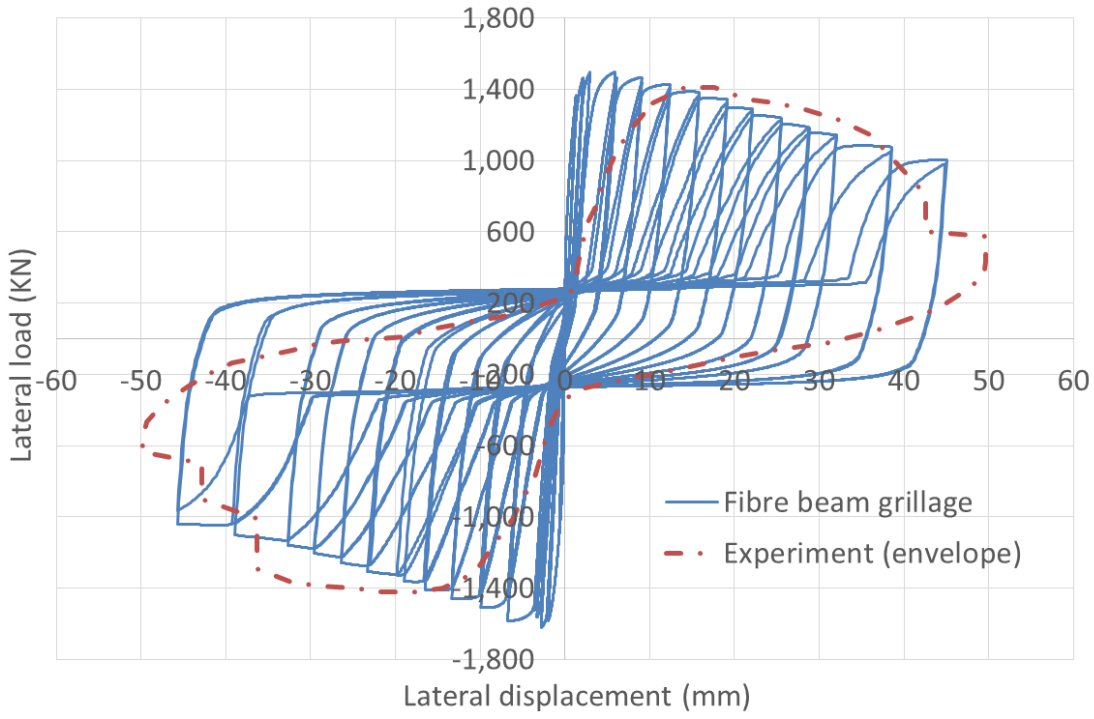

Figure 5.10: Comparison between the load displacement curves of the grillage model and the envelope of the results retrieved from the experiment.

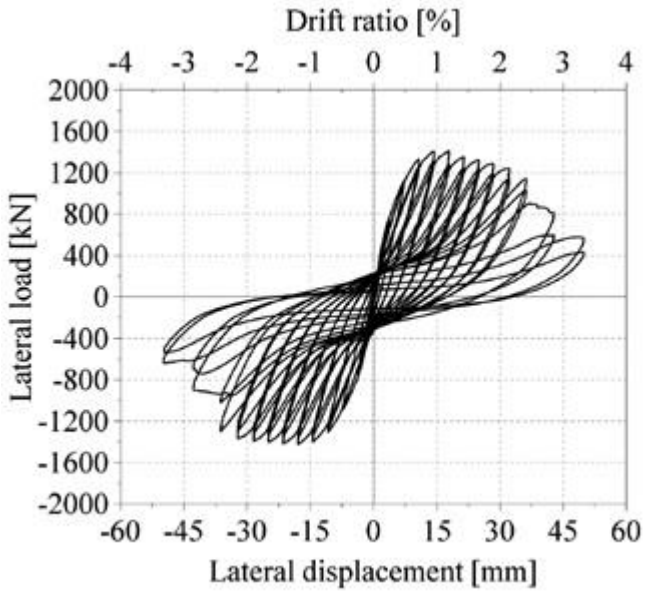

Figure 5.11: Experimental load-displacement relationships for SC1, Figure from **Epackachi et al. (2015)**.

5.3 Grillage modelling for out-of-plane loading

In order to allow the fibre beam elements to consider out of plane loading in grillage modelling a new proposed technique will be adopted by transforming the model into a 3D one, where the grillage is defined in a 2D coordinate and the load is assigned in the third perpendicular coordinate. Figure (5.12) shows the difference between in-plane and out-of-plane forces.

The fibre beam elements will be used to model the longitudinal and transversal members separately. However, each member will be composed of 5 DOF per node allowing for one extra translation DOF and one extra bending DOF in the out-of-plane direction. The elements will then be coupled at the global system in order to consider the 3D effect.

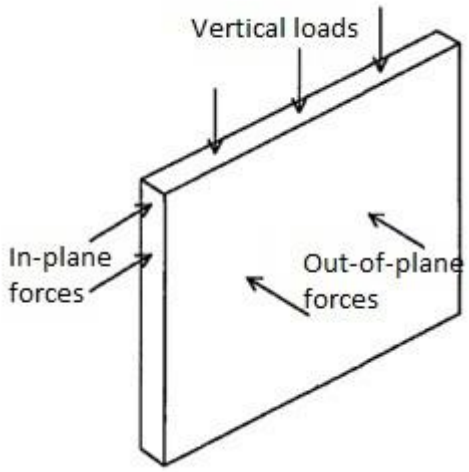

Figure 5.12: In plane and out-of-plane loading.

The global five DOF per node, shown in Figure (5.13), will be reduced in the element internal formulation by accounting for three DOF per node for the longitudinal member and another three DOF per node for the transversal member. So that the same formulation of the fibre beam elements previously presented in chapter (3) and (4) of this dissertation will be applicable within the element and its corotational formulation. However, the directions of the DOFs forming the longitudinal and transversal members will be different and are shown in Figures (5.14) and (5.15), where the word local refer to the status of the element internal formulation before removing the rigid body modes. Later, the elements will be transformed to the corotational formulation using the same procedure previously explained in detail in chapter (3) and (4).

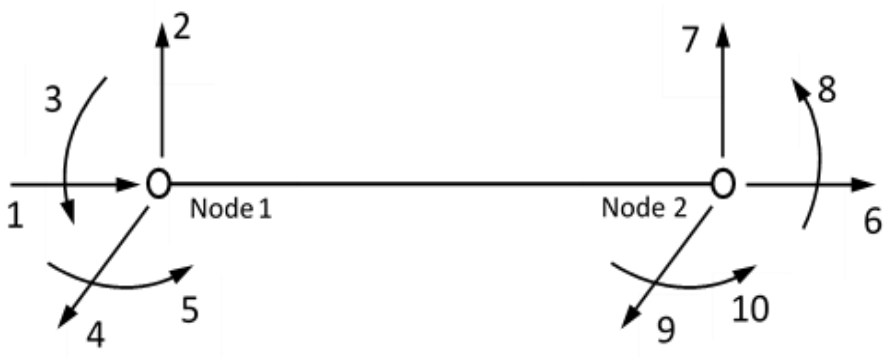

Figure 5.13: Element degrees of freedom in global system.

Figure 5.14: Element degrees of freedom in local system for longitudinal member.

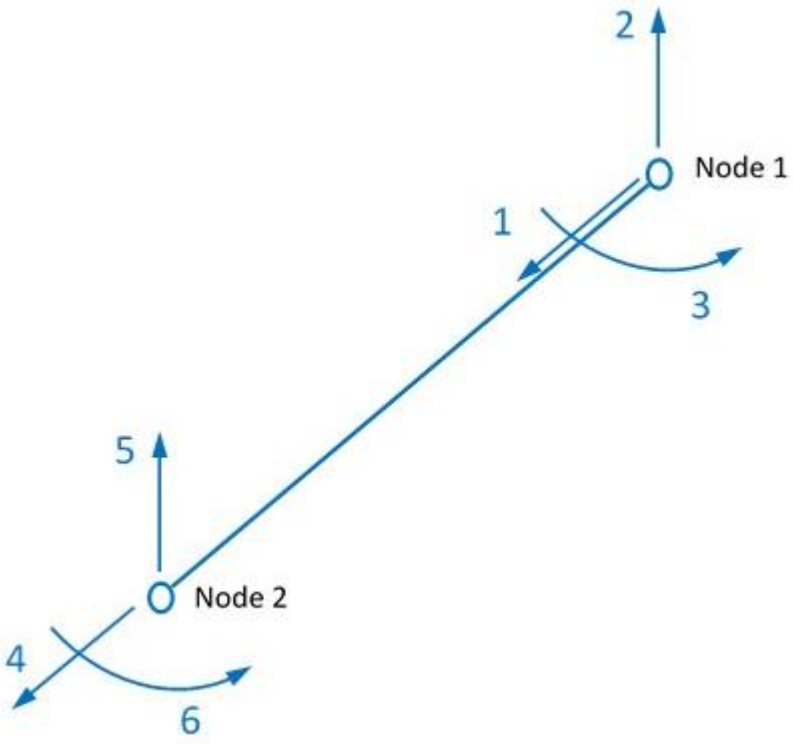

Figure 5.15: Element degrees of freedom in local system for transversal member.

In the local formulation of the transversal element, for node 1, the global DOF in direction (4), which is the axial force, will be stored in the local vector in direction

(1), while the global DOF in direction (2), the vertical DOF, will be stored in the local vector in direction (2). Finally, the global DOF in direction (5), representing the bending, will be stored in the local vector in direction (3). On the other hand, for the local formulation of the longitudinal element, global DOF (1) will be stored in local DOF (1), global (2) will be stored in local (2) and global (3) will be stored in local (3).

The resulting stiffness matrix of both elements will consist of a 10x10 matrix and the load vector will have a size of 10x1.

The assembly of the global stiffness matrix is as follows:

$k_{elem(global)}=$

$$\begin{bmatrix} k_{11} & k_{12} & k_{13} & 0 & 0 & k_{14} & k_{15} & k_{16} & 0 & 0 \\ k_{21} & k_{22}+\varkappa_{22} & k_{32} & \varkappa_{21} & \varkappa_{23} & k_{24} & k_{25}+\varkappa_{25} & k_{26} & \varkappa_{24} & \varkappa_{26} \\ k_{31} & k_{32} & k_{33} & 0 & 0 & k_{34} & k_{35} & k_{36} & 0 & 0 \\ 0 & \varkappa_{12} & 0 & \varkappa_{11} & \varkappa_{13} & 0 & \varkappa_{15} & 0 & \varkappa_{14} & \varkappa_{16} \\ 0 & \varkappa_{32} & 0 & \varkappa_{31} & \varkappa_{33} & 0 & \varkappa_{35} & 0 & \varkappa_{34} & \varkappa_{36} \\ k_{41} & k_{42} & k_{43} & 0 & 0 & k_{44} & k_{45} & k_{46} & 0 & 0 \\ k_{51} & k_{52}+\varkappa_{52} & k_{53} & \varkappa_{51} & \varkappa_{53} & k_{45} & k_{55}+\varkappa_{55} & k_{56} & \varkappa_{54} & \varkappa_{56} \\ k_{61} & k_{62} & k_{63} & 0 & 0 & k_{64} & k_{65} & k_{66} & 0 & 0 \\ 0 & \varkappa_{42} & 0 & \varkappa_{41} & \varkappa_{43} & 0 & \varkappa_{45} & 0 & \varkappa_{44} & \varkappa_{46} \\ 0 & \varkappa_{62} & 0 & \varkappa_{61} & \varkappa_{63} & 0 & \varkappa_{65} & 0 & \varkappa_{64} & \varkappa_{66} \end{bmatrix} \quad (5.1)$$

Where k denotes the stiffness of the longitudinal member and $\varkappa$ denotes the stiffness of transversal member.

Further the assembly of the load vector is:

$$F_{elem(global)} = \begin{bmatrix} F_1 \\ F_2 + \mathcal{F}_2 \\ F_3 \\ \mathcal{F}_1 \\ \mathcal{F}_3 \\ F_4 \\ F_5 + \mathcal{F}_5 \\ F_6 \\ \mathcal{F}_4 \\ \mathcal{F}_6 \end{bmatrix} \tag{5.2}$$

Where F denotes the load of the longitudinal member and $\mathcal{F}$ denotes the load of the transversal member.

It has to be noted that the transformation matrix T, previously defined in equation (4.22), must be multiplied by the matrix that accounts for the member inclination, T_R.

For the longitudinal element:

$$T_R = \begin{bmatrix} cos\,\beta & sin\,\beta & 0 & 0 & 0 & 0 \\ -sin\,\beta & cos\,\beta & 0 & 0 & 0 & 0 \\ 0 & 0 & 1 & 0 & 0 & 0 \\ 0 & 0 & 0 & cos\,\beta & sin\,\beta & 0 \\ 0 & 0 & 0 & -sin\,\beta & cos\,\beta & 0 \\ 0 & 0 & 0 & 0 & 0 & 1 \end{bmatrix} \tag{5.3}$$

While for the transversal element T_R must be modified to be in accordance with the local DOFs as follows:

$$T_R = \begin{bmatrix} sin\,\beta & cos\,\beta & 0 & 0 & 0 & 0 \\ cos\,\beta & -sin\,\beta & 0 & 0 & 0 & 0 \\ 0 & 0 & 1 & 0 & 0 & 0 \\ 0 & 0 & 0 & sin\,\beta & cos\,\beta & 0 \\ 0 & 0 & 0 & cos\,\beta & -sin\,\beta & 0 \\ 0 & 0 & 0 & 0 & 0 & 1 \end{bmatrix} \tag{5.4}$$

5.3.1 Two perpendicular beam models

The 3-dimensional general-purpose structural analysis software SAP2000 is first used to compare its results with the new developed technique to ensure its accuracy in the elastic range. A simple exercise is used in the validation. Two perpendicular beams, shown in Figure (5.16), are connected in their middle forming a cross. Each beam has a total length of 10000 mm. The beams have a depth of 600 mm and a width of 250 mm. They are assigned a steel material with a Young's modulus of 200 GPa and a yield stress of 1000 MPa to ensure a linear elastic behaviour. In the SAP2000 model, the intersecting joint of the two beams are loaded with a vertical downward force of 4000 N. According to SAP2000 3D output shown in Figure (5.17), the intermediate joint deflection is -0.04682 mm.

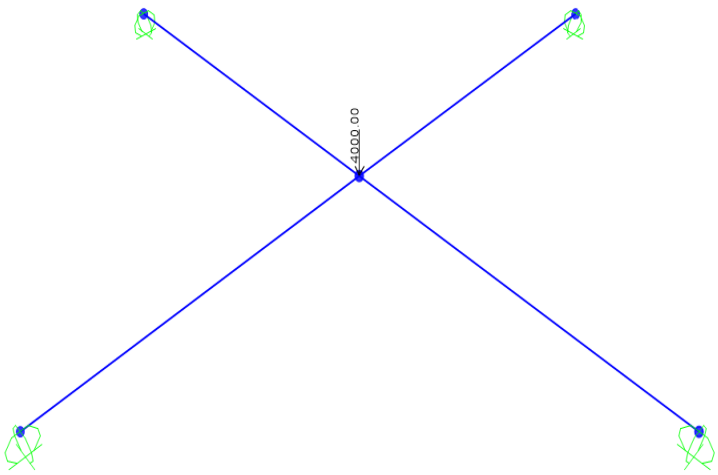

Figure 5.16: 3D model using SAP2000 software.

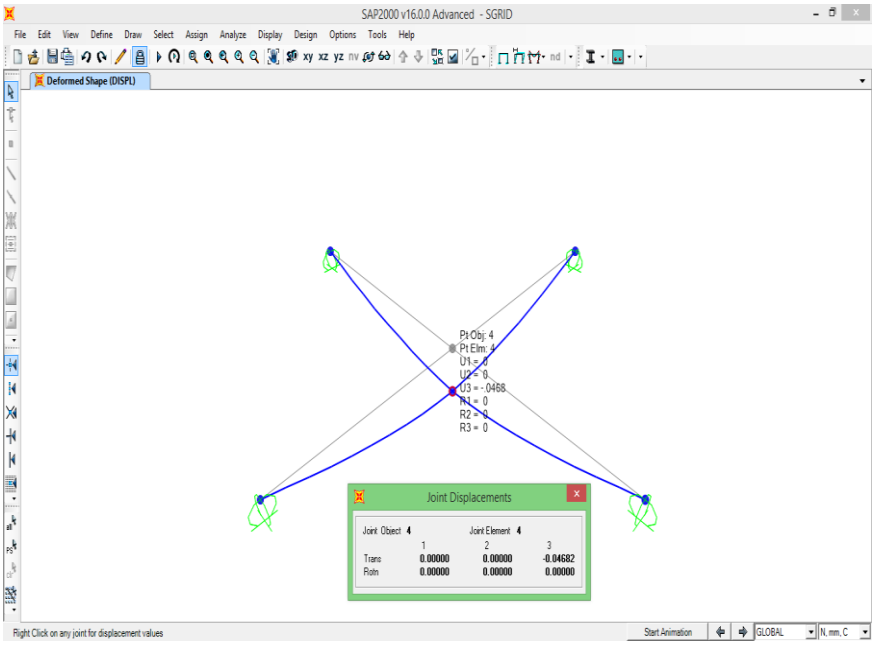

Figure 5.17: Displacement output at the middle joint using SAP2000.

The fibre beam element is then used to model the same two interconnected beams to simulate a simple grillage. Same section and materials were assigned to the model. The cross section was divided into 10 fibres. Each node has five DOF as previously explained and the load is first applied as a displacement control with a displacement value of -0.04682 mm. The summation of the output reactions of the grillage model is -4.0048E+03, which mean that the error is 0.001%. When a force control is adopted and a force value of 4000 N is applied at the intersection point of the connected beams, the output displacement is -4.6820E-02 with zero percent error.

This concludes that the simplified 3D grillage technique and the modified formulation could precisely model plane elements where the load is assigned on the third out-of-plane direction. The simplified 3D model can also be used to simulate impact and other dynamics out-of-plane loadings as discussed next.

5.3.2 Kishi experiment

The experiment of **Kishi et al. (2011)** will be used to validate the grillage modelling under out-of-plane impact loading. **Kishi et al. (2011)** analysed rectangular reinforced concrete slabs subjected to impact loading. LS-DYNA commercial software was used in the simulation and the results were compared with experimental output.

Slab S4 had a dimension of 2000x2000x180 mm. The slab was reinforced with a layer of Ø16 every 150 mm in both directions. The supports were restrained in the horizontal and vertical directions. However, they were permitted to rotate freely. A load of 300 kg was allowed to fall freely in the centre of the slab with a speed of 4 m/s. The sample had a concrete compressive strength of 26.6 MPa and a yield strain of 1,500 μ strain and the concrete tensile strength was 2.66 MPa. The slab had line supports on all sides.

The crack pattern of slab S4, retrieved from the experiment, is presented in Figure (5.18). The crack pattern shows that the crack progressed in both directions.

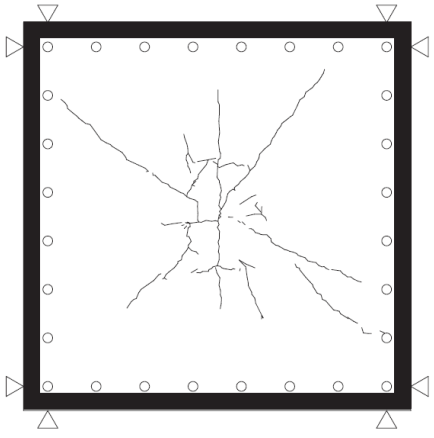

Figure 5.18: Crack patterns of slab S4, Figure from **Kishi et al.** (**2011**).

Kishi et al. (2011) modelled the quarter of the slab using eight-node solid elements for the concrete and two-node beam elements for the reinforcement bars. The solid cylinder was also modelled using solid elements. The LS-DYNA finite element model is shown in Figure (5.19).

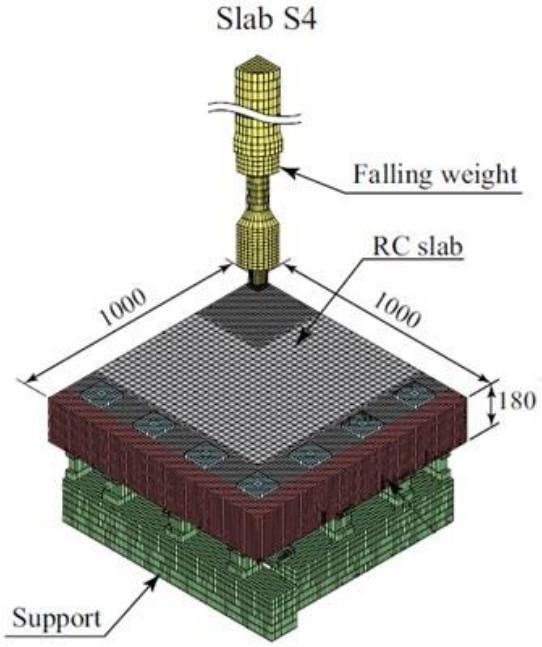

Figure 5.19: LS-DYNA finite element model, Figure from **Kishi et al. (2011)**.

Slab S4 is chosen to be modelled with the explicit fibre beam element. Two models were created. The first model is a simple 2D model with one row of beam elements in the longitudinal direction and another one in the perpendicular transversal direction (Figure 5.20). The two beams intersect each other at the middle node. Each beam is divided into 8 elements, each element is also divided into five sections, and the sections are similarly divided into 12 concrete fibres and 1 bottom steel fibre. In this model, the longitudinal and transversal members were assigned a section of 2000x180 mm.

The second model is a full 2D grillage model, where three beams are used in the longitudinal direction and another three beams are utilized in the transversal direction. The beams intersect each other at nine different nodes (Figure 5.21). In the second model, the longitudinal and transversal members were assigned a section of 666x180 mm.

The impact load, retrieved from the experiment, is applied in the middle node of the two grillages. The impact load is shown in Figure (5.22). The fibre beam models considered the strain rate effect of concrete and steel in order to model the impact behaviour appropriately.

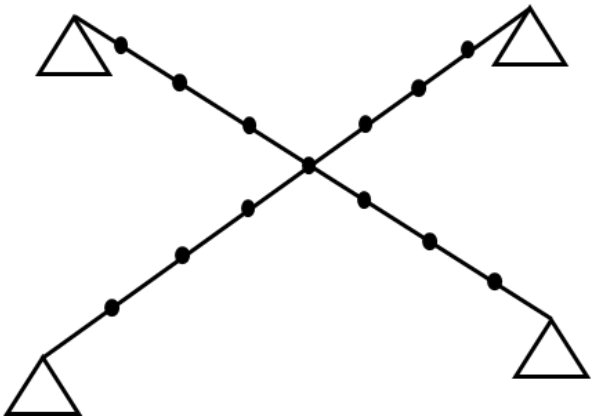

Figure 5.20: Fibre beam element 2D model (1 row/direction).

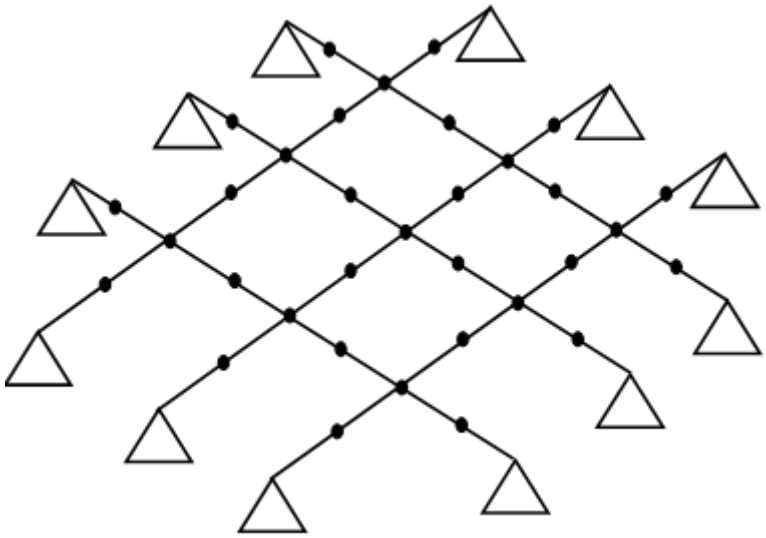

Figure 5.21: Fibre beam element 2D model (3 rows/direction).

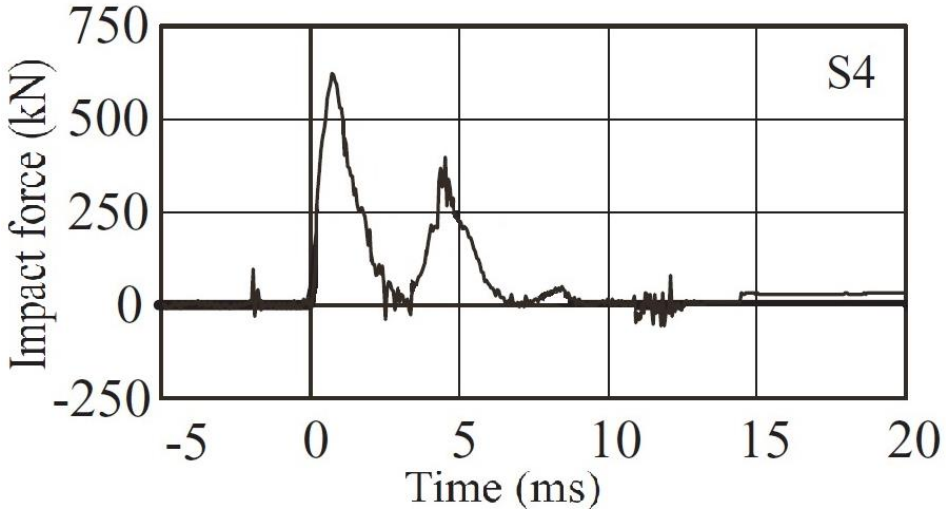

Figure 5.22: Impact force time history for sample S4, Figure from **Kishi et al. (2011)**.

The output results of the two models are shown in Figure (5.23). The models were able to estimate the maximum deflection value of the impact test since they consider the deflections in both directions. However, peak deflections were detected earlier than in the experimental results and the response-histories are generally different when compared with the experiment. The grillage modelling technique can

therefore be used to give preliminary estimates of the maximum deflection value and can save time and storage capacity when compared with solid models.

In conclusion, the grillage technique produced reasonable estimates of the maximum displacement values for slab modelled under out-of-plane impact loads. Models that are more sophisticated might be required to capture the full response-histories more precisely.

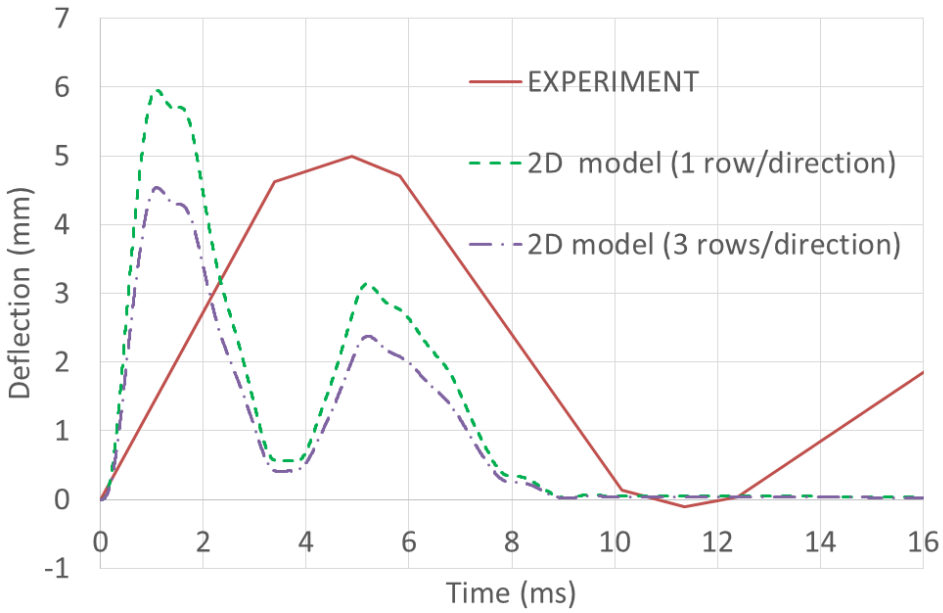

Figure 5.23: Deflection time history for different fibre beam models compared to the experimental result.

In the next section, the newly developed elements are used to investigate the effect of the different parameters affecting the impact behaviour of SC members.

5.4 Numerical study on SC panels

A numerical study is developed herein using the newly developed elements to investigate the most effective method of increasing the safety of SC panels to resist higher impact loads. Five parameters were chosen to be reasonably changed one by one, and their effect on the resistance is studied. The SC panel tested by **Sohel and Liew (2014)** was selected as a basis for this investigation. In the experiment, the SC sandwich slabs measured 1200 × 1200 mm^2 and were tested under the same impact loading previously shown in Figure (4.33). Each SC panel was modelled with 1D element only as it was sufficient to simulate the test as previously demonstrated in section 4.11.3.

All parameter values implemented in this study are based on practical available supplies from the construction industry in the UK. For example, the chosen thicknesses for the steel plates are available in the UK market and commonly used.

In this study, the steel plate thickness ranges between 2, 4, 5, 8, 10 and 12 mm. The concrete core thickness ranges between 60, 80, 100, 120 and 140 mm. The concrete compressive strength (f_c) varies between 22.5, 32.5, 42.5, 52.5 and 62.5 MPa, which present normal to high strength concrete. The concrete tensile strength (f_t) ranges between 1, 3, 5, 7 and 9 MPa, which present a steel fibre percentage that ranges between 1 and 3%. Finally, the yield strength of the steel plates varies between 240, 260, 320, 340 and 400 MPa. The study only covers the effect of steel fibre materials, while other fibrous nanomaterials such as carbon Nano fibres will affect both the tensile strength and the tension softening stiffness.

All SC panels were chosen to be impacted using the same impact force shown in Figure (4.33); and the same cross section division, shown in Figure (4.32), was maintained.

All other parameters were fixed with the same values as the original sample SLFCS6-80, except the parameter being investigated. The standard deviation, mean and coefficient of variation (CV) for every case were calculated at several displacements and finally an average coefficient of variation value for the load resistance of every case was determined, where the CV percentage is an adequate statistical tool to measure the dispersion of the probability. In the present case, the higher the CV, the more the studied parameter is able to affect the resistance of the SC panel. Such information can help the designer in choosing which parameter can be more efficient in increasing the resistance of the system.

Table 5.1. Coefficient of variation percentage for different parameters affecting the resistance of SC panels against impact

	Steel plate thickness	Concrete core thickness	Steel plate yield strength	Concrete compressive strength	Concrete tensile strength
Average CV (%)	40.6	36.8	9.6	7.5	3.5

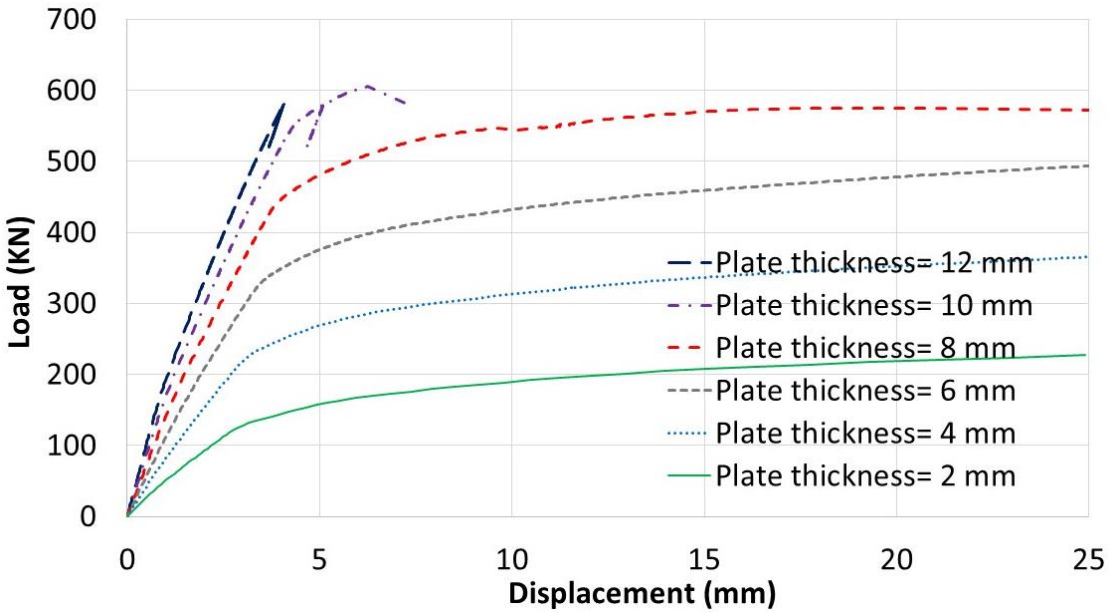

Figure 5.24: The effect of steel plate thickness on the load-deflection behaviour of SC panels.

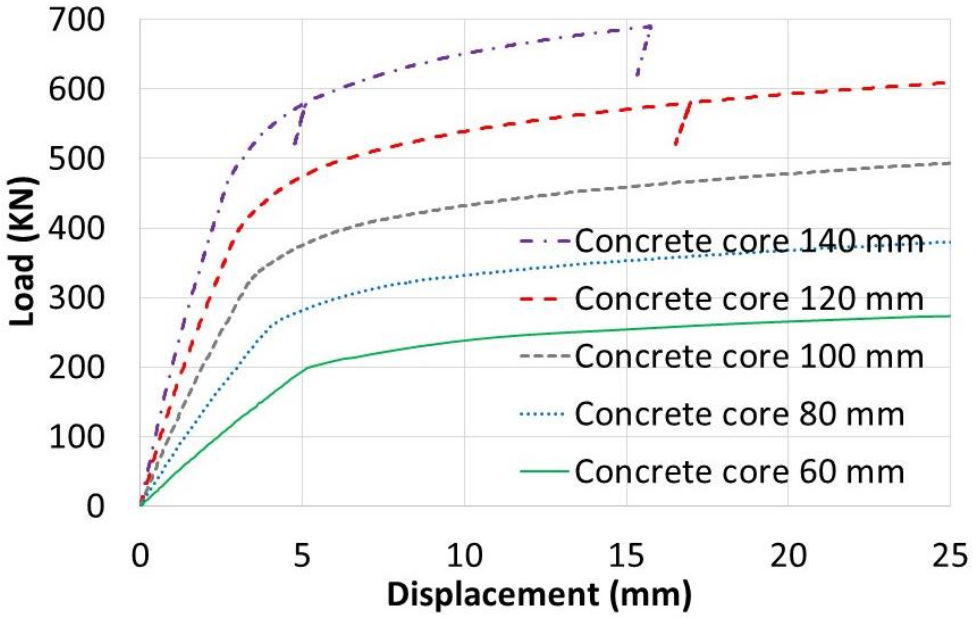

Figure 5.25: The effect of concrete core thickness on the load-deflection behaviour of SC panels.

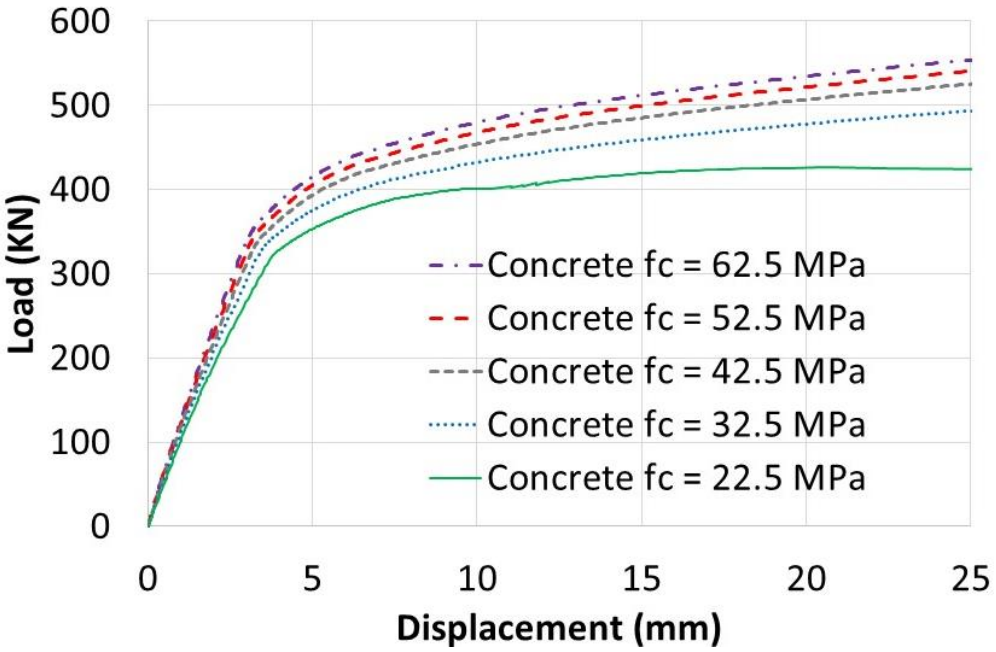

Figure 5.26: The effect of concrete compressive strength on the load-deflection behaviour of SC panels.

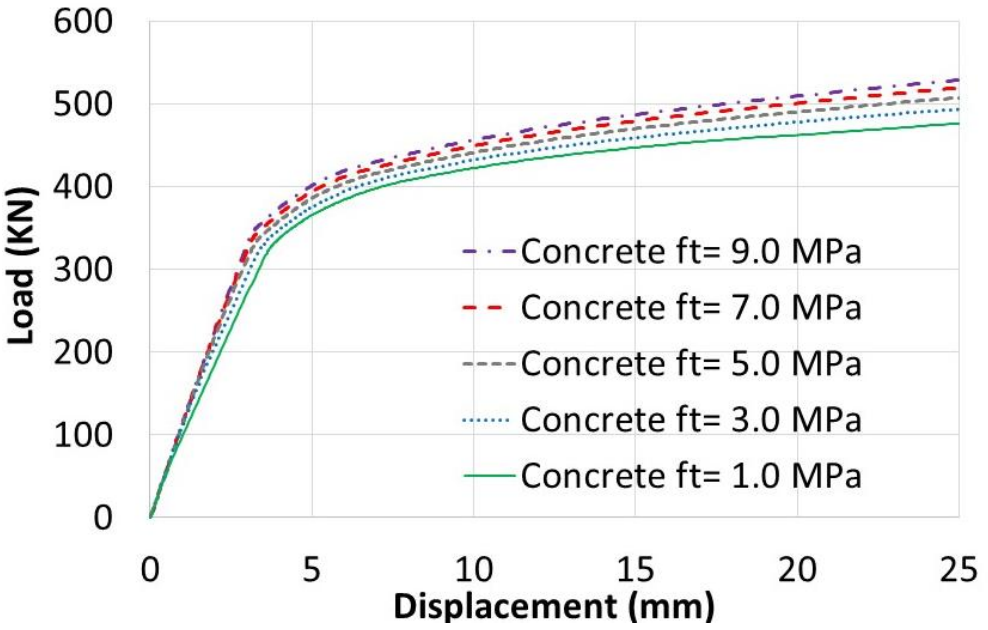

Figure 5.27: The effect of concrete tensile strength on the load-deflection behaviour of SC panels.

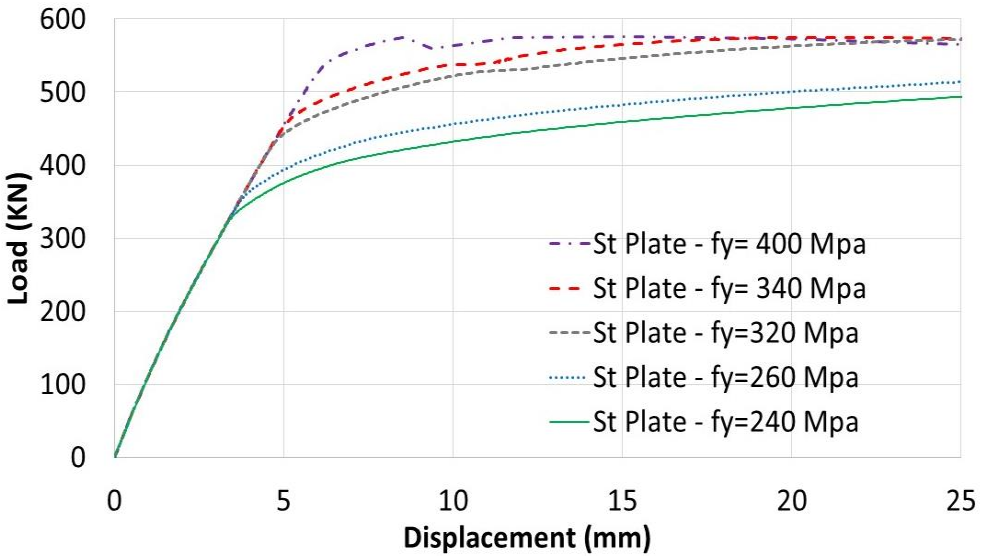

Figure 5.28: The effect of steel plates yield strength on the load-deflection behaviour of SC panels.

Figures (5.24 to 5.28) and Table (5.1) display the results of the parametric study. We can establish from Table (5.1) that increasing the steel plate thickness is the most effective way of increasing the resistance of SC panels under impact and shock load. The second most effective parameter is increasing the concrete core thickness, followed by increasing the steel plate yield strength and then increasing the concrete compressive strength.

Finally, it is clear that increasing the concrete tensile strength has a limited effect in increasing the resistance of the composite SC panels when compared to the other parameters.

5.5 Conclusion

The developed fibre beam elements are successfully used to model large-scale walls using grillage technique for in-plane and out-of-plane loadings. For the out-of-plane loading, a simplified 3D model is used where each node is assigned two extra DOF to combine the effect of longitudinal and transversal members in the global system. This innovative procedure allows the use of the planer formulation of fibre beam elements presented in chapter (3) and (4) in solving 3D models. The new technique was verified against a number of experiments under static and impact loading.

A numerical study is finally developed to investigate the most effective method of increasing the safety of SC panels to resist higher impact loads. The study demonstrated that increasing the steel plate thickness is the most effective method of increasing the resistance of SC panels under impact

Chapter 6

Summary and conclusions

6.1 Summary

A number of finite element models able to accurately simulate complex flexural-controlled structures such as composite steel concrete beams and panels under the effect of impact dynamic loading were developed. An explicit time integration approach known for its suitability for short term dynamic problems was employed instead of the traditional implicit method. The second order effect, that usually accompanies impact problems, is accounted for using the geometric stiffness matrix technique. The elements were formulated using displacement-based and mixed-based formulations to consider the second order effect and the explicit time integration method. Another force-based first-order element that uses the explicit time integration method was similarly developed. The proposed elements were developed in the research oriented, general-purpose finite element software FEAP.

Different RC structures containing fibrous material in the concrete mix were accurately simulated under impact loading and large deformations. Composite steel concrete panels, recently used in nuclear infrastructure, were also modelled using the developed fibre beam elements. In addition, a numerical study was performed on SC panels to investigate the most effective method of increasing the safety of SC panels to resist higher impact loads.

The recent elements were used to model different reinforced concrete beams and walls under impact loading and also several slender structures were simulated under monotonic and cyclic loading.

Furthermore, a grillage modelling technique was adopted in order to use the developed planar fibre beam elements in modelling large-scale walls. The new technique allows the simulation of in plane and out-of-plane loading which enhances the capability of the model. The emerging technique can be consider as 3D modelling, since two dimensions define the geometry and the third perpendicular dimension defines the load.

The proposed force-based and mixed elements along with the simplified 3D technique represent a simple and powerful tool for the analysis of complex impact problems efficiently while using a limited number of finite elements and avoiding convergence complications. The elements are computationally inexpensive when compared to continuum models.

All elements developed in the present dissertation were validated against a considerable number of experiments and benchmark problems available from the literature.

6.2 Conclusions and findings

It can be concluded that the new developed elements especially the explicit second order mixed element has potential advantages in capturing the nonlinear behaviour of reinforced concrete structures. The findings can be stated as follows:

1. The displacement and mixed-based elements are able to precisely model reinforced concrete slender members with high accuracy under monotonic and cyclic loading.

2. The mixed element requires less number of divisions (coarse mesh) to predict the curvature and load displacement curves compared to the displacement-based element.

3. The developed elements allows the monitoring of the fibre, section and element behaviour.

4. The developed elements can simulate the presence of steel and carbon Nano fibres in the concrete through the determination of the tensile strength and the tension softening stiffness while considering the second order effect.

5. The explicit displacement, force-based and mixed elements are able to solve short-term dynamic problems and overcome the difficulties and complications that accompany the implicit time integration method including the need to iterate in every time step and the convergence provisions.

6. The strain rate effects for steel, concrete and fibre reinforced concrete was successfully taken into account during the analysis of impact problems using available material models based on different SHPB tests.

7. The explicit elements necessitate the use of a diagonal lumped mass matrix and the chosen time increment has to be smaller than the stable time increment required to maintain the stability of the numerical solution.

8. In the force and mixed-based explicit approach, a new algorithm that eliminates the need for iterations at the element level is proposed. In addition to the condition of the stable time increment, if the selected time step is smaller than or

equal to a specific critical time step, a single iteration is sufficient to satisfy an element-level convergence criteria.

9. In the explicit analysis, the elimination of the internal and external iterations requires considerable longer execution time as the selected time step played the major role in the determination of the execution time.

10. For the explicit models, it is recommended to use a value of α equal to $(3.5/100)$ when calculating the rotational mass at each node of beam elements.

11. The fibre beam elements can generally be used to model large scale walls using a network of longitudinal and transversal beams.

12. A simplified technique was used to employ the developed 1D planar elements in solving 3D problems were the geometry is defined in 2 directions and the load is assigned in the out-of-plane direction. The technique is very useful in modelling slabs when a two-direction crack pattern is expected.

13. A numerical study was performed on SC panels subjected to impact loading. It can be established that the steel plate thickness is the most effective factor in increasing the resistance of SC panels subjected to impact loading followed by the concrete core thickness. The steel plate yield strength and the concrete compressive have a significant but lower effect, while, the concrete tensile strength has a minor effect on the SC panel resistance.

14. The proposed elements can be used reliably to analyse different reinforced concrete structures to ensure their safety against impact loading.

15. The accuracy of the elements is limited if the modelled beams or walls are dominated by shear failure.

6.3 Future work

Potential future studies can extend the scope of this dissertation. Some proposed directions for future research can be summarised as follows:

1. Developing an explicit fibre beam element that address the interaction between the axial force, shear, bending, and torsion loads while considering the second order effect.
2. Using the explicit fibre beam element to evaluate blast loading.
3. Redeveloping the elements to account for the full three-dimensional behaviour.
4. Enhancing the capabilities of the elements by considering bond-slip effect, reinforcement and steel-plate buckling, and warping deformations.
5. Studying the effect of different fibres on the impact resistance of RC structures.
6. Implementing the developed fibre beam elements in open source software framework (e.g. OpenSees) to allow for wider use by the community.
7. Using the grillage technique to study the seismic and blast behaviour of more complex 3D RC structures (e.g. containment structures).
8. Using the developed elements along with the grillage technique to conduct probabilistic studies (e.g. fragility analysis) on complex RC structures under the effect of seismic, impact, and blast loads.

REFERENCES

Abbas, A. A., Syed Mohsin, S. M., Cotsovos, D. M. (2010). Numerical Modelling of Fibre-Reinforced Concrete. Proc. of International Conference on Computing in Civil & Building Engineering icccbe 2010, (ed W. Tizani), University of Nottingham Press, Nottingham, UK, paper 237, p. 473, ISBN 978-1-907284-60-1.

Alarcon, C., Hube, M. and de la Llera, J. (2014). Effect of Axial Loads in the Seismic Behavior of Reinforced Concrete Walls with Unconfined Wall Boundaries. *Engineering Structures*, 73, pp.13-23.

Alemdar, B. and White, D. (2005). Displacement, flexibility, and mixed beam–column finite element formulations for distributed plasticity analysis. *Journal of structural engineering*, 131(12), pp.1811–1819.

Ammann, W., Muehlematter, M., & Bachmann, H. (1982). Stress-strain behaviour of non prestressed and prestressed reinforcing steel at high strain rates. *Proc. of RILEM-CEB-IABSE-IASS, Concrete structures under impact and impulsive loading*, p. 656, Berlin, BAM.

Anandavalli, N., Lakshmanan, N., Iyer, N., Samuel Knight, G. and Rajasankar, J. (2011). A Novel Modelling Technique for Blast Analysis of Steel-Concrete Composite Panels. *Procedia Engineering*, 14, pp.2429-2437.

Anandavalli, N., Lakshmanan, N., Rajasankar, J. and Prakash, A. (2012). Numerical Studies on Blast Loaded Steel-Concrete Composite Panels. *JCES*, 1(3), pp.102-108.

Ayoub, A. and Filippou, F. (2000). Mixed Formulation of Nonlinear Steel-Concrete Composite Beam Element. *Journal of Structural Engineering*, 126(3), pp.371-381.

Banthia, N., Mindess, S., Bentur, A. and Pigeon, M. (1989). Impact testing of concrete using a drop-weight impact machine. *Experimental Mechanics*, 29(1), pp.63-69.

Barrera, A., Bonet, J., Romero, M. and Miguel, P. (2011). Experimental tests of slender reinforced concrete columns under combined axial load and lateral force. *Engineering Structures*, 33(12), pp.3676-3689.

Bathe, K. and Cimento, A. (1980). Some practical procedures for the solution of nonlinear finite element equations. *Computer Methods in Applied Mechanics and Engineering*, 22(1), pp.59-85.

Berry, M. (2006). Performance modeling strategies for modern reinforced concrete bridge columns. Ph.D. thesis. University of Washington, Seattle.

Booth, P.N. (2008). Behavior of Steel Plate Reinforced Concrete Modular Walls Subjected to Combined Thermal and Mechanical Loads. M.S. Thesis, Purdue University, School of Civil Eng., West Lafayette, IN 47906, pp. 32-33.

Caballero-Morrison, K., Bonet, J., Navarro-Gregori, J. and Serna-Ros, P. (2013). An experimental study of steel fiber-reinforced high-strength concrete slender columns under cyclic loading. *Engineering Structures*, 57, pp.565-577.

Campbell, S. (1994). Nonlinear elements for three dimensional frame analysis. Ph.D. thesis. University of California, Berkeley.

Campione, G. and Letizia Mangiavillano, M. (2008). Fibrous reinforced concrete beams in flexure: Experimental investigation, analytical modelling and design considerations. *Engineering Structures*, 30(11), pp.2970-2980.

Chan, S. (1988). Geometric and material non-linear analysis of beam-columns and frames using the minimum residual displacement method. *International Journal for Numerical Methods in Engineering*, 26(12), pp.2657-2669.

Chang, S. (2009). An explicit method with improved stability property. *International Journal for Numerical Methods in Engineering*, 77(8), pp.1100-1120.

Chang, S. and Liao, W. (2005). An unconditionally stable explicit method for structural dynamics. *Journal of Earthquake Engineering*, 9(3), pp.349-370.

Chernobyl: Assessment of radiological and health impacts. (2002). 2002 update of Chernobyl: Ten years on. [online] OECD-NEA. Available at: http://www.oecd-nea.org/rp/pubs/2003/3508-chernobyl.pdf [Accessed 18 Dec. 2017].

Chen, L., Xiao, Y., and El-Tawil, S. (2016). Impact Tests of Model RC Columns by an Equivalent Truck Frame. *J. Struct. Eng.*, 10.1061/(ASCE)ST.1943-541X.0001449, 04016002.

Ciampi, V. and Carlesimo, L. (1986). A nonlinear beam element for seismic analysis of structures. In: *Proceedings of the European Conference on Earthquake Engineering*. pp.73–80.

Clough, R. (1990). Original formulation of the finite element method. *Finite Elements in Analysis and Design*, 7(2), pp.89-101.

Cowper, G. and Symonds, P. (1957). Strain-hardening and strain-rate effects in the impact loading of cantilever beams. *Providence, R.I.: Division of Applied Mathematics*, Brown University.

Crisfield, M. (1990). A consistent co-rotational formulation for non-linear, three-dimensional, beam-elements. *Computer Methods in Applied Mechanics and Engineering*, 81(2), pp.131-150.

Crisfield, M. A. (1991). Nonlinear finite element analysis of solids and structures, Vol. 1, Wiley, New York.

Curiel Sosa, J. and Gil, A. (2009). Analysis of a continuum-based beam element in the framework of explicit-FEM. *Finite Elements in Analysis and Design*, 45(8-9), pp.583-591.

Deierlein, G.G., Reinhorn, A. M. and Willford, M.R. (2010). Nonlinear structural analysis for seismic design, a guide for practicing engineers, NEHRP Seismic Design Technical Brief No. 4, NIST GCR 10-917-5.

Denavit, M. and Hajjar, J. (2012). Nonlinear Seismic Analysis of Circular Concrete-Filled Steel Tube Members and Frames. *Journal of Structural Engineering*, 138(9), pp.1089-1098.

De Souza, R. (2000). Force-based Finite Element for Large Displacement Inelastic Analysis of Frames. Doctor of Philosophy. University of California, Berkeley.

Dunand, M., Gary, G. and Mohr, D. (2013). Load-Inversion Device for the High Strain Rate Tensile Testing of Sheet Materials with Hopkinson Pressure Bars. *Experimental Mechanics*, 53(7), pp.1177-1188.

Dundar, C., Erturkmen, D. and Tokgoz, S. (2015). Studies on carbon fiber polymer confined slender plain and steel fiber reinforced concrete columns. *Engineering Structures*, 102, pp.31-39.

Elavenil, S. and Knight, G. (2012). Impact Response of Plates Under Drop Weight Impact Testing. *Daffodil International University Journal of Science and Technology*, 7(1).

Epackachi, S., Nguyen, N., Kurt, E., Whittaker, A. and Varma, A. (2015). In-plane seismic behavior of rectangular steel-plate composite wall piers. *J. Struct. Eng.*, 141(7).

Faghih, F., Das, D., Gendy, S. and Ayoub, A. (2016). Structural Behavior of Fibre-Reinforced Steel-Concrete Composite Elements under hazard Loads. In: *Proceedings of the World Congress on Advances in Civil, Environmental, and Materials Research*, Jeju, Korea.

Felippa, C. (2013). Matrix Finite Element Methods in Dynamics (Course in Preparation). 1st ed. [ebook] Colorado, Chapter 18. <http://www.colorado.edu/engineering/CAS/courses.d/MFEMD.d/MFEMD.Ch18.d/MFEMD.Ch18.pdf> (Dec. 6, 2016).

Fib Model Code for Concrete Structures 2010. (2013). Ernst & Sohn, a Wiley brand.

Filippou, F., Popov, E. and Bertero, V. (1983). Effects of bond deterioration on hysteretic behavior of reinforced concrete joints. Earthquake Engineering Research Center, Report No. UCB/EERC-83/19. Division of Structural Engineering and Structural Mechanics, University of California, Berkeley, p.191.

Fujikake, K., Li, B. and Soeun, S. (2009). Impact Response of Reinforced Concrete Beam and Its Analytical Evaluation. *Journal of Structural Engineering*, 135(8), pp. 938-950.

Fulei, W. and Yungui, L. (2011). A Nonlinear Dynamic Beam Element with Explicit Algorithms. *Communications in Computer and Information Scienc*, CCIS 163, pp. 311-318.

Gilat, A. and Pao, Y. (1988). High-rate decremental-strain-rate test. *Experimental Mechanics*, 28(3), pp.322-325.

Gu, L. and Wu, S. (2013). Introduction to the explicit finite element method for nonlinear transient dynamics. Hoboken, N.J.: Wiley, p.5.

Hajializadeh, D., Al-Sabah, A., OBrien, E., Laefer, D. and Enright, B. (2015). Nonlinear analysis of isotropic slab bridges under extreme traffic loading. *Canadian Journal of Civil Engineering*, 42(10), pp. 808-817.

Hambly Feng, E. (1991). Bridge deck behaviour. London: Taylor & Francis Group.

Hashimoto, J., Takiguchi, K., Nishimura, K., Matsuzawa, K., Tsutsui, M., Ohashi, Y., Kojima, I. and Torita, H. (2005). Experimental study on behavior of RC panels covered with steel plates subjected to missile impact. In: *18th International Conference on Structure Mechanics in Reactor Technology* (SMiRT 18).

Heidarpour, A. and Bradford, M. (2011). Beam–column element for non-linear dynamic analysis of steel members subjected to blast loading. *Engineering Structures*, 33(4), pp.1259-1266.

Hopkinson, B. (1914). A Method of Measuring the Pressure Produced in the Detonation of High Explosives or by the Impact of Bullets. Philosophical

Transactions of the Royal Society A: Mathematical, Physical and Engineering Sciences, 213(497-508), pp.437-456.

Hrynyk, T. and Vecchio, F. (2014). Behavior of Steel Fiber-Reinforced Concrete Slabs under Impact Load. *ACI Structural Journal*, 111(5).

Hube, M., Marihuén, A., de la Llera, J. and Stojadinovic, B. (2014). Seismic behavior of slender reinforced concrete walls. *Engineering Structures*, 80, pp.377-388.

IAEA-Topic: Banning atomic energy. (2016). Worldwide nuclear power phase-out till 2050. [online] IAEA. Available at: https://munog.de/media/IAEA%20-%20Banning%20Atomic%20Energy [Accessed 18 Dec. 2017].

Jiang, H., Wang, X. and He, S. (2012). Numerical simulation of impact tests on reinforced concrete beams. *Materials & Design*, 39, pp.111-120.

Jones, N. (1990). Structural Impact. *Cambridge*: Cambridge University Press, Chapter 8.

Kaba, S. and Mahin, S. A. (1984). Refined modeling of reinforced concrete columns for seismic analysis. Report No. UCB/EERC-84/03, *Earthquake Engineering Research Center*, University of California, Berkeley.

Kappos, A.J., Saiidi, M., Aydinoglu, N. and Isakovic, T. (2012). Seismic design and assessment of bridges: Inelastic methods of analysis and case studies. Springer, Dordrecht, The Netherlands

Kang, Y., and Scordelis, A. (1977). Nonlinear Geometric, Material and time Dependent Analysis of Reinforced and Prestressed Concrete Frames. Rep. UC-SESM No. 77-1, University of California, Berkeley, Calif.

Kang, Y. J. (1977). Nonlinear Geometric, Material and Time Dependent Analysis of Reinforced and Prestressed Concrete Frames. Report No. SESM 77-1, *Division of Structural Engineering and Structural Mechanics*, University of California, Berkeley.

Karadelis, J. and Zhang, L. (2015) On the Discrete Numerical Simulation of Steel Fibre Reinforced Concrete (SFRC). *Journal of Civil Engineering Research*, volume 5 (6): 151-157. DOI: 10.5923/j.jce.20150506.04.

Kent, D. and Park, R. (1971). Flexural members with confined concrete. *Journal of the Structural Division*, Proc. of the American Society of Civil Engineers, 97(ST7), pp.1969-1990.

Kishi, N., Kurihashi, Y., Ghadimi Khasraghy, S. and Mikami, H. (2011). Numerical Simulation of Impact Response Behavior of Rectangular Reinforced Concrete Slabs under Falling-Weight Impact Loading. *Applied Mechanics and Materials*, 82, pp.266-271.

Kolay, C. and Ricles, J. (2014). Development of a family of unconditionally stable explicit direct integration algorithms with controllable numerical energy dissipation. Earthquake Engineering & Structural Dynamics, 43(9), pp.1361-1380.

Kolay, C. and Ricles, J. (2017). Force-Based Frame Element Implementation for Real-Time Hybrid Simulation Using Explicit Direct Integration Algorithms. *Journal of Structural Engineering*, 144(2).

Kolsky, H. (1949). An Investigation of the Mechanical Properties of Materials at very High Rates of Loading. *Proceedings of the Physical Society*. Section B, 62(11), pp.676-700.

Kong, S., Remennikov, A. and Uy, B. (2012). Numerical simulation of the response of non-composite steel-concrete-steel sandwich panels to impact loading. *AJSE*, 12(3).

Körmeling, H. and Reinhardt, H. (1987). Strain rate effects on steel fibre concrete in uniaxial tension. *International Journal of Cement Composites and Lightweight Concrete*, 9(4), pp.197-204.

Kotsovos, M. (2015). Finite-Element Modelling of Structural Concrete: Short-Term Static and Dynamic Loading Conditions. CRC Press.

Kubin J, Fahjan M. and Tan MT (2008). Comparison Of Practical Approaches For Modelling Shearwalls In Structural Analyses Of Buildings. *The 14th World Conference on Earthquake Engineering*, October 12-17, 2008, Beijing, China.

Kujawski, J. (1988). Stable semi-explicit algorithms for non-linear dynamic problems. *Earthquake Engineering & Structural Dynamics*, 16(6), pp.855-865.

Kuo Mo Hsiao, Fang Yu Hou and Spiliopoulos, K. (1988). Large displacement analysis of elasto-plastic frames. *Computers & Structures*, 28(5), pp.627-633.

Lan, S., Lok, T. and Heng, L. (2005). Composite structural panels subjected to explosive loading. *Construction and Building Materials*, 19(5), pp.387-395.

Lee, H. and Kim, S. (2015). Structural behavior of SC panel subjected to impact loading using finite element analysis. *Nuclear Engineering and Design*, 295, pp.96-105.

Liew, J. and Wang, T. (2011). Novel Steel-Concrete-Steel Sandwich Composite Plates Subject to Impact and Blast Load. *Advances in Structural Engineering*, 14(4), pp.673-688.

Liew, J., Sohel, K. and Koh, C. (2009). Impact tests on steel–concrete–steel sandwich beams with lightweight concrete core. *Engineering Structures*, 31(9), pp.2045-2059.

Limberger, E., Brandes, K., & Herter, J. (1982). Influence of mechanical properties of reinforcing steel on the ductility of reinforced concrete beams with respect to high strain rates. In Plauk, G. (Ed.). *Concrete structures under impact and impulsive loading*, p. 656. Germany.

Lipscy, P., Kushida, K. and Incerti, T. (2013). The Fukushima Disaster and Japan's Nuclear Plant Vulnerability in Comparative Perspective. *Environmental Science & Technology*, 47(12), pp.6082-6088.

Lok, T. and Zhao, P. (2004). Impact Response of Steel Fiber-Reinforced Concrete Using a Split Hopkinson Pressure Bar. *J. Mater. Civ. Eng.*, 16(1), pp.54-59.

Lok, T., Zhao, P. and Lu, G. (2003). Using the split Hopkinson pressure bar to investigate the dynamic behaviour of SFRC. *Magazine of Concrete Research*, 55(2), pp.183-191.

Malvar, L. (1998). Review of Static and Dynamic Properties of Steel Reinforcing Bars. *ACI Materials Journal*, 95(5), pp.609-616.

Marion Bruenglinghaus, E. (2015). Nuclear power plants, world-wide. [Online] Euronuclear.org. Available at: http://www.euronuclear.org/info/encyclopedia/n/nuclear-power-plant-world-wide.htm [Accessed 7 Aug. 2017].

Mari, A. (1984). Nonlinear Geometric, Material and Time Dependent Analysis of Three Dimensional Reinforced and Prestressed Concrete Frames. Report No.

SESM 84-10, Division of Structural Engineering and Structural Mechanics, University of California, Berkeley.

Menegotto, M. and Pinto, P. (1973). Method of Analysis for Cyclically Loaded Reinforced Concrete Plane Frames Including Changes in Geometry and Nonelastic Behavior of Elements under Combined Normal Force and Bending. *In: IABSE symposium on resistance and ultimate deformability of structures acted on by well-defined repeated loads*. Final Report, Lisbon, pp.15-22.

Meyer, C., Roufaiel, M.S. and Arzoumanidis, S. G. (1983). Analysis of Damaged Concrete Frames for Cyclic Loads. *Earthquake Engineering and Structural Dynamics*, Vol. 11, pp. 207-228.

Miranda, I., Ferencz, R. and Hughes, T. (1989). An improved implicit-explicit time integration method for structural dynamics. *Earthquake Engineering & Structural Dynamics*, 18(5), pp. 643-653.

Mo, Y.L. and Roberts, R.H. (2013). Carbon Nanofiber Concrete for Damage Detection of Infrastructure, Advances in Nanofibers, Dr. Russel Maguire (Ed.), ISBN: 978-953-51-1209-9, InTech, DOI: 10.5772/57096. Available from: http://www.intechopen.com/books/advances-in-nanofibers/carbon-nanofiber-concrete-for-damage-detection-of-infrastructure.

Mullapudi, T. and Ayoub, A. (2010). Modeling of the seismic behavior of shear-critical reinforced concrete columns. *Engineering Structures*, 32(11), pp.3601-3615.

Mullapudi, T., Gao, D. and Ayoub, A. (2013). Non-destructive evaluation of carbon nanofibre concrete. *Magazine of Concrete Research*, 65(18), pp.1081-1091.

Mzconsultinginc.com, (2013). mzconsultinginc.com | The British are coming – new nuclear committed in the UK. [Online] Available at: http://mzconsultinginc.com/?p=558 [Accessed 7 Aug. 2017].

Nataraja, M., Dhang, N. and Gupta, A. (1999). Stress–strain curves for steel-fiber reinforced concrete under compression. *Cement and Concrete Composites*, 21(5-6), pp.383-390.

Neuenhofer, A. and Filippou, F. (1997). Evaluation of nonlinear frame finite-element models. *Journal of Structural Engineering*, 123(7), pp.958–966.

Newmark, N. (1959). A method of computation for structural dynamics. J. Engineering Mechanics, ASCE, 85, pp.67-94.

Ngo, T., Mendis, P., Gupta, A. and Ramsay, J. (2007). Blast Loading and Blast Effects on Structures – An Overview. *EJSE International*, Special Issue: Loading on Structures, pp.76-91.

Nguyen, D. and Tran, T. (2016). A Corotational Formulation for Large Displacement Analysis of Functionally Graded Sandwich Beam and Frame Structures. *Mathematical Problems in Engineering*, 2016, pp.1-12.

Nukala, P. K. (1997). Three-dimensional second-order inelastic analysis of steel frames. PhD thesis, Purdue Univ., West Lafayette, Ind.

Otani, S. (1974). Inelastic Analysis of R/C Frame Structures. *Journal of Structural Engineering, ASCE*, 100 (ST7) pp.1433-1449.

O'Brien EJ, Keogh DL (1999) Bridge deck analysis. E & FN Spon, London.

Pająk, M. (2011). The Influence of the Strain Rate on the Strength of Concrete Taking Into Account the Experimental Techniques. *ACEE Journal*, 3/2011, pp.77-86.

Perrone N, Bhadra P. (1984). Simplified large deflection mode solutions for impulsively loaded, viscoplastic, circular membranes. *J Appl Mech*;51(3): pp.505-509.

Pezeshk, S. and Camp, C. (1995). An explicit time integration technique for dynamic analyses. *International Journal for Numerical Methods in Engineering*, 38(13), pp.2265-2281.

Pros, A., Diez, P. and Molins, C. (2011). Modeling steel fiber reinforced concrete: numerical immersed boundary approach and a phenomenological mesomodel for concrete-fiber interaction. *International Journal for Numerical Methods in Engineering*, 90(1), pp.65-86.

Rahai, A. and Nafari, S. (2013). A comparison between lumped and distributed plasticity approaches in the pushover analysis results of a pc frame bridge. *International Journal of Civil Engineering*, 11(4).

Riera, J. (1968), Full-scale aircraft impact test for evaluation of impact force, *Nucl. Engrg. Des.*, 8 (1968), pp.415-426.

Ross, C., Thompson, P. and Tedesco, J. (1989). Split-Hopkinson Pressure-Bar tests on Concrete and Mortar in Tension and Compression. *ACI Materials Journal*, 86(5), pp.475–481.

Saatci, S. and Vecchio, F. (2009.a). Nonlinear Finite Element Modeling of Reinforced Concrete Structures under Impact Loads. *ACI Structural Journal*, 106(5).

Saatci, S. and Vecchio, F. (2009.b). Effects of Shear Mechanisms on Impact Behavior of Reinforced Concrete Beams. *ACI Structural Journal*, 106(1).

Sadiq, M., Xiu Yun, Z. and Rong, P. (2014). Simulation analysis of impact tests of steel plate reinforced concrete and reinforced concrete slabs against aircraft impact and its validation with experimental results. *Nuclear Engineering and Design*, 273, pp.653-667.

Sanchez, F. and Sobolev, K. (2010). Nanotechnology in concrete – A review. Construction and Building Materials, 24(11), pp.2060-2071.

Sbia, L., Peyvandi, A., Soroushian, P., Lu, J. and Balachandra, A. (2014). Enhancement of Ultrahigh Performance Concrete Material Properties with Carbon Nanofiber. *Advances in Civil Engineering*, 2014, pp.1-10.

Scott, B., Park, R. and Priestley, M. (1982). Stress-Strain Behavior of Concrete Confined by Overlapping Hoops at Low and High Strain Rates. *ACI Journal Proceedings*, 79(1), pp.13-27.

Scott, M. and Hamutçuoğlu, O. (2008). Numerically consistent regularization of force-based frame elements. *International Journal for Numerical Methods in Engineering*, 76(10), pp.1612-1631.

Scrivener, K. and Kirkpatrick, R. (2008). Innovation in use and research on cementitious material. *Cement and Concrete Research*, 38(2), pp.128-136.

Segel, L. and Handelman, G. (2007). Mathematics applied to continuum mechanics. Philadelphia: *Society for Industrial and Applied Mathematics*, p.260.

Sluys, L. J., and De Borst, R. (1992). Computational modelling of impact tests on steel fibre reinforced concrete beams. HERON, 37, 315.

Sohel, K. and Liew, J. (2014). Behaviour of steel–concrete–steel sandwich slabs subject to impact load. *Journal of Constructional Steel Research*, 100, pp.163-175.

Sohel, K., Liew, J. and Zhang, M. (2011). Analysis and design of steel-concrete composite sandwich systems subjected to extreme loads. *Frontiers of Architecture and Civil Engineering in China*, 5(3), pp.278-293.

Sohel, K., Richard Liew, J. and Koh, C. (2015). Numerical modelling of lightweight Steel-Concrete-Steel sandwich composite beams subjected to impact. *Thin-Walled Structures*, 94, pp.135-146.

Soleimani, D., Popov, E.P. and Bertero, V. V. (1979). Nonlinear Beam Model for R/C Frame Analysis. 7th ASCE Conference on Electronic Computation, St. Louis.

Spacone, E., Filippou, F. and Taucer, F. (1996). Fibre beam-column model for non-linear analysis of r/c frames: part i. formulation. *Earthquake Engineering & Structural Dynamics*, 25(7), pp.711-725.

Spacone, E. and Filippou, F. (1992). A Beam Model for Damage Analysis of Reinforced Concrete Structures Under Seismic Loads. Department of Civil Engineering, University of California.

Sun, J., Lee, K. and Lee, H. (2000). Comparison of implicit and explicit finite element methods for dynamic problems. *Journal of Materials Processing Technology*, 105(1-2), pp.110-118.

Takayanagi, T. and Schnobrich, W. (1979). Non Linear Analysis of Coupled Wall Systems. *Earthquake Engineering and Structural Dynamics*, Vol. 7, pp.1-22.

Tao, M. and Nie, J. (2014). Element mesh, section discretization and material hysteretic laws for fiber beam–column elements of composite structural members. *Materials and Structures*, 48(8), pp.2521-2544.

Tatasteelconstruction.com. (2017). About Us, About Tata Steel Construction, Company Details | Tata Steel. [online] Available at: https://www.tatasteelconstruction.com/en_GB/About-us [Accessed 7 Aug. 2017].

Taucer, F., Spacone, E. and Filippou, F.e. (1991). A Fiber Beam-Column Element for Seismic Response Analysis of Reinforced Concrete Structures. Report EERC 91-17, Earthquake Engineering Research Center, University of California, Berkeley.

Taylor, R. (2014). FEAP - Finite Element Analysis Program. Berkeley: University of California.

Tenek, L. (2015). A Beam Finite Element Based on the Explicit Finite Element Method. *International Review of Civil Engineering (IRECE)*, 6(5), p. 124.

Timoshenko, S. and Goodier, J. (1951). Theory of elasticity, by S. Timoshenko and J.N. Goodier. 2nd ed. New York: McGraw~Hill Book Co., Inc., Princeton.

Trujillo, D. (1977). An unconditionally stable explicit algorithm for structural dynamics. *International Journal for Numerical Methods in Engineering*, 11(10), pp.1579-1592.

Turner, M., Clough, R., Martin, H. and Topp, L. (1956). Stiffness and Deflection Analysis of Complex Structures. *Journal of the Aeronautical Sciences*, 23(9), pp.805-823.

Tyson, B., Abu Al-Rub, R., Yazdanbakhsh, A. and Grasley, Z. (2011). Carbon Nanotubes and Carbon Nanofibers for Enhancing the Mechanical Properties of Nanocomposite Cementitious Materials. *J. Mater. Civ. Eng.*, 23(7), pp.1028-1035.

Westinghousenuclear.com. (2017). AP1000 Pressurized Water Reactor | Westinghouse Nuclear. [online] Available at: http://www.westinghousenuclear.com/New-Plants/AP1000-PWR [Accessed 6 Oct. 2017].

Wiki.csiamerica.com. (2017). P-Delta effect for a cantilevered column - Test Problems - Computers and Structures, Inc. - Technical Knowledge Base. [online] Available at: https://wiki.csiamerica.com/display/tp/P-Delta+effect+for+a+cantilevered+column [Accessed 6 Sep. 2017].

Williams, F. (1964). An approach to the non-linear behaviour of the members of a rigid jointed plane framework with finite deflections. *The Quarterly Journal of Mechanics and Applied Mathematics*, 17(4), pp.451-469.

Wilson, E. (1998). Three dimensional static and dynamic analysis of structures. Berkeley, Calif.: Computers and Structures Inc.

World-nuclear.org. (2017). World Energy Needs and Nuclear Power | Energy Needs | Nuclear Energy meeting Energy Needs - World Nuclear Association. [online] Available at: http://www.world-nuclear.org/information-library/current-and-future-generation/world-energy-needs-and-nuclear-power.aspx [Accessed 18 Dec. 2017].

Xu, Z., Hao, H. and Li, H. (2012). Mesoscale modelling of fibre reinforced concrete material under compressive impact loading. *Construction and Building Materials*, 26(1), pp.274-288.

Yang, D., Jung, D., Song, I., Yoo, D. and Lee, J. (1995). Comparative investigation into implicit, explicit, and iterative implicit/explicit schemes for the simulation of sheet-metal forming processes. *Journal of Materials Processing Technology*, 50(1-4), pp.39-53.

Yaw, L. (2009). 2D Corotational Beam Formulation. [ebook] Available at: https://gab.wallawalla.edu/~louie.yaw/Co-rotational_docs/2Dcorot_truss.pdf [Accessed 1 Sep. 2017].

Yina, S. (2011). An Unconditionally Stable Explicit Method for Structural Dynamics. *Procedia Engineering*, 14, pp.2519-2526.

Yoshida, Y., Masuda, N., Morimoto, T. and Hirosawa, N. (1980). An incremental formulation for computer analysis of space framed structures. *Journal of Structural Mechanics and Earthquake Engineering*, JSCE 300, pp.21-32. (in Japanese)

Youssef, M., Chowdhury, A. and Meshaly, M. (2014). Seismic capacity of reinforced concrete interior flat plate connections. *Bulletin of Earthquake Engineering*, 13(3), pp.827-840.

Yousuf, M., Uy, B., Liew, R., Tao, Z. and Shasha, W. (2011). Dynamic properties of concrete strength using Split Hopkinson's Pressure Bar (SHPB) test. *In: International Conference on Concrete*.

Zeris, C. A. and Mahin, S. A. (1988). Analysis of Reinforced Concrete Beam-Columns Under Uniaxial Excitation. *Journal of Structural Engineering*, ASCE, 114 (ST4), pp.804-820.

Zhang, H., Gao, Y., Li, F., Lu, F. and Sun, H. (2013). Experimental study on dynamic properties and constitutive model of polypropylene fibre concrete under high-strain rates. *European Journal of Environmental and Civil Engineering*, 17(sup1), pp.s294-s303.

Zhan, T., Wang, Z. and Ning, J. (2015). Failure behaviors of reinforced concrete beams subjected to high impact loading. *Engineering Failure Analysis*, 56, pp.233-243.

Zhou, X. and Hao, H. (2008). Modelling of compressive behaviour of concrete-like materials at high strain rate. *International Journal of Solids and Structures*, 45(17), pp.4648-4661.

Zhu, X., Pan, R. and Sun, F. (2013). FEM Analysis of Impact Tests for Steel Plate Concrete Panels against Scaled-Aircraft Impact. *Applied Mechanics and Materials*, 477-478, pp.777-783.

APPENDIX 1

THE EXTERNAL GEOMETRIC STIFFNESS MATRIX

The external geometric stiffness matrix is composed of 6 by 6 matrix.

$$K_G = \begin{bmatrix} K_{11} & K_{12} & 0 & K_{14} & K_{15} & 0 \\ K_{21} & K_{22} & 0 & K_{24} & K_{25} & 0 \\ 0 & 0 & 0 & 0 & 0 & 0 \\ K_{41} & K_{42} & 0 & K_{44} & K_{45} & 0 \\ K_{51} & K_{52} & 0 & K_{54} & K_{55} & 0 \\ 0 & 0 & 0 & 0 & 0 & 0 \end{bmatrix}$$

The non-zero terms are defined as follows:

$$K_{11} = -(Q_1 + Q_2)\frac{-(y_{21} + v_{21})2L\frac{\partial L}{\partial u_1}}{L^4} - Q_3\frac{-L - (x_{21} + u_{21})\frac{\partial L}{\partial u_1}}{L^2}$$

$$K_{12} = (Q_1 + Q_2)\frac{-L^2 - (x_{21} + u_{21})2L\frac{\partial L}{\partial u_1}}{L^4} - Q_3\frac{-(y_{21} + v_{21})\frac{\partial L}{\partial u_1}}{L^2}$$

$$K_{14} = (Q_1 + Q_2)\frac{-(y_{21} + v_{21})2L\frac{\partial L}{\partial u_1}}{L^4} + Q_3\frac{-L - (x_{21} + u_{21})\frac{\partial L}{\partial u_1}}{L^2}$$

$$K_{15} = -(Q_1 + Q_2)\frac{-L^2 - (x_{21} + u_{21})2L\frac{\partial L}{\partial u_1}}{L^4} + Q_3\frac{-(y_{21} + v_{21})\frac{\partial L}{\partial u_1}}{L^2}$$

$$K_{21} = -(Q_1 + Q_2)\frac{-L^2 - (y_{21} + v_{21})2L\frac{\partial L}{\partial v_1}}{L^4} - Q_3\frac{-(x_{21} + u_{21})\frac{\partial L}{\partial v_1}}{L^2}$$

$$K_{22} = (Q_1 + Q_2)\frac{-(x_{21} + u_{21})2L\frac{\partial L}{\partial v_1}}{L^4} - Q_3\frac{-L - (y_{21} + v_{21})\frac{\partial L}{\partial v_1}}{L^2}$$

$$K_{24} = (Q_1 + Q_2)\frac{-L^2 - (y_{21} + v_{21})2L\frac{\partial L}{\partial v_1}}{L^4} + Q_3\frac{-(x_{21} + u_{21})\frac{\partial L}{\partial v_1}}{L^2}$$

$$K_{25} = -(Q_1 + Q_2)\frac{-(x_{21} + u_{21})2L\frac{\partial L}{\partial v_1}}{L^4} + Q_3\frac{-L - (y_{21} + v_{21})\frac{\partial L}{\partial v_1}}{L^2}$$

$$K_{41} = -(Q_1 + Q_2)\frac{-(y_{21} + v_{21})2L\frac{\partial L}{\partial u_2}}{L^4} - Q_3\frac{-L - (x_{21} + u_{21})\frac{\partial L}{\partial u_2}}{L^2}$$

$$K_{42} = (Q_1 + Q_2)\frac{L^2 - (x_{21} + u_{21})2L\frac{\partial L}{\partial u_2}}{L^4} + Q_3\frac{-(y_{21} + v_{21})\frac{\partial L}{\partial u_2}}{L^2}$$

$$K_{44} = (Q_1 + Q_2)\frac{-(y_{21} + v_{21})2L\frac{\partial L}{\partial u_2}}{L^4} + Q_3\frac{L - (x_{21} + u_{21})\frac{\partial L}{\partial u_2}}{L^2}$$

$$K_{45} = -(Q_1 + Q_2)\frac{L^2 - (x_{21} + u_{21})2L\frac{\partial L}{\partial u_2}}{L^4} + Q_3\frac{-(y_{21} + v_{21})\frac{\partial L}{\partial u_2}}{L^2}$$

$$K_{51} = -(Q_1 + Q_2)\frac{L^2 - (y_{21} + v_{21})2L\frac{\partial L}{\partial v_2}}{L^4} - Q_3\frac{-(x_{21} + u_{21})\frac{\partial L}{\partial v_2}}{L^2}$$

$$K_{52} = (Q_1 + Q_2)\frac{-(x_{21} + u_{21})2L\frac{\partial L}{\partial v_2}}{L^4} - Q_3\frac{L - (y_{21} + v_{21})\frac{\partial L}{\partial v_2}}{L^2}$$

$$K_{54} = (Q_1 + Q_2)\frac{L^2 - (y_{21} + v_{21})2L\frac{\partial L}{\partial v_2}}{L^4} + Q_3\frac{-(x_{21} + u_{21})\frac{\partial L}{\partial v_2}}{L^2}$$

$$K_{55} = -(Q_1 + Q_2)\frac{-(x_{21} + u_{21})2L\frac{\partial L}{\partial v_2}}{L^4} + Q_3\frac{L - (y_{21} + v_{21})\frac{\partial L}{\partial v_2}}{L^2}$$

Where:

$$\frac{\partial L}{\partial u_1} = -\frac{x_{21} + u_{21}}{L}$$

$$\frac{\partial L}{\partial u_2} = \frac{x_{21} + u_{21}}{L}$$

$$\frac{\partial L}{\partial v_1} = -\frac{y_{21} + v_{21}}{L}$$

$$\frac{\partial L}{\partial v_2} = \frac{y_{21} + v_{21}}{L}$$

Such that:

$$y_{21} = y_2 - y_1$$

$$x_{21} = x_2 - x_1$$

Similarly:

$$u_{21} = u_2 - u_1$$

$$v_{21} = v_2 - v_1$$

And $x_1, x_2, u_1, u_2, y_1, y_2, v_1$& v_2 were defined in figure 3.3.